UNIVERSITY OF OKLAHOMA

GRADUATE COLLEGE

ACOUSTIC ANISOTROPY MEASURMENETS AND CALIBRATION OF THE NON-HYDROSTATIC IN-SITU STRESSES IN A WELLBORE

A DISSERTATION

SUBMITTED TO THE GRADUATE FACULTY

in partial fulfillment of the requirements for the

degree of

Doctor of Philosophy

By

ASHRAF AL-TAHINI
Norman, Oklahoma
2007

ACOUSTIC ANISOTROPY MEASURMENETS AND CALIBRATION OF THE NON-HYDROSTATIC IN-SITU STRESSES IN A WELLBORE

A DISSERTATION APPROVED FOR THE
MEWBOURNE SCHOOL OF PETROLEUM AND GEOLOGICAL ENGINEERING

BY

_____
Dr. Younane Abousleiman (Chair)

_____
Dr. Carl Sondergeld

_____
Dr. Chandra Rai

_____
Dr. Dean Oliver

_____
Dr. Subhash Shah

_____
Dr. Roger Slatt

Acknowledgement

I would like to offer sincere thanks and appreciation to my major advisor, Dr. Younane Abousleiman, for suggesting the research topic and offering guidance throughout this work. I appreciate his professional advisement as well as providing conducive environment for research at the Poromechanics Institute, University of Oklahoma. It is a great honor for me to be one of his students and to have the chance to sharpen my knowledge through him. I extend my appreciation to the members of the dissertation committee, Dr. Carl Sondergeld, Dr. Chandra Rai, Dr. Dean Oliver, Dr. Subhash Shah, and Dr. Roger Slatt for sharing with me their valuable professional experience in this work. I would also like to thank the members of the Poromechanics consortium at the University of Oklahoma for their discussion and sharing their knowledge, which certainly improved the quality of this work. I am very thankful to my peers and friends at the Poromechanics Institute and at the Petroleum Engineering Department for their support. Special thanks are extended to John Brumley for his help, support, and discussion in the experimental work. Also, I would like to thank Dr. Jieliang Pan for his help and discussion in the numerical work.

I am greatly indebted to my parents and family members; no words can adequately describe my thankfulness for their understanding, love, sacrifice and support. It is to them I dedicated my education. I would like to acknowledge the invaluable help provided by my academic advisors Kathy Fry and Hashim

Mukhtar at Aramco Service Company in Houston. Finally, I would like to thank Saudi Aramco Oil Company for their financial support, which made this work possible, and the Researches and Development Center at Saudi Aramco for their confidence in my technical abilities.

Table of Contents

List of Tables

List of Illustrations

Abstract

In-situ stress induced anisotropy and inherent rock formation anisotropy have in many instances been hard to distinguish by most deep in-situ tools designed to estimate the deep earth stress anisotropy and/or rock inherent anisotropy. In the oil and gas industry, in particular, the prior knowledge of the magnitude of in-situ stresses is essential in many aspects including exploration, well planning, reservoir stimulation, reservoir subsidence, and production. Present techniques for measuring rock stresses in a borehole can predict two out of the three principal stresses with acceptable engineering errors. These are the vertical and the minimum horizontal stresses. However, the measurement of the maximum horizontal stress remains the least explored. Moreover, the presence of intrinsic rock anisotropy around the borehole, along with the in-situ stress anisotropy, makes an accurate estimation of the latter extremely challenging when using acoustic techniques.

The purpose of the work reported in this dissertation is to estimate experimentally the effect of both inherent and stress-induced anisotropies on rock mechanical properties and on the in-situ stress measurements within the geometry of the borehole for different types of rock. In particular, the effective in-situ stress estimation is immediately linked to the pore pressure coefficients (also known as Biot's effective stress coefficients), which relate total stresses with pore pressure and weighs the effect of the pore pressure on the value of effective stresses according to Terzaghi's principle.

The role of both inherent and stress-induced anisotropies on stiffness components, elastic moduli, and Biot's pore pressure coefficients using both acoustic and quasi-static measurements is first investigated. Lyons Colorado sandstone cores with observable finely-layered dipping beds are assumed to exhibit a transverse inherent anisotropy. The core samples are used and tested under a non-hydrostatic state of stress to emphasize and maximize both inherent and stress-induced effects on the measurements. The effect of stress-induced anisotropy appears to have significant control on measured stiffness components, elastic moduli, and Biot's effective stress coefficients compared with inherent anisotropy effect. For example, the presence of transverse inherent anisotropy in these sandstones has shown an increase in the magnitude of the Biot's effective stress parameter in transverse plane by 16% whereas a reduction of 60% is observed in the same plane due to the stress-induced anisotropy over an applied stress range of 21,000 psi.

In the second part of this work, the technique of estimating the in-situ stresses is revisited by studying experimentally the effect of stresses on borehole strains, displacements, and acoustic wave velocities within the theory of elasticity. The experiments involve measurement of acoustic velocities (compressional and shear), radial, axial and transversal strains, and corresponding displacements around a borehole for different rock types including Berea sandstone, chalk, white limestone and Pierre shale. The borehole strain, displacement, and velocity measurements were first conducted on an aluminum block sample to validate the

measurements by comparing them with the theoretical behavior of such medium from the dynamic and static equations of elasticity. The borehole acoustic measurements for aluminum showed constant velocities as a function of stress indicating that properties of the material do not vary with stress (i.e., Young's modulus and Poisson's ratio). The basic understanding of aluminum behavior under applied stress was then extended for the rock samples.

Quasi-static and dynamic uniaxial compressive tests were performed initially on cylindrical core samples corresponding to the different types of rock to evaluate their mechanical properties and their stress dependency which then were used to calibrate the measurements on large cubical block samples. Furthermore, the uniaxial compressive tests under small strain loading and unloading procedures were used to correlate the quasi-static and dynamic behaviors of each rock type and extrapolate them with the measurements performed on the large cubical block samples with the borehole geometry included.

The measured induced tangential compressive stresses at the borehole for the tested rock materials were found to be non-linearly correlated with the external applied stress at the boundary. As a result, assumptions of borehole stress concentration factor of 3 based on Kirsch's equations for a uniaxial stress field may under or over estimate the actual induced compressive stresses at the borehole wall in rocks. Four empirical correlations were reported for each rock type being tested that estimate the maximum induced compressive stresses at the

borehole by knowing the uniaxial far field stresses. The measurements show that stress magnitude measured at the wellbore wall varies considerably depending on the type of rocks being tested and their stress dependence has to be taken into account for stress estimation. Borehole failures, including breakouts, were observed during the rock experiments and confirmed from borehole strain measurements. The applied boundary stress level at which tensile failure and breakouts occur at the borehole is observed to be correlated with the measured tensile strength from Brazilian tests and the uniaxial compressive strength of each tested rock material, respectively.

The comparison of the static and dynamic stress-strain data (measured from borehole strain gages and velocities) indicates that velocities have to be calibrated according to the rock type to take into account the specific rock mechanical properties and their stress anisotropy dependence when stresses are estimated from the velocities in and around the borehole geometry. Also, estimated in-situ stresses from borehole velocity measurements based on the non-linear model that is currently used by the industry showed significant difference in the magnitude of the actual experimentally measured stresses; yet, an empirical calibration at this stage is necessary for each type of reservoir.

Chapter 1

Introduction

The knowledge of the in-situ stresses is essential for many applications in the oil and gas industry such as exploration; including drilling and borehole stability, well planning; including casing set points and depletion, reservoir stimulation; including hydraulic fracturing and acidizing, reservoir subsidence; including compaction and pore collapse, and production; including enhance oil recovery and sand control.

The in-situ stress state is characterized by the magnitude and direction of three principal stresses: vertical stress (overburden stress), σ_v, and two horizontal stresses known as maximum horizontal stress, σ_H, and minimum horizontal stress, σ_h. The vertical stress can be reliably obtained from the average density of the overlying rock. However, estimating the other two principal stresses is important to fully characterize the complete in-situ stress state, and to be able to conduct geomechanical analysis and interpretation of problems and solutions.

1.1 Importance of In-situ Rock Stress

Knowledge of rock in-situ stress field is of fundamental importance in a wide range of applications in petroleum engineering, civil engineering, mining, as well as in geology and geophysics. In petroleum engineering, stability of the borehole due to the in-situ stresses is one of the major challenges. The in-situ stress state, including the stress magnitude and orientation, affects the stability of oil and gas wells. Stress concentration around the excavation walls may be large enough to overstress the rock, creating tensile or shear failures. In deep environments, where most of the current oil and gas wells are drilled, the stability of the borehole is one of the priorities in drilling design, borehole completion, and critical decision making. The knowledge of in-situ stress is essential not only in drilling but also in production and reservoir management. In production, the knowledge of in-situ stress field is important in the hydraulic fracturing of oil and gas formations. Also, modeling of water flooding and further increase of recovery requires that the displacement processes are understood, especially in relation to the stress dependency (Lykke and Foged, 2003). In reservoir management, the change in the in-situ stress field must be known during reservoir depletion. Oil and gas production causes changes in the effective stress field in a reservoir, resulting in reservoir compaction and subsidence (Mulders, 2003). Moreover, in-situ stress field can change some rock properties such as porosity and/or permeability, for example, compressive stresses tend to close pore space whereas tensile stresses tend to open them (Amadei and Stephansson, 1997).

1.2 In-situ Stress Components

The in-situ stresses acting within a rock formation could be defined by three mutually perpendicular components, called principal stresses. In general, one principal stress axis is vertical stress, σ_v, due to the overburden load generated by the weight of the overlying rock. The other two principal stresses, called horizontal stresses (maximum horizontal stress, σ_H, and minimum horizontal stress, σ_h), are perpendicular to σ_v and at 90˚ angle in the plane. Figure 1-1 shows a schematic diagram of a vertical borehole in a formation subjected to the three principal stresses. The stress state has also other classifications or terms that are commonly used by the oil and gas industry as summarized in Table 1-1 (as referring to the boxed numbers in Figure 1-2).

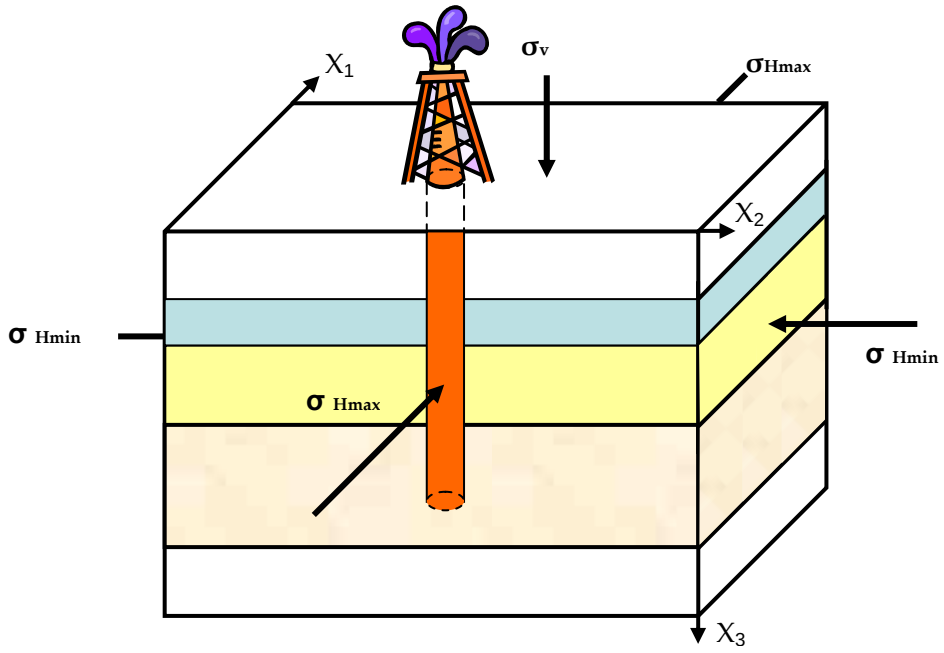

Figure 1-1: Schematic of a borehole in the presence of formation principal stresses.

1	Tectonic stress	The stress state caused by tectonic plate movement.
2	Gravitational stress	The stress state caused by the weight of the rock above.
1&2	Natural stress	The *in situ* stress which exists prior to engineering
1&2	Regional stress	The stress state in relatively large geological domain.
1&2	Far-field stress	The stress state beyond the near-field.
3	local stress	The stress state in small domain.
3	Near field stress	The stress state in the region of an engineering perturbation.
3	Induced stress	The natural stress state as perturbed by engineering.
4	Residual stress	A locked-in stress state caused by previous tectonic activity but currently acting.
4	Thermal stress	The stress state caused by temperature change.
-	Palaeostress	A previous natural stress that is no longer acting.

Table 1-1: Explanation of stresses classifications and terms as referring to the boxed numbers in Figure 1-2 (Hudson, 2003).

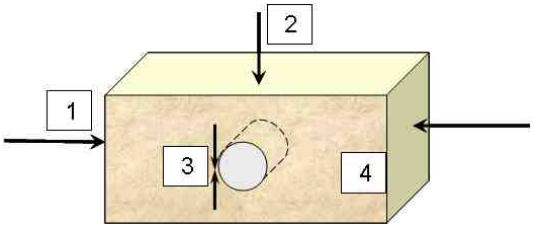

Figure 1-2: Types of stresses (see Table 1-2 for the list of terms (Hudson, 2003).

1.3 Measurements of In-situ Stress Components

Many techniques are in current use for the determination of the in-situ rock stresses. Ljunggren et al., (2003) have published a comprehensive review of stress determination methods. They classified the methods for rock in-situ stress determination into two parts. The first classification is methods that disturb the in-situ rock behavior, i.e., by induced strains, deformations or fracture opening, which includes (1) hydraulic methods, such as hydraulic fracturing and hydraulic tests on pre-existing fractures (HTPF) (2) borehole relief methods and (3) surface relief methods. The second classification is methods that are based on the rock observation without any major influence from the measuring tool, and includes

(1) core-discing, (2) borehole breakouts, (3) acoustic methods such as measured velocity and Kaiser effect, and (4) strain recovery method. Table 1.2 shows an overview of these methods and their limitations.

Methods	2D/3D	Advantages	Limitations	Suitable for
Overcoring	2D/3D	Most developed technique in both theory and practice.	Scattering due to small rock volume. Requires drill rig.	Measurements, depth down to 1000 m.
Doorstopper	2D	Works in jointed and high stressed rocks.	Only-two dimensional. Required drill rig.	For weak or highly stresses rocks.
Hydraulic fracturing	2D	Measurements in existing hole. Low scattering in the results. Involves a fairly large rock volume, quick.	Only two-dimensions. There are theoretical limitations in the evaluation of σ_H. Disturbs water chemistry.	Shallow to deep measurements. To obtain stress profiles.
HTPF	2D/3D	Measurements in existing hole can be applied when high stresses exist and over-coring and hydraulic fracturing fail.	Time-consuming. Requires existing fractures in the hole with varying strikes and dips.	Of interest in situations where other methods fail.
Coring discing	2D	Existing information, which is obtained already at drilling stage.	Only qualitative estimation.	Estimation of stress at early stage.
Borehole breakouts	2D	Existing information, obtained at an early stage. Relatively quick.	Restricted to information on Orientation. Theory needs to be further developed to infer the stress magnitude.	Occurs mostly in deep holes.
Focal mechanisms	2D	For great depths.	Information only from great depths.	
Kaiser effect	2D/3D	Simple measurements.	Relatively low reliability.	Rough estimates.
ASR/DSCA RACOS	2D/3D	Usable for great depths.	Complicated measurements on the microscale, sensitive to several factors.	Estimation at great depth.
Back calculation	2D	Quick and simple. High certainty due to large rock volume.	Theoretically not unique solution.	Can only be used during construction.
Analysis of geological data	2D/3D	Low cost.	Very rough estimation low reliability.	At early stage of project.

Table 1-2: Stress measurement methods and key issues related to their applicability (Hudson et al., 2003).

Discussion of some of these methods is highlighted in this section. Hydraulic fracturing is one of the techniques widely used in the oil and gas operations for horizontal stress determination. In the hydraulic fracturing method, a fluid is

injected during a massive operation in a sealed-off interval to induce and propagate tensile fractures in a plane perpendicular to the minimum principal stress for the case of vertical wellbore as shown in Figure 1-3 (Hubbert and Willis, 1957). The hydraulic fracturing method allows a direct measurement of the minimum horizontal stress, σ_h, typical schematic of the field results are shown in Figure 1-3. Hubbert and Willis established the basic principles of hydraulic fracture initiation and propagation that have become the foundation for minimum in-situ stress measurements and made hydraulic fracturing to be one of the most accepted methods for determining the minimum horizontal in-situ stress component. The method is a good candidate for the measurement of the minimum horizontal stress, σ_h, the accuracy is in the range of ±5% (Ljunggren et al., 2003).

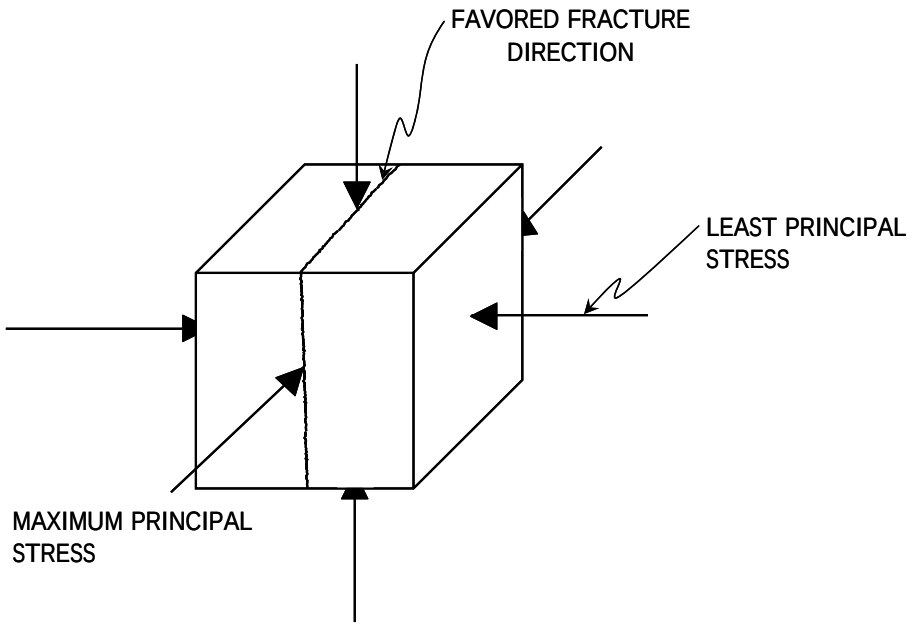

Figure 1-3: Stress element and preferred plane of fracture (Hubbert and Willis, 1957).

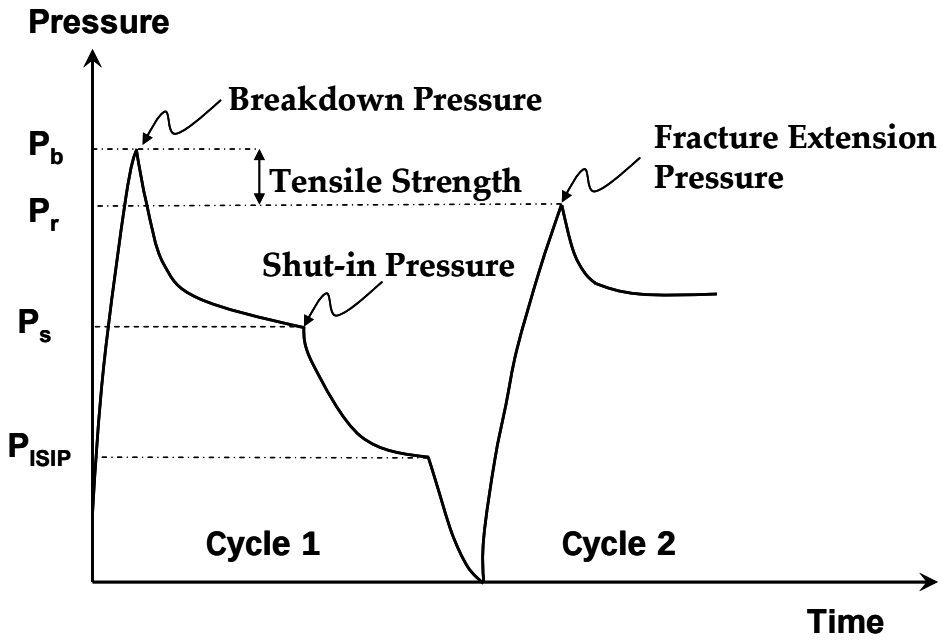

Figure 1-4: Idealized pressure-time recording on the surface during fracturing. P_b is the breakdown pressure; P_s is the shut in pressure; P_r is the re-opening pressure or fracture extension pressure and PISIP is the instantaneous shut-in pressure.

Recently, an acoustic technique is being used by the oil and gas industry to estimate the in-situ horizontal stresses. The technique utilizes the dependence of acoustic velocity around a borehole on stress to predict in-situ stresses. Extensive work was performed on acoustic technique to evaluate rock in-situ stresses by many researchers, i.e. Esmersoy et al., (1995), Sinha et al., (1996), and Plona et al., (1997), which helped in developing the technique and overcoming its limitations in the applications of stress measurements. However, the assumptions associated with in-situ stress estimation using acoustic technique, such as rock inherent anisotropy, affect the application of this technique. Moreover, the change in the velocity with stress is significant at low stress level, but becomes almost independent of stress at the higher stress level, thus limiting the applications of

the acoustic technique “Dipole Sonic Log”. The last two statements were the motivation behind this work and the main subject of the dissertation, where the consistency of this technique is evaluated through laboratory measurements as will be discussed in the following section.

1.4 Objectives, Initial Assumptions and Dissertation Outlines

In this section the dissertation objectives, assumptions used in generating and processing the experimental data, and outlines are presented. Future recommendations related to this topic are also given in the last chapter, titled Conclusions and Recommendations.

1.4.1 Objectives

The objectives of this dissertation can be summarized as follows:

- Identify and isolate the effect of inherent rock anisotropy from the rock induced stress anisotropy on cylindrical core samples.

- Establish empirical correlations for different rock types to estimate the stress from borehole velocity measurements on large cubical rock samples.

- Use the velocity measurements to evaluate the current modeling of borehole stresses estimation using dipole sonic log, which is commonly used by the industry, especially at high stress conditions where the change

in velocities is insignificant compared with the magnitude change of applied stress.

- Measure the magnitude of stress concentrations at borehole using borehole strain gages.

- Calibrate the velocity measurements (dynamic) with borehole strain measurements (quasi-static) around the borehole.

- Correlate borehole velocity measurements along (logging tool measurements) and across (radially) the borehole.

Achieving the above objectives with good measurements reliability is performed by:

- Calibrating the measurements with a large cube of aluminum and compare the measurements to the analytical solution in order to ensure the accuracy of the laboratory measurements before and after carrying out the technique on rock samples.

- Performing finite element elastic analysis using ABAQUS to simulate laboratory experiments and compare the numerical and analytical solutions with laboratory results.

1.4.2 Initial Assumptions

The assumptions used in generating and processing the experimental data can be summarized as follows:

- The geometry of the tested samples (6×6×6 inches) is considered large enough where the loading edge effects are minimal (based on the mean of the elastic solution).

- The borehole size (0.93 inches) is small relative to side length of the tested samples so that the distance from the borehole center to the outer boundaries is larger than 5R, where R is the borehole radius.

- Plane strain conditions: the block samples were considered to be infinitely long, so that the borehole strain along the axis of the borehole is negligible and does not affect the circumferential deformation.

- Homogeneity and isotropy: the samples are assumed to have the same properties at any point within the samples and along all directions. The assumption is reasonable for most of the tested block samples including Berea, chalk, and white limestone. However, the effect of anisotropy on the quasi-static and dynamic measurements is discussed in Chapter 3.

1.4.3 Dissertation Outlines

Following the introductory chapter, Chapter 2 of this dissertation includes a literature review of the major studies performed on the acoustic technique relevant to the work conducted in this dissertation. Chapter 3 includes a general introduction and literature review of the effect of the inherent and stress-induced anisotropy on rock properties and reviews the constitutive and field equations required to determine stiffness components, elastic moduli, and Biot's pore pressure coefficients in sandstones. Chapter 4 discusses in detail the experimental work including the procedures, material, and equipments used throughout this work. Chapter 5 discusses the numerical work including the stress and strain contour results for the cubical samples using ABAQUS. Chapter 6 presents the results and discussions of the experimental work including cylindrical core testing and large block sample testing. The conclusions of the dissertation are presented in Chapter 7.

Chapter 2

Literature Review

Several techniques are available for measuring in-situ stresses, but not all of them are capable of providing a complete description of the stress state including the magnitude and orientation of the principal stresses. The acoustic anisotropy technique using Dipole Sonic Log measurements around a borehole has become one of the popular methods used by the oil and gas field operations to provide the magnitude and orientation of the principal horizontal stresses. The method utilizes the formation acoustic waveforms velocity through an array of receivers on the logging tool in the presence of induced stresses around the wellbore to estimate the magnitude and orientation of the in-situ stresses.

2.1 Borehole Acoustic Anisotropy

The recent advances in borehole acoustic logging have extended the use of acoustic measurements beyond the ordinary geophysical applications for seismic interpretation and petrophysical analysis (Kane, 2001). The method of estimating the in-situ stresses from dipole sonic measurements has now been in use for some

years (Sinha et al., 2005). However, assumptions associated with in-situ stress estimation from the acoustic technique with respect to the rock type, shape, and structure or to the in-situ mechanical characteristics of the rock and its anisotropy, affect the existing data interpretation and models. Moreover, the velocity dependence on stress varies with rock formation which may limit the data interpretation from the acoustic technique.

Velocity anisotropy near and around the borehole may be caused by many phenomena and operational procedures, in particular, formation damage due to drilling, rock heterogeneity, and tensile and compressive fractures. In general, a porous medium undergoes anisotropic behavior when subjected to anisotropic type of loading when its measured acoustic signature is capable to detect material characteristics variations in different directions. This can be illustrated by different stress perturbation applied on a linear elastic porous medium as shown in Figure 2-1. In addition to loading, inherent rock anisotropy is also detectable by acoustic technique (i.e., Podio et al., 1968; King, 1969; and Jones and Wang, 1981). In the borehole geometry, all of these operational physical and mechanical phenomena, such as rock damage, rock inherent anisotropy, stress anisotropy, etc., could play an important role in the interpretation of acoustic data and possible stress anisotropy measurements in magnitude and direction.

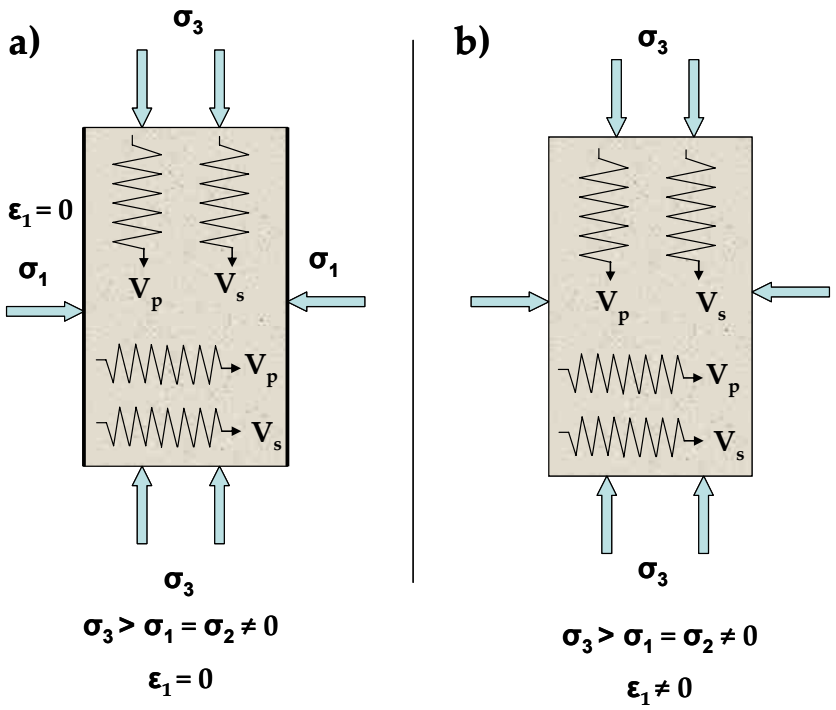

Figure 2-1: An example of acoustic velocity variations for a porous medium due to stress perpetuation, where: (a) represent a uniaxial loading with lateral strain = 0, as the case for reservoir subsidence, and (b) represent a triaxial stress state, as the case of a borehole.

2.1.1 Dipole Sonic Logging Tool

Dipole sonic logging tool is a technology in the industry which provides a capability of measuring stress induced anisotropy, direction and magnitude, from acoustic measurements in a borehole. It provides the capability of measuring the stress, anisotropy from the shear velocities propagation in the borehole direction (Winkler et al., 1998). Dipole shear velocity measurements are used to provide appropriate data to estimate the direction and magnitude of the in-situ stresses. The tool combines both monopole and dipole sonic acquisition capabilities. The transmitter section consists of a piezoelectric monopole transmitter and two electro-dynamic dipole transmitters perpendicular to each other as shown in

Figure 2-2. The monopole transmitter is used to excite compressional wave propagation in the formation by an electric pulse at high frequency. The dipole transmitters are operated at low frequency to excite the flexural wave along the borehole (Schlumberger, 2004).

In the dipole acoustic logging, the tool is lowered into the borehole and a flexural sound wave is generated by a dipole source at the bottom of the tool, and measured by dipole receivers oriented in the same direction at the top of the tool. The flexure wave mode is dispersive in that the wave speed varies with frequency. As a result, the recorded flexure waveforms are transformed to shear speed by incorporating corrections based on formation shear velocity, borehole size, borehole fluid velocity, and the frequency (Kane, 2001). The dependence of the flexure wave speed on frequency allows measuring the formation shear speed near and far from the borehole. At low frequencies (in the range of 1 to 5 kHz), the flexure wave has a larger radial depth of investigation (about 2 to 3 borehole diameter) which should allow mapping the far field stress state and formation shear properties away from the damage rock zones, while at high frequency (monopole transmitters and receivers), the short wavelength maps the shallow region around the borehole (Sinha and Kostek, 1996). The existence of stress-induced anisotropy around the borehole creates a dispersion signature that can be analyzed to compute the in-situ stresses around the borehole as will be discussed in the next part.

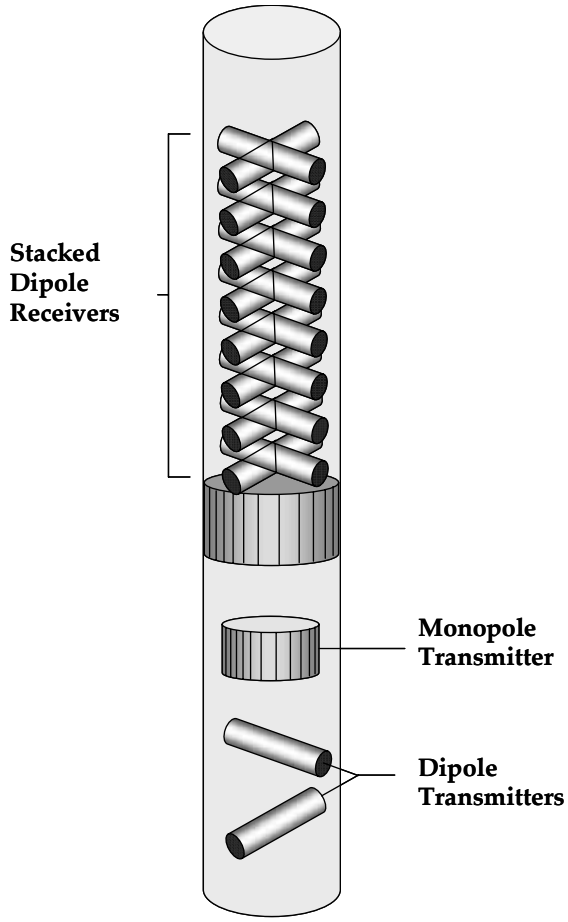

Figure 2-2: Typical configurations of dipole sonic logging tool consist of an array of cross-dipole receivers, and monopole and dipole sources (Kane, 2001).

The monopole and dipole measurement configurations in the tool can be used to distinguish the stress-induced anisotropy by the degree of shear splitting in the monopole shear wave form (fast and slow), or the dipole crossover phenomenon in the fast and slow principal flexural wave dispersion curves (Esmerosy et al., 1995). In the case of fast formation, where the formation shear wave velocity is higher than the borehole fluid velocity, the monopole shear wave splitting (fast and slow) can be observed where the shear wave resulting from the converted P-

wave from the monopole source is refracted back. It is important to mention that the monopole shear wave has relatively shallow depth of penetration due to its higher frequency (7 kHz and higher) (Tang and Cheng, 2004).

2.1.2 Previous Studies

Previous studies can be divided into two categories: (1) laboratory scale measurements and (2) field calibrated models and observations. The work conducted in this dissertation includes laboratory scale measurements which were used to calibrate and estimate applied stresses in the field. The laboratory measurements were also utilized to shed some light on the applicable field models for in-situ stress determination.

2.1.2.1 Laboratory Scale Measurements

Mao and Sweeney (1986) developed a laboratory technique for estimating in-situ stresses by measurements of stress-induced anisotropy around a borehole in which they used the measured biaxial velocity data to estimate the applied stress. Winkler (1994) conducted a laboratory experiment on Berea sandstone to determine if borehole stress concentrations produce velocity variations that are measurable within the borehole, and to determine whether or not useful information can be derived from such velocity variations. His conclusions were that the stress concentration around a borehole produces measurable acoustic velocity variations, which can give a robust measurement of the direction of

maximum stress perpendicular to the borehole. Also, the study related the changes in the velocity magnitude around a borehole with borehole failure.

A similar study conducted by Winkler et al., (1994) examined experimentally and theoretically how the velocity field around a borehole is affected by stress concentrations, and how the velocity field influences dipole wave propagation. Their experiment setup is shown in Figure 2-3, and the shear velocity measurements as a function of stress are shown in Figure 2-4. Their results show that at low frequencies the dipole mode is primarily sensitive to the far-field stresses and at higher frequencies a crossover of the dispersion curves is observed (Figure 2-5). Their results and observations allow one to distinguish between stress anisotropy and intrinsic anisotropy in a borehole through the crossover signature which is a characteristic of stress-induced anisotropy, as opposed to intrinsic anisotropy. Sinha et al., (1995) performed an experiment on Berea sandstone to verify the theoretical prediction of the crossover phenomenon in the borehole flexural wave dispersion in the presence of a uniaxial stress.

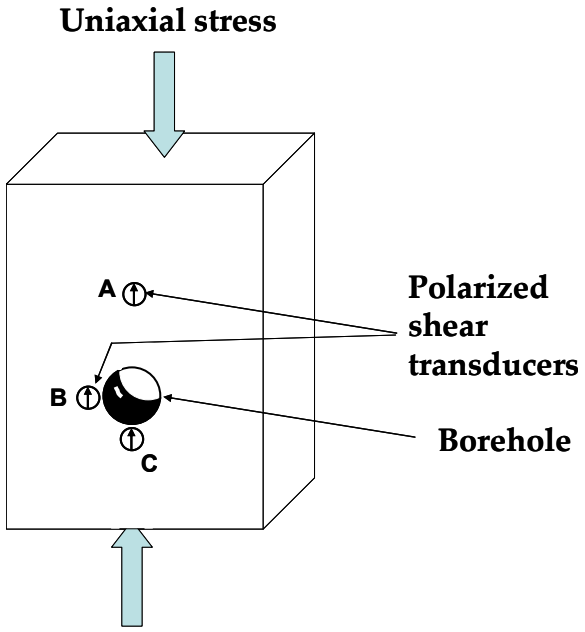

Figure 2-3: Experimental schematic. Uniaxial stress is applied vertically to a rock sample, and polarized shear velocity measurements are made at locations A, B, and C (Winkler et al., 1994).

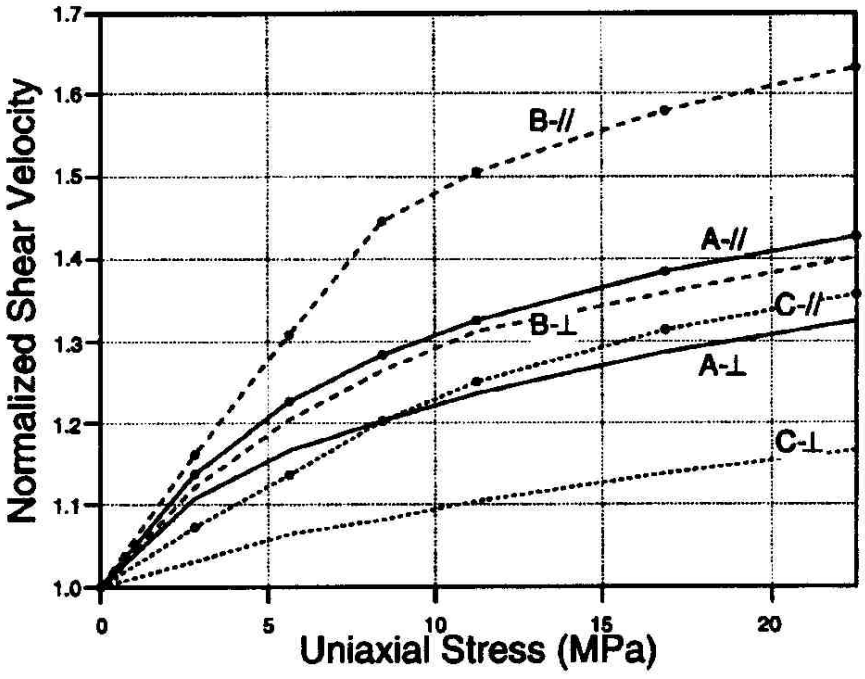

Figure 2-4: Shear velocity measurements normalized to zero stress value. Positions A, B, and C refer to Figure 2-3 (Winkler et al., 1994).

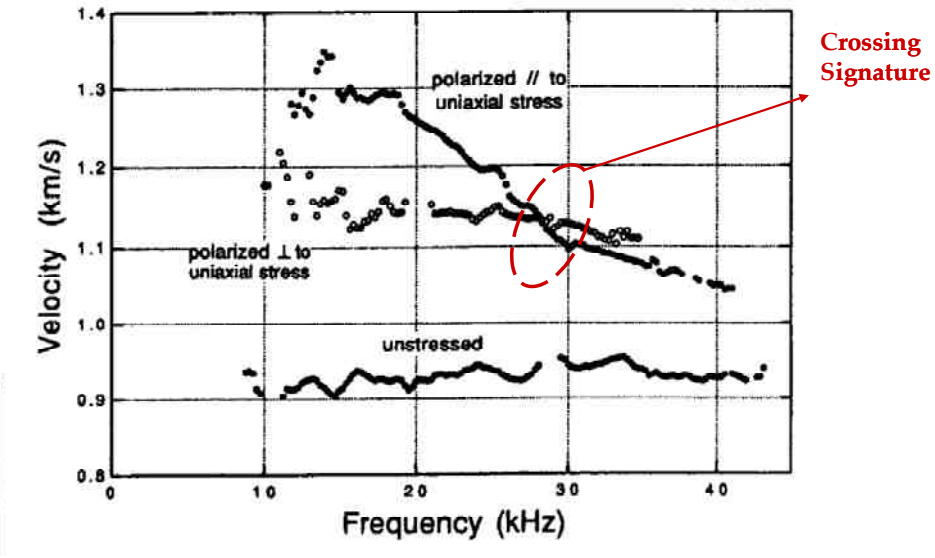

Figure 2-5: Experimentally measured flexure wave dispersion curves in an unstressed borehole, and in a uniaxially stressed borehole showing the crossing signature of the two polarizations (Winkler et al., 1994).

Winkler (1996) extended his work by conducting a laboratory experiment on Berea and Hanson sandstone blocks with uniaxial stress applied perpendicular to the axis of the borehole. His work indicated that as the uniaxial stress increased, significant variations of compressional wave velocity with azimuth can be developed on the order of 10% variation. Also, the azimuth of minimum velocity provides an excellent indicator of the direction of the maximum far-field uniaxial stress with accuracy to 5˚. Plona et al., (1997) conducted experimentally an azimuthal microsonic measurement to determine the axially propagated and refracted compressional wave in the 50-100 kHz band to detect the stress-induced damage around a 10 cm borehole in a 0.5 m cube of Massillon sandstone under uniaxial stress range of 0-21 MPa. Their key results indicated that the compressional velocity variations around the borehole map the near wellbore stress concentrations due to the far-field applied stress, and the variations are

measurable even in the absence of borehole breakouts. Winkler et al., (1998) continued their early observations to study the effect of borehole stress concentrations on dipole anisotropy measurements experimentally and theoretically. They stated that at low frequencies the dipole mode is sensitive to the far field stresses, so the standard sonic logging interpretation correctly yields the maximum stress. At higher frequencies, the dipole mode is sensitive to near field stress concentration, such that the fast polarization direction is aligned with the direction of minimum stress. The observation of velocity as a function of frequency can be combined to generate the crossover in the dipole dispersion curves measured in the fast and slow directions. They verified their theoretical model with measurements performed on a Berea sample at zero stress where no crossover is observed, and at stress of 5 MPa with observable crossover of the dispersion curves as shown in Figure 2-6.

2.1.2.2 Field Calibrated Models

Sinha and Kostek (1996) have developed a method for estimating the horizontal in-situ stresses from the low frequency measurement of the dipole fast and slow shear wave speeds in a vertical borehole as shown in Figure 2-7. Their model, which combines the non-linear parameters of rock, is given as:

$$S_H - S_h = \frac{\rho\left(V_{12}^2 - V_{13}^2\right)}{\left(1 + \frac{C_{456}}{C_{66}}\right)} \tag{2.1}$$

where V_{12} and V_{13} are the low frequency velocities for flexure wave propagation along the borehole x_1-direction, with radial polarization along x_2-and x_3-directions respectively; ρ is formation bulk density; C_{66} is the formation shear modulus, and C_{456} is a non-linear constant given as

$$C_{456} = \left(C_{111} - 3C_{112} + 2C_{123}\right)/8 \tag{2.2}$$

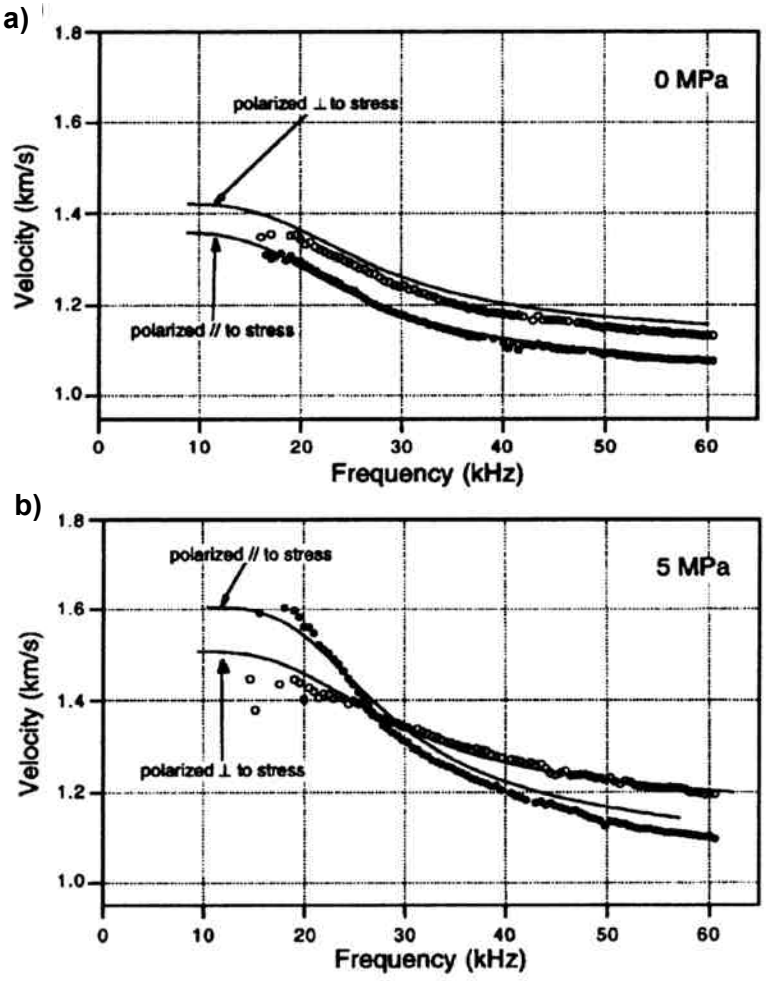

Figure 2-6: Experimental and theoretical flexure dispersion curves in Berea sandstone: (a) is at 0 MPa; (b) is at a 5 MP uniaxial stress. Theoretical curves are the solid lines, filled circles are for dipole aligned parallel to stress, and open circles are for dipoles aligned normal to the stress. At zero stress, parallel flexure mode dispersion curves indicate intrinsic anisotropy while crossover at 5 MPa indicates stress-induced anisotropy (Winkler et al., 1998).

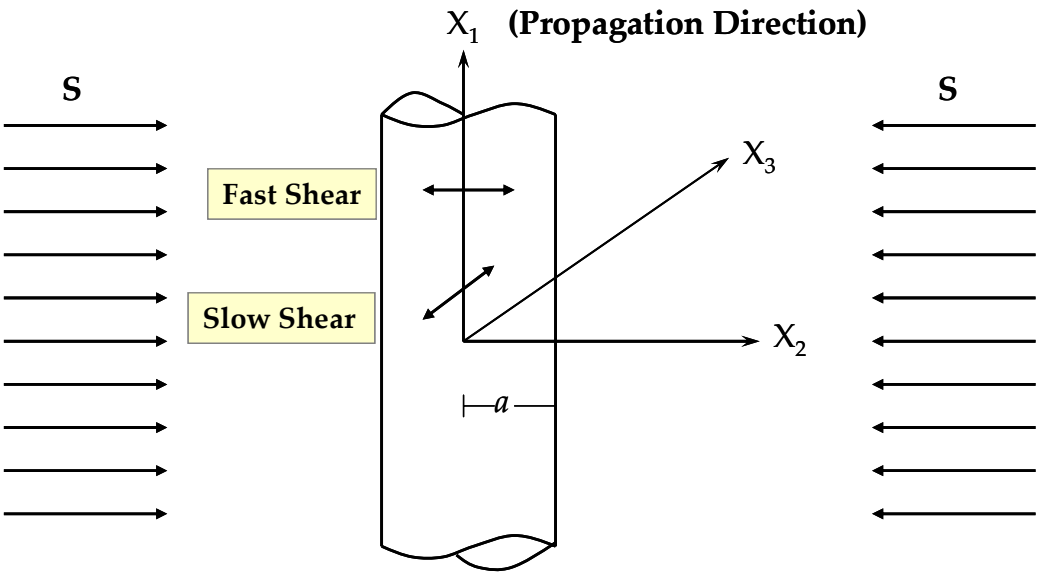

Figure 2-7: Schematic diagram of a borehole with radius '*a*' and a uniaxial stress in the far field (Sinha and Kostek, 1996).

The constant C_{456} combines three independent third-order material elastic constants C_{111}, C_{112}, and C_{123} resulted from including the higher-order terms in the strain tensor. They are a function of rock type and can be determined using acoustic velocity measurements under a triaxial test. Their model utilizes the observation of the flexure crossovers due to stress-induced anisotropy in the computation of the applied stress. Other cases of borehole flexure anisotropy due to intrinsic anisotropy, such as in shale formations, limit the application of the model since intrinsic anisotropy exhibit neither radial heterogeneities nor flexure dispersion crossovers, hence, the existence of a dispersion crossover can be used for distinguishing stress-induced anisotropy from intrinsic anisotropy (Plona et al., 1999). Kane (2001) conducted an experimental study to verify the acoustic method for estimating stresses using the proposed model by Sinha and Kostek (1996). He used known stresses applied on a 60 cm cubical sample of Berea

sandstone. He recorded waveforms from a dipole source in a 3.2 cm borehole and obtained the flexure mode speeds for the fast and slow orientations, which are then used to estimate the stresses applied on Berea based on the non-linear elastic model. His study showed a good comparison (within 10%) of the measured stress to the actual applied stress as shown in Table 2-1 with recorded slownesses.

Applied Stress (MPa)	**Fast Shear Slowness (μs/ft)**	**Slow Shear Slowness (μs/ft)**	**Estimated Stress (MPa)**
0.5	228	232	0.5
1.0	217	225	1.2
2.0	200	214	2.4
5.0	182	206	5.1

Table 2-1: Stress estimated from measured slownesses for Berea sandstone (Kane, 2001).

The results appear promising, but one of the limitations is that the comparison of the measured stress to the actual applied stress is performed to a relatively small stress magnitude that is approximately 10% of the failure strength of most Berea sandstones. As mentioned earlier, the changes in the velocity with stress is significant at a low stress level becoming almost independent of stress at higher levels. This might be one of the limitations of estimating stresses from the acoustic technique in general and from the non-linear elastic model specifically. This observation brings the importance of velocity calibration for in-situ-stress from velocity measurements especially at a high stress state where the change in velocity is minimal. Al-Tahini et al., (2001) conducted a study to estimate the in-situ stresses of Hawiyah field at Saudi Arabia from core samples using Kaiser effect. They compared their in-situ stress measurements using Kaiser effect with

available in-situ stresses computed from the dipole shear measurements at the same field as shown in Table 2-2.

Principal Stress	*From Kaiser (MPa)*	*Dipole Measurements (MPa)*	*Stress Orientation*
σ_v	104.5	104.5	-
σ_{hmin}	88.2	82.8	141°
σ_{Hmax}	123.6	86.8	51°
$\Delta\sigma_{horizontal}$	35.1	3.9	-

Table 2-2: Principal stresses estimated from the Kaiser effect and from dipole shear measurements (Al-Tahini et al., 2001).

The Kaiser effect measurement predicts a high horizontal stress anisotropy (35.1 MPa) compared with acoustic technique (3.9 MPa). They reported evidence to confirm Kaiser effect in-situ measurements using formation image log which provided indication of high stress anisotropy due to observable borehole breakouts. The previous study give an example of under estimating horizontal stresses, mainly the maximum horizontal stress from sonic log data, which supports the need for calibrating acoustic velocity around a borehole. Prioul et al., (2004) performed a study to compute stress sensitivity parameters for intrinsically transverse isotropy shales and sandstones under a hydrostatic stress using published literature data. They suggested that velocity-stress relationships have to be calibrated in the lab before they can be extended to estimate field or boundary stress conditions. The uniqueness of this work is that the velocity dependence of stress around a borehole is investigated and calibrated by borehole strain measurements for different rock types.

Chapter 3

Acoustic Rock Properties of Inherent and Stress-Induced Anisotropy

Assumptions advanced about rocks to be homogeneous and isotropic in the absence of any stresses made the measurements of rock mechanical properties such as elastic moduli, stiffness components, and Biot's pore pressure coefficients, PPC, as function of the stress-induced anisotropy rather straightforward. It is well known, however, that most rocks are neither homogenous nor isotropic. This is true for rocks that exhibit apparent inherent anisotropy (deposition layers, etc.) and are subjected to stress perturbation. Therefore, it is necessary in these types of rocks to measure rock properties while isolating the intrinsic anisotropy from the stress-induced anisotropy. As discussed earlier in Chapter 2, the presence of inherent anisotropy in rock formation affects the measured velocities around a borehole making the estimation of stresses from the dipole tool challenging. As a result, the effect of the inherent and stress-induced anisotropy on rock elastic and poroelastic properties is important in calibrating in-situ stresses especially when stresses are estimated from borehole velocities.

3.1 Introduction and Literature Review

Understanding the effect of anisotropy on the measured rock elastic and poroelastic properties is crucial for many engineering applications. In petroleum engineering, in-situ stress interpretation, directional drilling, hydraulic fracturing, and accurate pore pressure prediction, are important in optimizing oil and gas recovery. In most of the above mentioned applications, rock is usually assumed to be isotropic. However, rocks in general exhibit anisotropy due to layered or microstructure characteristics such as fractures. Anisotropy results from a complex physical and chemical process associated with transportation, deposition, compaction, and cementation, etc., (Amadei, 1996). Rocks with properties that vary with directions are called inherently or intrinsically anisotropic. However, after drilling or formation subsidence, rocks undergo stress variation. The difference in the magnitude between the in-situ stress components especially at great depth also forms rock anisotropy. The anisotropy that results under these conditions is termed as "stress-induced" anisotropy.

Numerous studies exist on the effect of stress-induced anisotropy on measured rock properties (i.e., King, 1969; Nur and Simmons, 1969; Rai and Hanson, 1987; Vernik and Nur, 1992; and Stanchits et al., 2003). Inherent rock anisotropy has been also studied extensively especially for the case of transverse isotropy (i.e., Podio et al., 1968; Jones and Wang, 1981; White et al., 1983; and Lo et al., 1986). The effect of anisotropy on poroelastic moduli including Biot's pore pressure coefficients, PPC, was also investigated by many researchers (i.e., Biot, 1955;

Thompson and Wills, 1991) and measured for Berea outcrops, subjected to three different stress paths, by Scott and Abousleiman, 2005. The constitutive relations for anisotropic poroelasticity were first presented by Biot (1955), and later extended by Biot and Willis (1957), to describe the various mechanical properties of an anisotropic fluid saturated porous medium. Lately, Thompson and Wills (1991) reformulated the anisotropic poroelastic constitutive relations following the work of Rice and Cleary (1976). Many attempts have been made after Thompson and Wills' (1991) work to illustrate the physical meaning of the poroelastic constants, and extensive reviews and simplifications have been performed in this field, i.e., Abousleiman and Cheng (1993), Abousleiman et al. (1996), Cheng (1997), and Abousleiman and Cui (1998 & 2001). These efforts and simplifications made the measurements of the PPC to be experimentally possible.

While poroelastic anisotropic response has been modeled and predicted theoretically, i.e., Abousleiman and Cui (1998), Abousleiman and Ekbote (2005), Kanj and Abousleiman (2005), and many others, laboratory and field experimental verification of the anisotropy effects has been limited. Abousleiman et al., (1996) utilized available measurements of the poroelastic constants conducted by Aoki et al., (1993) on Trafalgar shale under an isotropic state of stress to compute Biot's transverse isotropic pore pressure coefficients (PPC) (Al-Tahini, and Abousleiman, 2005). Lockner and Beeler (2003) performed a quasi-static experiment to compute the elastic moduli and PPC for Berea sandstone

which is relatively isotropic. They were unable to complete the stiffness matrix because they could not obtain the shear modulus in the transverse plane. Scott and Abousleiman (2005) conducted a comparative study of stress-induced anisotropy effects using various state paths (hydrostatic, triaxial and uniaxial loading) on the Biot's PPC. They performed their measurements acoustically on Berea sandstone. The uniqueness of the study presented in this chapter is that the role of both inherent anisotropy and stress-induced anisotropy on stiffness components, elastic moduli, and Biot's PPC are investigated using both acoustic and quasi-static measurements. Sandstone rocks with observable finely layered dipping beds, which reflect their inherent anisotropy, are used and tested under a non-hydrostatic state of stress to emphasize and maximize both inherent and stress-induced effects on the measurements and the poromechanical characterization.

3.2 Theory and Background

Within the assumption that anisotropic rocks behave in a linear, elastic, homogenous, and continuous manner, their constitutive relation can be expressed as (Biot, 1955; Thompson and Wills, 1991)

$$\sigma_{ij} = M_{ijkl}\varepsilon_{kl} + \alpha_{ij} p \tag{3.1}$$

$$p = M(\zeta - \alpha_{ij} e_{ij}) \tag{3.2}$$

where, M_{ijkl}, α_{ij}, and M are material constants. Due to the symmetry of both stress and strain tensors (and the assumption of strain energy function) (Biot, 1955), it can be shown that

$$M_{ijkl} = M_{jikl} = M_{ijlk} = M_{klij} \tag{3.3}$$

$$\alpha_{ij} = \alpha_{ji} \tag{3.4}$$

With the above symmetry, only 21 M_{ij} , 6 α_{ij} , and one M are independent. Therefore, the total number of independent constitutive coefficients for general anisotropic poroelasticity is 28, as compared with the 21 coefficients for anisotropic elasticity. For the elastic transverse isotropy case, where the material has uniform elastic properties along the horizontal plane but they vary vertically, there are 5 independent stiffness components required to fully characterize the material. The five independent stiffness components can be expressed in a matrix form as

$$M_{ij} = \begin{bmatrix} M_{11} & M_{12} & M_{13} & 0 & 0 & 0 \\ M_{12} & M_{11} & M_{13} & 0 & 0 & 0 \\ M_{13} & M_{13} & M_{33} & 0 & 0 & 0 \\ 0 & 0 & 0 & (M_{11} - M_{12})/2 & 0 & 0 \\ 0 & 0 & 0 & 0 & M_{55} & 0 \\ 0 & 0 & 0 & 0 & 0 & M_{55} \end{bmatrix} \tag{3.5}$$

In terms of an engineering representation (Boresi and Chong, 1987), these components can be expressed as

$$M_{11} = \frac{E(E' - E\nu'^2)}{(1+\nu)(E' - E'\nu - 2E\nu'^2)} \tag{3.6}$$

$$M_{12} = \frac{E(E'\nu + E\nu'^2)}{(1+\nu)(E' - E'\nu - 2E\nu'^2)} \tag{3.7}$$

$$M_{13} = \frac{EE'\nu'}{(E' - E'\nu - 2E\nu'^2)} \tag{3.8}$$

$$M_{33} = \frac{E'^2(1-\nu)}{(E' - E'\nu - 2E\nu'^2)} \tag{3.9}$$

$$M_{55} = G' \tag{3.10}$$

where E and E` are the drained Young's moduli in the isotropic plane and transverse plane, respectively; ν and ν` are the drained Poisson's ratios in the isotropic plane and transverse plane, respectively; and G` is shear modulus associated with the transverse plane.

The compliance tensor, C_{ijkl}, defined as the inverse of the stiffness tensor, can be written explicitly in a matrix form for transverse isotropic material using engineering notations as:

$$C_{ij} = \begin{bmatrix} \frac{1}{E_x} & -\frac{\nu_{xy}}{E_x} & -\frac{\nu_{zx}}{E_z} & 0 & 0 & 0 \\ -\frac{\nu_{xy}}{E_x} & \frac{1}{E_x} & -\frac{\nu_{zx}}{E_z} & 0 & 0 & 0 \\ -\frac{\nu_{xz}}{E_x} & -\frac{\nu_{zx}}{E_z} & \frac{1}{E_z} & 0 & 0 & 0 \\ 0 & 0 & 0 & \frac{1}{G_{xy}} & 0 & 0 \\ 0 & 0 & 0 & 0 & \frac{1}{G_{yz}} & 0 \\ 0 & 0 & 0 & 0 & 0 & \frac{1}{G_{xz}} \end{bmatrix} \tag{3.11}$$

where the *x*-*y* plane defines the isotropic plane and *z*-direction defines the vertical axis of symmetry. The constitutive relation defined in Equation (3.1) can be rewritten as

$$\sigma_{ij} - \alpha_{ij} p = M_{ijkl} e_{kl} \tag{3.12}$$

Therefore, it can be observed from the above equation that there exists an "effective stress tensor" similar to the Terzaghi one

$$\sigma'_{ij} = \sigma_{ij} - \alpha_{ij} p \tag{3.13}$$

The coefficients α_{ij} are then referred to the generalized Biot's effective stress tensor, or directional dependence of the PPCs. Without violating much of the physics the rock mechanical behavior is mostly governed by the rock matrix and structure which are the dominant features in rock deformation. That is the solid grain stiffness is of little effect on the pore pressure coefficient variation when the rock is subjected to stress perturbation, Abousleiman et al., 1996. That is by considering the assumption of rock solid grain homogeneity and isotropy that is the inherent apparent transverse isotropy is only due to the structural rock matrix and pore size distribution, the Biot's PPC, α_{ij}, can be expressed as in Abousleiman and Cheng (1993), Abousleiman et al., (1996), Cheng (1997) and Abousleiman and Cui (2001) with relation only to the components of the solid rock stiffness matrix:

$$\alpha_{ij} = \delta_{ij} - \frac{M_{ijkk}}{3K_s} \tag{3.14}$$

where Ks is the solid grain bulk modulus. Biot's PPC as well as elastic rock moduli can be determined using quasi-static and dynamic methods. Both methods require measurements of strain and acoustic velocity as functions of stress on three different rock samples cored parallel, perpendicular and at a 45˚ inclination relative to the vertical axis of symmetry (King, 1969; Amadei 1983). In the quasi-static method, the elastic rock moduli including E, $E`$,$\nu$, $\nu`$ and $G`$ can be determined from the stress-strain measurements of the three oriented samples, and stiffness components can be computed using Equations (3.6) through (3.10). For the case of the quasi-static method, Biot's PPC can be obtained from measurements of plug samples cored in the directions of the isotropic and transverse planes. Utilizing Equation (3.14), the lateral Biot's PPC (α_{11}-in the isotropic plane) during quasi-static uniaxial compressive test with lateral stresses set to zero could be determined by (Abousleiman et al., 1996)

$$\alpha_{11} = 1 - \frac{M_{11} + M_{12} + M_{13}}{3K_s} \tag{3.15}$$

and the axial Biot's PPC (α_{33}-in the transverse plane) by

$$\alpha_{33} = 1 - \frac{2M_{13} + M_{33}}{3K_s} \tag{3.16}$$

The dynamic method involves acquisition of acoustic compression and shear wave velocities within the three oriented samples under the assumption of transverse isotropy as shown in Figure 3.1. It requires a minimum of five acoustic

wave velocities to compute the full set of dynamic stiffness components (King, 1969; Lo et al., 1986). Acoustic measurements include two compressional wave velocities that are parallel and normal to the plane of symmetry, two shear wave velocities in the same directions of P-wave with polarization oriented parallel and normal to the plane of symmetry, and one compressional wave velocity measured for the core plug oriented at a 45˚ relative to the axis of material symmetry. The relationships between the five independent stiffness components and velocities for transverse isotropic material can be expressed by (Lo et al., 1986)

$$M_{11} = \rho V_{p11}^2 \tag{3.17}$$

$$M_{12} = M_{11} - 2\rho V_{sH1}^2 \tag{3.18}$$

$$M_{33} = \rho V_{p33}^2 \tag{3.19}$$

$$M_{55} = \rho V_{s3a,3b}^2 \tag{3.20}$$

$$M_{13} = -M_{55} + \sqrt{4\rho^2 V_{P45}^4 - 2\rho V_{P45}^2 (M_{11} + M_{33} + 2M_{55}) + (M_{11} + M_{55})(M_{33} + M_{55})} \tag{3.21}$$

where V_{P11}, V_{SH1}, V_{P33}, $V_{S3a,3b}$ and V_{P45} are P- and S- wave velocities in different directions as shown in Figure 3-1. From above computed stiffness components, the five elastic components E, $E`$, $\nu$, $\nu`$ and $G`$ can be determined using the formulas given in King (1969) as

$$E' = \frac{D}{M_{11}^2 - M_{12}^2} \tag{3.22}$$

$$E = \frac{D}{M_{11}M_{33} - M_{13}^2} \tag{3.23}$$

$$\nu = \frac{M_{12}M_{33} - M_{13}^2}{M_{11}M_{33} - M_{13}^2} \tag{3.24}$$

$$\nu' = \frac{M_{13}(M_{11} - M_{12})}{M_{11}M_{33} - M_{13}^2} \tag{3.25}$$

where D is the determinant of the matrix given as

$$D = \begin{vmatrix} M_{11} & M_{12} & M_{13} \\ M_{12} & M_{11} & M_{13} \\ M_{13} & M_{13} & M_{33} \end{vmatrix} \tag{3.26}$$

The isotropic ratio, defined as (E/E`), determines the degree of anisotropy. The dynamic Biot's PPC are determined from the dynamic stiffness components using Equations (3.15) and (3.16).

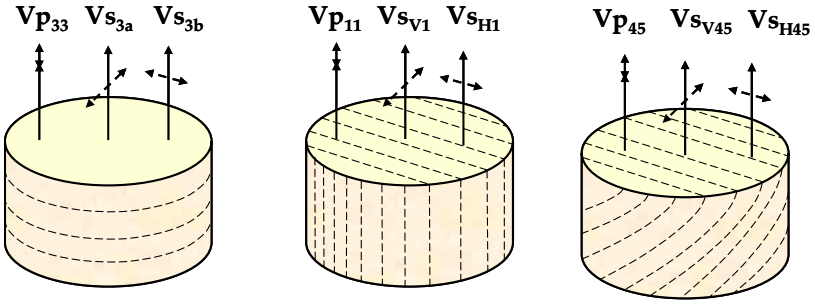

Figure 3-1: Convention used in the experimental work for velocity measurements in three oriented samples relative to the bedding planes. Solid arrows represent directions of wave propagation; dashed arrows represent direction of polarization (particle motion) of the shear waves (Lo et al., 1986).

3.3 Laboratory Measurements

Laboratory compression experiments were conducted under non-hydrostatic stress conditions on reservoir type sandstone rocks, with observable finely-layered dipping beds reflecting the inherent apparent anisotropy (Figure 3-2). The objectives were to investigate the role of both stress-induced anisotropy and intrinsic anisotropy on the stiffness components, elastic moduli and Biot's PPC, using acoustic and quasi-static measurements. The experiments involved measurement of the axial and lateral strains and acquisition of compressional and shear velocities as a function of stress on three different oriented rock samples that exhibited apparent transverse isotropy as shown in Figure 3-2.

3.3.1 Samples Description and Preparations

The rock sample plugs were drilled and cut perpendicular, parallel and at 45° inclination to the visual foliation as shown by Figure 3-2. The samples are from Lyons, Permian age, outcrop sandstone located in northeastern Colorado. The samples are nominally 1.5 inches in diameter and 3 inches in length. The flat ends of the samples were machined to obtain parallel contacts with applied load by the loading frame. The samples were dried in a vacuum oven at 90 °F for a day. An X-ray Diffraction Mineralogical Analysis (XRD) was performed on the samples. Two samples were taken from the visible light and red colored bands. The XRD data are shown in Table 3-1. It can be observed from the mineralogy analysis that both bands mainly consist of quartz (95%-97%). The contrast in color between

the two observable colored bands is due to the trace of iron minerals (i.e., Magnetite, Hematite, Goethite and Akaganeite) in the red band. The porosity was measured to be ~3%.

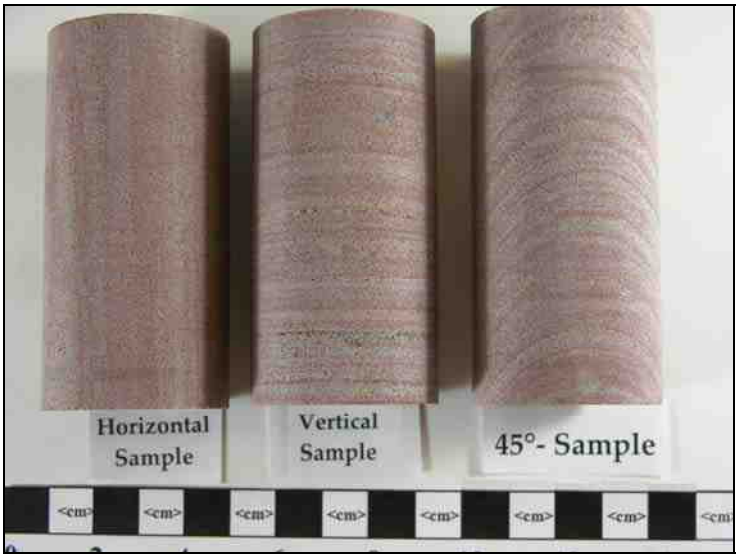

Figure 3-2: Pictorial view of the candidate samples submitted for testing with designated directions. Notice the finely-layered dipping beds reflecting the assumption of their inherent apparent anisotropy.

Mineral Constituents	Light Colored Band	Black Colored Band
	RELATIVE ABUNDANCE (%)	
Quartz	97	95
K-Feldspar	1	1
Calcite	trc	trc
Magnetite	-	1
Hematite	-	trc
Goethite	-	trc
Akaganeite	-	trc
Kaolinite	trc	trc
Illite/Mica	1	1
Mixed-Layered Illite/Smectite	1	2
% Illite Layers in M. L. Illite/Smectite	*50-60%*	*50-60%*
TOTAL	*100*	*100*

Table 3-1: X-Ray Diffraction Mineralogical Analysis (XRD) on the light and red colored bands.

Thin section Analysis

Thin sections were prepared from both red and light colored bands to characterize the microstructure of the samples. The thin section analysis confirms the extensive amount of quartz in both bands. Figure 3-3 and 3-4 display the thin section of the light and red colored bands, respectively. The thin section analysis showed that the light colored band has more intraporosity compared with the red colored band. This observation is considered as one of the indications of the inherent anisotropy in these samples. Also, it is clear from the thin section views below that quartz cement is the dominant cement in these samples.

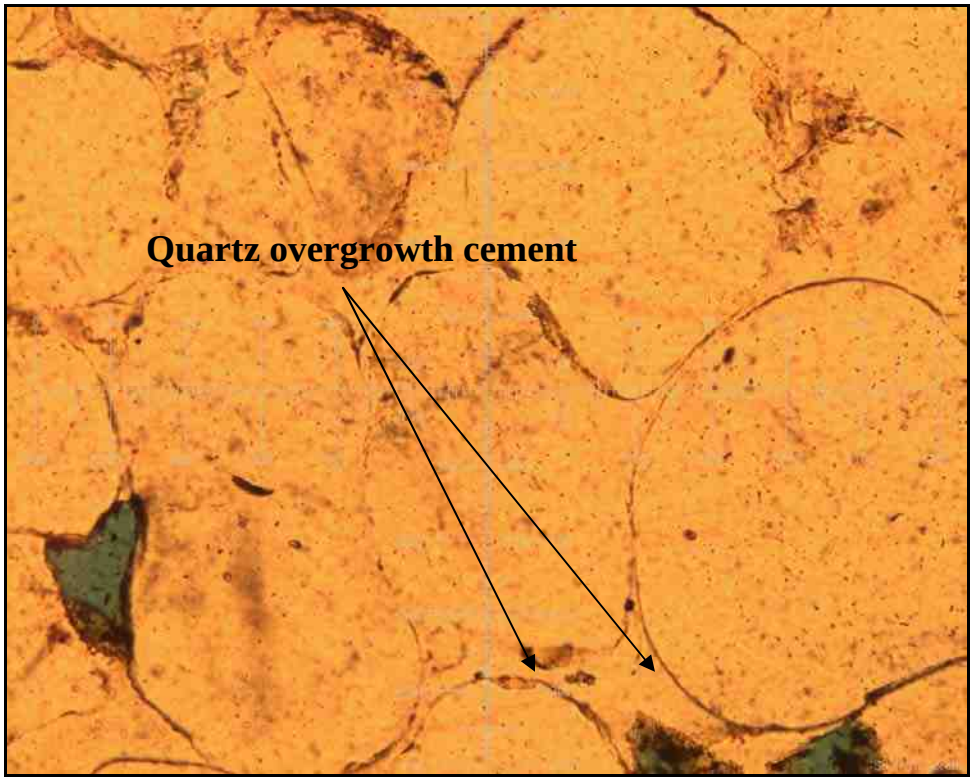

Figure 3-3: Thin section display taken from the light colored band.

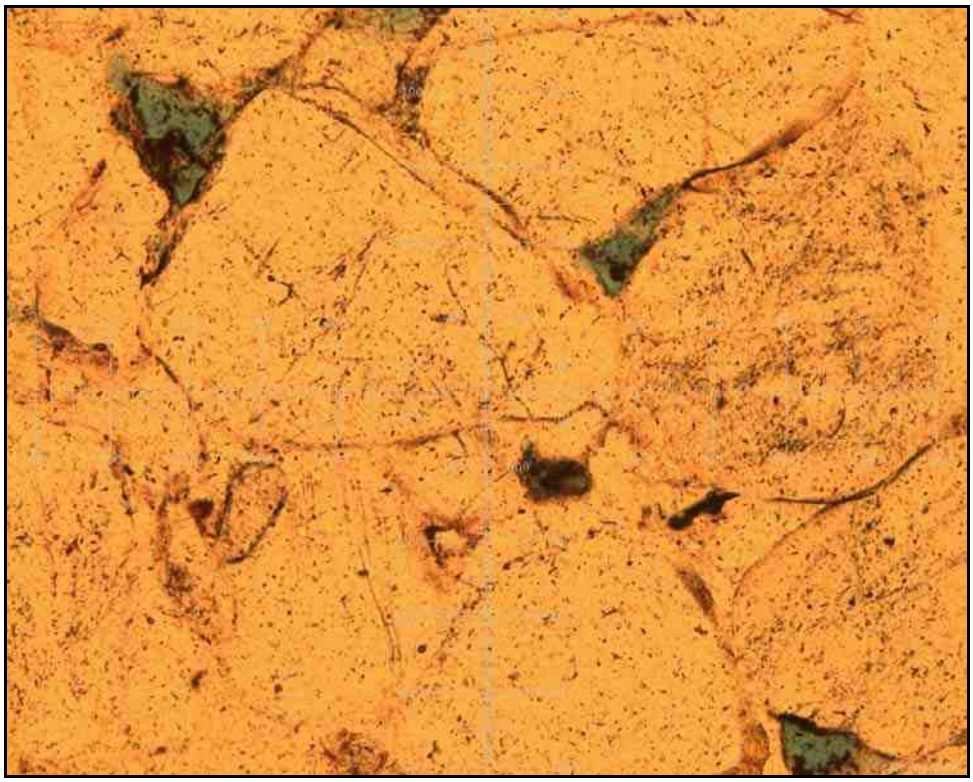

Figure 3-4: Thin section display taken from the red colored band.

3.3.2 Experimental Equipments

The tests were performed using an MTS servo control load frame (model 815) with maximum loading capabilities of 2,669 kN (600,000 lb_f). The samples were tested under dry conditions and loaded in a loading cell (shown in Figure 3-5a) with multiple feedthroughs used for acoustic leads and strain gage wires. The axial and radial strains were measured by two different tools to gain an insight about the repeatability of the strain measurements. Two T-grid strain gages were mounted directly to each sample for the measurements of both lateral and axial strains. Linear Variable Differential Transformers (LVDTs) and an MTS extensometer were also used to measure the displacement and corresponding

strain in the axial and lateral directions, respectively. The sample set-up is shown in Figure 3-5b. The measurements were performed under stroke control. The acoustic measurements were conducted simultaneously with strain measurements using a Tektronix digital oscilloscope and pulse generator to excite the piezoelectric acoustic crystals. One compressional and two polarized shear crystals were prepared from 600 kHz PZT-5a piezoelectric crystals. The crystals were mounted on the end of the loading platens; velocities were measured in the direction of load. Two data acquisition systems were available to collect data simultaneously from different inputs and store the data. The data acquisition system is incorporated with an adjustable resistor to balance the strain gage bridge; the resistor is called a strain conditioner. The data input includes the raw voltage readings for load, stroke displacement, strain gage, LVDTs and extensometer. The voltage values are converted to engineering units before the data are analyzed. The load and raw strain gages voltage data (axial and radial) are plotted using an external plotter connected to the data acquisition. Figures 3-5c and 3-5d show a strain gage mounted on one of the samples and the experimental set-up, respectively.

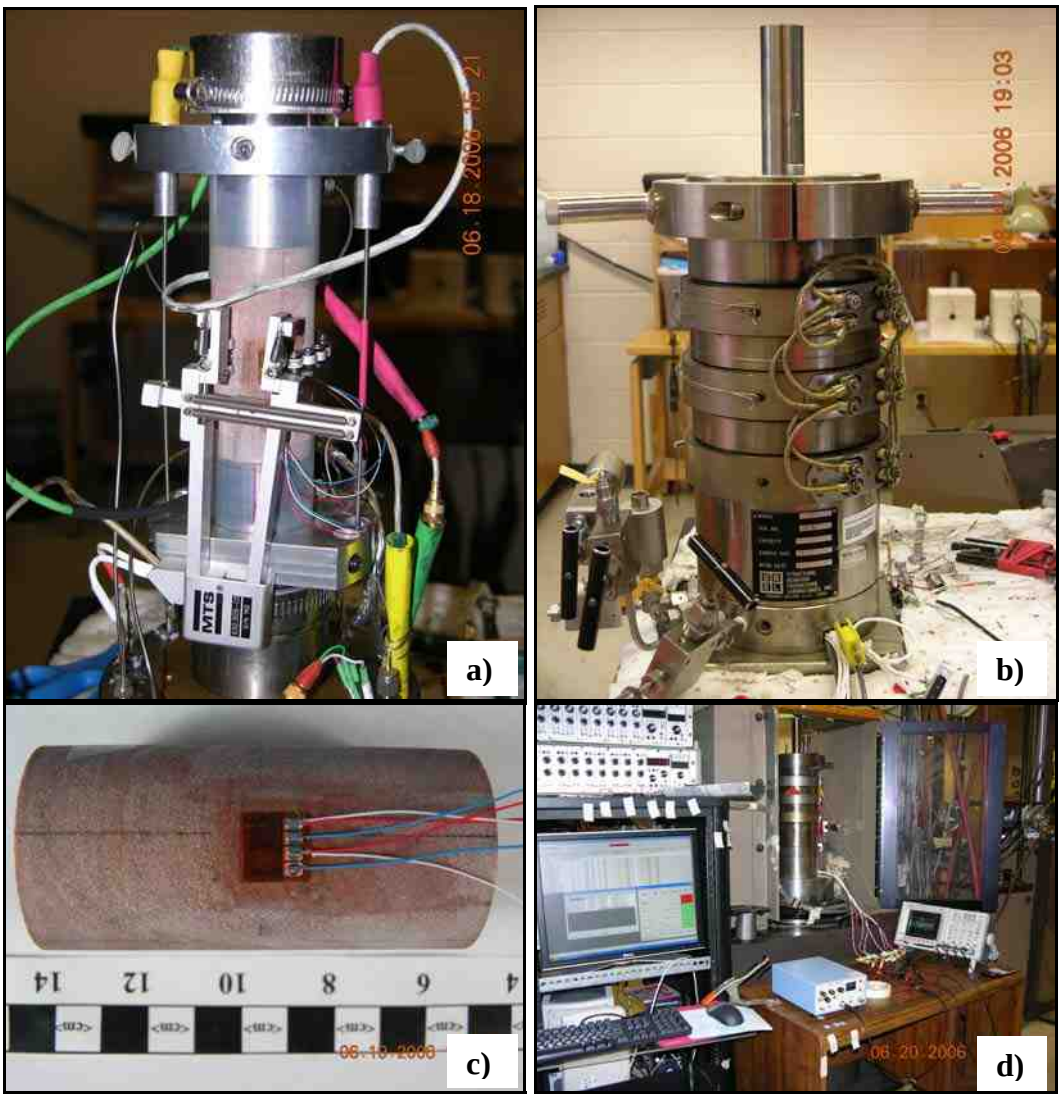

Figure 3-5: a) Horizontal sample loaded with strain gages, LVDTs and extensometer for strain measurements, b) Load cell used in the test, c) strain gage mounted on the 45° oriented sample, and d) Pictorial view shows one of the data acquisitions systems, strain conditioner pulse generator and the oscilloscope.

3.3.3 Experimental Methods

3.3.3.1 Loading and Unloading (Stress Cycling)

It is well known in literature that the magnitude of the static moduli determined from stress-strain curve is lower than dynamic moduli. The difference between the static and dynamic moduli can be significant, especially for high porosity rocks. There are several explanations for the differences ranging from viscoelastic behavior to strain effects (Plona and Cook, 1995). Figures 3-6 and 3-7 illustrate an example of the uniaxial static stress-strain curve including a major cycle and four minor cycles for Berea sample (porosity ~ 20%) and for a vertical Lyons tested sample (porosity ~ 3%). The figures also include the computed dynamic modulus from measured velocities at each cycle. It can be noticed that by cycling the rock sample at small strain amplitude, the slopes (i.e., Young's modulus) for the minor cycles are comparable with the slope of the dynamic stress-strain especially at high stress.

The experiments include 7 minor cycles before samples failed. Stress magnitudes at unloading were 7,000, 10,000, 15,000, 18,000 and 21,000 psi. The elastic moduli, i.e., Young's modulus and Poisson's ratio, are determined from the slope of the stress-strain curve for the minor cycles during loading and unloading.

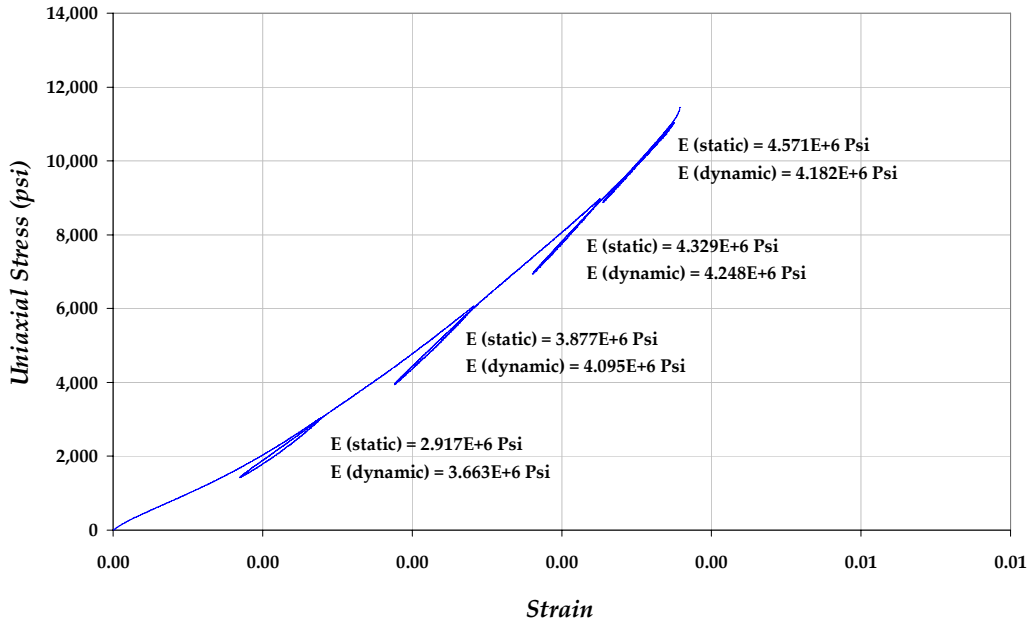

Figure 3-6: Stress-strain curve for Berea sample with computed quasi-static and dynamic Young's moduli (porosity ~ 20%).

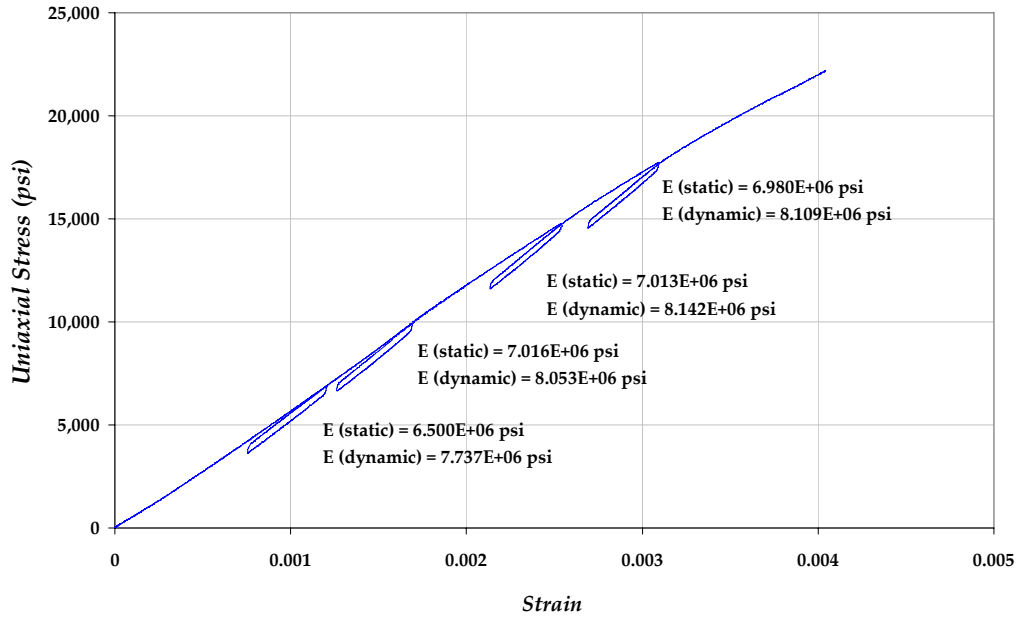

Figure 3-7: Stress-strain curve for Lyons sandstone vertical sample with computed quasi-static and dynamic Young's moduli (porosity ~ 3%).

3.3.3.2 Velocity Acquisitions

The Initial compressional and polarized shear velocities were taken before submitting the samples for testing, i.e., zero stress and used to compute the stiffness components corresponding to the inherent anisotropy effect in the samples.

The velocity measurements under stress were acquired at every stress increment of 1,000 psi. The acoustic velocities were calculated from the time interval needed for acoustic pulse to travel across the sample; after correcting for the travel time through the steel end platens. The time correction was about 10 μsec for compressional velocity arrival and 20 μsec for shear arrival; these corrections were obtained by measuring velocities with platens clamped together. The initial velocities were also measured with acoustic crystals directly clamped to the samples which utilized as a second alternative for velocity correction under uniaxial applied stress. The polarization of the shear wave crystals were marked as straight-lines on the loading platens and used to align the shear wave polarizations with the directions of bedding on the samples as shown in Figure 3-8.

Figure 3-8: Alignment of sample bedding with the polarization of the shear crystals (horizontal sample).

3.3.3.3 Effect of Frequency

Inherent anisotropy in the rock structure affects the propagation of the wave velocities. This effect is tied to the scaling between the wavelength and the anisotropy boundaries that exist within the rock. For example, in laboratory measurements one cannot measure anisotropy at scale smaller than the wave frequency since the measurements are affected by the scaling or boundary conditions when the rock sample is shorter than a half wavelength (Wang and Nur, 1990).

3.3.3.4 Calibration of the System and Measurements

Large errors in the displacements can be introduced when attempting to determine the axial strain from LVDTs displacement without correcting for the elastic distortion of the frame and the platens. Figure 3-5a showed that the LVDTs are screwed to two rings attached to the top and bottom loading platens. As a result, the total measured displacement contributes to the deformation of the specimen and the platens. A correction can be made by testing a standard sample with known properties, i.e., aluminum. The measured displacement can be compared with theoretical displacements (given known property i.e., E) and a correction as function of applied force can be established. The correction can be avoided by measuring the axial strain directly on the specimen using a strain gage. The axial displacements of the LVDTs were corrected utilizing strain gage measurement on an aluminum specimen as shown in Figure 3-9.

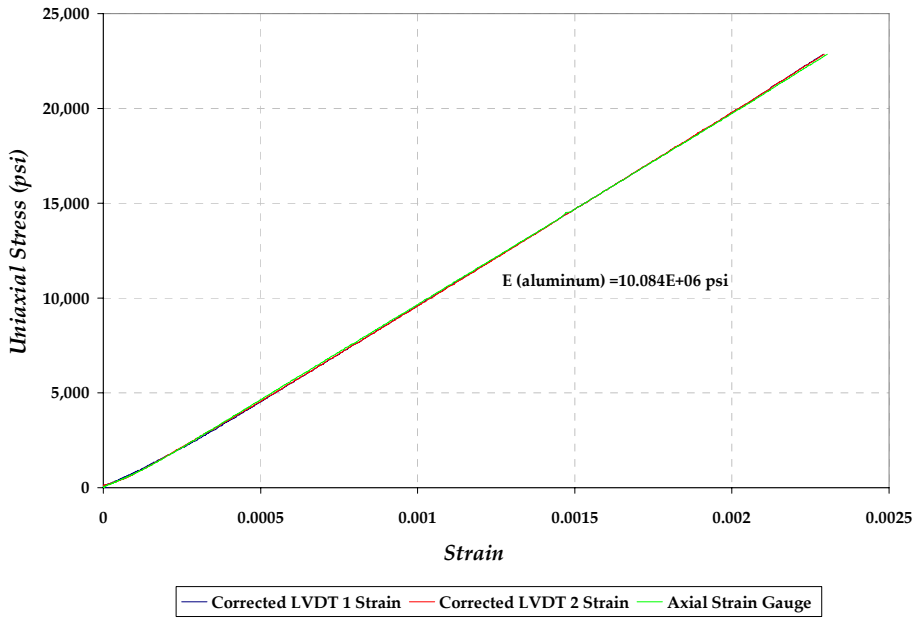

Figure 3-9: Comparison of the axial strains from LVDT and strain gage for aluminum.

3.3.4 Experimental Results

3.3.4.1 Quasi-static Testing

Figure 3-10 shows the stress-strain curves using strain gages for the vertical sample during loading and unloading. The sample is cycled initially four times to stress levels of 7,000 psi (2 cycles) and 10,000 psi. Both strain gages showed the repeatability of strain measurement in both axial and lateral directions. The Young's modulus and Poisson's ratio are computed from the stress-strain curves of the minor cycles. The axial and lateral strain measurements using LVDTs and extensometer are shown in Figure 3-11. It can be noticed that the vertical sample failed at uniaxial stress of ~22,000 psi. The lateral strains measured by strain gages are compared with strain measured with the extensometer. This comparison was utilized to validate the strain measurements for each tested sample. Figure 3-12 shows the comparison of measured lateral strains using both strain gages and extensometer.

The stress-strain measurements for the oriented sample at a 45° using strain gages and LVDTs are given in Figures 3-13 and 3-14, respectively. The sample failed at 23,400 psi compared with 22,000 psi for the vertical sample. The comparison of measured lateral strains using both strain gages and extensometer as a function of uniaxial applied stress is shown in Figure 3-15.

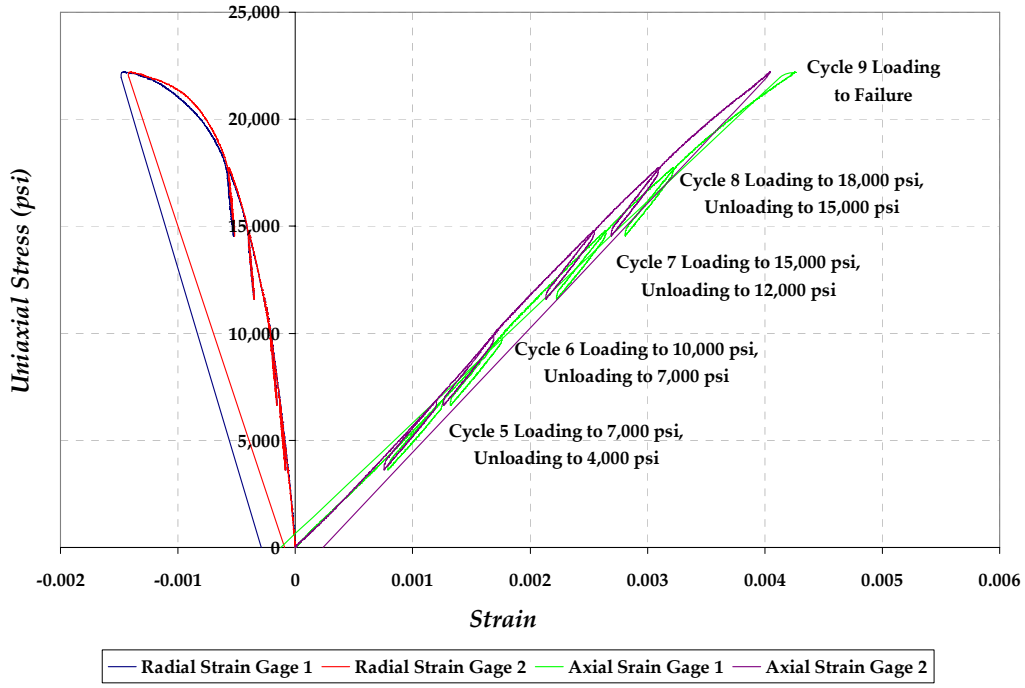

Figure 3-10: Complete loading stress-strain curves from strain gages for the vertical sample V-3.

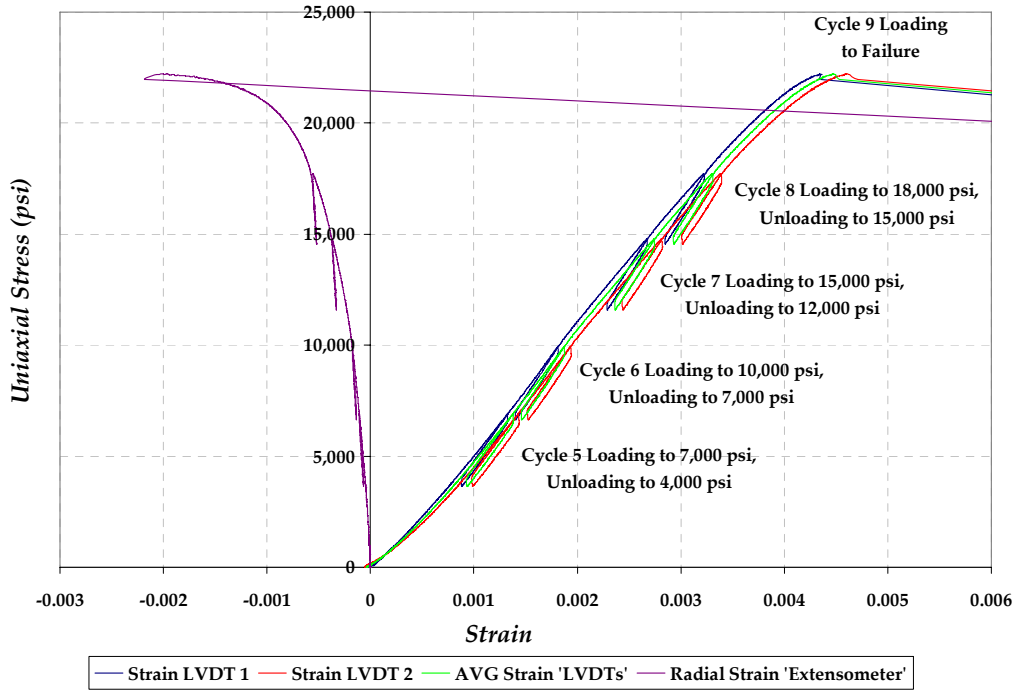

Figure 3-11: Complete loading stress-strain curves from LVDTs (after elastic distortion correction) and extensometer for the vertical sample V-3.

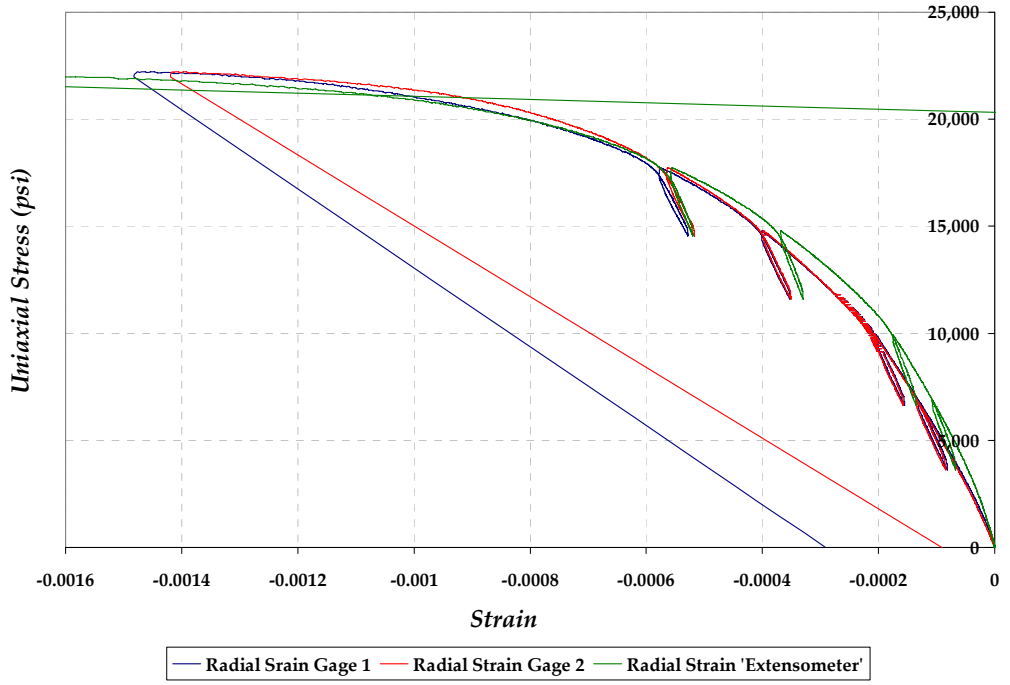

Figure 3-12: Comparisons of the circumferential strain measurements from strain gages and extensometer for the vertical sample V-3.

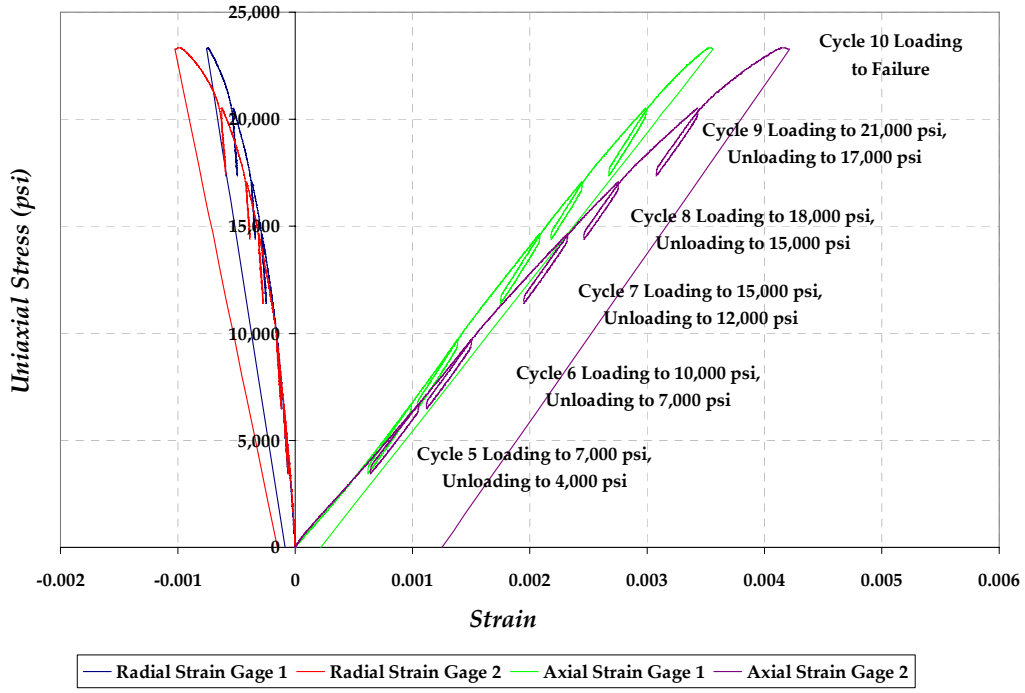

Figure 3-13: Complete loading stress-strain curves from strain gages for the 45° sample.

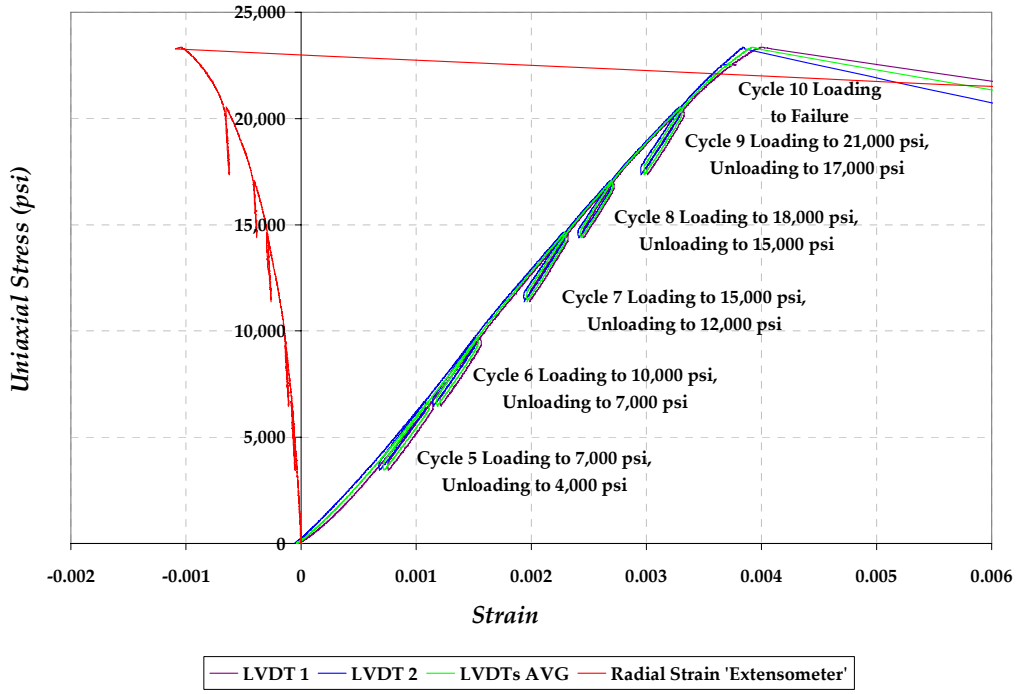

Figure 3-14: Complete loading stress-strain curves from LVDT (after elastic distortion correction) and extensometer for the 45° sample.

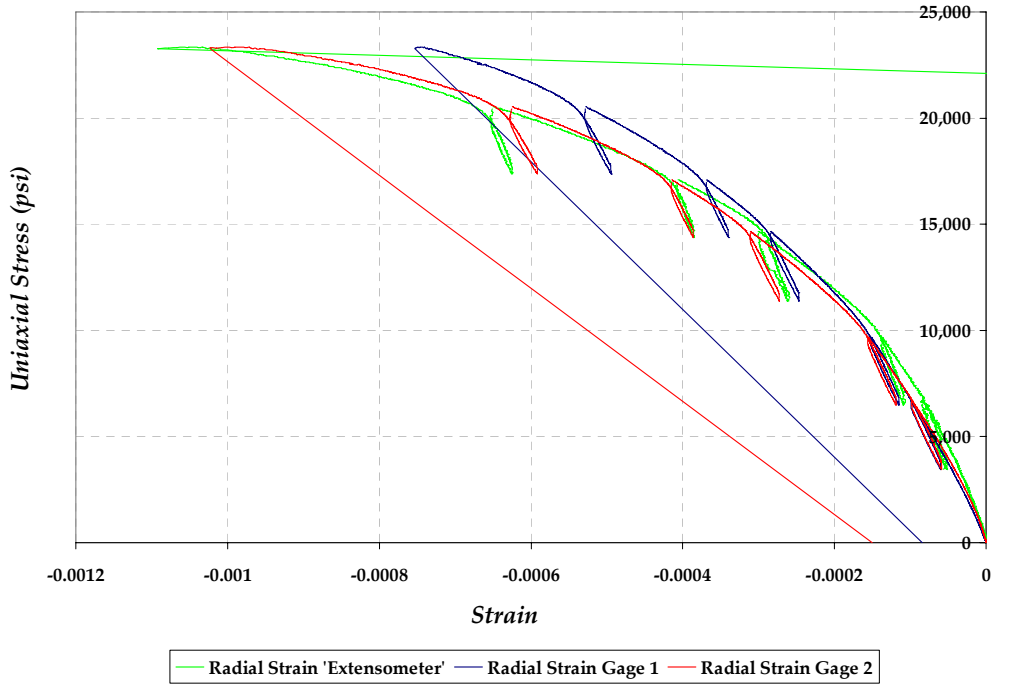

Figure 3-15: Comparison of the circumferential strain measurements from strain gages and extensometer for the 45° sample.

The horizontal sample behaved much stiffer than the other two samples. The sample did not fail catastrophically; the sample is chipped on the side at stress of ~28,500 psi. Figure 3-16 shows the complete axial and lateral stress-strain curves using the strain gage during loading and unloading. The average axial strain measurements from LVDTs and the lateral strain using extensometer are shown in Figure 3-17. The comparison of measured lateral strains using both strain gages and extensometer is shown in Figure 3-18. For the purpose of comparison, a second horizontal sample H-2 was tested. The strain measurements using strain gages and LVDTs are shown in Figures 3-19 through 3-21. The sample failed at ~27,200 psi, about 1,300 psi less than the other horizontal sample.

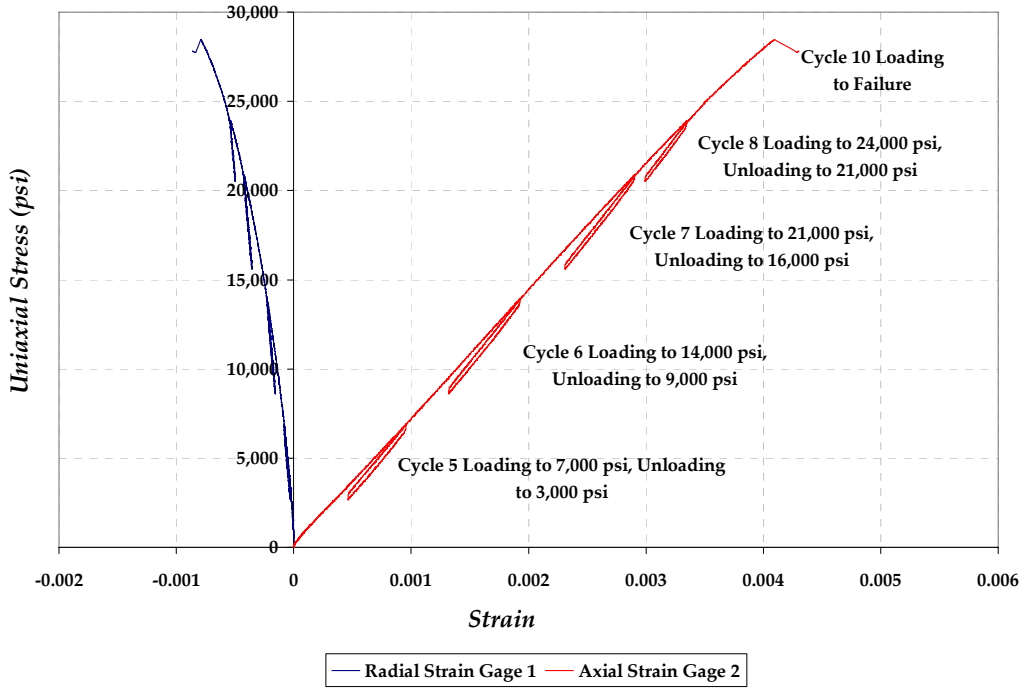

Figure 3-16: Complete loading stress-strain curves from strain gage for the horizontal sample H-1.

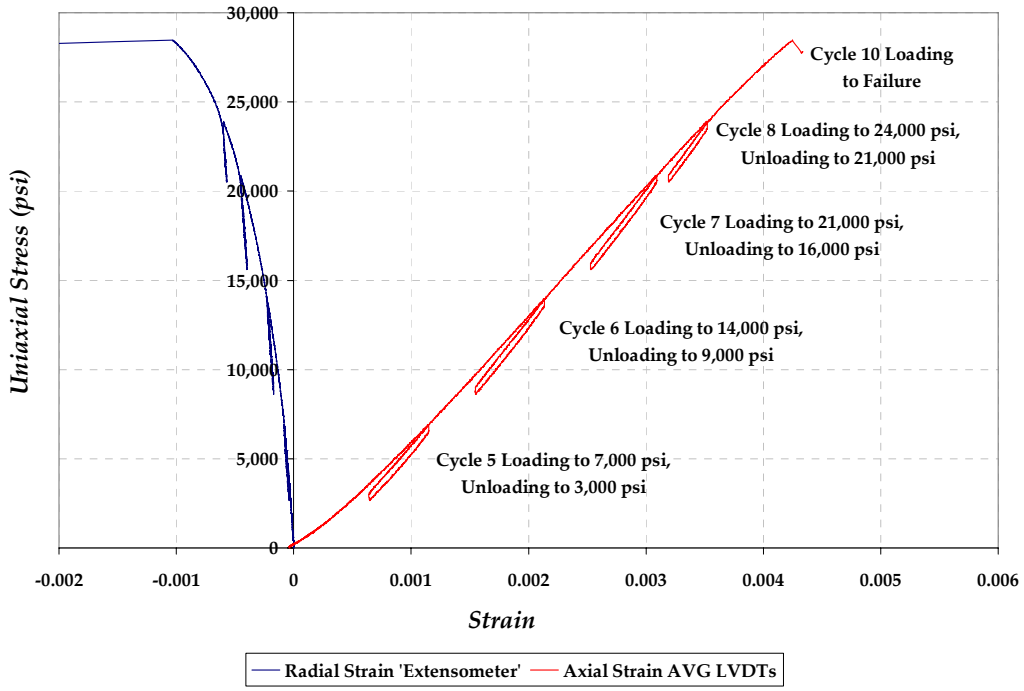

Figure 3-17: Complete loading stress-strain curves from (after elastic distortion correction) LVDTs for the horizontal sample H-1.

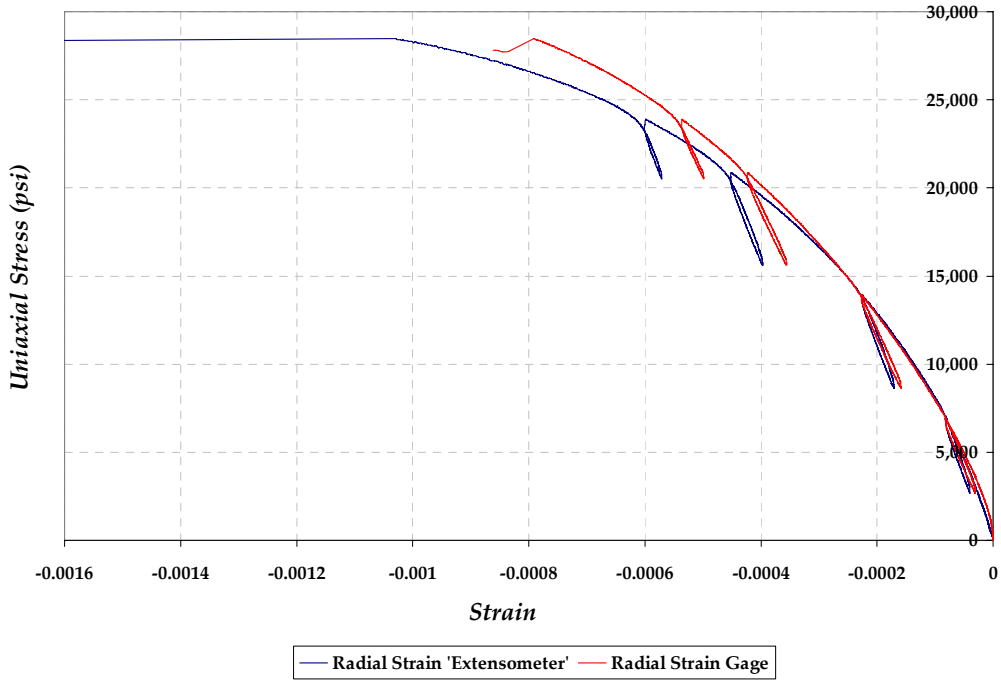

Figure 3-18: Comparisons of the circumferential strain measurements from strain gages and extensometer, horizontal sample H-1.

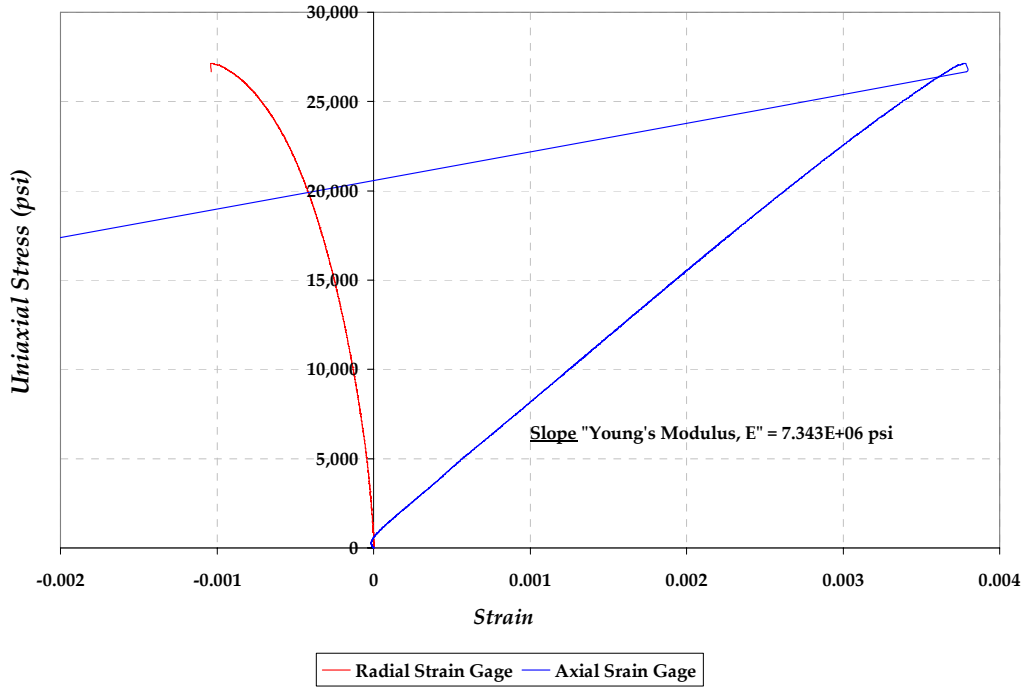

Figure 3-19: Complete loading stress-strain curves from strain gage for the horizontal sample H-2.

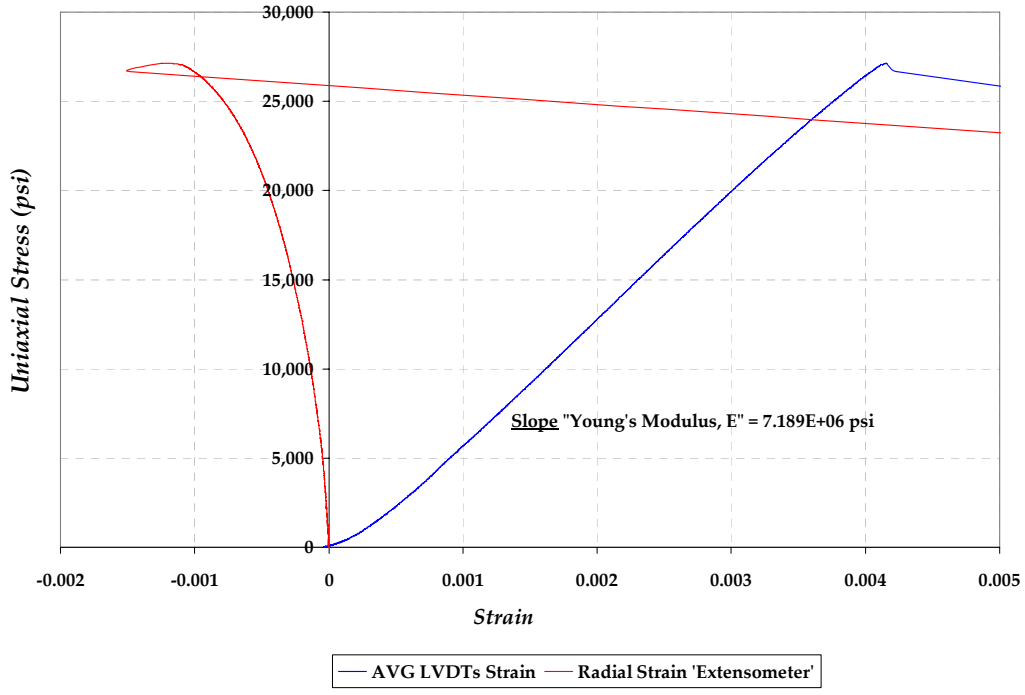

Figure 3-20: Complete loading stress-strain curves from LVDTs (after elastic distortion correction) for the horizontal sample H-2.

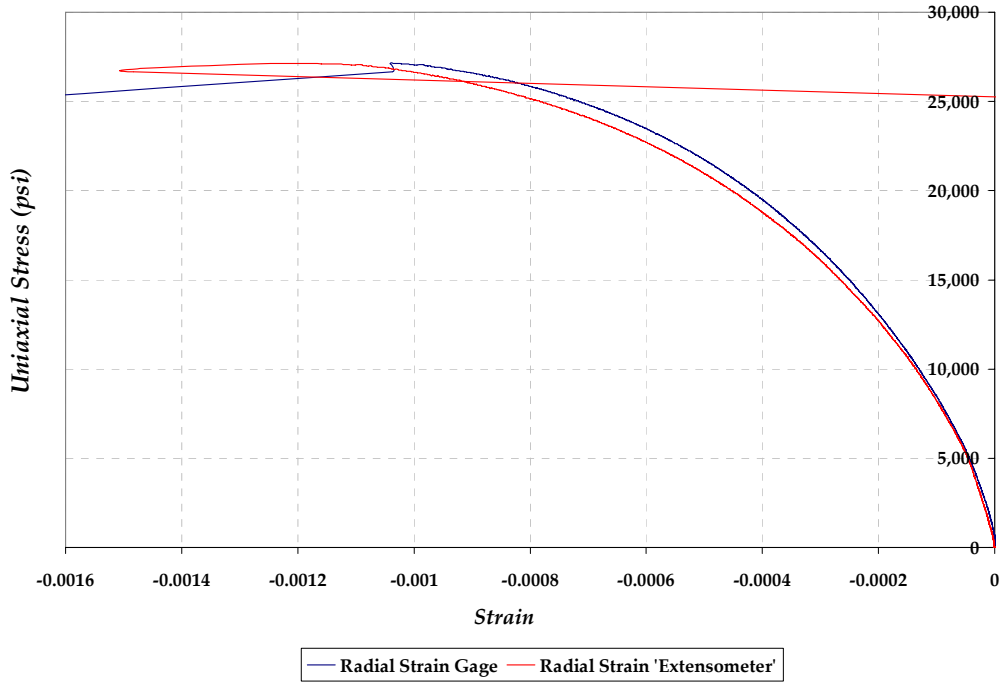

Figure 3-21: Comparisons of the circumferential strain measurements from strain gages and extensometer, horizontal sample H-2.

3.3.5 Quasi-static Data Summary

The computed quasi-static Young's moduli and Poisson's ratios from minor cycles are given in Table 3-2 as a function of stress for the three oriented samples. The magnitudes of the static Young's moduli and Poisson's ratios are reported for both strain gages and LVDTs measurements. This allowed for comparing the values of the moduli at each stress and selecting the proper values for further computations of the quasi-static stiffness components and the anisotropic Biot's PPC. The values were selected based on their repeatability with different measuring tools (i.e., strain gages, LVDTs, and extensometer) and average values were taken in some cases and are reported in Table 3-3. Table 3-4 displays

computed quasi-static stiffness components in the isotropic and transverse planes as a function of applied uniaxial stress. The bulk moduli and Biot's PPC corresponding to both planes are listed in Table 3-5, with K_s value assumed to be 38 GPa based on the high percentage of quartz present in Lyons samples. The degree of anisotropy from static measurements were computed and listed in Table 3-5.

Uniaxial Stress (psi)	**(E) SG 1 (psi)**	**(E) SG 2 (psi)**	**(E) AVG LVDTs (psi)**	**(ν) SG 1**	**(ν) SG 2**	**(ν) LVDT**
	Horizontal Sample					
7,000	7.849E+06	7.539E+06	7.655E+06	0.10	0.08	0.09
10,000	8.210E+06	8.357E+06	8.278E+06	0.11	0.09	0.10
18,000	8.348E+06	8.663E+06	8.475E+06	0.12	0.10	0.11
Vertical Sample						
7,000	6.228E+06	6.501E+06	6.359E+06	0.11	0.11	0.09
10,000	6.800E+06	7.017E+06	6.984E+06	0.11	0.11	0.10
18,000	6.761E+06	6.981E+06	7.277E+06	0.13	0.14	0.11
45° Sample						
7,000	7.902E+06	7.080E+06	7.282E+06	0.11	0.10	0.08
10,000	8.405E+06	7.531E+06	7.961E+06	0.11	0.10	0.09
18,000	7.749E+06	8.669E+06	8.290E+06	0.12	0.11	0.10

Table 3-2: Measured quasi-static moduli for the oriented samples at three different stress levels using strain gages, LVDTs and extensometer (minor cycles).

Uniaxial Stress (psi)	**7,000**	**10,000**	**18,000**
***E* (isotropic plane), psi**	7.694E+06	8.283E+06	8.505E+06
***E`* (traverse), psi**	6.365E+06	6.909E+06	6.871E+06
ν (isotropic plane), psi	0.11	0.11	0.11
ν`(traverse), psi	0.10	0.11	0.13
G`(traverse), psi	3.308E+06	3.544E+06	3.670E+06
Degree of anisotropy (E/E`)	1.24	1.19	1.20

Table 3-3: Quasi-static material properties measured in the isotropic and transverse planes as a function of uniaxial stress.

Uniaxial Stress (psi)	M_{11} (GPa)	M_{33} (GPa)	M_{55} (GPa)	M_{12} (GPa)	M_{44} (GPa)	M_{13} (GPa)
7,000	55.73	45.26	22.81	7.02	24.35	6.44
10,000	58.33	48.95	24.44	7.40	25.47	7.00
18,000	60.91	51.24	25.31	8.14	26.39	8.81

Table 3-4: Computed quasi-static stiffness components from the moduli as a function of uniaxial stress (minor cycles).

Uniaxial Stress (psi)	K (GPa)	α	K` (GPa)	α`
7,000	66.21	0.42	55.29	0.52
10,000	71.32	0.37	60.30	0.47
18,000	75.50	0.34	65.77	0.42

Table 3-5: Computed quasi-static bulk modulus and Biot's effective stress coefficients (minor cycles).

3.3.6 Dynamic Data Summary

The dynamic stiffness components were computed from measured velocities using relationships discussed earlier. The major velocities used to compute the stiffness components are shown in Figures 3-22 and 3-23. Also, Figure 3-23, also shows the shear velocity measured for the horizontal sample with polarization oriented parallel to the plane of symmetry which compared with average shear velocity measured for the vertical sample to verify that these rocks exhibit transverse isotropy. The computed stiffness components are given in Table 3-6 as a function of applied uniaxial stress and also plotted in Figure 3-24. It can be noticed that the difference in the magnitudes for M_{12} and M_{13} at low and high stress magnitude are quite large. This is due to the increase in the compressional velocity in the horizontal sample which increases both M_{11} and M_{13}. The increase in the stiffness components as a result of applied stress is given by Figure 3-25. The computed dynamic moduli and the Biot's PPC coefficients are given in Table

3-7. To illustrate the effect of stress on the magnitude of the Biot's PPC, the coefficients measured in both planes are plotted in Figure 3-26.

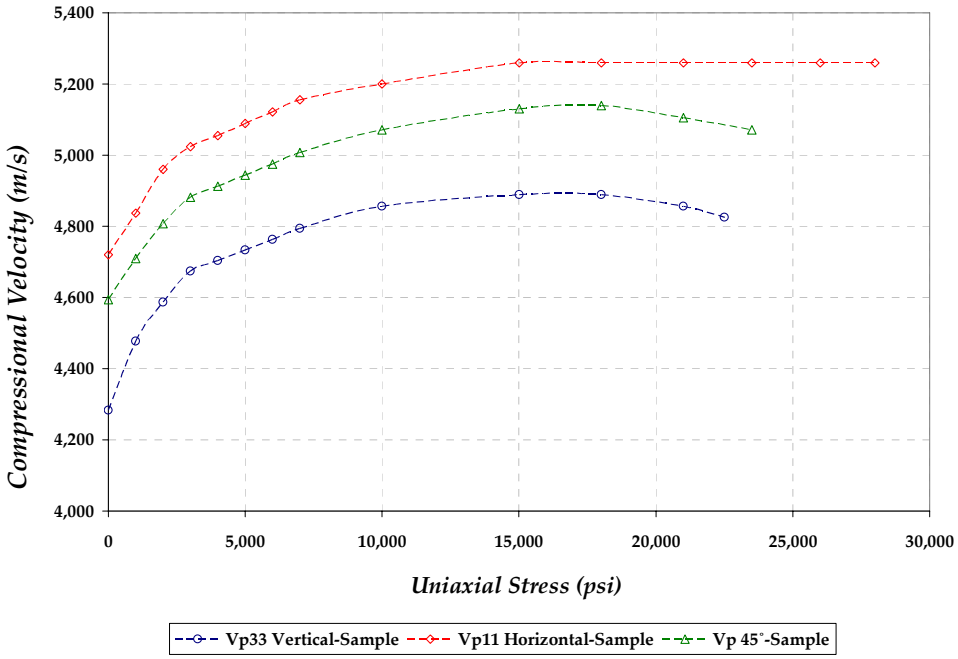

Figure 3-22: Compressional velocity measured for the three samples as function of uniaxial stress.

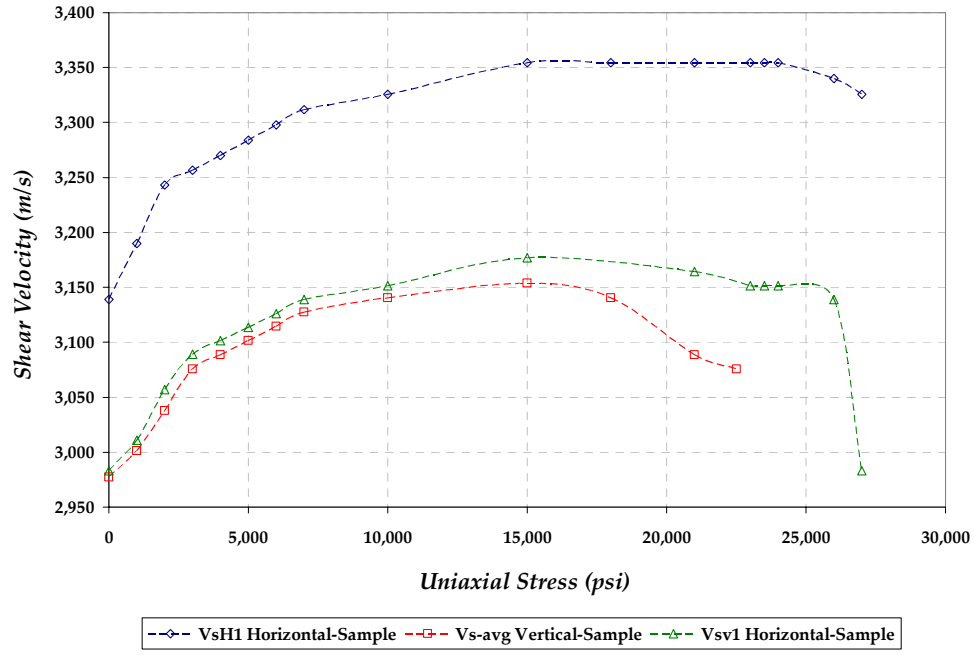

Figure 3-23: Shear velocity measured for the horizontal and vertical samples as function of uniaxial stress.

Uniaxial Stress (psi)	M_{11} (GPa)	M_{33} (GPa)	M_{55} (GPa)	M_{12} (GPa)	M_{44} (GPa)	M_{13} (GPa)
0	55.00	45.28	21.88	6.36	24.32	9.95
1,000	57.75	49.46	22.23	7.51	25.12	11.19
2,000	60.71	51.93	22.78	8.79	25.96	11.96
3,000	62.28	53.91	23.35	9.93	26.18	12.60
4,000	63.08	54.60	23.54	10.29	26.40	12.95
5,000	63.91	55.29	23.74	10.67	26.62	13.31
6,000	64.74	56.00	23.94	11.06	26.84	13.67
7,000	65.60	56.73	24.14	11.46	27.07	14.04
10,000	66.73	58.22	24.35	12.13	27.30	15.59
15,000	68.27	58.99	24.55	12.72	27.77	16.92
18,000	68.27	58.99	24.35	12.72	27.77	17.77
21,000	68.27	58.22	23.54	12.72	27.77	18.01

Table 3-6: Dynamic stiffness components computed from velocities.

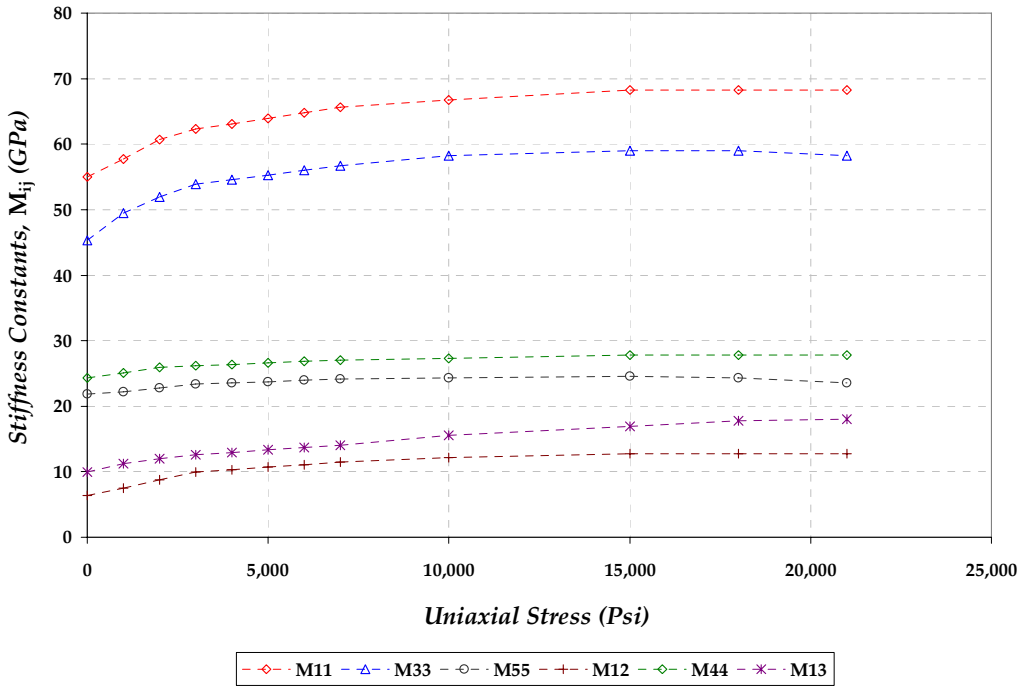

Figure 3-24: Measured dynamic stiffness components as a function of uniaxial stress.

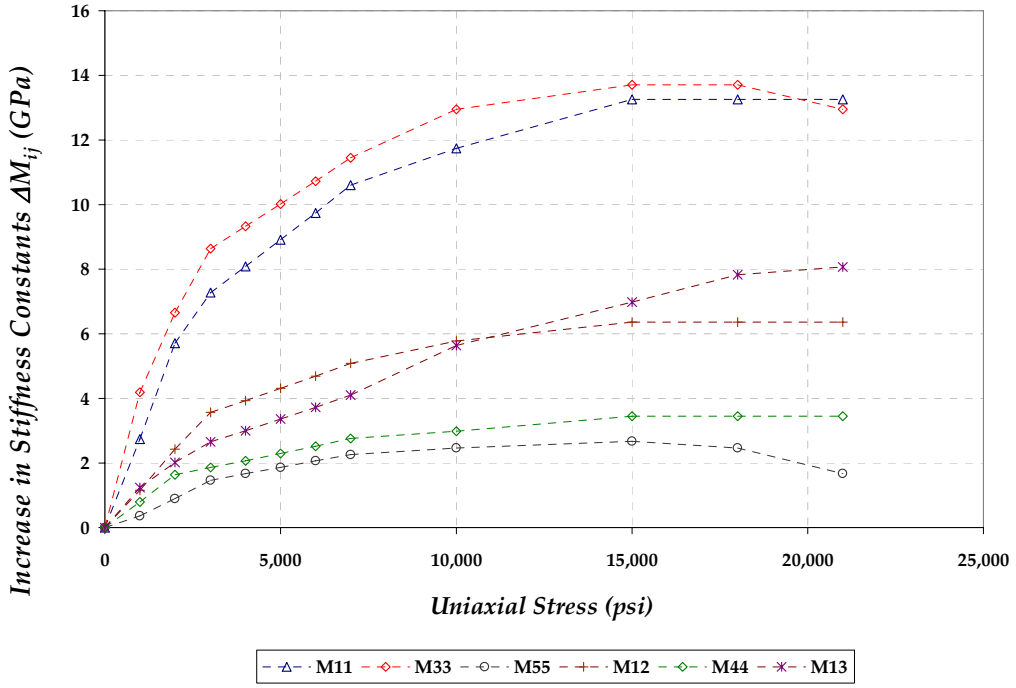

Figure 3-25: Increase in the dynamic stiffness components as a function of uniaxial stress.

Uniaxial Stress (psi)	E (GPa)	E` (GPa)	ν (GPa)	ν` (GPa)	G` (GPa)	E/E`	α	α`
0	52.48	42.05	0.0791	0.2023	21.88	1.25	0.37	0.43
1,000	54.77	45.62	0.0902	0.2058	22.23	1.20	0.33	0.37
2,000	57.33	47.82	0.1042	0.2063	22.78	1.20	0.29	0.33
3,000	58.51	49.51	0.1176	0.2063	23.35	1.18	0.26	0.31
4,000	59.14	50.02	0.1203	0.2087	23.54	1.18	0.24	0.29
5,000	59.78	50.55	0.1230	0.2110	23.74	1.18	0.23	0.28
6,000	60.44	51.07	0.1257	0.2134	23.94	1.18	0.22	0.27
7,000	61.10	51.61	0.1285	0.2158	24.14	1.18	0.20	0.26
10,000	61.55	52.06	0.1272	0.2336	24.35	1.18	0.17	0.22
15,000	62.44	51.92	0.1241	0.2512	24.55	1.20	0.14	0.19
18,000	62.05	51.19	0.1171	0.2660	24.35	1.21	0.13	0.17
21,000	61.88	50.21	0.1140	0.2741	23.54	1.23	0.13	0.17

Table 3-7: Computed dynamic moduli and the Biot's effective stress coefficients as a function of uniaxial stress.

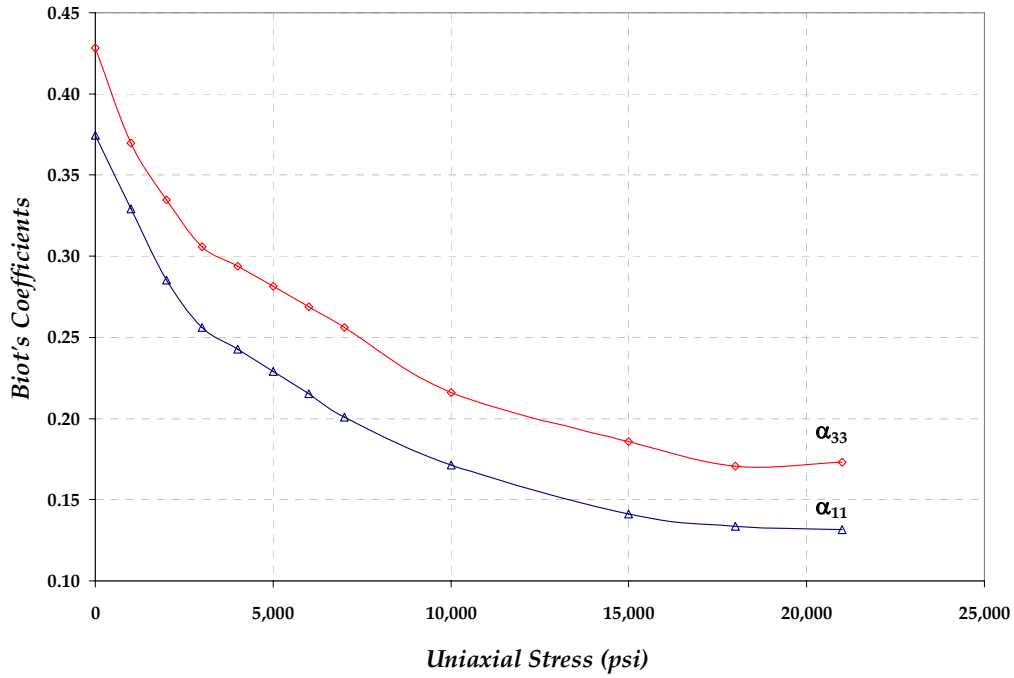

Figure 3-26: Plot of the anisotropic dynamic Biot's effective stress coefficients as a function of uniaxial stress.

3.3.7 Failure Analysis

The observations of the failure mechanism as a function of sample orientations are analyzed and compared with the recent work of Tien et al., (2006). Their work included analysis of the failure modes of a transversely anisotropic artificial rock made out of two layers where the anisotropy is in the form of the constituent, porosity and mechanical properties of each layer. They interpreted the failure mechanisms as a function of orientation using surface image scanner during the failure process which then used to reconstruct a 3-D image of the specimen with the failure pattern. Their major conclusions for the samples with layers orientated at 0˚, 45˚and 90˚ with reference to the loading direction under zero confining pressure (same as Lyons testing conditions) are listed as:

Sample with 0˚ orientation: The cracks develop initially in the softer layer before reaching peak strength and grow rapidly and become interconnected parallel to the direction of loading and across the layers when peak strength is reached. The authors explain this type of failure mode as due to the deformation of the softer material resulting in cracks that exerted tensile stress on the hard layer due to the circumferential deformation (Poisson's ratio effect) without lateral constraint. This also explains the wider tensile cracks between the layers of the tested material. As shown in Figure 3-27a through 3-27c, the macro-cracks developed parallel to the direction of axial load after the failure has occurred. This is compared with the Lyons tested sample with same beddings orientation relative to loading direction (0˚) as illustrated in Figure 3-27d.

Sample with 45˚ orientation: They observed that a sudden failure has occurred along the boundary of the two layers (discontinuity). They attributed that to the higher shear stress acting at the boundary than could be maintained by its shear strength, and the resulting fracture orientation is parallel to the discontinuity. Figure 3-28a through 3-28d show the comparison of their observations with the case of Lyons sample oriented at a 45˚ relative to the direction of loading.

Sample with 90˚ orientation: Tien et al., 2006 observed that there are no obvious cracks that can be identified until the stress level reaches the peak strength. This was the case of one of the Lyons samples with bedding planes parallel to the loading direction (H-2, the one chipped on the side). The development of major cracks was occurred when the strain level increased slightly after post failure with

direction parallel to the loading. They also observed that the number of cracks observed on the discontinuity is much greater than those developed within the two materials forming the bedding planes. The macroscopic observations are identical to the failure mode observed for the Lyons sample with vertical beddings relative to the direction of loading. Figure 3-29 shows the comparison of their observations with the case of the Lyons sample oriented at 90˚ relative to the direction of loading.

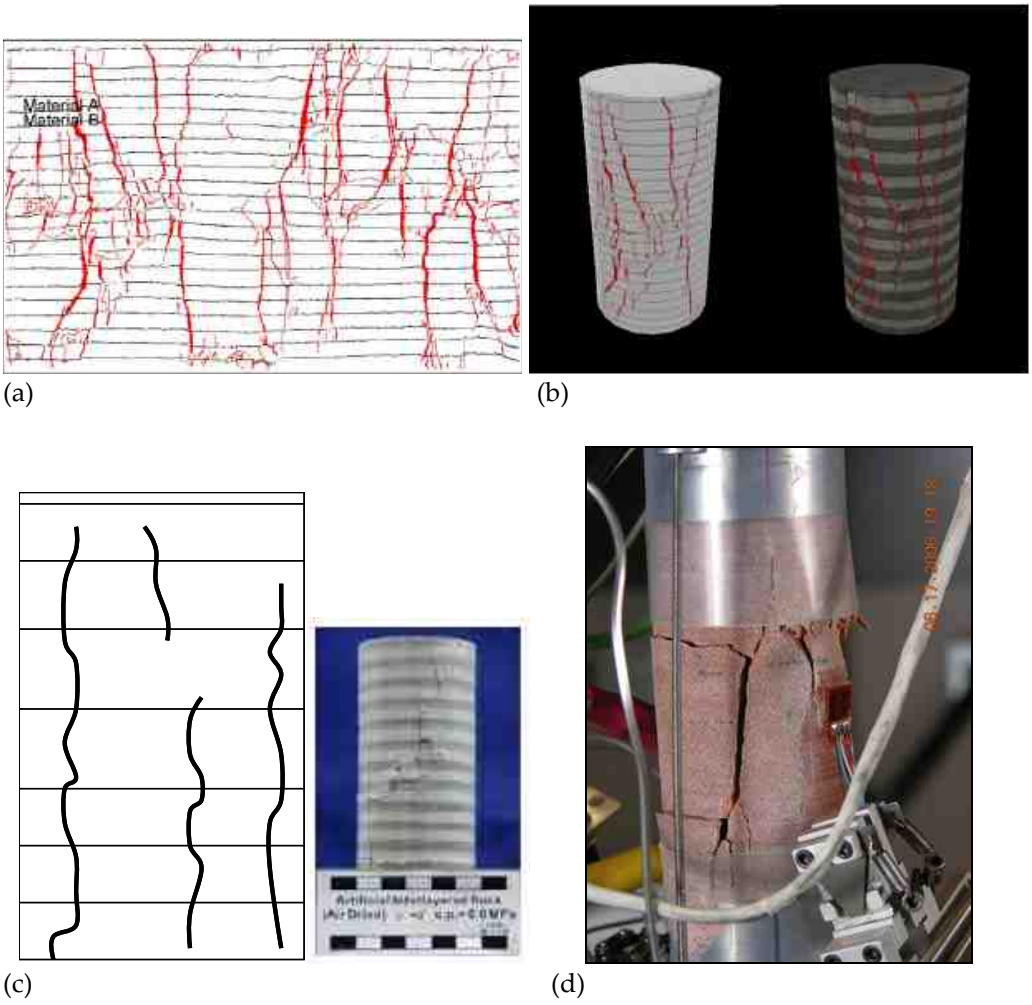

(a) (b)

(c) (d)

Figure 3-27: (a) Enhanced image during the deformation for the sample with a 0˚ orientation, (b) reconstructed image of the sample after failure, (c) sample with a 0˚ orientation after testing with illustration of the direction of developed micro-cracks (Tien et al., 2006), (d) Lyons sample with a 0˚ orientation after failure.

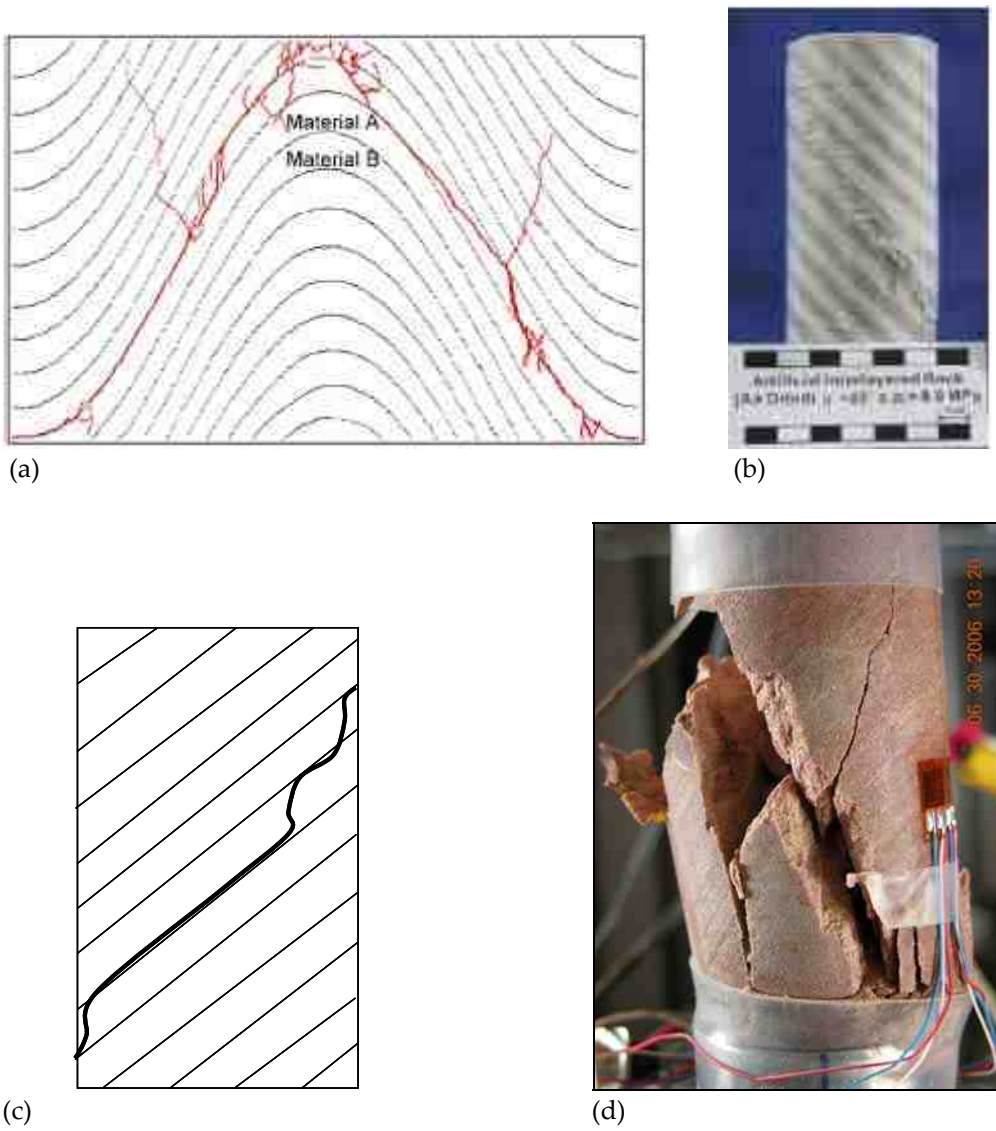

Figure 3-28: (a) Enhanced image during the deformation of the sample with a 45° orientation, (b) photograph of a tensile fracture across discontinuities for a 45° sample, (c) illustration of the 45° sample after testing with the direction of developed micro-cracks (Tien et al., 2006). (d) Lyons sample with a 45° orientation after failure.

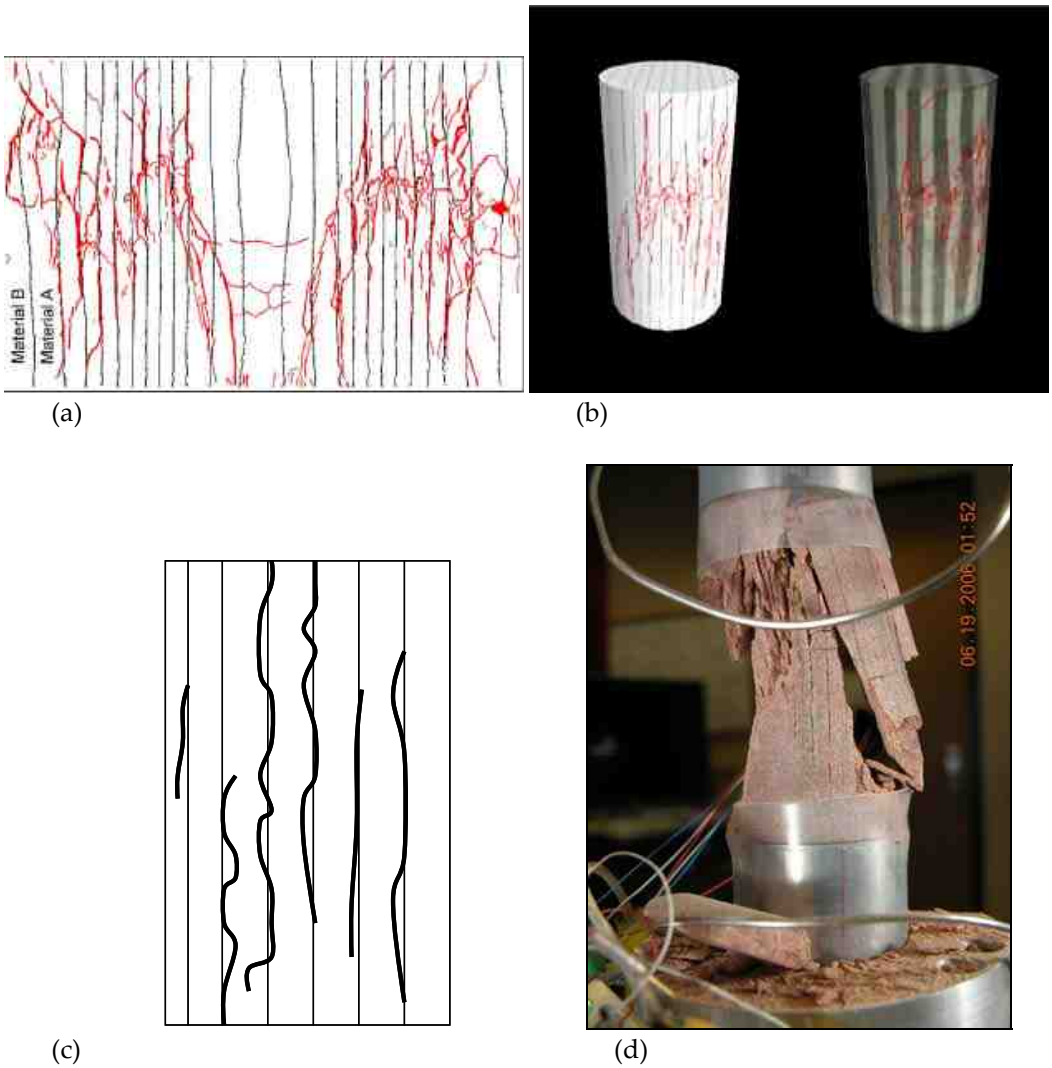

Figure 3-29: (a) Enhanced image during the deformation of the sample with a 90° orientation, (b) photograph of a tensile fracture across discontinuities for the a 90° sample, (c) illustration of the 90° sample after testing with the direction of developed micro-cracks (Tien et al., 2006), (d) Lyons sample with a 90° orientation after failure.

3.4 Discussion of Results

Low porosity and observed microstructural extensive quartz overgrowth cement play a major role in the observed stiffness of these Lyons samples. The measured velocities as a function of sample orientation at zero stress confirmed the existence of inherent transverse anisotropy. One notices that the ratio of the uniaxial compressive strength of the horizontal to the vertical sample is 1.24 which is comparable to initial quasi-static and dynamic degree of anisotropy (E/E`). More work is needed to verify this observation before it can be utilized as an alternative check for measuring anisotropic ratio when dynamic measurements are not available. A comparison of the shear velocities measured on the horizontal sample with polarization oriented parallel to the axis of symmetry with these measurements on the vertical sample indicate that these rocks exhibit transverse isotropy.

The presence of micro cracks can affect the measured velocity and anisotropy. It has been documented that the presence of cracks, even as small as a fraction of 1% of rock volume, decreases the moduli and velocities (Lo et al., 1986; Nur and Simmons, 1969). The initial linear behavior of the stress-strain curves during loading especially from strain gage measurements indicates that the contribution of micro cracks in the inherent anisotropy in these samples is minimal. At low stress, the difference between the computed stiffness components from the quasi-static and dynamic measurements is within 10%. The effect of stress-induced anisotropy on the dynamic stiffness components is significant especially for the

components M_{12} and M_{13}, where the increase in their magnitudes at a stress level of 21,000 psi is measured to be 100% and 81%, respectively. This can be observed in Table 3-6. The increase in stiffness components is also reflected by the measured elastic moduli.

The increase in the magnitude of Biot's PPC due to the effect of inherent anisotropy in the transverse plane relative to the isotropic plane is 24% and 16% from quasi-static and dynamic measurements, respectively. It was also observed that the difference between Biot's PPC is constant as a function of stress. The Biot's PPC measured in the vertical and horizontal directions showed significant reduction in their magnitudes due to stress anisotropy. The vertical Biot's parameter, α_{33}, from dynamic measurements decreased from 0.43 to 0.17 corresponding to a reduction of 60% over a stress range of 21,000 psi; whereas, the horizontal parameter, α_{11}, decreased from 0.37 to 0.13, corresponding to a reduction of 65% over the same stress range.

Chapter 4

Laboratory Procedures of Measuring Strain and Velocity around Borehole

The laboratory experiments were carried out on different rock types in order to determine strain, displacement, and acoustic velocity around a borehole on cubic block samples corresponding to different types of rock as a function of stress. Velocities, including compressional and polarized shear (V_{S1} and V_{S2}), were measure around the borehole at the two principal directions where the largest compressive and tensile stresses are induced. Borehole strains and displacements were also measured simultaneously with borehole acoustic velocities at the two principal directions. The measurements were first calibrated on aluminum and then performed on different rock types. Uniaxial compressive tests were also conducted on core samples of the tested rock materials to provide both quasi-static and dynamic mechanical properties. The mechanical properties were used to calibrate both quasi-static and dynamic measurements on the large samples.

4.1 Sample Types and Geometry

The measurements were performed on $6\times6\times6$ inches cube samples. Different types of rocks tested include Berea sandstone, chalk, white limestone and Pierre shale. The block faces were ground to insure parallel faces and avoid uneven loading on the blocks. A hole of 0.93 inches in diameter was drilled through the center of each tested block. Four Berea blocks, two chalk blocks, two white limestone blocks, and one Pierre shale block were tested for final acoustic and strain measurements. However, three Berea blocks were used initially as candidates for benchmark testing to standardize the testing procedures on rock samples.

4.2 Uniaxial Compressive and Tensile Testing

Uniaxial tests were also performed on 2:1 cylindrical cores taken from the tested block samples with diameter and length of 1.5 inches and 3.0 inches, respectively, to determine the mechanical properties, mainly E and ν, which then were used to compute borehole strains and displacements. Also, acoustic velocity measurements, including compressional and shear velocity, were performed during the uniaxial testing of cylindrical samples. The velocities were measured in the loading direction using one compressional and two orthogonal shear PZT-5a piezoelectric crystals mounted on the end platens. Thin sheets of lead foil were used as a coupling between the sample and the loading platens. The core velocity data were used in calibrating borehole velocity measurements. The mechanical

properties for tested rock samples, including porosity, grain density and compressive strength for the tested rock samples, are given in Table 4-1.

Sample Type	Porosity, (%)	Grain Density, (g/cc)	Uniaxial Compressive Strength, (Psi)
Berea Sandstone	19.20	2.69	11,300
Chalk	47.42	2.68	1,200
White Limestone	24.37	2.71	3,200
Pierre Shale	17.54	2.67	1,350

Table 4-1: Rock properties for the tested block samples

Tensile strength tests (Brazilian tests) were performed on disc geometry samples belonging to different material types. The test is mainly intended for determining the tensile strength for rock samples which were used to confirm borehole strain gage measurements placed at the maximum induced tensile stress directions (i.e., $\theta = 90^{\circ}$ and $\theta = 270^{\circ}$). Tensile sample testing size is 1.5" diameter and 0.5" length. All samples were tested at a loading rate of 200 N/s (ISRM standards) such that failure in the weakest rocks occurs within 15-30 s. The loading is controlled by displacement using machine stroke and strain gage attached to the disc sample. Figure 4-1 shows the typical failure pattern for tensile testing while Figure 4-2 illustrates chalk samples under preparation and a white limestone sample during tensile testing. The tensile strength is computed, from the sample's geometry (length and diameter) and the load (P) at which tensile failure occurs (Aydin & Basu 2005), as:

$$\sigma_t = \frac{2P}{\pi LD} \tag{4.1}$$

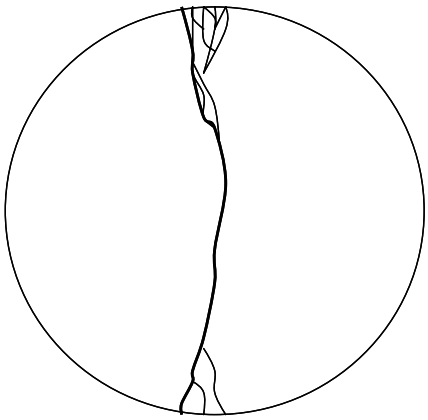

Figure 4-1: Typical failure pattern in tensile strength testing (Brazilian test).

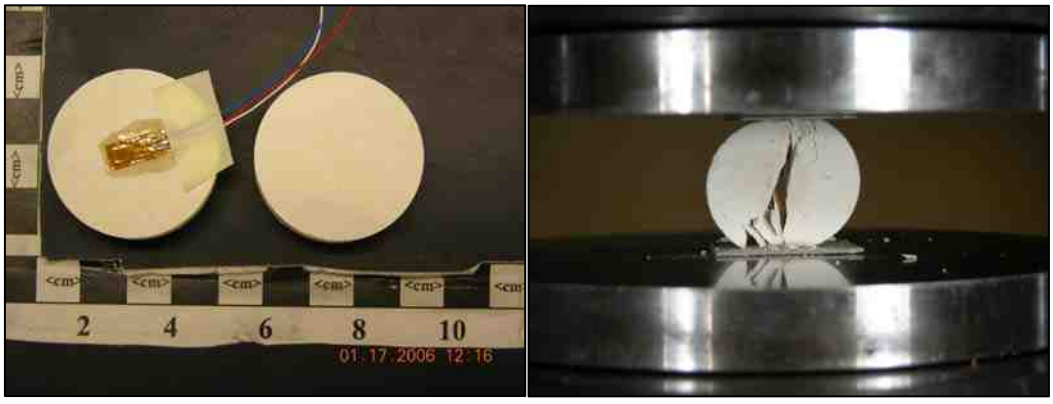

Figure 4-2: Sample geometry with strain gage mounted for strain measurements on chalk (left picture). Right picture shows a white limestone sample after tensile failure.

4.3 Borehole Strain Gauging

Borehole strains were measured using strain gages placed at the center of the borehole at the two preferred directions, perpendicular and parallel to loading direction (i.e., $\theta = 0^{\circ}$ and $\theta = 90^{\circ}$). To test the repeatability of the strain measurements, another set of gages was also placed at the opposite directions ($\theta = 180^{\circ}$ and $\theta = 270^{\circ}$) as shown in Figure 4-3. The borehole strain gages are T-shape gages with two girds (0.125" by 0.165") oriented along the circumference and the axis of the borehole similar to the ones used in the measurements performed in Chapter 3. The borehole gauging process is done for one gage at a time. First, the lead wires are soldered to the gage terminals before it is carried inside the borehole. The gage is then aligned and placed backside on a special tape before the glue is applied as shown in Figure 4-4. After applying the glue on the gage backside, the tape is carefully placed inside the borehole and aligned with marked orientations; a pressure of 5 psi is applied in the borehole using a sealed ends tube to hold the gages in place to dry for a day. The sign convention for strain gage measurement is positive for tension and negative for compression. The functionality of the borehole strain gages and their repeatability are checked by loading the rock samples to a small stress level before being used for final loading. Rosette gages were used on borehole faces to measure strain at a distance from the borehole. Two clip gages were also used to measure the displacements of the borehole. The gages were mounted on the borehole using four spacers with curved surface to have good contacts with borehole wall. The displacement

measurements were taken in the vertical and horizontal directions with respect to the loading direction.

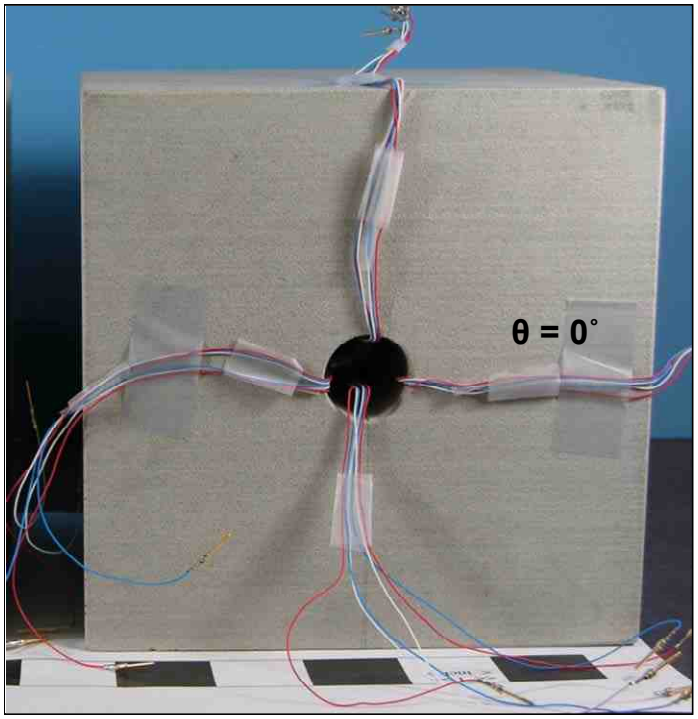

Figure 4-3: Pictorial display of a Berea block under strain gages instrumentation.

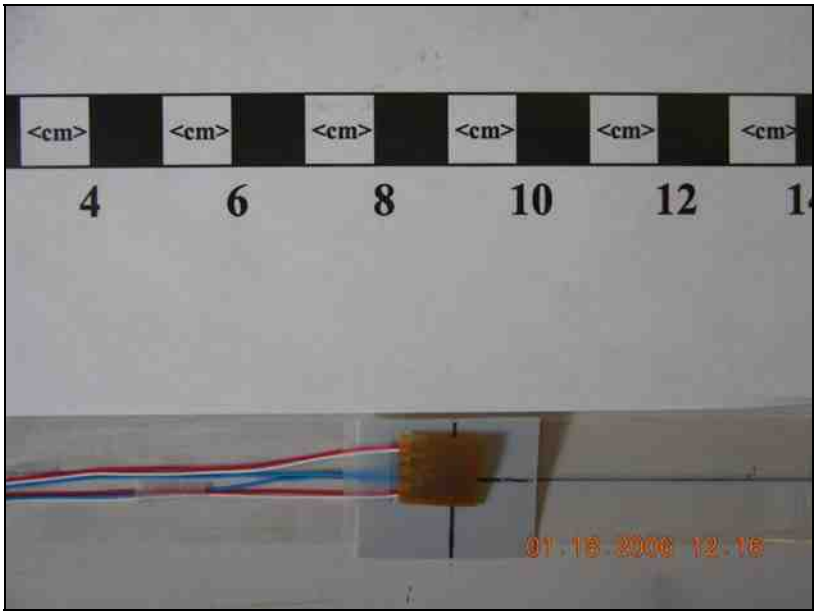

Figure 4-4: Strain gage alignment prior to being mounted in the borehole.

4.4 Velocity Measurements in Borehole

Acoustic velocities in a borehole were measured for the tested samples as a function of applied boundary stress simultaneously with borehole strain measurements using a standard pulse transmission technique. Piezoelectric (PZT-5a) crystals (0.25" in diameter) glued directly on the samples at preferred directions were used to generate and receive P- and polarized S-waves at a frequency of 600 kHz. The P- and polarized S-wave velocities (V_p, V_{s1} and V_{s2}) were measured perpendicular (radially) and parallel to the borehole axis at the two preferred orientations, $\theta = 0^\circ$ and $\theta = 90^\circ$. For the velocities measured perpendicular to the borehole, the transmitters are placed on the side and top faces of each tested sample and the receivers are mounted inside the borehole with similar orientations. The polarization of the two shear velocities was parallel and perpendicular to the applied uniaxial boundary loading direction as shown in Figure 4-5.

To avoid load on transmitters, a thin loading plate with small holes that fit transmitting crystals is used on the top of each tested sample. Figure 4-6 shows the aluminum sample after being instrumented with strain gages and velocity transducers. Compressional and oriented shear velocities are also measured parallel to the axis of the borehole where the transmitters and receivers are placed on the block faces perpendicular to the borehole axis. In the later velocity arrangements, one compressional and two oriented shear velocities are measured at the borehole wall 'near borehole measurements'. Two additional shear

velocities with different polarizations relative to loading (slow and fast) are also acquired in the major orientations at a distance from the borehole 'far borehole measurements' (about 1.5 borehole diameters away). The slow and fast shear velocities acquired at a distance from the borehole were used to simulate low frequency measurement and utilized to estimate applied stresses from measured shear velocities based on the Sinha and Kostek (1996) model using Equation (2.1). The configuration of the face velocities acquisition and far shear velocities polarization are illustrated in Figures 4-7 and Figure 4-8, respectively. Figure 4-9 shows one of the Berea block samples after instrumentation with strain gages and acoustic transducers. The initial borehole and face compressional and shear velocities were acquired prior to loading and calibrated with velocities measured on core samples for validation of final velocity measurements.

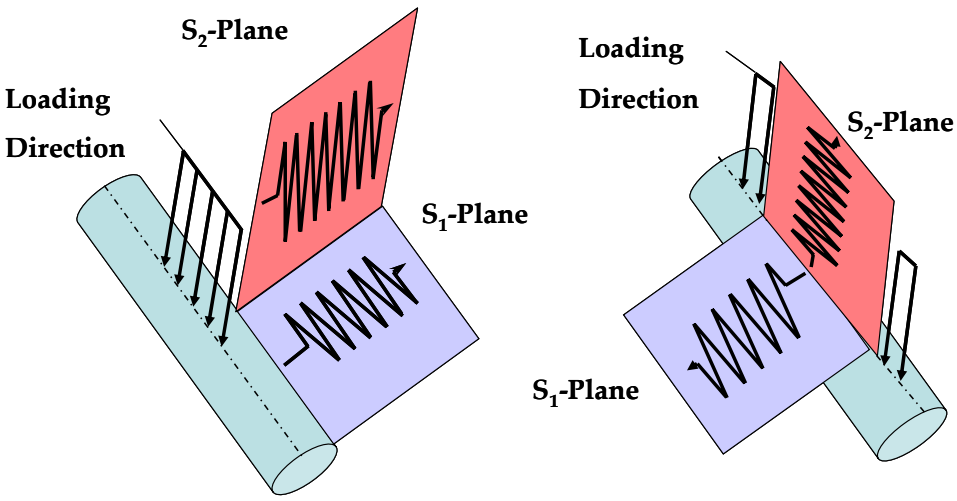

Figure 4-5: Borehole shear velocity, V_{s1} and V_{s2}, orientations at the side of the borehole at $\theta = 0^{\circ}$ (left) and at the top of the borehole at $\theta = 90^{\circ}$ (right) with respect to the loading direction.

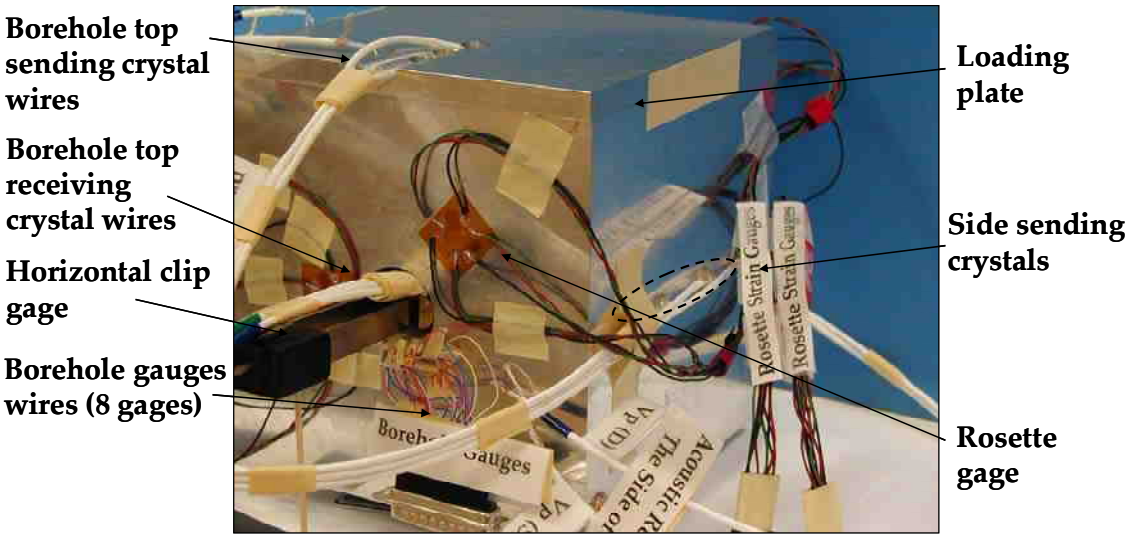

Figure 4-6: Aluminum calibration sample after complete strain and velocity instrumentations.

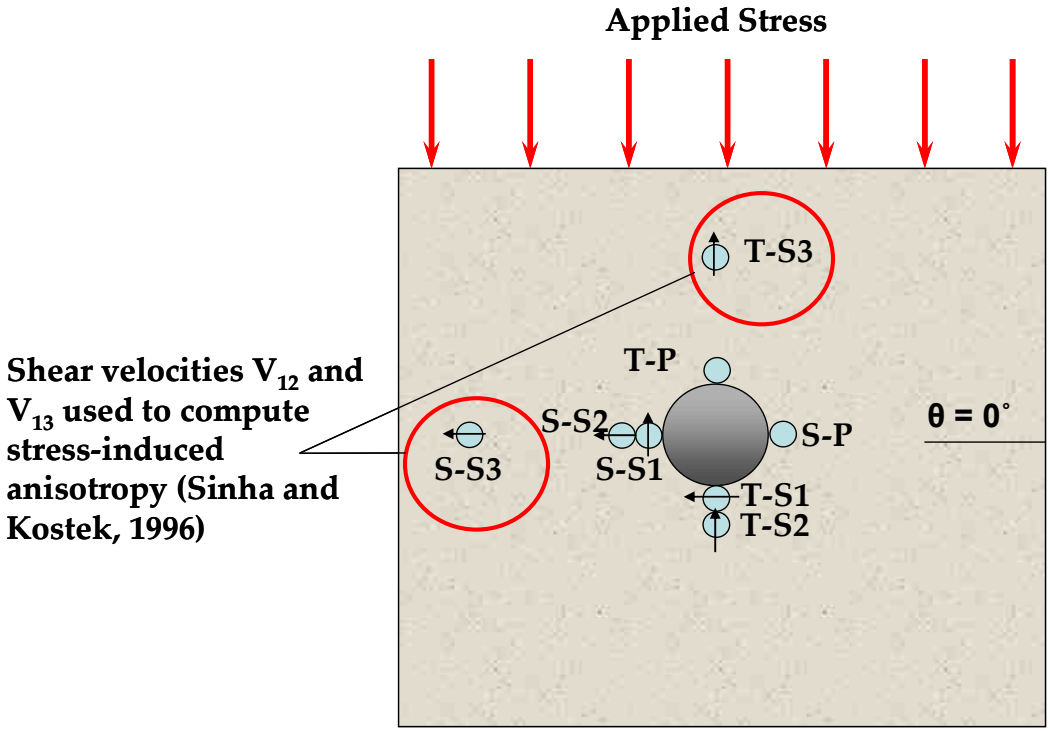

Figure 4-7: Face velocity transmitters and receivers arrangement for rock samples, where the arrows on the shear transmitters indicate the polarization of the shear velocities.

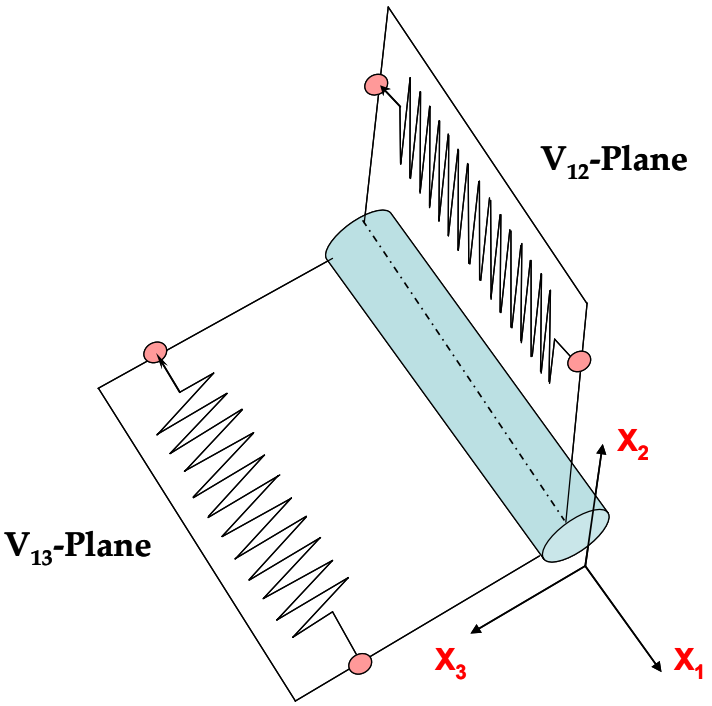

Figure 4-8: Orientations of the far fast and slow shear velocity measurements acquired for stress estimation.

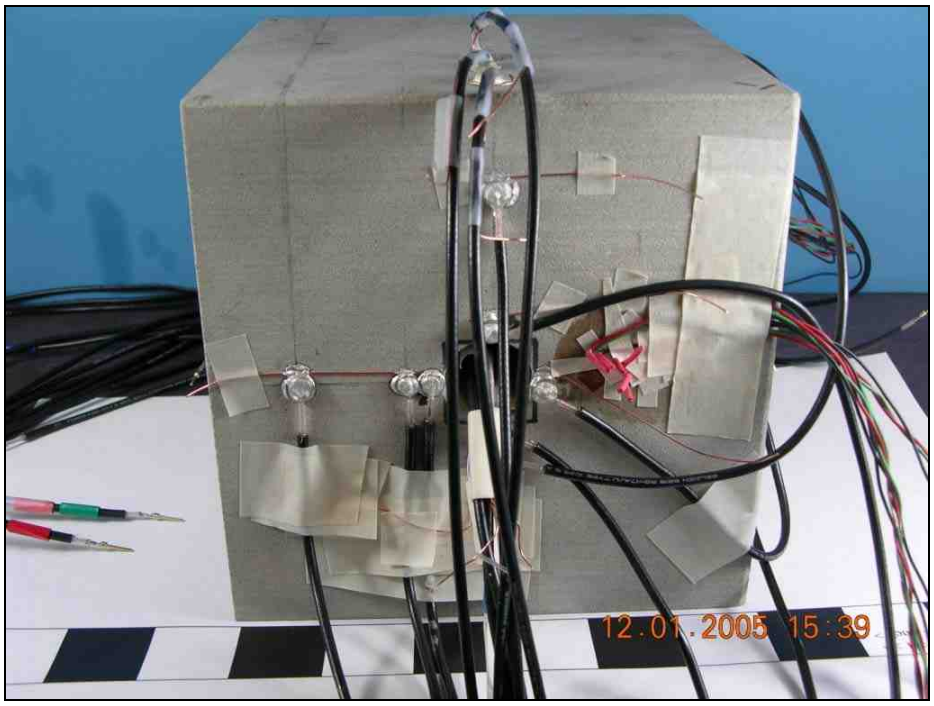

Figure 4-9: A pictorial view of one of the Berea rock samples after acoustic and strain instrumentation.

4.5 Equipment and Acquisition

For simplicity, a uniaxial loading condition was used in all the measurements. A servo-controlled MTS load (Model 815) frame with maximum loading capabilities of 2,669 kN (600,000 lb_f) was used to perform the measurements. The cube samples were loaded under stroke control to a uniaxial stress of 6,000 psi for aluminum, 8,500 psi for Berea block samples, 1,000 psi for chalk, 2,400 for white limestone block samples, and 450 psi for Pierre shale block samples where borehole failure is observed in the rock samples at these applied stresses.

Data were acquired digitally and stored in a compute. The number of the data inputs recorded is 18, including voltage raw readings for load, stroke displacement, borehole strain gages, rosette gages and borehole displacement readings. The voltage values are converted to engineering units before the data are analyzed. The raw voltage from the load and strain gages are plotted in real-time using an external plotter connected to the data acquisition for monitoring and controlling the experiments. The acoustic measurements were taken as function of load. Two oscilloscopes and one pulse generator (square wave pulse with amplitude of 100 volts) were used for acquiring 14 velocity measurements across and along the borehole. Figure 4-10 shows one of the white limestone samples under loading and data acquisition.

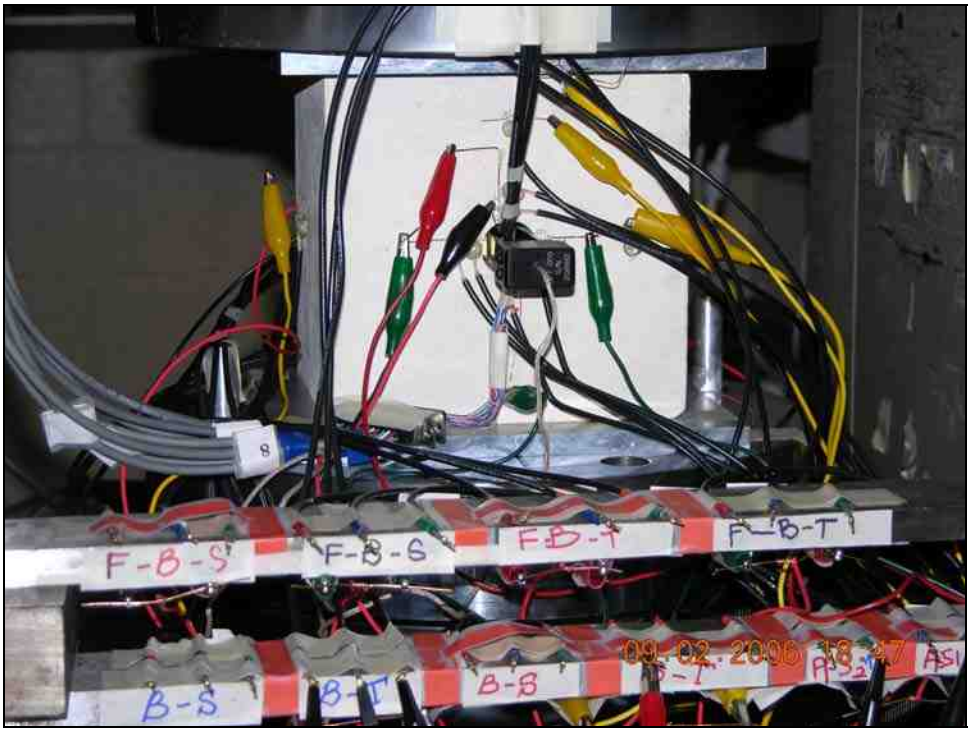

Figure 4-10: A white limestone block sample under loading and data acquisition.

Chapter 5

Finite Element Modeling of the Experiments Using ABAQUS

Finite element simulations were performed to validate the borehole quasi-static measurements during laboratory experiments. The motivation for conducting the finite element analysis was to generate the complete 3D stress and strain contours around the borehole and compare the results with the measurements at the borehole wall for selected types of sample. Also, simulations were used to ensure the optimum size ratio of the tested specimen relative to the borehole that allows the induced stresses to dissipate and reach applied stresses at the boundaries.

This chapter serves the two purposes discussed above, and it briefly covers an overview of the modeling approach used to develop the numerical data. The data output including the stress and strain contours for the Berea and chalk samples are presented in this chapter whereas the comparison with experimental data is presented later in Chapter 6.

5.1 Conventions and Generated Model

A 3-D finite element model (FEM) was constructed using a Hexahedral 3-D stress element with 20 nodes and used to predict the behavior of the tested samples with 0.93 inches wellbore size. The dimensions used in the numerical simulations were the same as the dimensions of the actual tested samples. Figures 5-1 and 5-2 illustrate the convention used in generating the model and geometry. The total number of the elements and nodes are 64,000 and 284,160, respectively, as shown in Figure 5-3. Mesh refinement was done to ensure accuracy of the results by comparing the elastic analysis with Kirsch's solution (1898) which is given for a hole in an infinite plate subjected to a far field stress as:

$$\sigma_{rr} = \frac{\sigma}{2}\left[\left(1-\frac{a^2}{r^2}\right)+\left(1+\frac{3a^4}{r^4}-\frac{4a^2}{r^2}\right)\cos 2\theta\right] \tag{5.1}$$

$$\sigma_{\theta\theta} = \frac{\sigma}{2}\left[\left(1+\frac{a^2}{r^2}\right)-\left(1+\frac{3a^4}{r^4}\right)\cos 2\theta\right] \tag{5.2}$$

where σ_{rr} and $\sigma_{\theta\theta}$ are the radial and circumferential stress components, respectively; θ is the angle with reference to the far field compressive stress σ, a is borehole radius, and r is the distance from the borehole. The borehole radial and tangential displacements u_r and v which will be used in Chapter 6 to compute the borehole displacements are also given as:

$$u_r = \frac{1}{E}\left[\frac{\sigma}{2}\left(r + \frac{a^2}{r}\right) + \frac{\sigma}{2}\left(r + \frac{4a^2}{r} - \frac{a^4}{r^3}\right)\cos 2\theta\right] - \frac{\nu}{E}\left[\frac{\sigma}{2}\left(r - \frac{a^2}{r}\right) - \frac{\sigma}{2}\left(r - \frac{a^4}{r^3}\right)\cos 2\theta\right] \quad (5.3)$$

$$\mathrm{v} = -\frac{1}{E}\left[\frac{\sigma}{2}\left(r + \frac{2a^2}{r} + \frac{a^4}{r^3}\right)\sin 2\theta\right] - \frac{\nu}{E}\left[\frac{\sigma}{2}\left(r - \frac{2a^2}{r} + \frac{a^4}{r^3}\right)\sin 2\theta\right] \quad (5.4)$$

It can be noticed that the tangential displacement, v, along the angle θ is zero for all value of *r* when θ = 0 or θ = (π/2). The tangential strain $\varepsilon_{\theta\theta}$, which is a function of the borehole radial displacement u_r, derivative of the tangential displacement with respect to the angle, $\frac{\partial \mathrm{v}}{\partial \theta}$, and borehole radius *r* is given at the borehole wall as:

$$\varepsilon_{\theta\theta} = \frac{\sigma}{E}(1 - 2\cos 2\theta) \quad (5.5)$$

The mesh is also refined around the borehole to capture the large change in stresses and strains as a function of the boundary applied stress (Figure 5-4). The model is assumed to be elastic with actual input parameters (Young's modulus, E, and Poisson's ratio,ν) determined from a uniaxial test performed on Berea and chalk samples. Once the model is divided into elements, material properties are assigned and loads are prescribed. The loads are defined in steps, and the results are obtained at incremental loads.

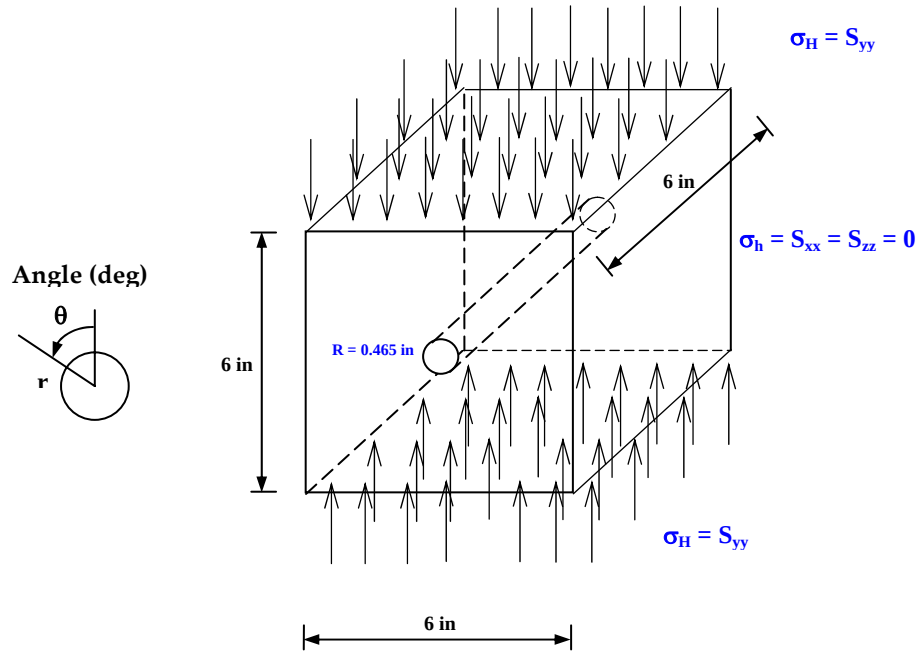

Figure 5-1: Convention used in generating the model.

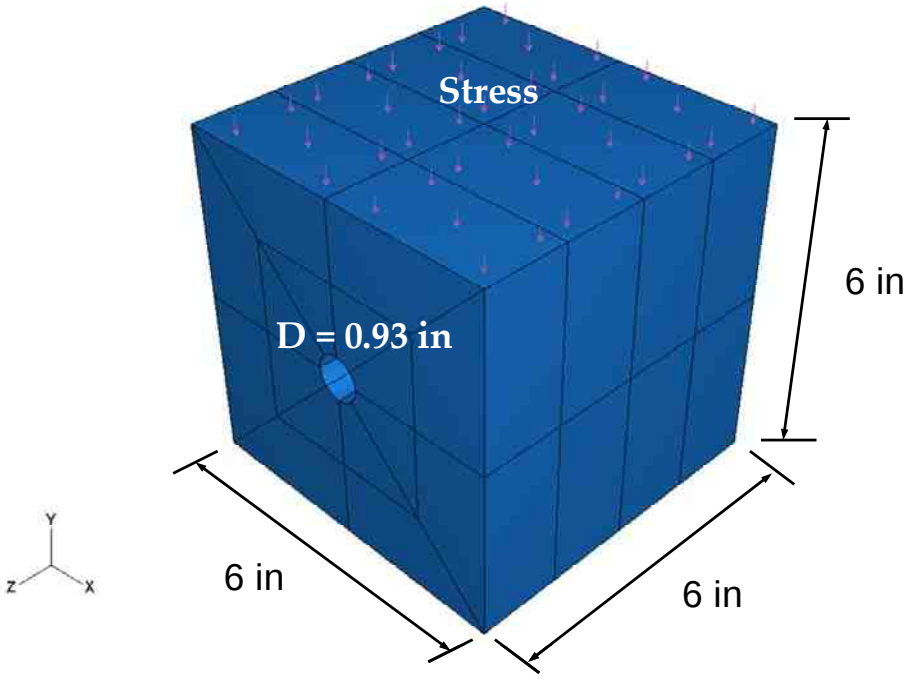

Figure 5-2: Model geometry generated in ABAQUS.

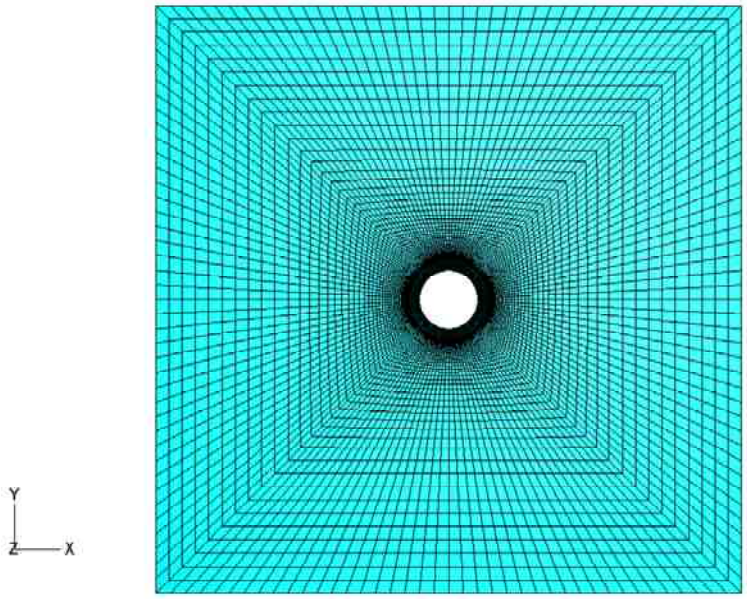

Type of elements:
Hexahedral 3D Stress (20 nodes)

No. of elements:
64,000

No. of nodes:
284,160

Figure 5-3: 3-D stress element and nodes used in generating the mesh around the borehole.

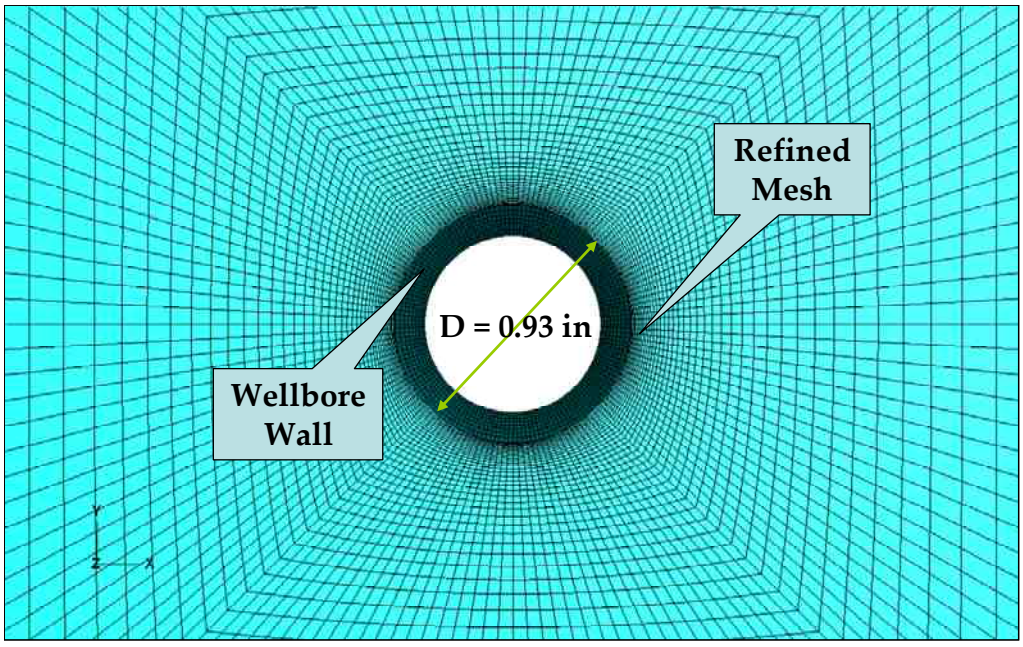

Figure 5-4: Mesh refinement around the borehole.

5.2 ABAQUS Simulation Outputs

The radial and tangential strain contours generated using ABAQUS are shown in Figures 5-5 through 5-8 for Berea and chalk samples at an applied stress of 5,000 psi for Berea and 1,000 psi for chalk. The high magnitude of the compressive stress concentration is reflected by the large tangential strain computed at the same orientations. Also, the high tensile stresses are shown by the contours in the direction of loadings. The results of the computed radial and tangential strains at a load of 1,000 psi are compared with the analytical solution of Kirsch as a function of both orientation and distance from the borehole as shown in Figures 5-9 through 5-14 for both Berea and chalk samples.

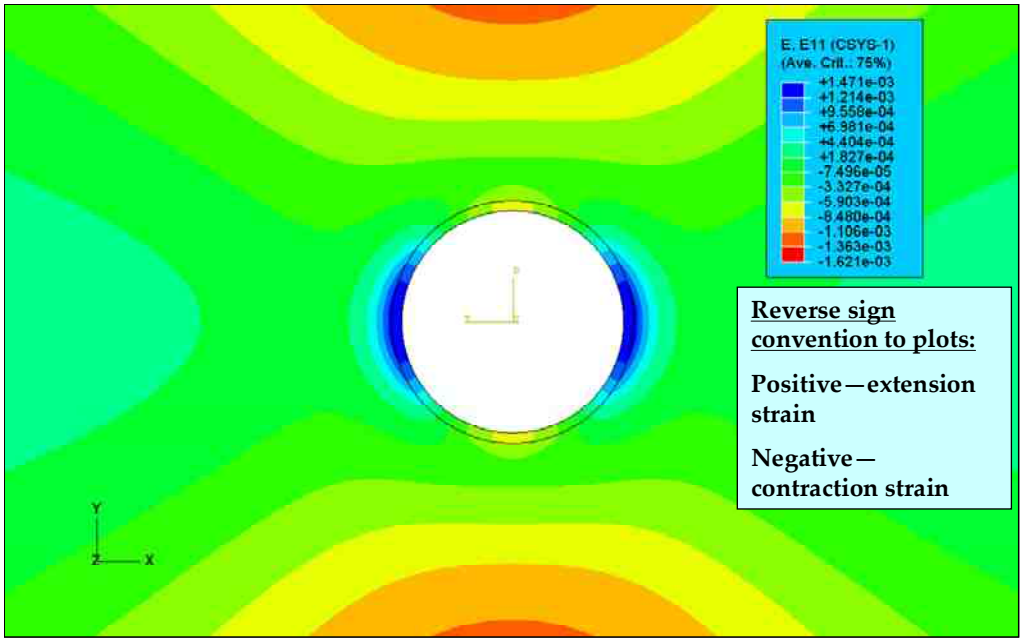

Figure 5-5: Midsection contours of radial strain around a borehole for Berea samples at 5,000 psi applied stress generated using ABAQUS.

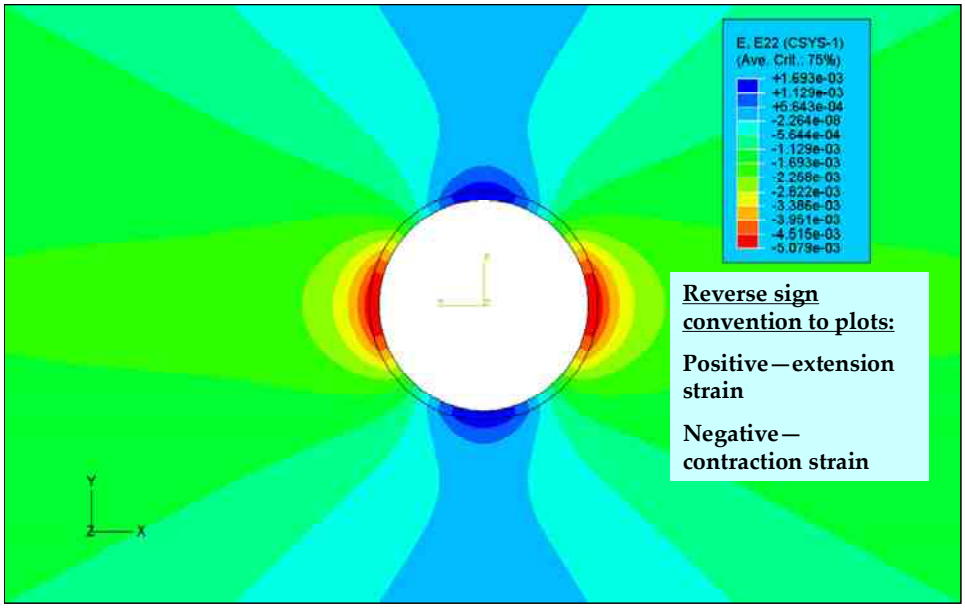

Figure 5-6: Midsection contours of tangential strain around a borehole for Berea samples at 5,000 psi applied stress generated using ABAQUS.

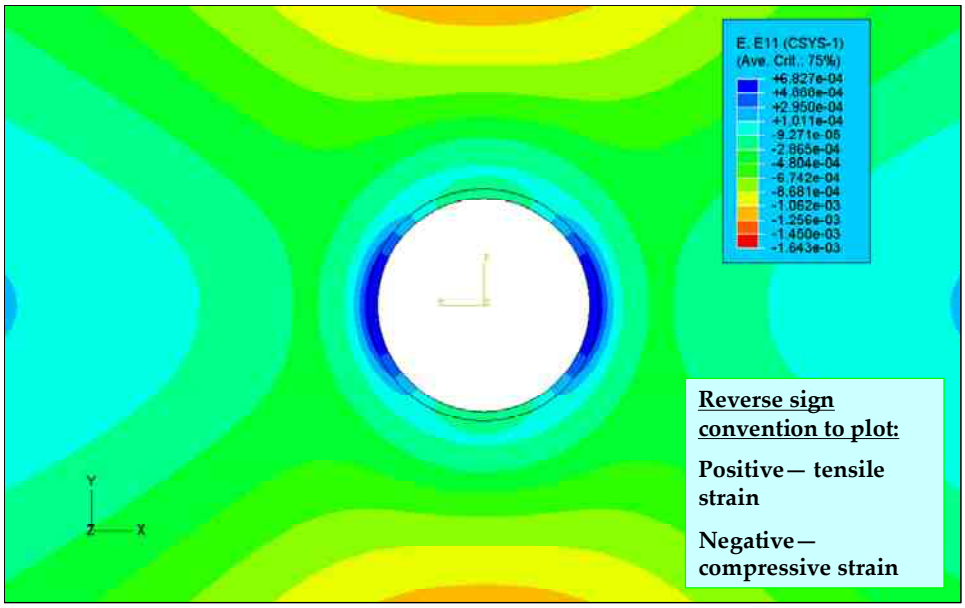

Figure 5-7: Midsection contours of radial strain around a borehole for chalk samples at 1,000 psi applied stress generated using ABAQUS.

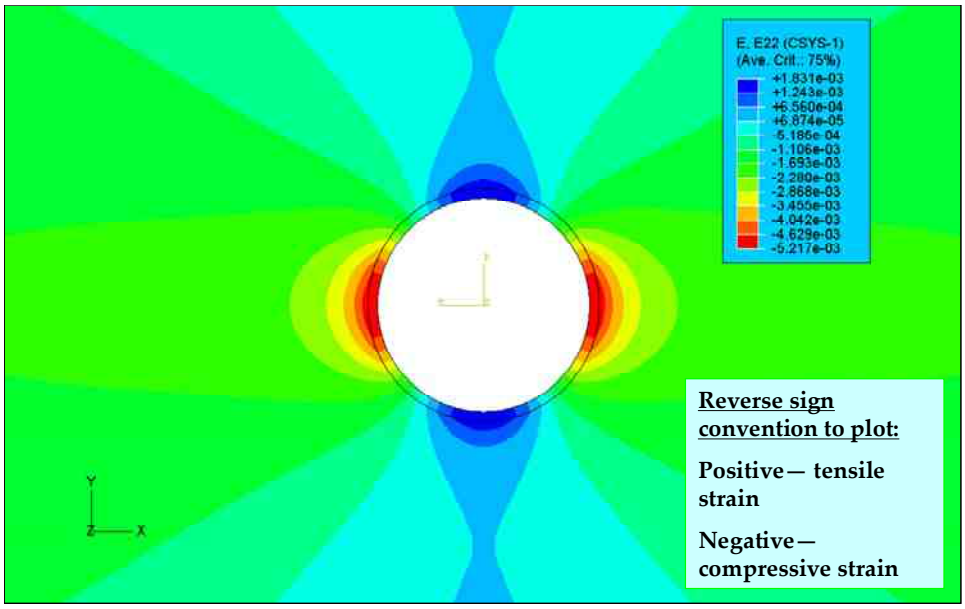

Figure 5-8: Midsection contours of tangential strain around a borehole for chalk samples at 1,000 psi applied stress generated using ABAQUS.

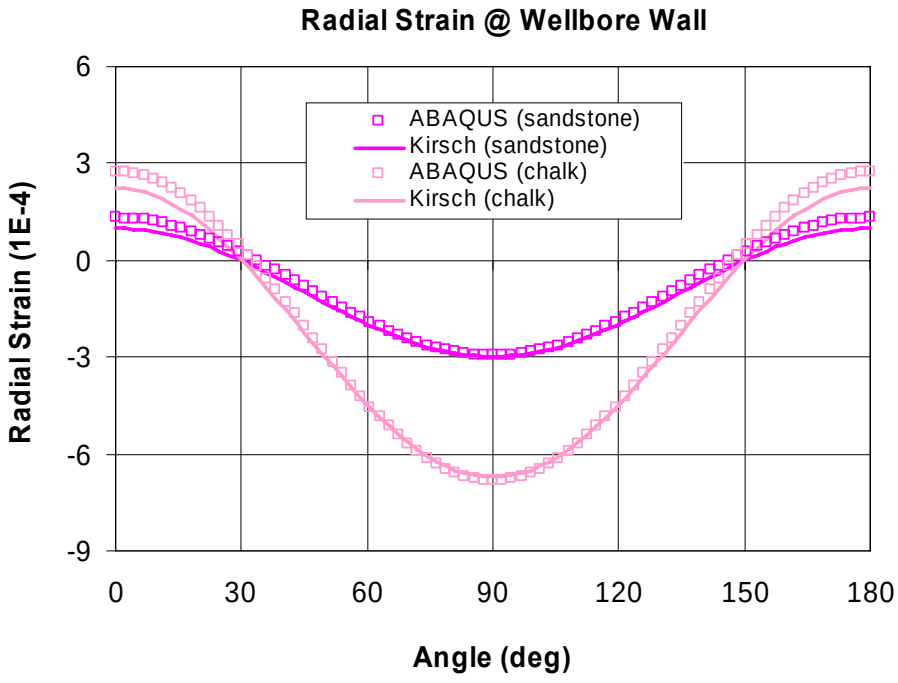

Figure 5-9: Generated radial strain around the borehole using ABAQUS as a function of orientation compared with Kirsch's solution for Berea and chalk samples at an applied load of 1,000 psi. The sign convention is based on Kirsch solution, positive for tensile strain and negative for compressive strain.

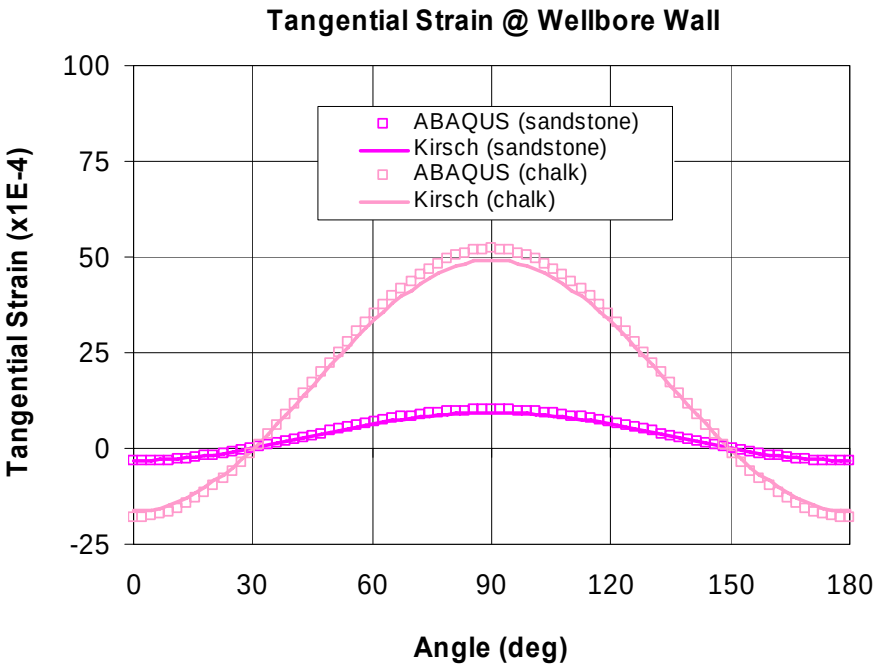

Figure 5-10: Generated tangential strain around the borehole using ABAQUS as a function of orientation compared with Kirsch's solution for Berea and chalk samples at an applied load of 1,000 psi. The sign convention is based on Kirsch solution, positive for tensile strain and negative for compressive strain.

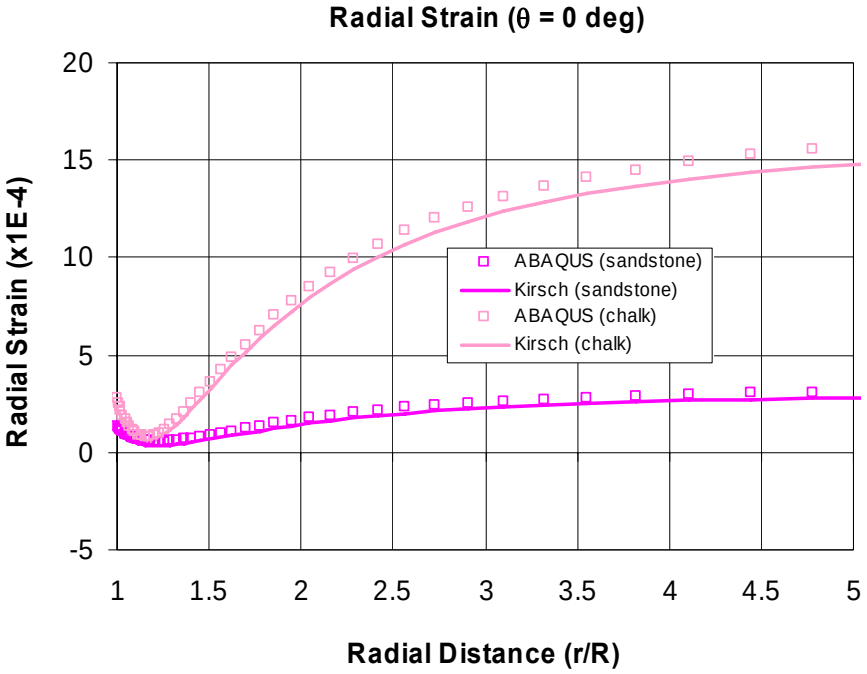

Figure 5-11: Generated radial strain in the direction of loading as a function distance from borehole using ABAQUS compared with Kirsch's solution for Berea and chalk samples at an applied load of 1,000 psi. The sign convention is based on Kirsch solution, positive for tensile strain and negative for compressive strain.

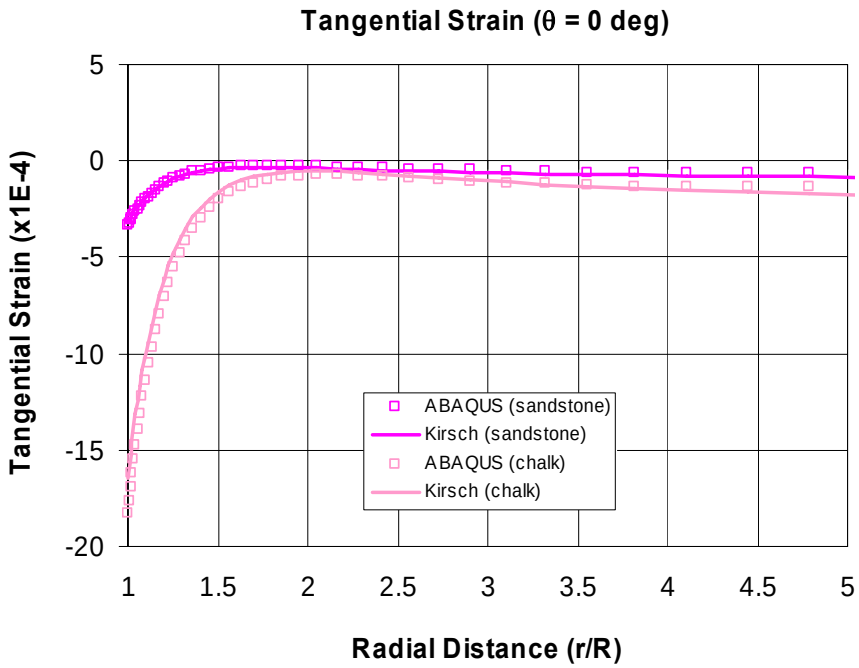

Figure 5-12: Generated tangential strain in the direction of loading as a function distance from borehole using ABAQUS compared with Kirsch's solution for Berea and chalk samples at an applied load of 1,000 psi. The sign convention is based on Kirsch solution, positive for tensile strain and negative for compressive strain.

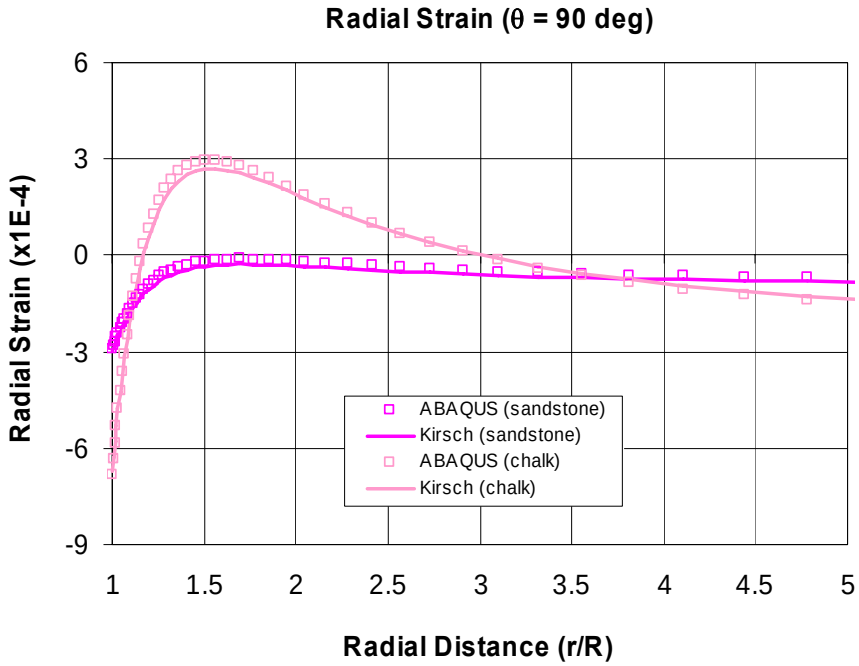

Figure 5-13: Generated radial strain at 90° from direction of loading of loading as a function distance from borehole using ABAQUS compared with Kirsch's solution for Berea and chalk samples at an applied load of 1,000 psi. The sign convention is based on Kirsch solution, positive for tensile strain and negative for compressive strain.

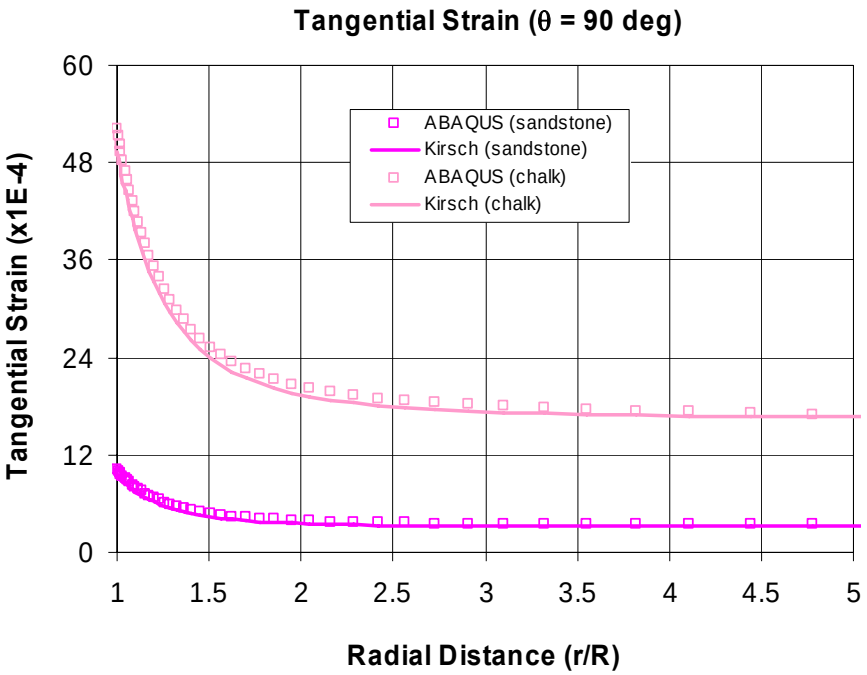

Figure 5-14: Generated tangential strain at 90° from direction of loading of loading as a function distance from borehole using ABAQUS compared with Kirsch's solution for Berea and chalk samples at an applied load of 1,000 psi. The sign convention is based on Kirsch solution, positive for tensile strain and negative for compressive strain.

Chapter 6

Results and Discussions

This chapter presents the results and discussions of the laboratory measurements. The chapter is divided into five major sections. The first comprises the results and discussions of the quasi-static and dynamic mechanical properties of the core samples, while the second deals with the quasi-static block experiments including measured borehole strains and displacements. The third section reviews the velocity measurements around the borehole. The fourth part provides an application of the borehole velocity measurements for estimating applied horizontal stresses. The application includes Berea borehole acoustic measurements for determining applied stresses using the model of Sinha and Kostek (1996). The last section includes the comparison of the laboratory measurements and ABAQUS results.

6.1 Measurements of Rock Mechanical Properties

In this section the measurements of the quasi-static and dynamic mechanical properties of the rock samples, including Berea sandstone, chalk, white limestone, and Pierre shale in addition to the material used for calibration (aluminum), are presented and discussed.

6.1.1 Aluminum Cylindrical Sample Testing

The stress-strain data from the uniaxial test performed on aluminum cylindrical sample are shown in Figure 6-1. The measured Young's modulus for the aluminum using strain gage is about 10.092E+06 psi and Poisson's ratio is measured to be 0.33 reflecting the typical values of aluminum. For linear elastic material, a straight line with constant slope should be observed for the stress-strain relations in the axial and lateral directions. This indicates that Young's modulus and Poisson's ratio for aluminum as a function of stress are constants implying that the velocities measured on aluminum do not vary with stress according to the relationship between dynamic mechanical properties and velocities given as:

$$E = \frac{\rho V_s^2 (3V_p^2 - 4V_s^2)}{(V_p^2 - V_s^2)} \tag{6.1}$$

$$\nu = \frac{V_p^2 - 2V_s^2}{2(V_p^2 - V_s^2)} \tag{6.2}$$

The typical waveforms and corresponding arrivals recorded for aluminum cylindrical sample are shown in Figures 6-2 and 6-3 for compressional and shear velocity measurements at applied stresses of 0, 5,000, 10,000, 15,000 and 20,000 psi. It can be observed that time arrivals are the same implying similar dynamic properties as function of stress. The measured velocities, dynamic Young's modulus and dynamic Poisson's ratio are shown in Table 6-1.

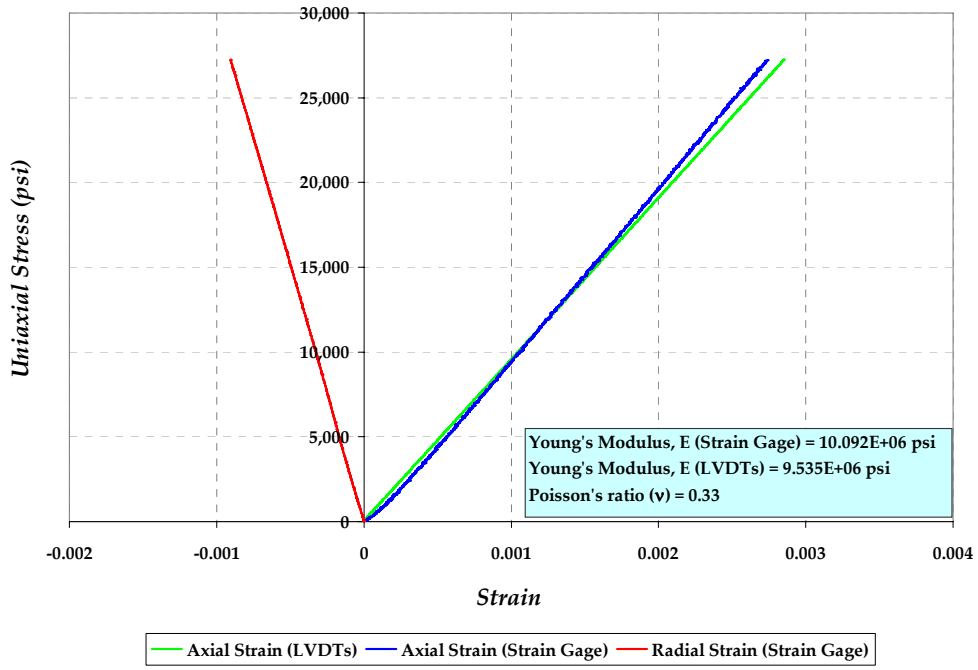

Figure 6-1: Stress-strain curves for the aluminum calibration sample measured from using strain gage and LVDTs with computed quasi-static moduli.

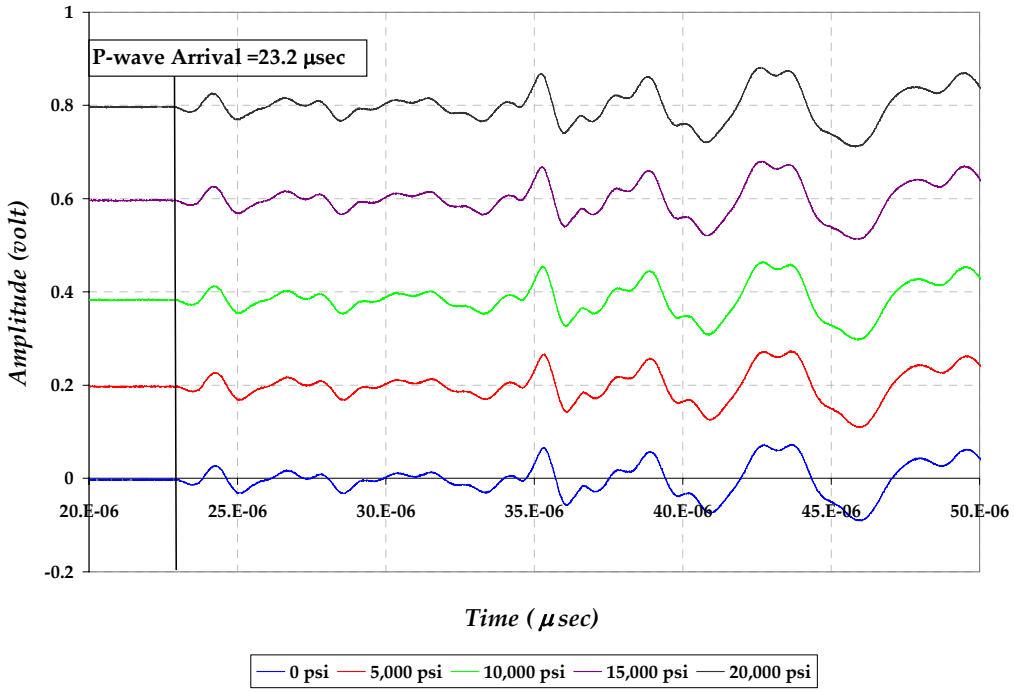

Figure 6-2: Respective compressional arrivals for the aluminum cylindrical sample at different applied uniaxial stress levels. Notice that the platens time correction (10 µsec for P-wave arrival) is included.

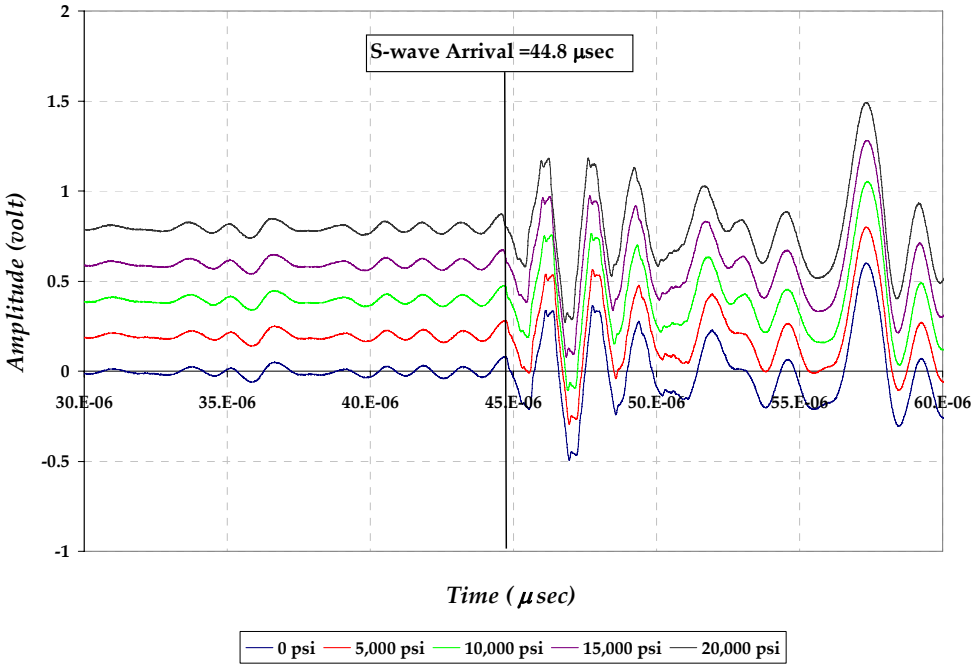

Figure 6-3: Respective S_1-shear arrivals for the aluminum cylindrical sample at different applied uniaxial stress levels. Notice that the platens time correction (20µsec for S-wave arrival) is included.

Uniaxial Stress (psi)	Compressional Velocity, V_P (m/s)	Average Shear Velocity, $V_{S(avg)}$ (m/s)	Dynamic Young's Modulus (psi)	Dynamic Poisson's ratio, ν
0	6,317	3,159	10.426E+06	0.33
5,000	6,317	3,159	10.426E+06	0.33
10,000	6,317	3,159	10.426E+06	0.33
15,000	6,317	3,159	10.426E+06	0.33
20,000	6,317	3,159	10.426E+06	0.33

Table 6-1: Compressional and average shear velocities with computed dynamic mechanical properties at different stresses for the aluminum sample.

6.1.2 Berea Cylindrical Sample Testing

The axial and radial stress-strain curves for a Berea core sample during loading and unloading procedures are shown in Figures 6-4 and 6-5 using strain gages and LVDTs, respectively. The sample was initially load cycled to a stress of 3,000 psi twice. The stresses at unloading before sample failure were 3,000, 6,000, 9,000 and 11,000 psi. Table 6-2 shows the computed Young's modulus and Poisson's ratio during loading and unloading for each cycle using strain gage measurements. It can be clearly noticed that at a higher stress level, the slope of the stress-strain curves at loading and unloading do not vary. This behavior is linked to the velocity measurements as will be discussed next. Young's modulus and Poisson's ratio computed at 50% peak strength from the major stress-strain curve are 3.062E+06 psi and 0.23, respectively.

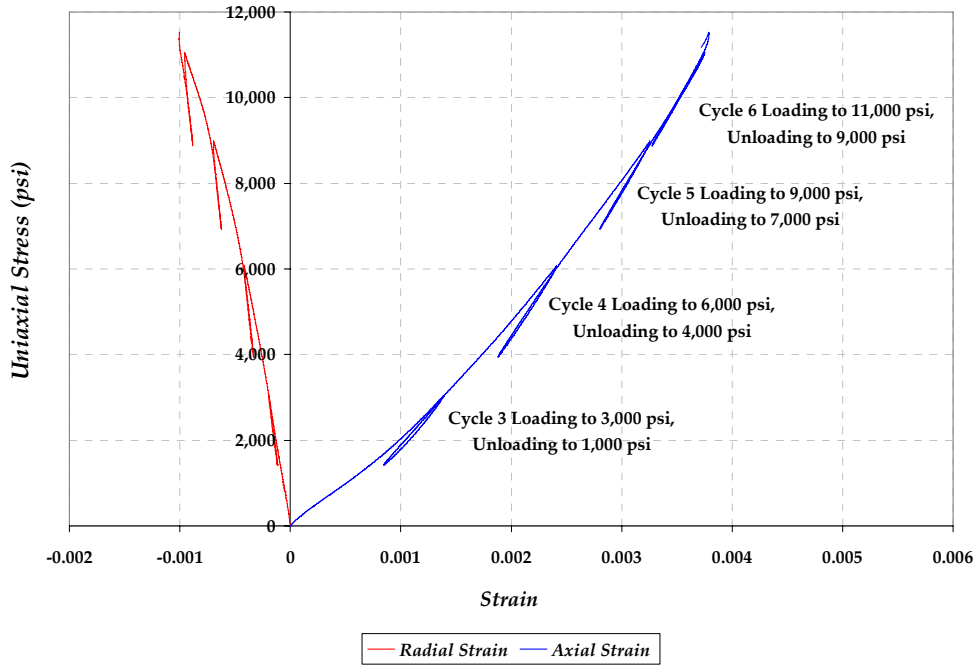

Figure 6-4: Stress-strain curves for a Berea sample during loading and unloading measured using a strain gage.

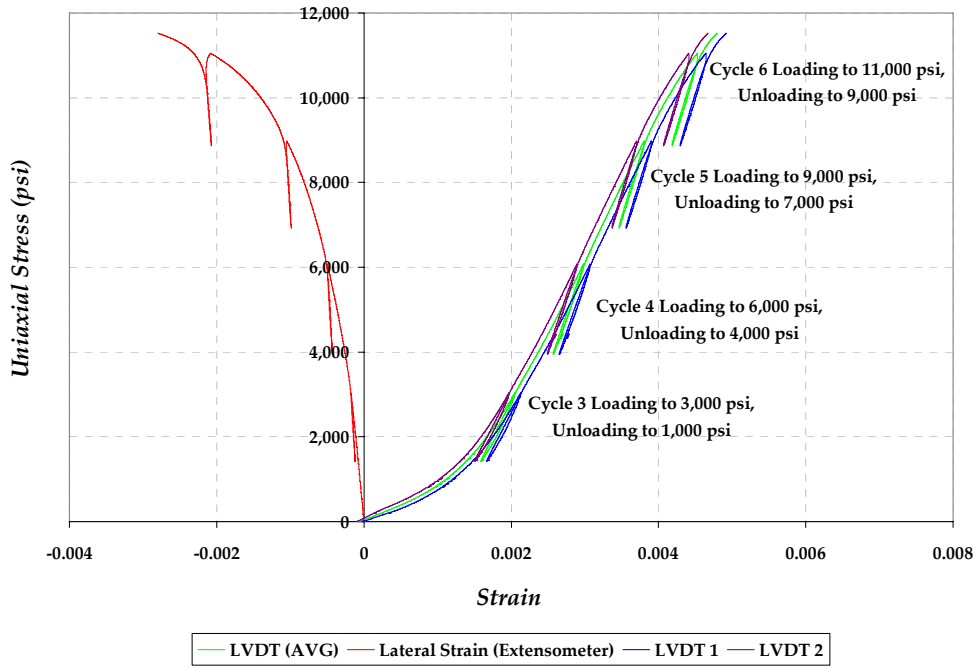

Figure 6-5: Stress-strain curves for a Berea sample during loading and unloading measured using LVDTs and extensometer.

Uniaxial Stress Range (psi)	Loading		Unloading	
	Young's Modulus E, (psi)	Poisson's Ratio ν	Young's Modulus E, (psi)	Poisson's Ratio ν
3,000-1,000	2.917E+06	0.14	3.307E+06	0.13
6,000-4,000	3.877E+06	0.17	4.091E+06	0.17
9,000-7,000	4.329E+06	0.19	4.421E+06	0.18
11,000-9,000	4.571E+06	0.23	4.554E+06	0.23

Table 6-2: Mechanical properties for a Berea sample computed from loading and unloading cycles using a strain gage.

The acoustic velocity measurements for the Berea core sample were collected simultaneously with strain measurements during loading and unloading. The compressional and shear velocities are shown in Table 6-3 at the major stresses

where load cycling is performed. Also the compressional and average shear velocities are given in Figures 6-6 and 6-7, acquired at each stress during loading and unloading. As discussed in Chapter 3, the difference between quasi-static and dynamic moduli can be minimized by cycling the rock sample at small strain amplitude. The difference between the Young's moduli from quasi-static and dynamic measurements (Tables 6-2 and 6-3) is small at high stress magnitude. This is because at a high stress level, the sample is compacted and the effect of micro cracks on velocities is minimal. This can be observed from the difference in the magnitudes of the quasi-static and dynamic Young's moduli and Poisson's ratios at a stress of 11,000 psi (about 5%). As a final remark, the slope of the stress-strain curve varies significantly at early loading, indicating that the velocities are strongly influenced by applied stress, also the measured velocity for Berea sample showed relatively constant velocities at high stresses.

Uniaxial Stress (psi)	**Compressional Velocity, V_P (m/s)**	**Average Shear Velocity, $V_{S(avg)}$ (m/s)**	**Dynamic Young's Modulus (Psi)**	**Dynamic Poisson's Ratio ν**
0	2,584	1,747	2.101E+06	0.08
3,000	3,501	2,214	3.664E+06	0.18
6,000	3,804	2,302	4.095E+06	0.21
9,000	3,882	2,334	4.248E+06	0.21
11,000	3,862	2,313	4.166E+06	0.22
11,500	3,843	2,313	4.150E+06	0.22

Table 6-3: Compressional and average shear velocities with computed dynamic mechanical properties at major stresses during load cycling for a Berea core sample.

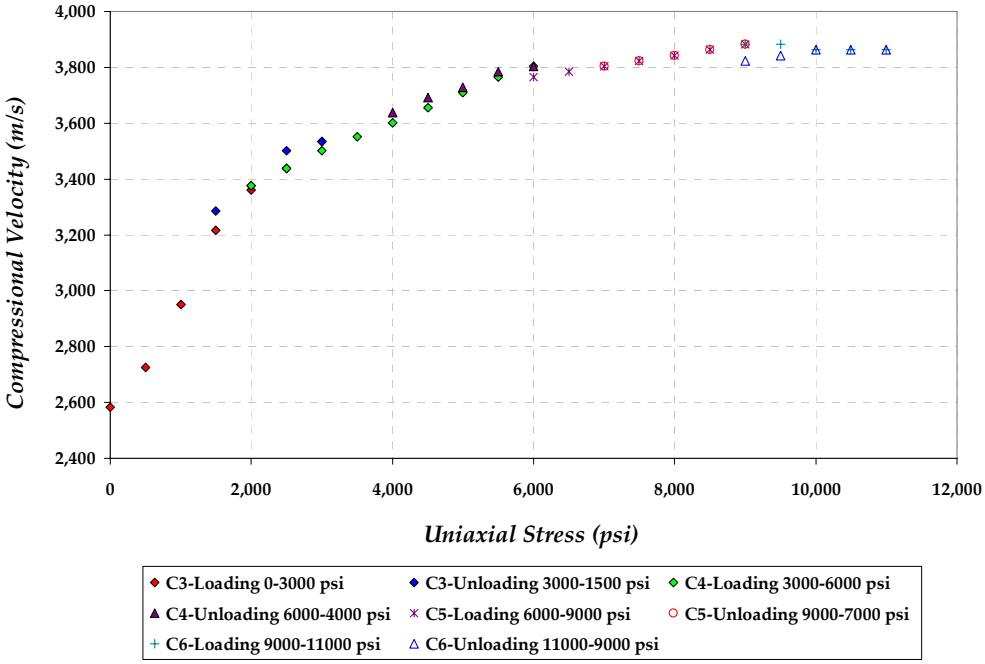

Figure 6-6: Acquired compressional velocities during loading and unloading for a Berea core sample.

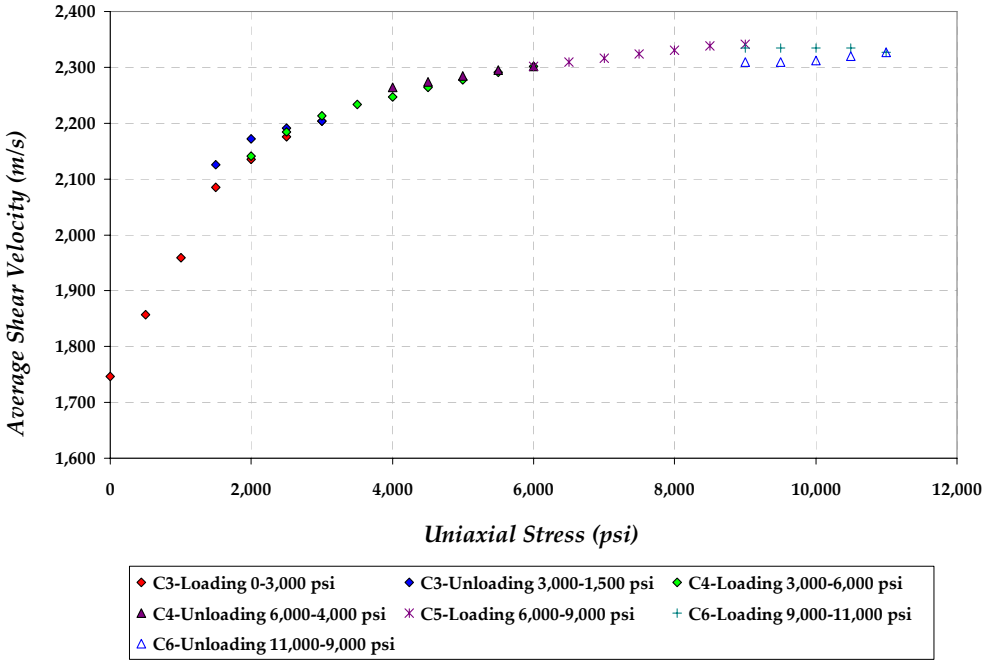

Figure 6-7: Measured average shear velocities during loading and unloading for a Berea core sample.

6.1.3 Chalk Cylindrical Sample Testing

The axial and radial stress-strain curves for the chalk core sample are shown in Figure 6-8 using LVDTs and circumferential extensometer measurements. The computed Young's modulus and Poisson's ratio at 50% peak strength are 597E+06 psi and 0.13, respectively. It can be observed that the change in slope is insignificant as a function of applied uniaxial stress. This insignificant change in the slope is reflected by the velocity measurements for the chalk sample. The measured velocities are shown in Figure 6-9. The velocity increased slightly at early stress and decreased at higher stress where the variation of velocity is insignificant as a function of applied stress.

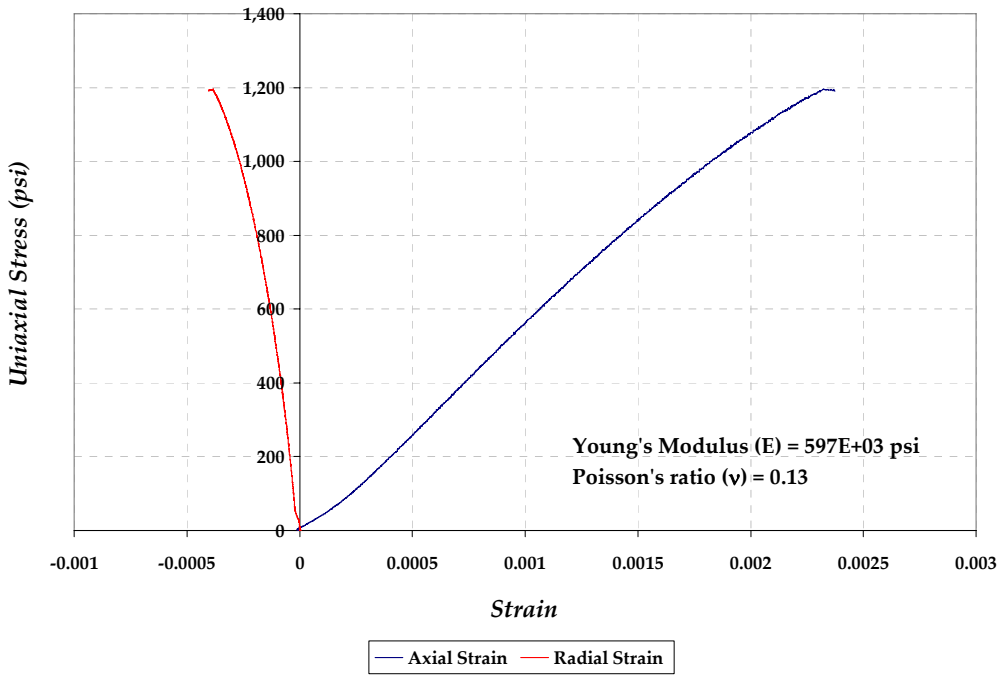

Figure 6-8: Stress-strain curves for a chalk core sample measured from LVDTs (corrected) and extensometer.

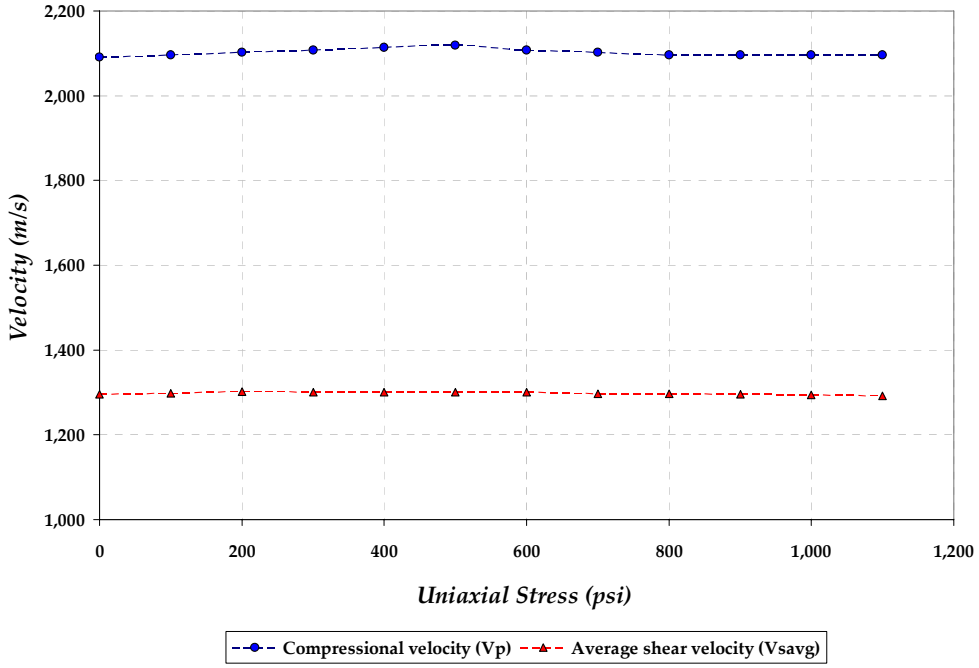

Figure 6-9: Measured compressional and average shear velocities for a chalk core sample as a function of uniaxial applied stress.

The decrease of chalk acoustic velocities at higher stresses is most likely caused by the dilatancy and pore collapse prior to borehole failure. This observation is supported by the work conducted by Scott et al., (1998) on the same type of chalk. In this case, the measured velocities were independent of the applied uniaxial stress.

6.1.4 White Limestone Cylindrical Sample Testing

The axial and radial stress-strain curves from a white limestone core sample during loading and unloading procedures are shown in Figure 6-10 and 6-11 from strain gage and LVDTs, respectively. The sample was initially load cycled to a stress of 800 psi twice. The white limestone uniaxial experiment included 7 minor cycles before the sample is failed. Stress magnitudes at unloading were 800,

1,600, 2,200, 2,600 and 3,000 psi. The elastic moduli, i.e., Young's modulus and Poisson's ratio, are determined from the slope of the stress-strain curve for the minor cycles during loading and unloading portions. The slope of stress-strain curves at the minor cycle shows a change in slope initially, but remains unchanged until the sample fails at 3,200 psi. This also can be observed from the computed Young's modulus and Poisson's ratio during loading and unloading for each cycle from strain gages given in Table 6-4.

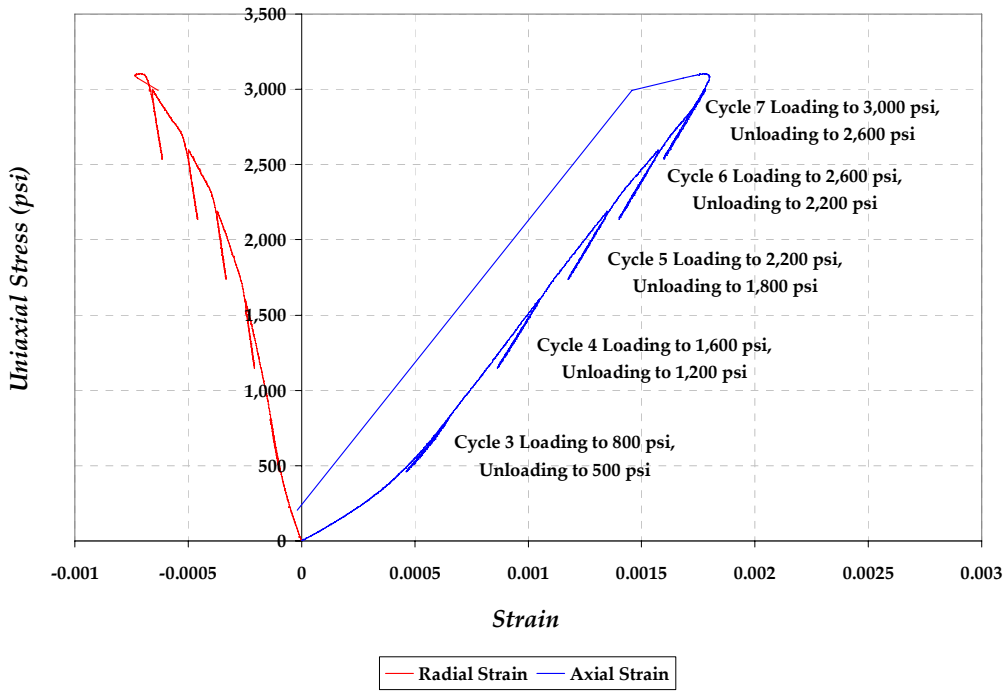

Figure 6-10: Stress-strain curves for a white limestone sample during loading and unloading measured using a strain gage.

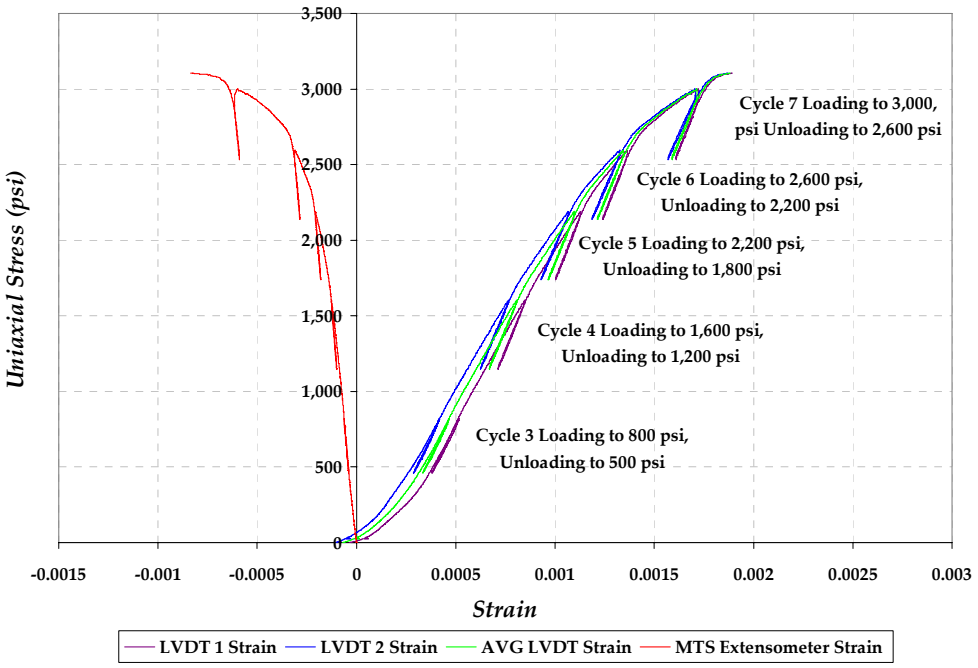

Figure 6-11: Stress-strain curves for a white limestone sample during loading and unloading measured using LVDTs (corrected) and extensometer.

Uniaxial Stress Range (psi)	Loading		Unloading	
	Young's Modulus E, (psi)	Poisson's Ratio, ν	Young's Modulus E, (psi)	Poisson's Ratio, ν
800-500	1.892E+06	0.21	1.872E+06	0.21
1,600-1,200	2.405E+06	0.23	2.437E+06	0.27
2,200-1,800	2.489E+06	0.25	2.542E+06	0.28
2,600-2,200	2.488E+06	0.27	2.542E+06	0.29
3000-2600	2.542E+06	0.30	2.515E+06	0.28

Table 6-4: Mechanical properties for a white limestone sample computed for loading and unloading cycles using strain gages.

The compressional and shear acoustic velocities were acquired during uniaxial testing for the white limestone sample. Figure 6-12 shows the typical compressional and shear waveforms recorded for the white limestone at zero stress. The compressional and shear velocities are shown in Table 6-5 at the major applied stresses where load cycling is performed. The velocity measurement

reflects similar behavior of the quasi-static measurements. The change in velocities and thus dynamic properties is insignificant indicating the complexity of velocity dependence on stress.

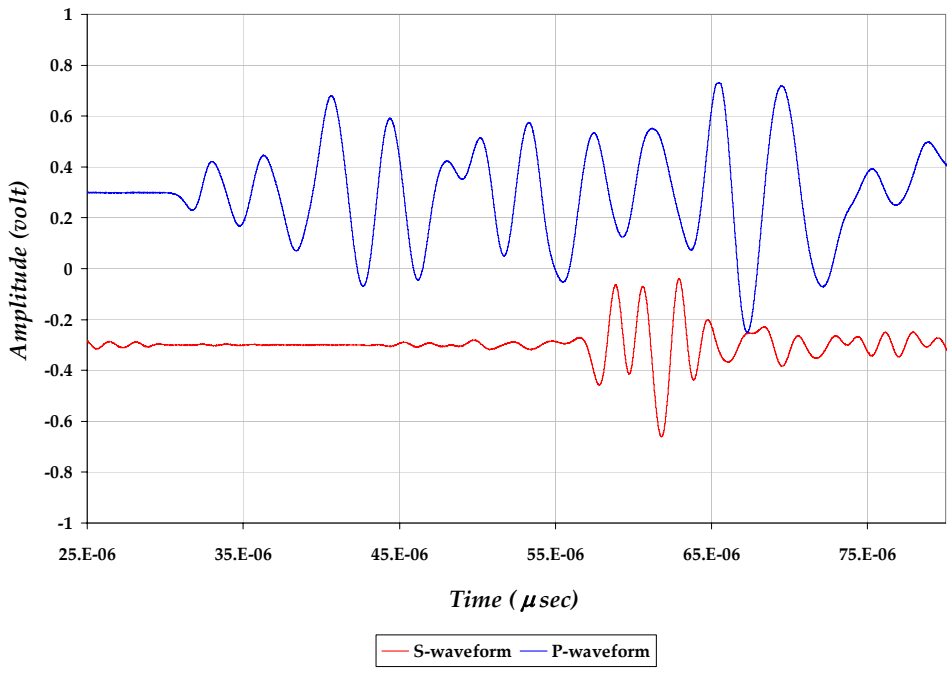

Figure 6-12: Examples of P- and S-waveforms recorded through a 3.0 inch core sample of a white limestone at zero applied stress. These signals clearly show the respective arrivals are unambiguous.

Uniaxial Stress (psi)	Compressional Velocity, V_P (m/s)	Average Shear Velocity, $V_{S(avg)}$ (m/s)	Dynamic Young's Modulus (psi)	Dynamic Poisson's Ratio ν
0	3,368	1,914	2.785E+06	0.26
800	3,428	1,931	2.849E+06	0.27
1,600	3,431	1,945	2.879E+06	0.27
1,800	3,431	1,940	2.868E+06	0.27
3,000	3,337	1,899	2.739E+06	0.26

Table 6-5: Compressional and average shear velocities with computed dynamic mechanical properties at major stresses during load cycling for a white limestone core sample.

6.1.5 Pierre Shale Cylindrical Sample Testing

The Pierre shale samples submitted for uniaxial testing were prepared and handled differently compared with other rock samples. The samples are preserved in PG-1 mineral oil before and during sample preparation, including the coring and grinding processes. Two samples were tested with orientations parallel and perpendicular with reference to the loading direction of the tested shale block sample (beddings are 30˚ with reference to the block loading direction and 60˚ to the borehole axis). The axial and radial stress-strain curves for Pierre shale core samples using LVDTs and circumferential extensometer measurements are shown in Figures 6-13 and 6-14. The measured Young's modulus and Poisson's ratio at 50% peak strength for the case of the parallel sample with respect to the loading direction are 219E+03 psi and 0.39, whereas the measured Young's modulus and Poisson's ratio for the perpendicular sample with respect to loading direction are 200E+03 psi and 0.35. The measured velocities did not vary significantly as a function of applied stress. Figures 6-15 and 6-16 show an example of velocity measurements performed on the sample cored parallel the loading direction of the Pierre shale block sample. Figure 6-16 also indicates the measured shear velocity anisotropy in Pierre shale.

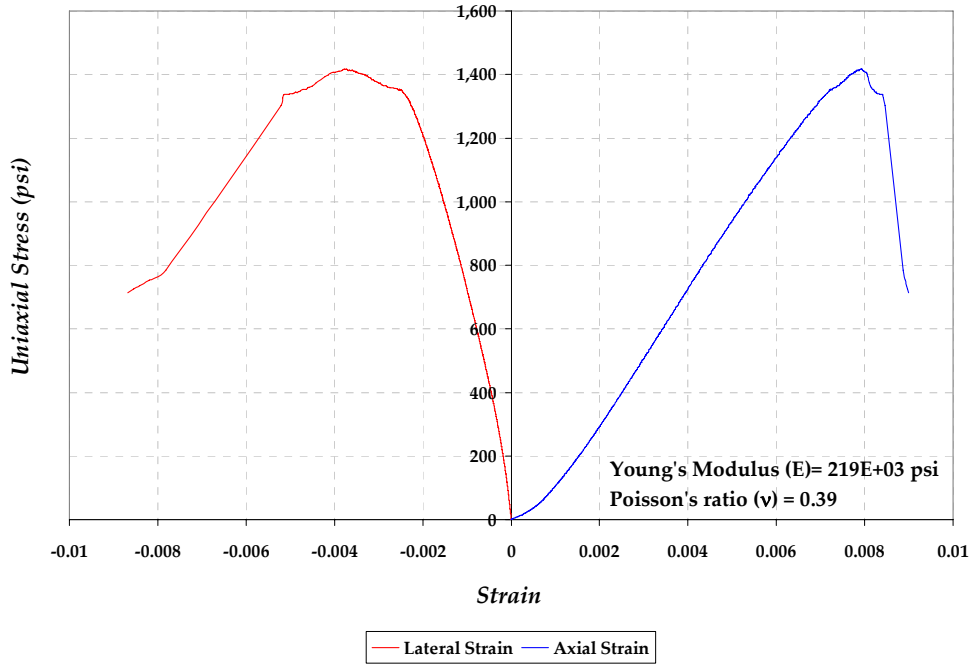

Figure 6-13: Stress-strain curves measured from LVDTs and extensometer for the Pierre shale core sample cored parallel with reference to the loading direction of the tested shale block sample.

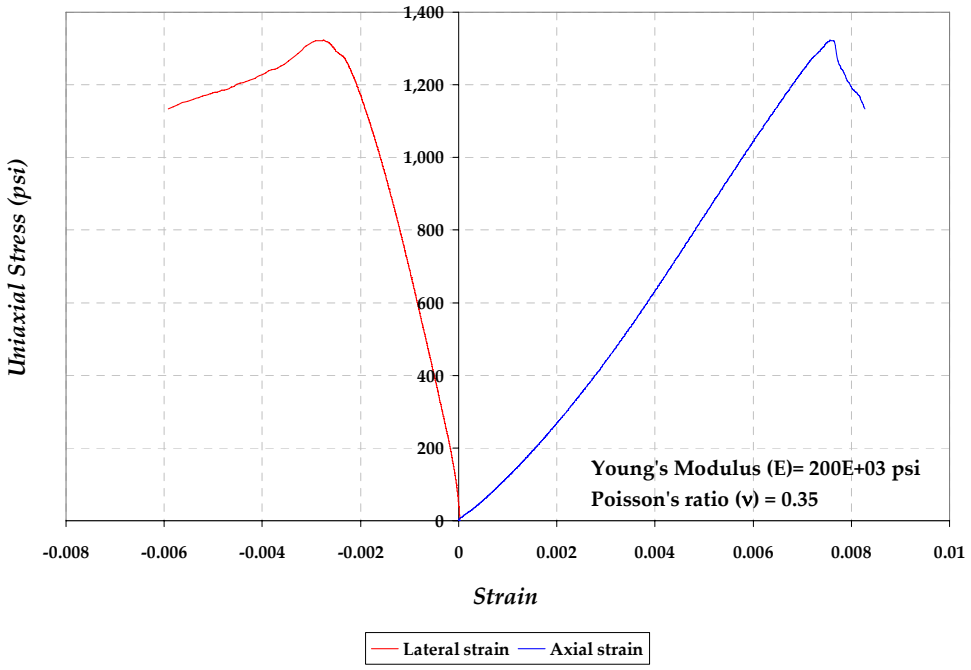

Figure 6-14: Stress-strain curves measured from LVDTs and extensometer for the Pierre shale core sample cored perpendicular with reference to the loading direction of the tested shale block sample.

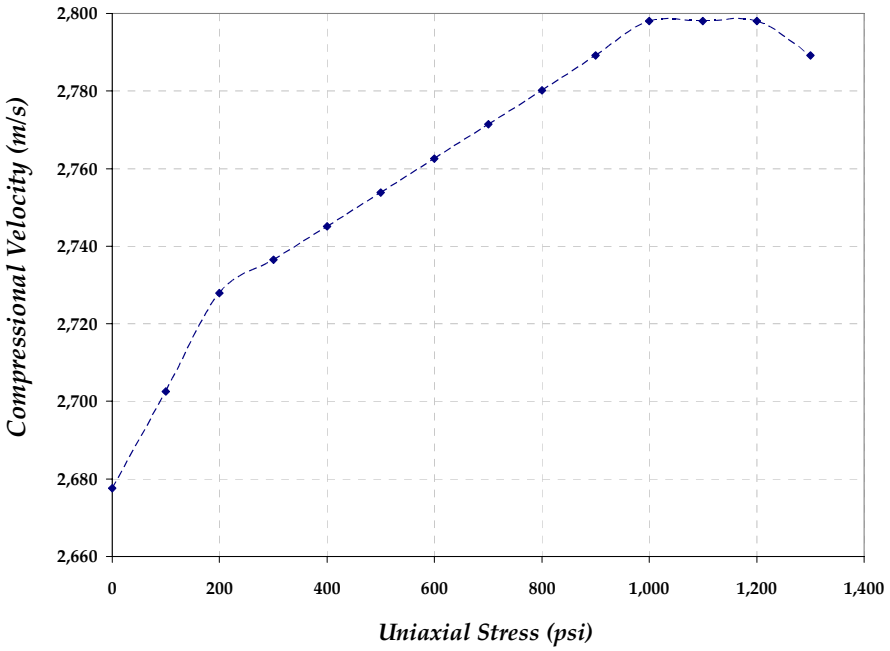

Figure 6-15: Compressional velocity measurements as a function of applied uniaxial stress for the Pierre shale core sample cored parallel with reference to the loading direction of the tested shale block sample.

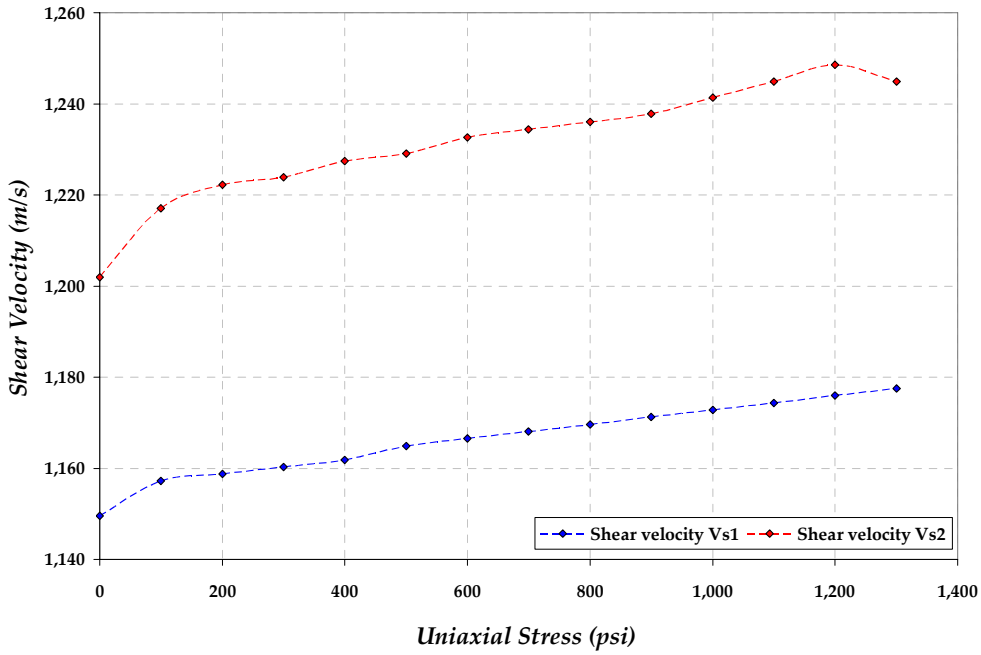

Figure 6-16: Polarized shear velocity measurements as a function of applied uniaxial stress for the Pierre shale core sample cored parallel with reference to the loading direction of the tested shale block sample.

6.1.6 Tensile Strength Measurements

The tensile strength is mainly intended for determining the intactness of rock samples in tension, which were used to confirm borehole strain measurements at the maximum induced tensile stress directions. The tensile strength is computed from the sample geometry and the load at which the sample fails using Equation (4.1). Figure 6-17 shows one of the test results of the chalk disc specimen. For Berea and chalk tensile testing, seven samples were tested and reflected an average tensile strength of 846±166 psi for Berea and 164±17 psi for chalk samples as shown in Tables 6-6 and 6-7. The average tensile strength for the white limestone samples is 624±30 psi based on two measurements as shown in Table 6-8. Only one Pierre shale sample is tested and resulted in a tensile strength of 198 psi, which is in the range of the tensile measurements performed by Lefrere (2001) on the same type of shale.

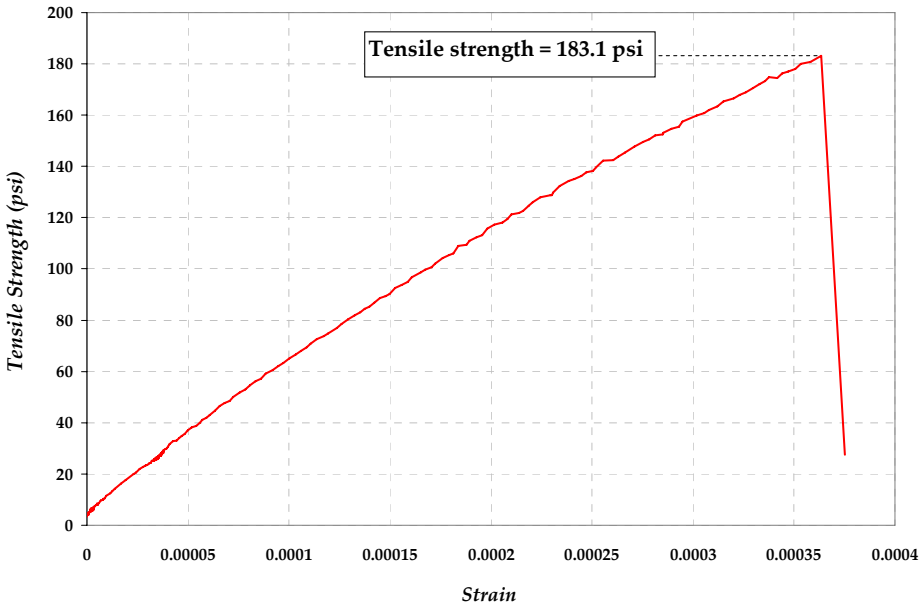

Figure 6-17: An example of tensile stress-strain curve for the chalk tested specimen.

Sample No.	D (inch)	L (inch)	Maximum Load (lb_f)	Tensile Strength, σ_t (psi)
1	1.480	0.518	749	623
2	1.480	0.489	1,093	944
3	1.475	0.510	717	608
4	1.475	0.493	1,124	985
5	1.475	0.498	1,122	974
6	1.475	0.488	1,089	963
7	1.475	0.498	951	825

Table 6-6: Tensile strength results from measurements performed on disc samples of Berea.

Sample No.	D (inch)	L (inch)	Maximum Load (lb_f)	Tensile Strength, σ_t (psi)
1	1.409	0.442	179	183
2	1.408	0.449	174	172
3	1.408	0.477	183	173
4	1.406	0.468	185	179
5	1.403	0.51	165	147
6	1.405	0.441	185	137
7	1.406	0.501	174	157

Table 6-7: Tensile strength results from measurements performed on disc samples of chalk.

Sample No.	D (inch)	L (inch)	Maximum Load (lb_f)	Tensile Strength, σ_t (psi)
1	1.4935	0.5405	765	603
2	1.4935	0.5455	700	645

Table 6-8: Tensile strength results from measurements performed on disc samples of white limestone.

6.2 Quasi-static Block Samples Testing

In this section the results of quasi-static experiments conducted on block cube samples with a borehole are presented. The results involve the presentation of the measured borehole strains and displacements under stroke control at the four principal directions defined at $\theta = 0^{\circ}$, 90°, 180° and 270° where the maximum induced compressive and tensile stresses occur. The strain measurements are compared with computed strains from measured borehole displacements and the theoretical strains using Kirsch's linear elastic solution. Also, the computed induced stresses at the borehole wall are presented for each type of tested rock.

6.2.1 Aluminum Block Sample

The strain and velocity measurements were performed on a standard material 'aluminum' to calibrate and insure the reliability of the measurements before being conducted on rock samples. The borehole strains are measured using four strain gages placed at the principal induced stress orientations, with applied stress defined at the infinite boundary ($\theta = 90^{\circ}$). For the case of aluminum block, the sample is loaded to stress of 6,000 psi. The tangential borehole strains measured at the four orientations compared with the computed strain from Kirsch's analytical solution for aluminum is shown in Figure 6-18 as a function of applied boundary stress. The tangential strain measurements at the borehole wall reflect the high magnitude of induced stresses. The measured horizontal and vertical displacements from clip gages relative to the direction of loading compared with theoretical displacements are shown in Figure 6-19.

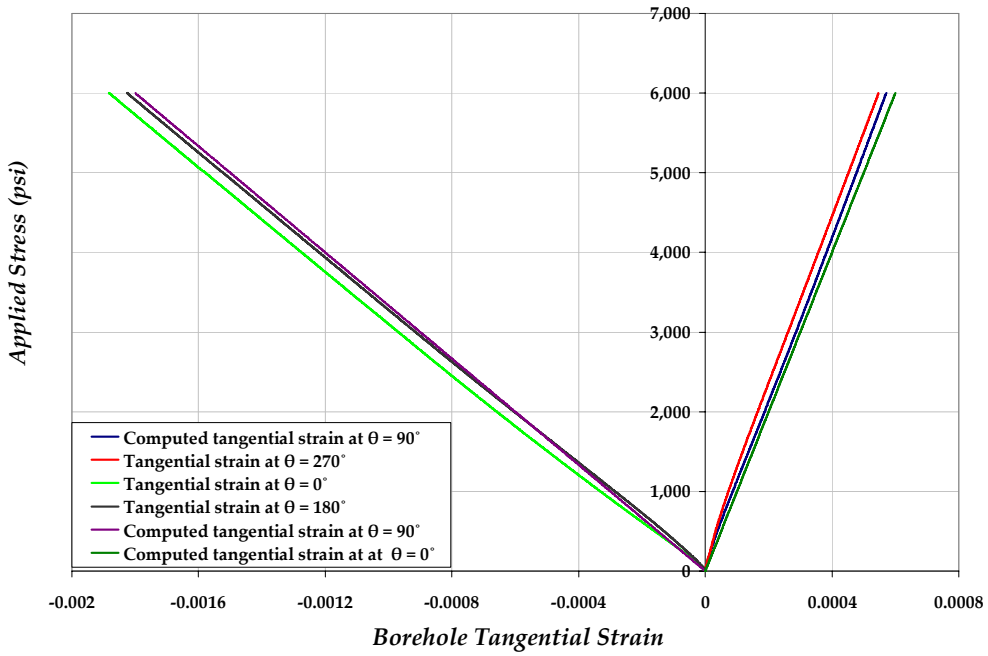

Figure 6-18: Tangential borehole strains measured at the four principal orientations compared with the computed tangential strains from Kirsch's analytical solution for aluminum block sample.

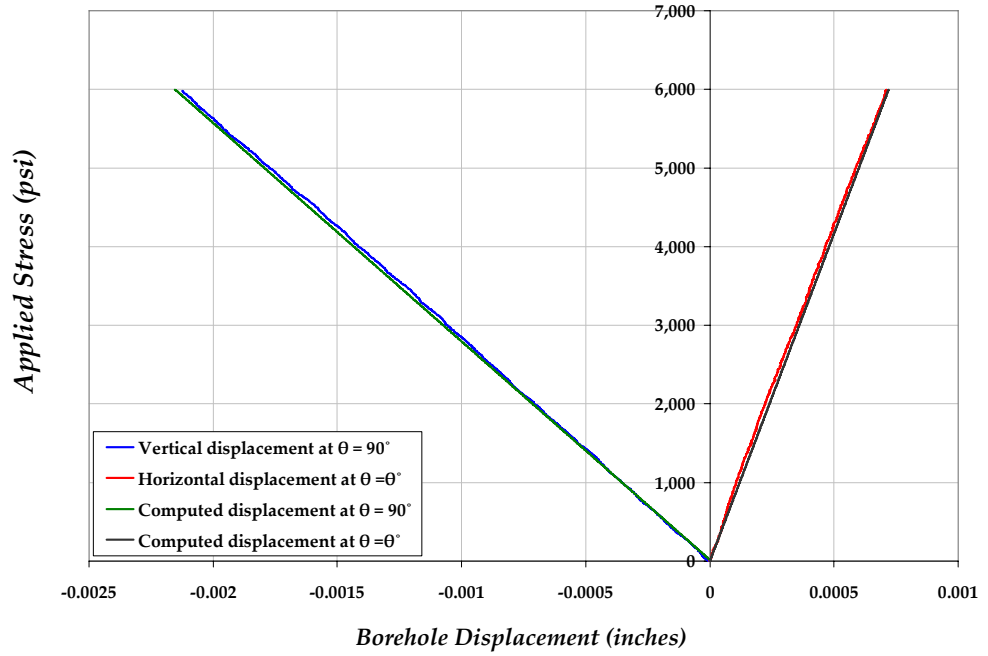

Figure 6-19: Measured horizontal and vertical displacements for aluminum from clip gages relative to the direction of loading compared with computed displacements.

The borehole displacement measurements can be used to compute the tangential strains at the major orientations using Equation (5.5). This allows comparing the measured and computed tangential borehole strains using strain gages and displacement measurements, respectively. Figure 6-20 shows the measured borehole tangential strains compared with computed tangential strains from displacements. Two 45˚ rosette gages were also used on the borehole faces to measure strain at a distance from the borehole and compare with analytical solution. The rosette gages were also used to compare strains in parallel planes. Figures 6-21 shows the raw strain measured at the borehole faces using rosette gages at directions 0˚, 45˚, and 90˚. It can be noticed from the rosette strain measurements that the strain of the parallel planes is identical. The rosette strain measurements were also utilized to compute the principal strains at a distance of r = 1.60 inches away from the borehole and compared with the computed strain from Kirsch's analytical solution as shown in Figure 6-22.

The tangential measured strains were utilized to compute the borehole induced tangential stresses at major orientations. Figure 6-23 presents the computed tangential stresses from borehole strain measurements compared with Kirsch's analytical solution. The measured stress concentration factors at the maximum tensile and compressive stresses are 0.96 and -3.04, respectively. The aluminum testing showed good comparison of the quasi-static measurements with the analytical solution at the borehole, which is an important step to calibrate the measurements before being carried on rock samples.

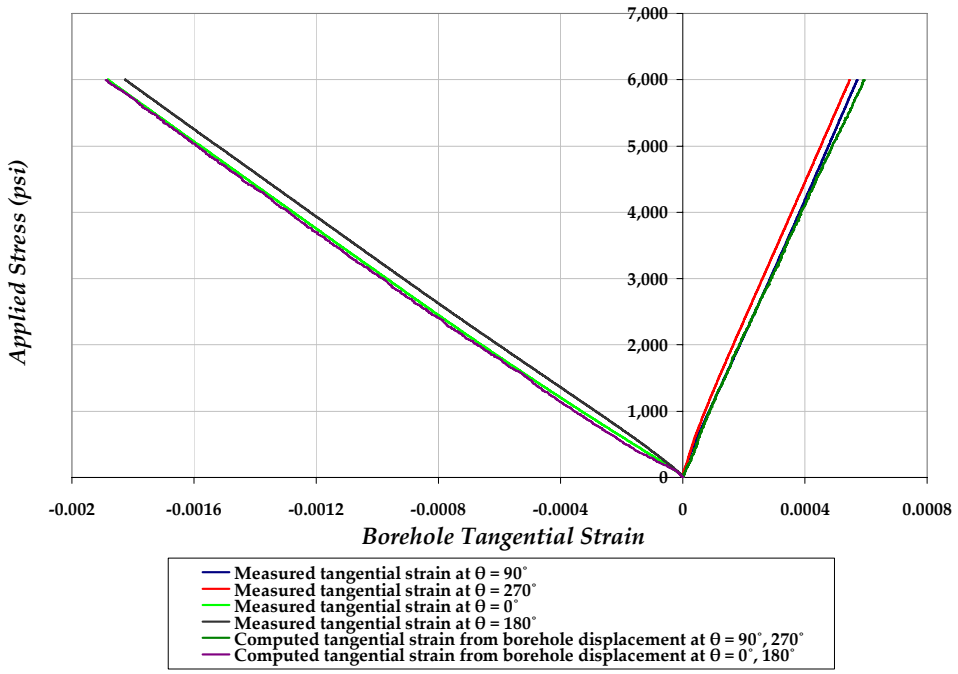

Figure 6-20: Comparison of the measured borehole tangential strains from strain gages and computed tangential strains from measured borehole displacements for the aluminum block sample.

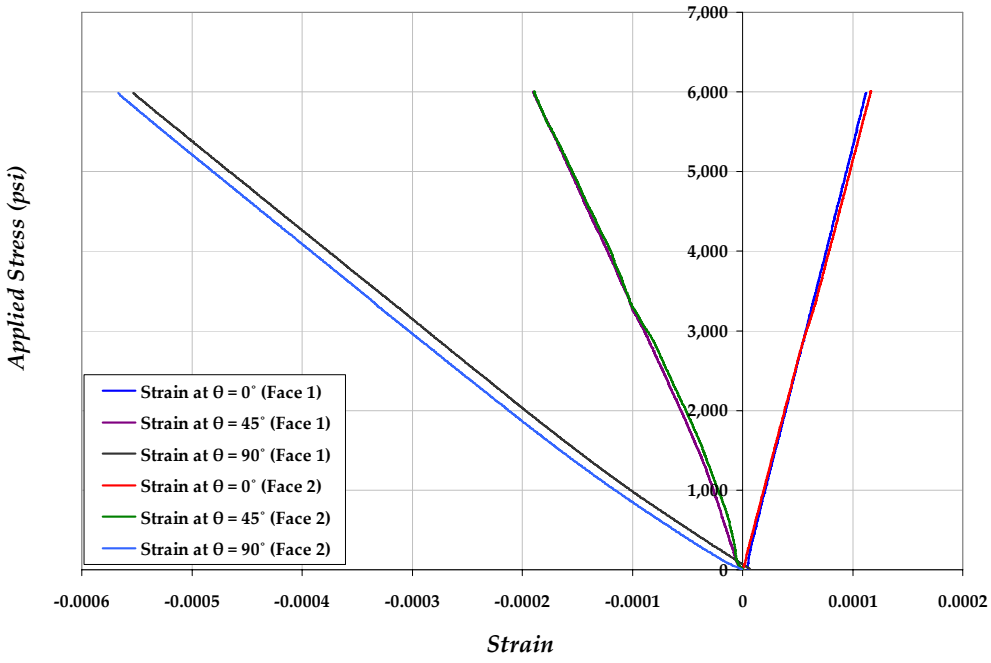

Figure 6-21: 45°rosette strain measurements at three different directions on borehole faces at a radius of r = 1.60 inches.

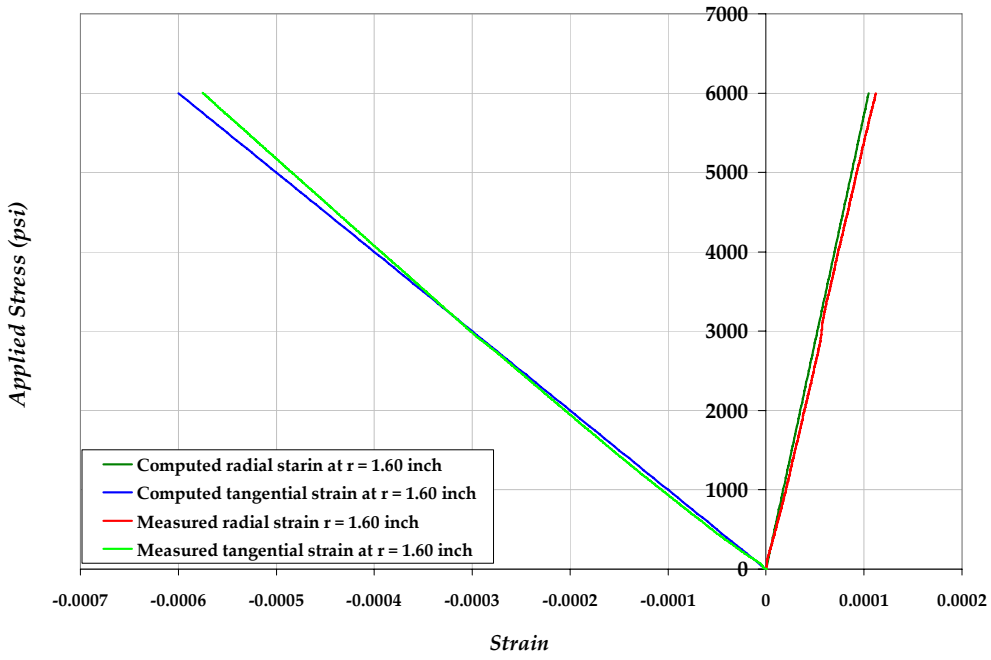

Figure 6-22: Computed and measured principal strains at a radius of r = 1.60 inches compared with the analytical strain at same distance for the aluminum block sample.

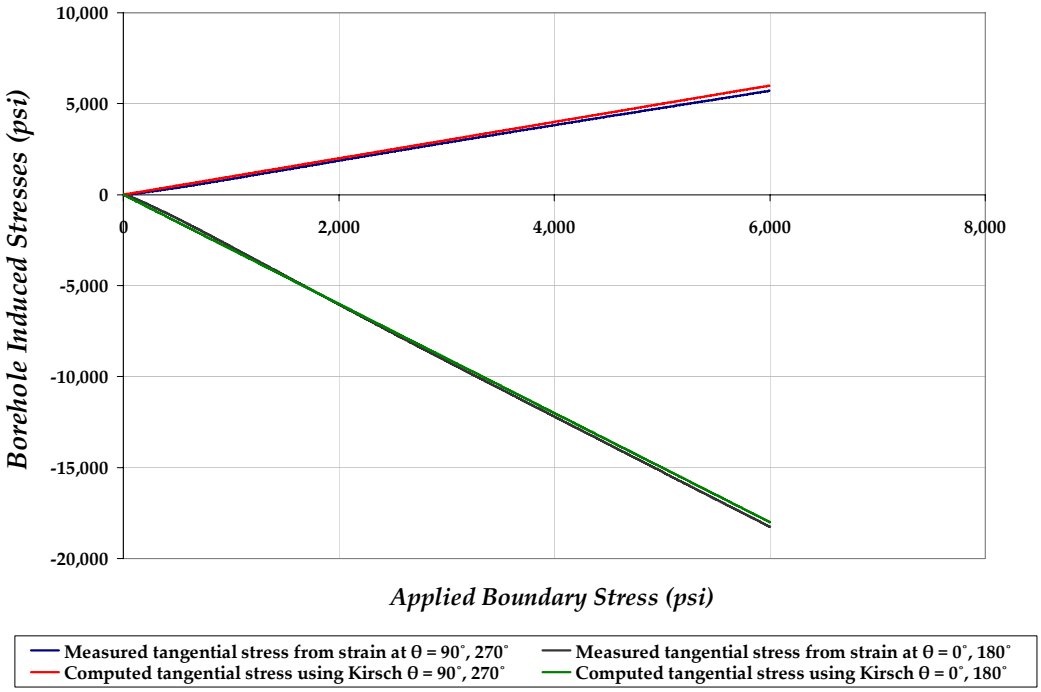

Figure 6-23: Computed tangential stress at borehole from strain measurements compared with the analytical borehole stresses for the aluminum block sample.

The strain measured along the borehole generator (z-direction) using strain gages at $\theta = 0^{\circ}$ and $\theta = 90^{\circ}$ is shown in Figure 6-24. It can be noticed that the measured strain along the z-direction is small relative to tangential strains measured at the same directions.

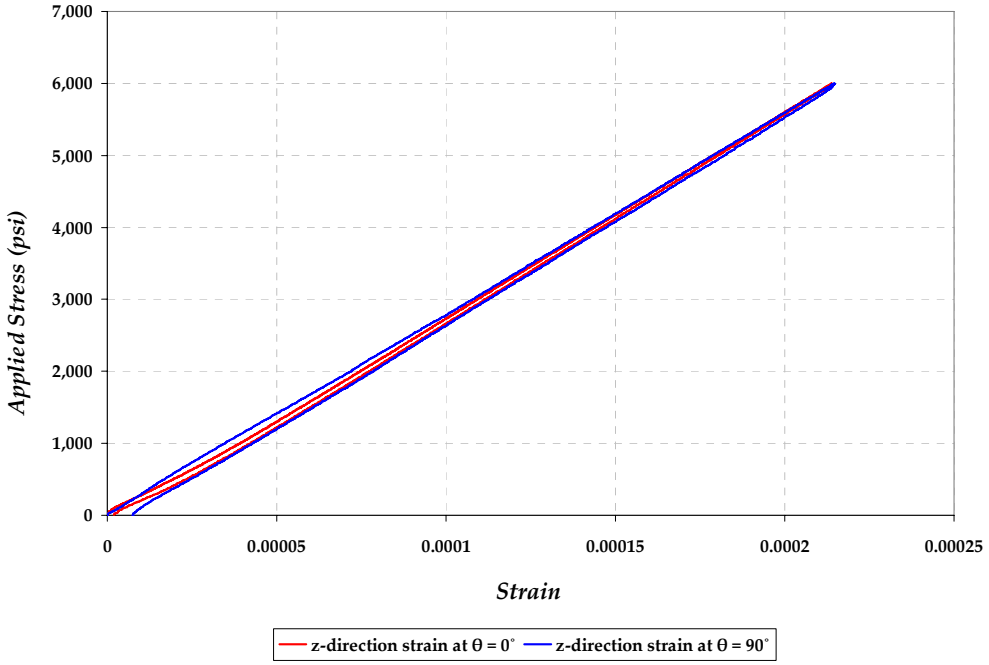

Figure 6-24: Measured strain in the z-direction from the two strain gages at $\theta = 0^{\circ}$ and $\theta = 90^{\circ}$.

6.2.2 Berea Block Samples

Similar analysis performed on aluminum is carried out for the rock block samples, including Berea sandstone. Four Berea block samples were tested and the results of borehole strains, displacements and computed stresses are presented in this section. Figure 6-25 shows the measured and computed borehole strain at $\theta = 90^{\circ}$ and $\theta = 270^{\circ}$ for the four tested Berea block samples. In the case of Berea block samples 1 and 2, which were the first prepared blocks for final testing, a 5-minutes epoxy glue is used to coat the area of contact between the borehole and strain gages to insure good adhesion. This resulted in observing a continuous strain measured at the tension sides ($\theta = 90^{\circ}$ and $\theta = 270^{\circ}$) without indication of developing tensile failures in the measured stress-strain curves. This was avoided in the later experiments, which resulted in clear indication of a tensile failure as was the case for block 3 where only two strain gages were used at $\theta = 0^{\circ}$ and $\theta = 90^{\circ}$. The measurements of Berea block 3 indicated a tensile failure at a borehole stress of $\sigma_t \approx 760$ psi, which is in the range of the tensile strength measurements performed earlier on Berea using Brazilian tests (σ_t = 600 to 1,000 psi). The tangential borehole strains measured at $\theta = 0^{\circ}$ and $\theta = 180^{\circ}$ for the four tested Berea block samples are given in Figure 6-26 compared with the computed strain at the same directions. The slope of the computed strain is comparable with the slope of the measured strains. The borehole breakouts were observed at the maximum induced compression stress directions ($\theta = 0^{\circ}$ and $\theta = 180^{\circ}$) as shown in Figure 6-27 at an applied stress of $\sigma \approx 7{,}500$ psi, and the gages were detached at an average stress of 8,200 psi for the four tested Berea block samples.

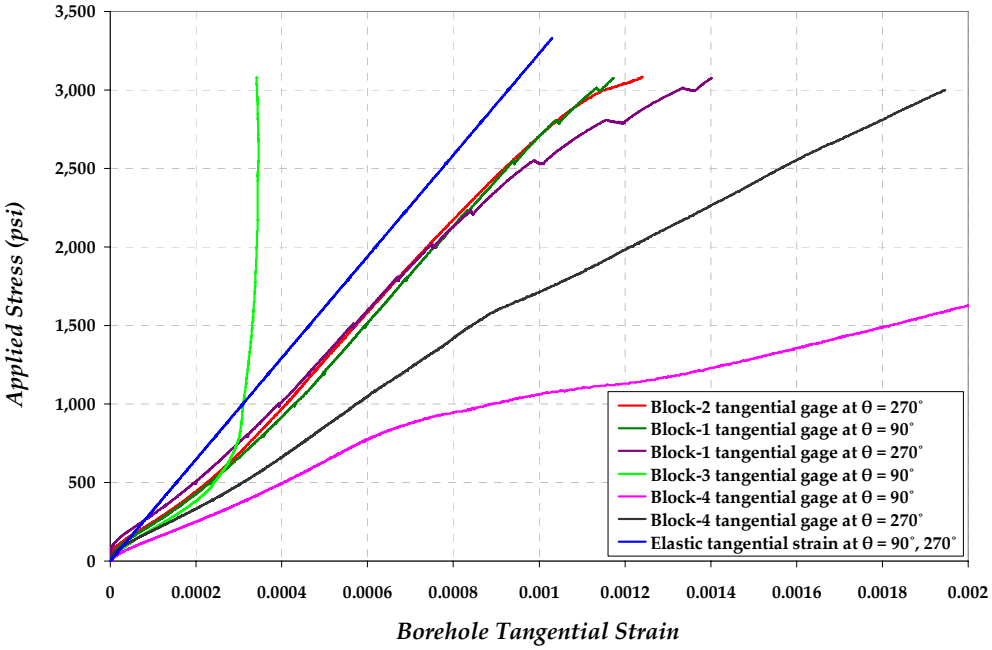

Figure 6-25: Measured and computed borehole tangential strains at θ = 90˚ and θ = 270˚ for the four tested Berea block samples.

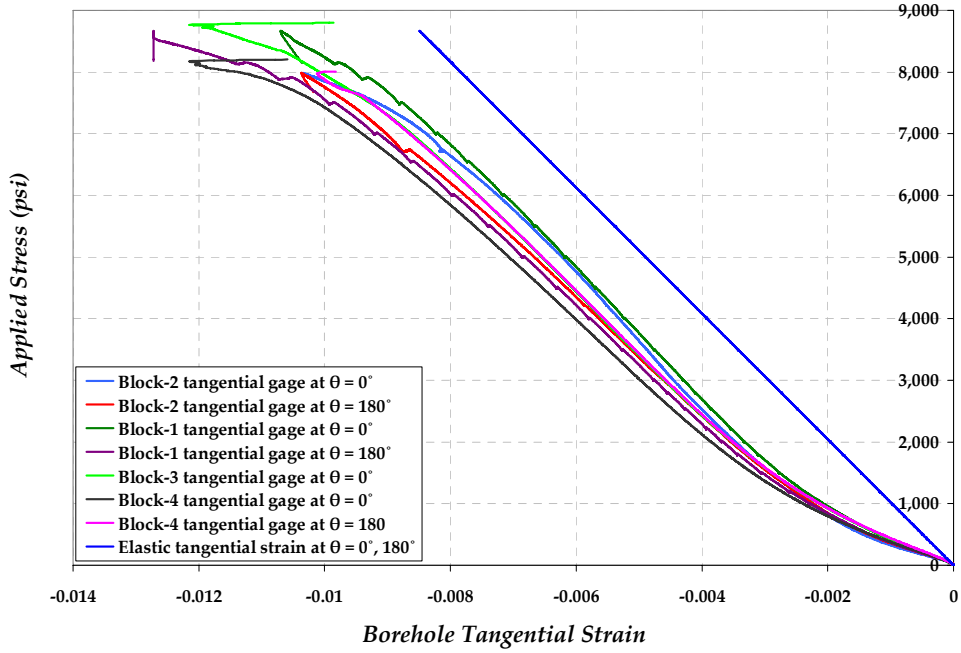

Figure 6-26: Measured and computed borehole tangential strain at θ = 0˚ and θ = 180˚ for the four tested Berea block samples.

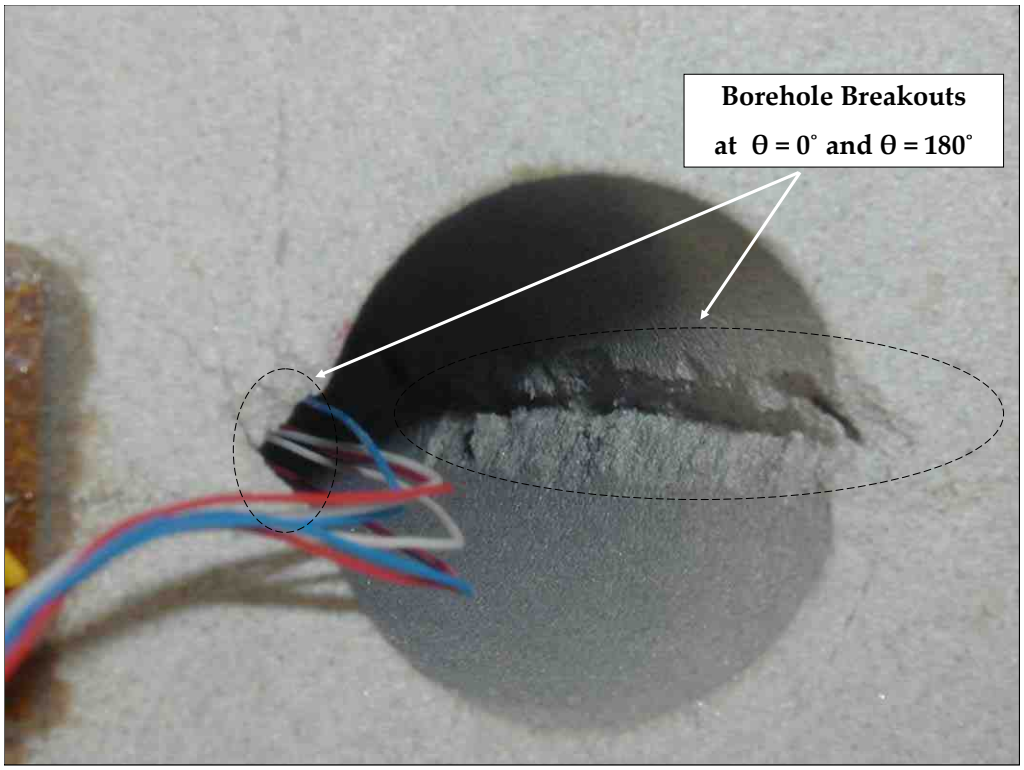

Figure 6-27: Close view to the borehole collapse after testing one of the Berea samples.

The borehole failures were investigated after the experiment is performed by sawing the block diagonally as shown in Figure 6-28. Figures 6-29 and 6-30 show a close view of the borehole wall illustrating the tensile and shear failures at the principal orientations. The repeatability of the measured strain was also checked by cycling the samples at a small stress magnitude before final loading is performed as shown in Figure 6-31.

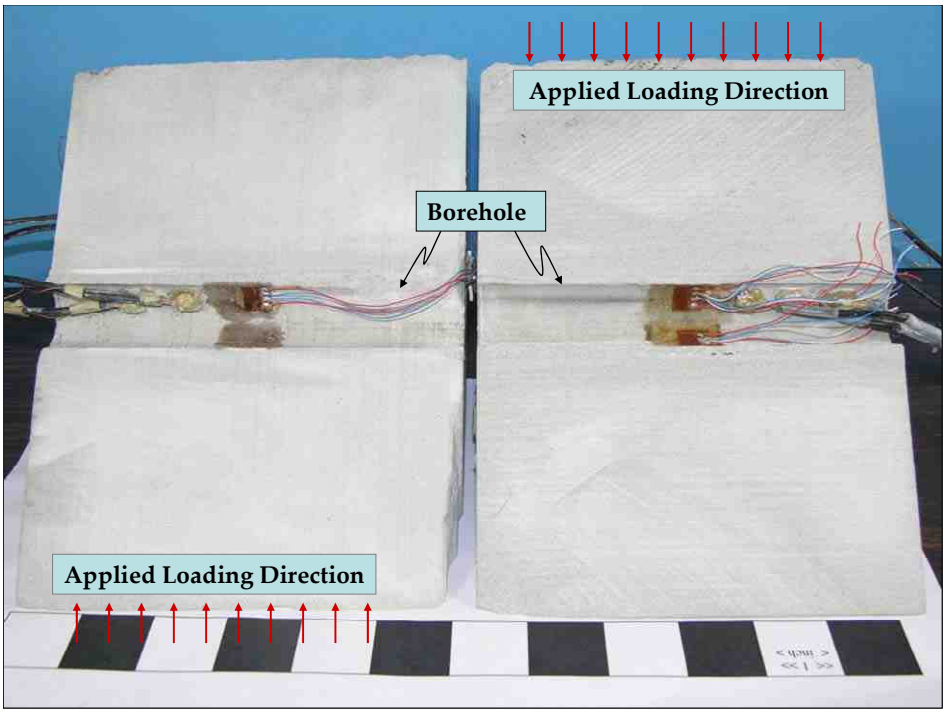

Figure 6-28: A borehole view for Berea block sample cut along the diagonal in the direction of the borehole axis to investigate borehole failures.

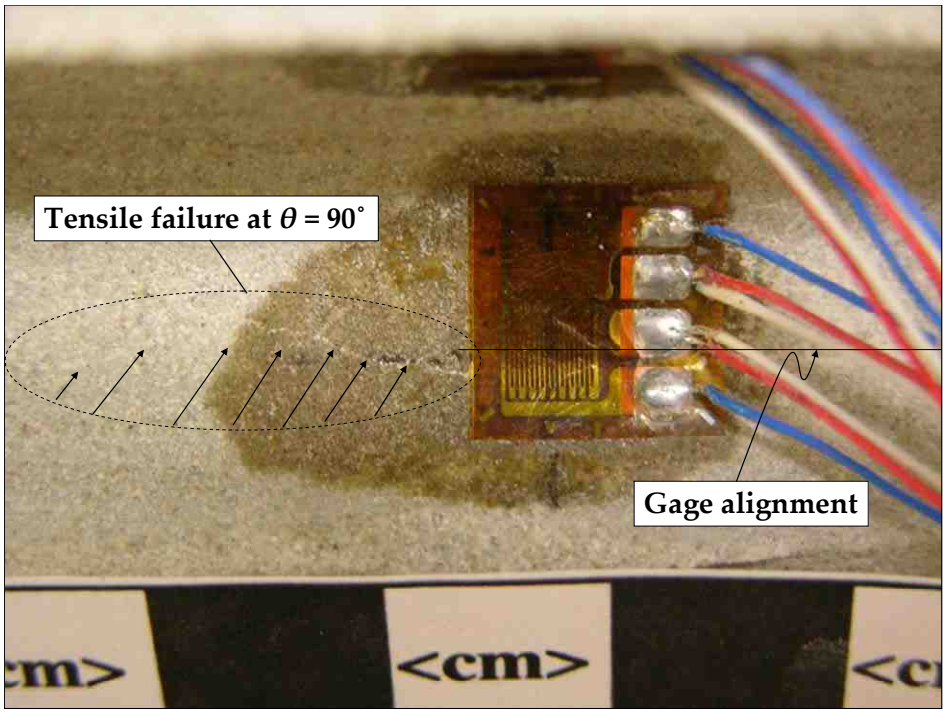

Figure 6-29: Close view of the borehole wall (Berea) illustrating the tensile failure at 90˚. Notice the alignment of the strain gage tangential grid with the tensile failure.

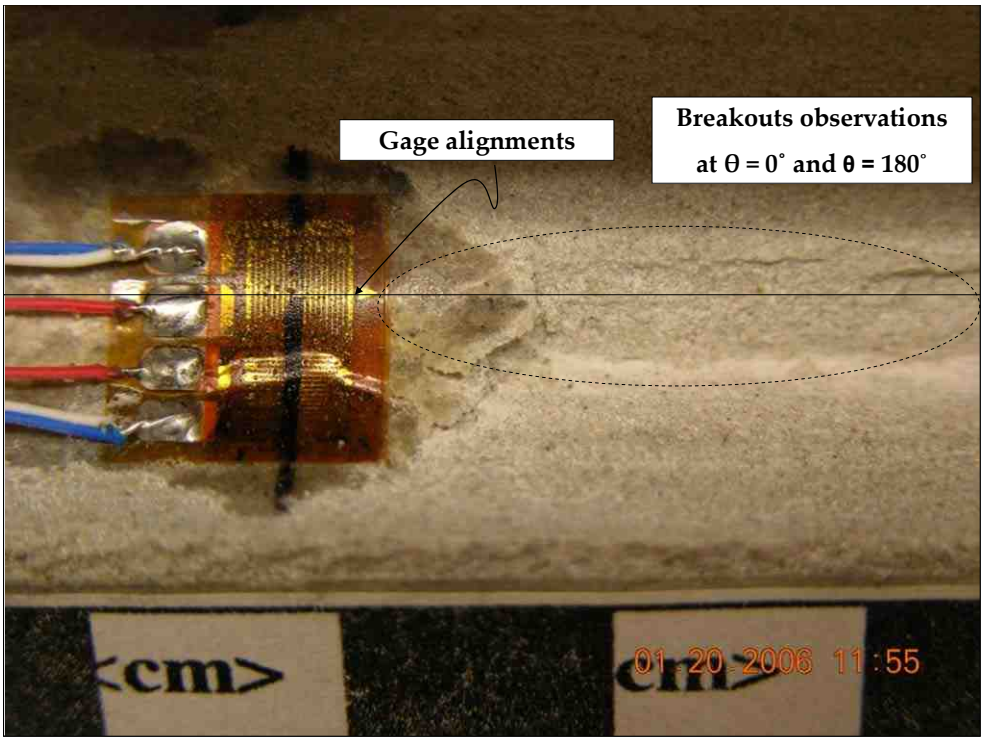

Figure 6-30: Close view of the borehole wall (Berea) illustrating the breakouts at θ = 0°, same observations at θ = 180°. Notice the alignment of the strain gage tangential grid with the breakouts failure.

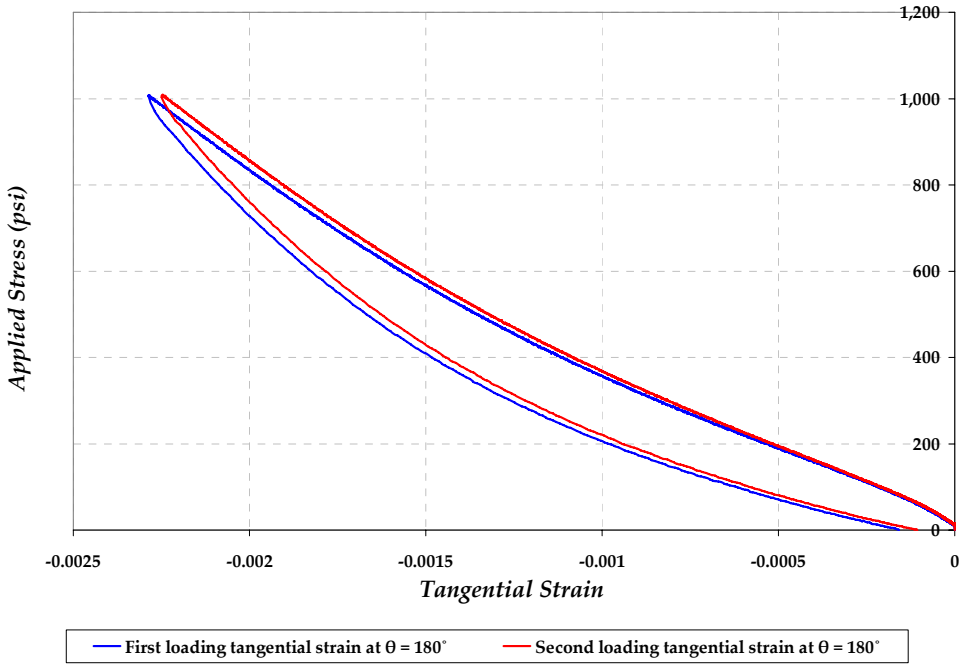

Figure 6-31: Repeatability of the Berea measured strain from one of the borehole gages at θ = 180° from two cycle loadings to an applied stress of 1,000 psi.

The measured borehole displacements using clip gages compared with analytical displacements are shown in Figure 6-32. The indication of the borehole shear failure is shown by the plateau of the displacement trend in the horizontal direction. Borehole displacements were also used to compute the borehole tangential strain at major orientations and which then compared with measured borehole strain. Figure 6-33 and 6-34 show the comparison of the measured and computed tangential strains at $\theta = 0^\circ$ and $\theta = 90^\circ$ for one of the Berea samples using borehole strain gages and displacements, respectively. The borehole shear failure can be observed from both the measured and computed tangential strain at $\theta = 0^\circ$ in Figure 6-33. The measured strains along the borehole axis (z-axis) are shown in Figure 6-35.

Rosette gages were also used on the borehole faces of one of the Berea blocks (block 1). The rosette gages were placed at a radius of $r = 1.065$ inches on both faces. The raw strain measurements using multiple-element rosette gages with 45° grid-spacing are shown in Figure 6-36. The advantage of using a 45° rosette gage is that the principal strains along r- and θ- directions can be directly measured if the gage is placed at the principal stress directions (i.e., the 0°-grid is aligned with the x-direction 90° from loading). The measured strains at $r = 1.065$ using rosette gages placed at the borehole faces compared with analytical strain using Kirsch's solution are shown in Figure 6-37.

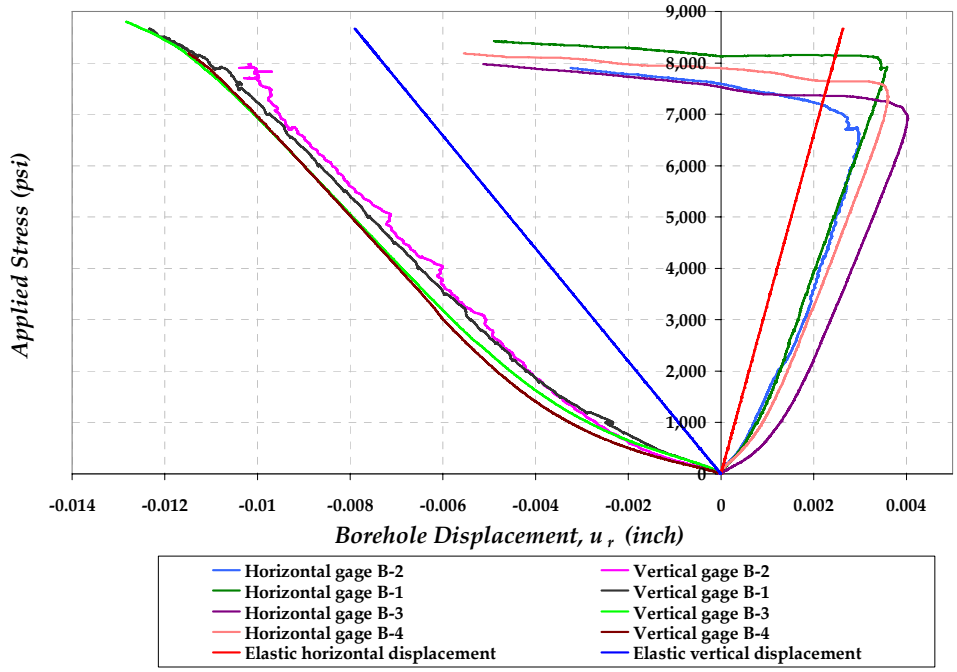

Figure 6-32: Measured and computed borehole horizontal and vertical displacements for the four tested Berea block samples.

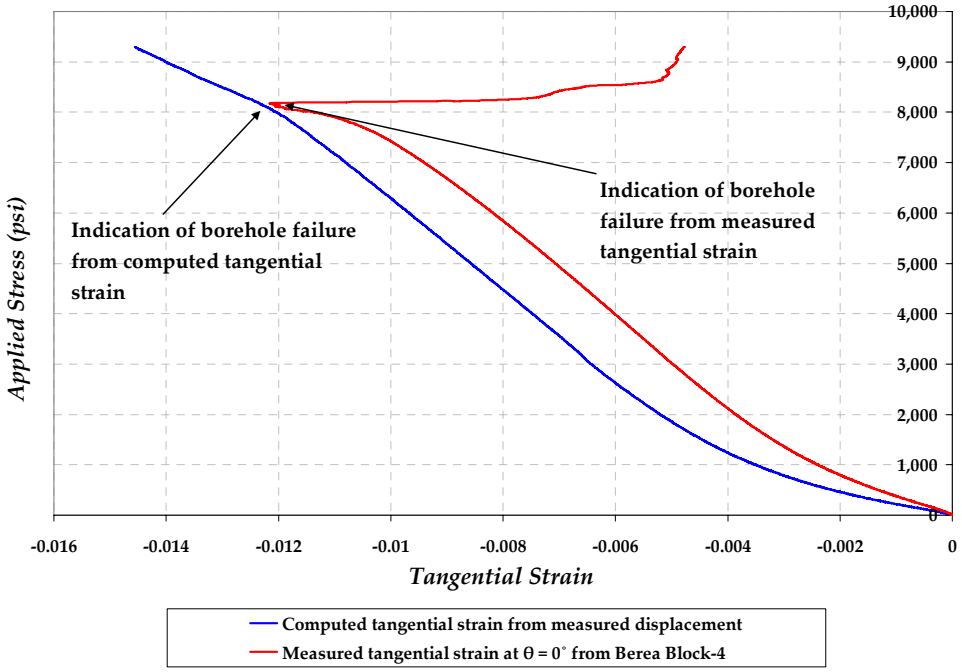

Figure 6-33: Measured and computed borehole tangential strains at $\theta = 0^{\circ}$ for Berea block 4 from strain gage and displacement, respectively. Notice the indication of borehole failure from both stress-strain curves.

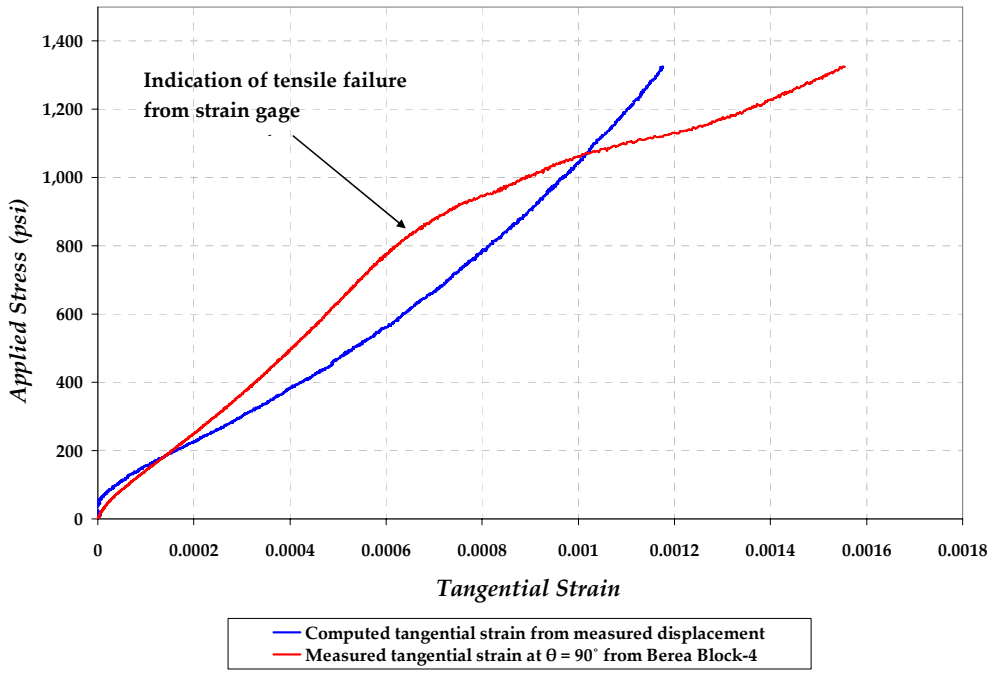

Figure 6-34: Measured and computed borehole tangential strains at θ = 90° for Berea block 4 from strain gage and displacement, respectively.

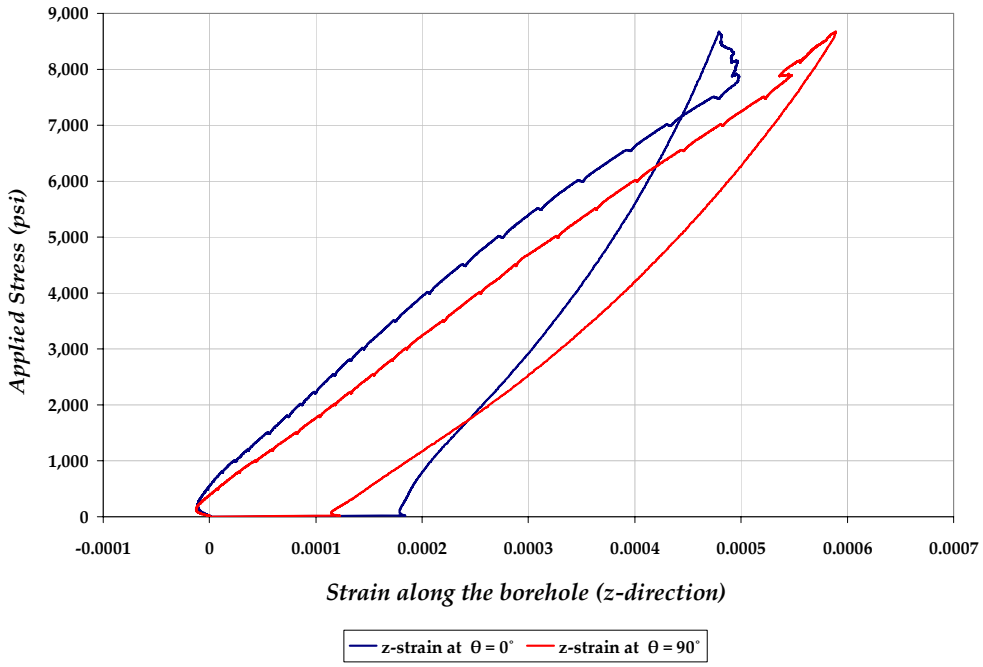

Figure 6-35: Measured strain along the generator (z-direction) at the two principal directions θ = 0° and θ = 90° as a function of far applied boundary stress.

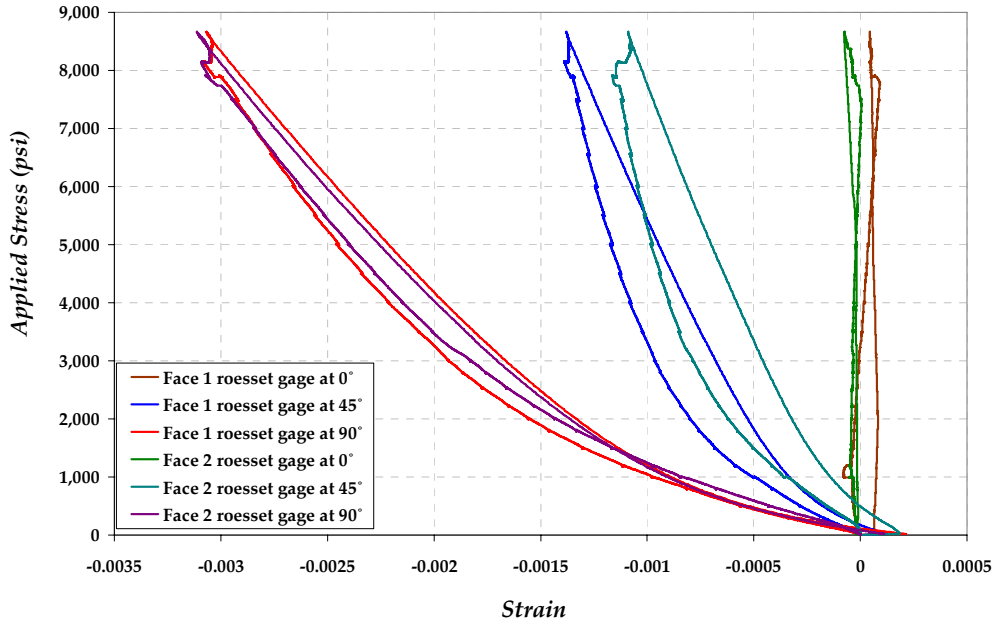

Figure 6-36: 45° Rosette raw gages measurement on the borehole faces for Berea block 1 placed at a radius of r = 1.065 inches.

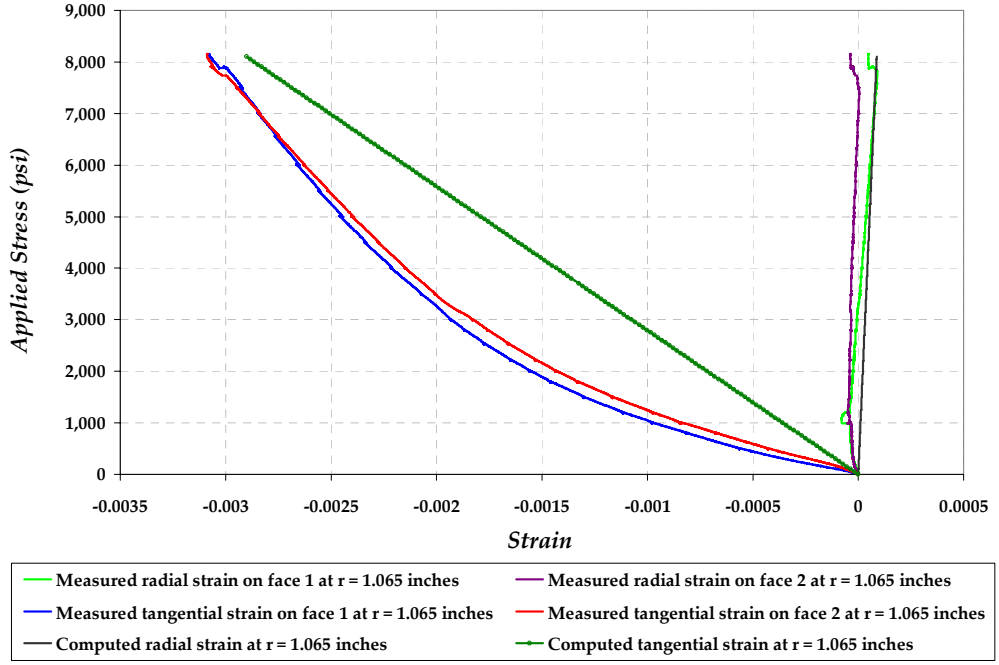

Figure 6-37: Measured strains at a radius of r = 1.065 inches from the rosette gages on borehole faces compared with analytical strain using Kirsch.

The tangential compressive stress at a borehole is computed using the average strains measured using strain gages mounted at θ = 0° and θ = 180°. The computed tangential compressive stress at the borehole as a function of applied boundary stress prior to borehole breakouts is given in Figure 6-38. It can be observed that the borehole induced compressive stress increases nonlinearly at early applied boundary stress before the relationship becomes linear. The slope of the linear part of the curve is 3.14 with a y-intercept of 5,163 psi. The relationship between borehole compressive stress, $\sigma_{\theta\theta}$, and applied boundary stress, σ_H, for Berea, over the entire experiment applied stress range before borehole breakouts are reached, is determined by regression analysis and given by Equation (6.1) with correlation coefficient of $R^2 = 0.9993$.

$$\sigma_{\theta\theta} = 7.902\times10^{-8}\sigma_H^3 - 1.041\times10^{-3}\sigma_H^2 + 7.344\sigma_H + 147.4 \qquad (6.1)$$

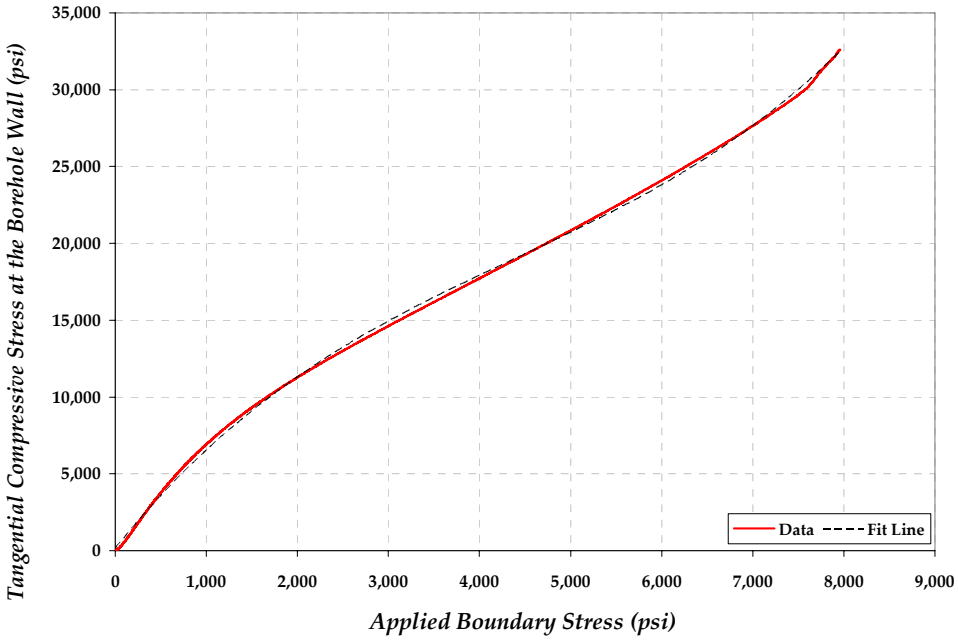

Figure 6-38: Computed average borehole tangential compressive stress before breakouts are developed for Berea.

6.2.3 Chalk Block Samples

A similar analysis is carried out for the two chalk block samples tested. The tangential and axial borehole strains at the principal directions are measured as a function of applied boundary stress. The first block sample is tested with two borehole strain gages placed at $\theta = 0^{\circ}$ and $\theta = 90^{\circ}$, whereas, the second block sample is tested with four gages placed at the four principal orientations. Figure 6-39 shows the measured tangential strain using strain gages compared with analytical tangential strain at the same orientations. The chalk measurements show inconsistency of the measured borehole strain as compared with Berea. This is probably due to inadequate gage bonding since chalk has high porosity (47%) and the pores tend to absorb the glue coating underneath the gage before it dries out. In this case, the comparison of measured strains computed tangential strains from displacements can be used as a tool to confirm the strain gage measurement. The measured tangential strains at the other directions ($\theta = 90^{\circ}$ and $\theta = 270^{\circ}$) are shown in Figure 6-40. Similar inconsistency in the borehole strain measurements is observed at maximum induced tensile stress orientations, and it is clear that the borehole tangential strain measurement of block 2 at $\theta = 270^{\circ}$ should be ignored. Borehole tensile and shear failures are reflected by borehole tangential strain measurements. The borehole strain measurements indicated that borehole shear and tensile failures have occurred at average stresses of 800 and 330 psi, respectively.

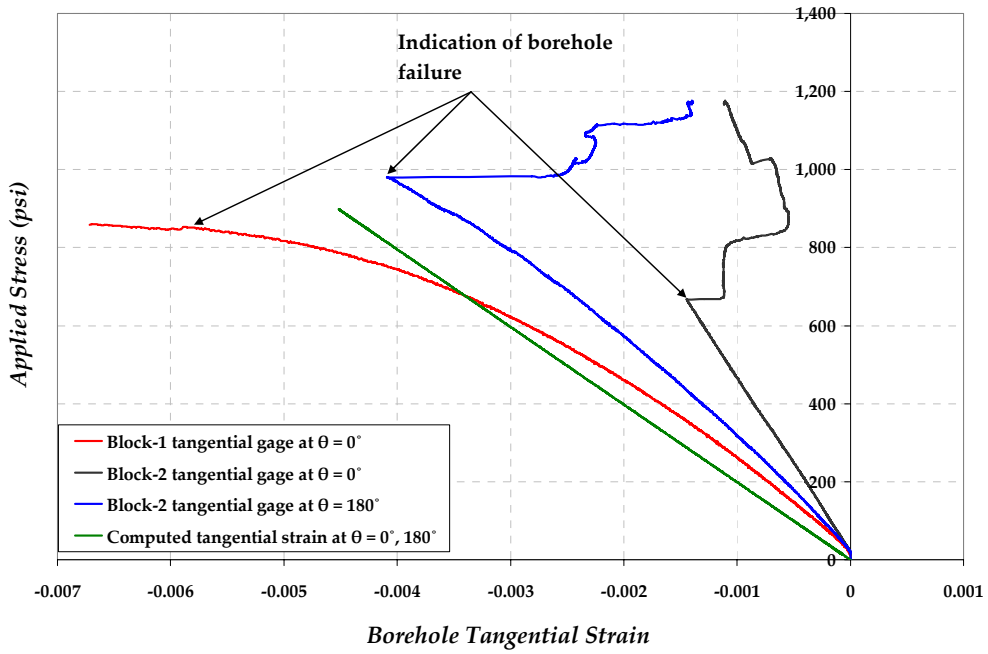

Figure 6-39: Measured tangential strain for chalk samples from strain gages placed at $\theta = 0^{\circ}$ and $\theta = 180^{\circ}$ compared with computed analytical tangential strain at the same orientations.

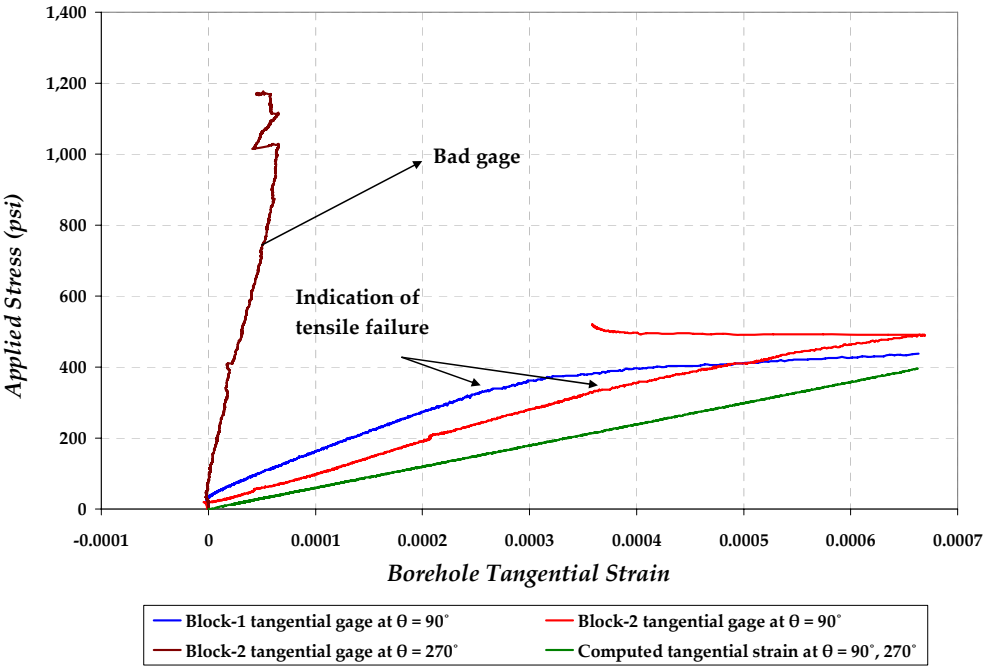

Figure 6-40: Measured tangential strain for chalk from strain gages placed at $\theta = 90^{\circ}$ and $\theta = 270^{\circ}$ compared with computed analytical tangential strain at the same orientations.

The development of borehole shear failures as a result of high stress concentrations around the borehole for chalk samples during testing is observed to be different than the case of Berea samples. In chalk samples, cracks with multiple branches are developed at the borehole due to the high induced compressive stresses. The chalk block samples were also cut along the diagonal in the direction of the borehole axis when the test is complete as shown in Figure 6-41. This allowed investigating the breakouts and tensile failures as shown in Figures 6-42 and 6-43.

The measured and computed borehole displacements from clip gages for chalk samples are shown in Figure 6-44. Figures 6-45 and 6-46 display the comparison of the measured and computed tangential strains using strain gages and clip displacements at the directions of maximum induced compressive and tensile stresses, respectively. It can be noticed from both Figures 6-45 and 6-46 that the strains measured using strain gages at $\theta = 0^{\circ}$ for block 1 and at $\theta = 90^{\circ}$ for block 2 are comparable with borehole strains computed from clip displacements at the same orientations. The borehole axial strain measured along the z-direction is shown in Figure 6-47 at the principal orientations. The indication of borehole breakouts and tensile failure can also be inferred from the trend of the axial strain measurements as illustrated in Figure 6-47.

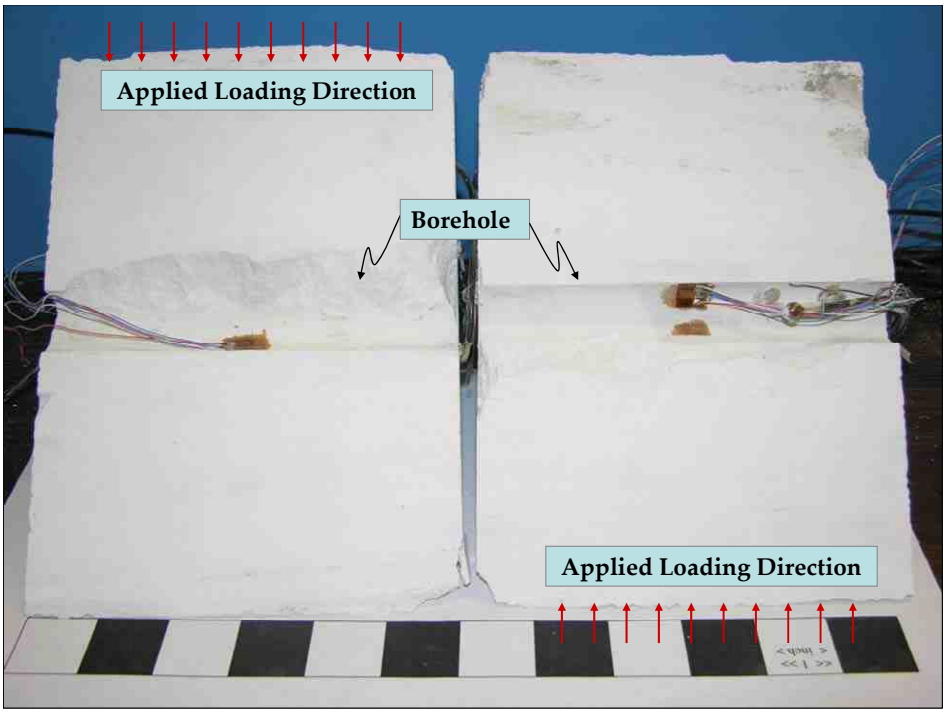

Figure 6-41: A borehole view for one of the chalk samples cut along the diagonal in the direction of the borehole axis to investigate borehole failures.

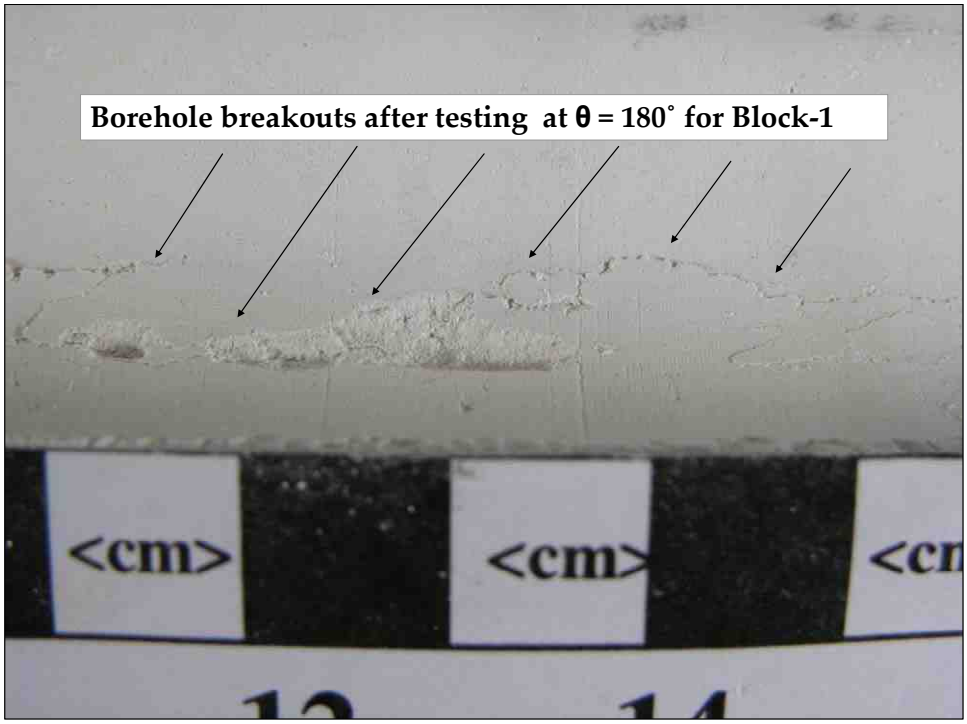

Figure 6-42: Close view of the borehole wall (chalk) showing breakouts and borehole failure at θ = 180˚.

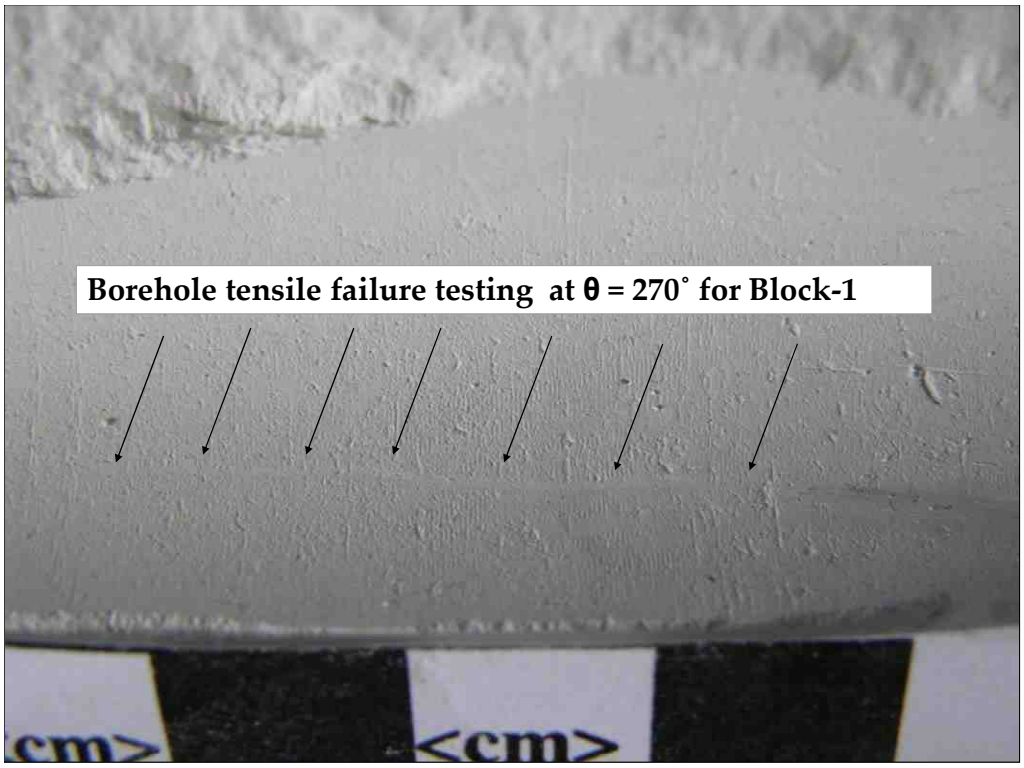

Figure 6-43: Close view of the borehole wall (chalk) showing tensile failure at θ = 270˚.

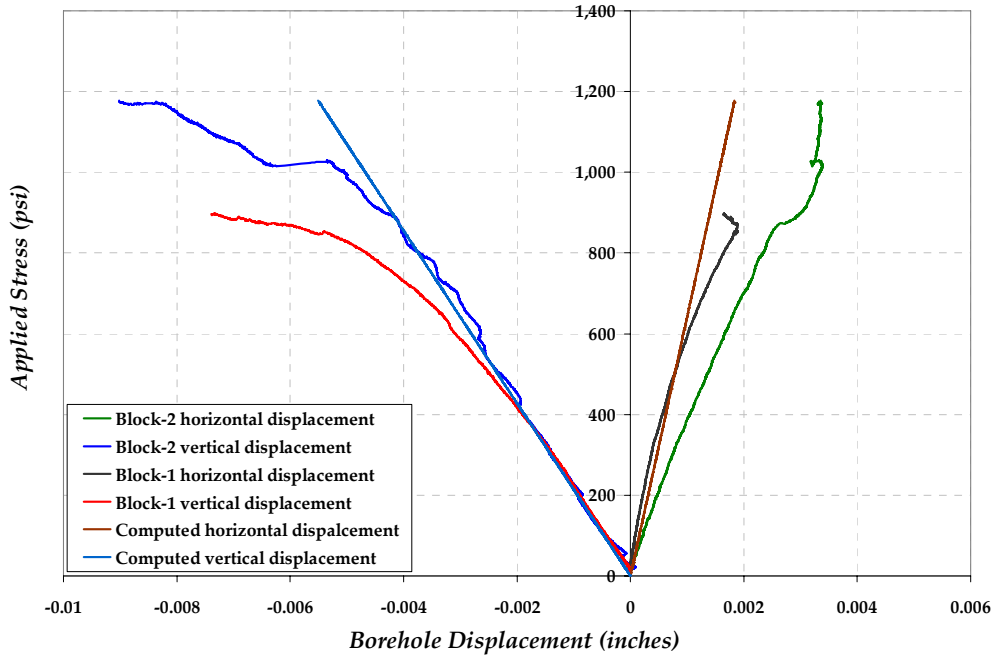

Figure 6-44: Measured and computed borehole displacements from clip gages for chalk block samples.

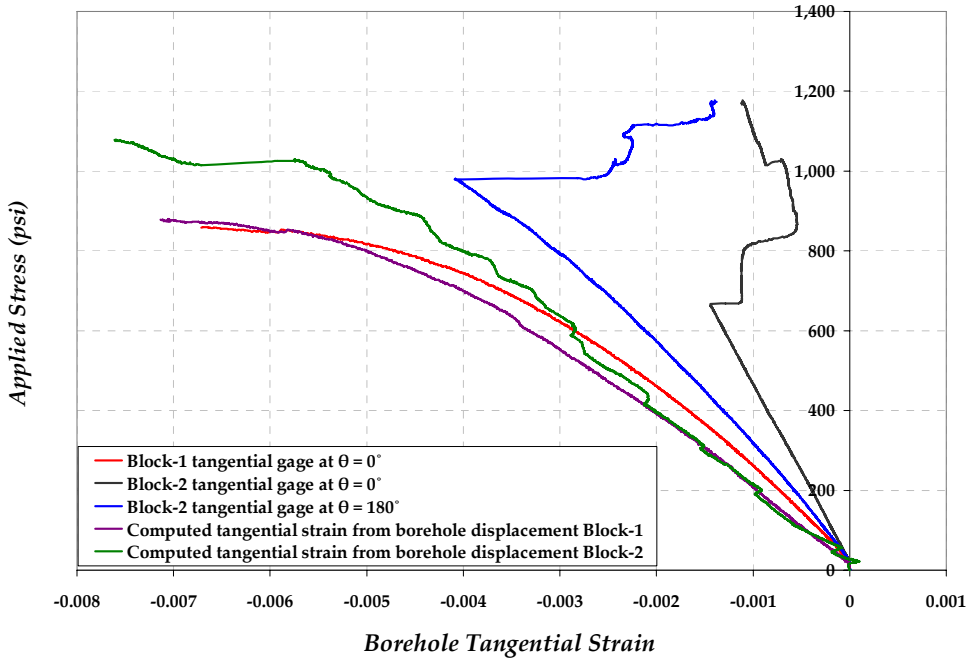

Figure 6-45: Measured and computed tangential strains for chalk samples from strain gages and clip displacements at the induced compressive stress directions.

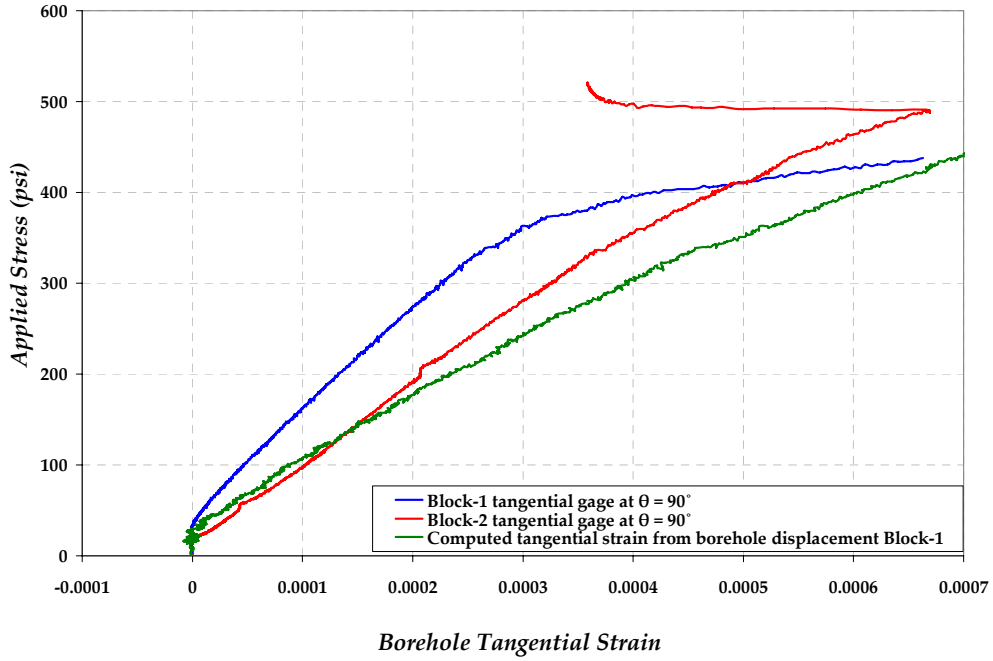

Figure 6-46: Measured and computed tangential strains for chalk from strain gages and clip displacements at the induced tensile stress directions.

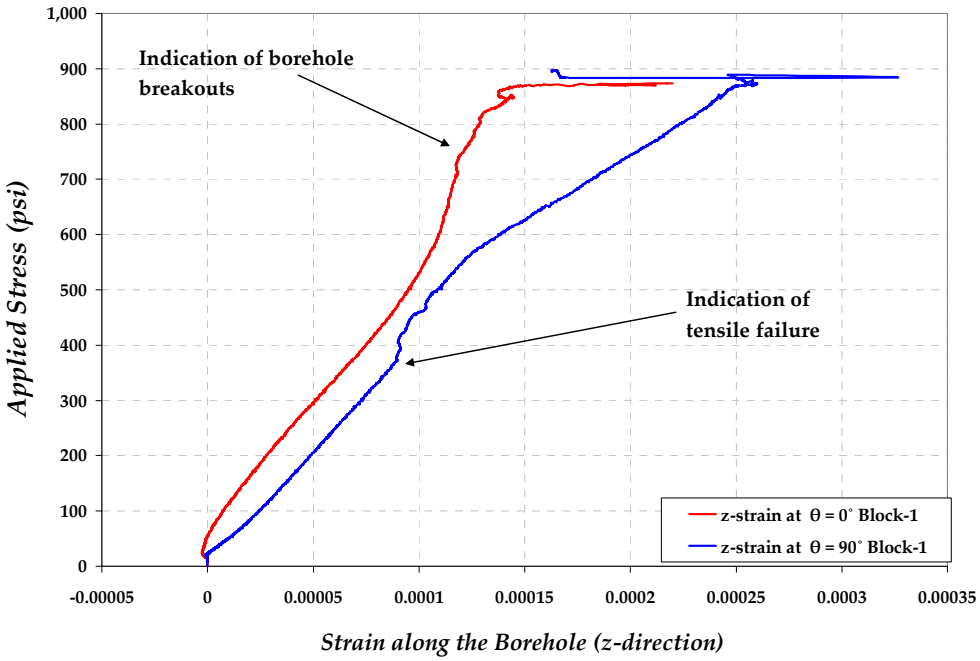

Figure 6-47: Measured strain along the generator (z-direction) at the two principal directions θ = 0° and θ = 90° as function of applied stress, chalk block 1.

The computed tangential compressive stress for chalk samples at the borehole as function of applied boundary stress prior to borehole breakouts is given in Figure 6-48 using the measured tangential strain for block 1 at θ = 0°. The ratio of the borehole compressive stress to the applied boundary stress taken at 50% of the applied boundary stress is about 3.09 with a y-intercept of -226 psi. The relationship between induced borehole compressive stress, $\sigma_{\theta\theta}$, and applied stress at the boundary, σ_H, for chalk samples, over the entire experiment applied stress range, is obtained by regression analysis with correlation coefficient of R^2 = 0.9997 as:

$$\sigma_{\theta\theta} = 2.592\times10^{-6}\sigma_H^3 - 8.983\times10^{-4}\sigma_H^2 + 2.539\sigma_H - 54.72 \qquad (6.2)$$

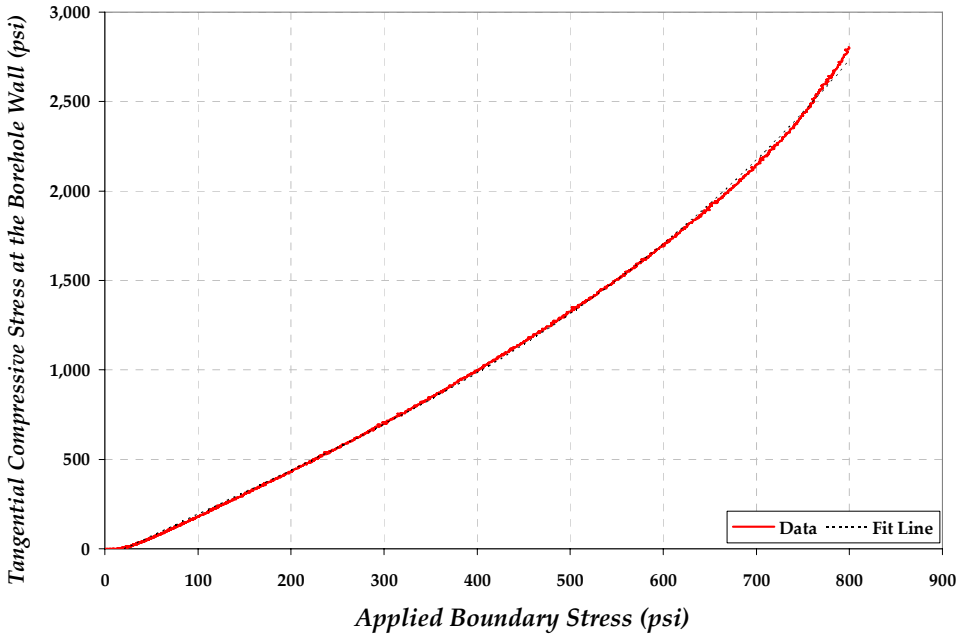

Figure 6-48: Computed tangential compressive stress before breakouts for chalk.

6.2.4 White Limestone Block Samples

Two white limestone block samples were tested with four strain gages mounted at the borehole for each block. The borehole tangential strain measurements at the main orientations are shown in Figures 6-49 and 6-50 compared with computed borehole strain. The borehole tangential strain measurements at the induced compressive stress directions indicated borehole shear failures at applied stresses of 2,200 and 2,400 psi for block 1 and block 2, respectively. The applied stress is stopped at each 100 psi increment during testing of block 1 for velocity acquisition; this leads a jagged stress-strain curve as in Figure 6-49. Borehole tensile failure at the maximum induced tensile stress directions can be observed

from the strain measurements of block 1 at applied stress of 950 psi. Borehole strain measurements for block 2 showed continuous strain as a function of applied stress without being influenced by the development of borehole tensile failure. This may be caused by excessive glue used to bond the strain gages as the case for Berea block samples 1 and 2. Figure 6-51 shows a pictorial view of a white limestone block sample after being cut along the diagonal in the direction of the borehole axis where the observation of borehole breakouts is shown in Figure 6-52.

The measured borehole displacements using clip gages compared with analytical displacements are shown in Figure 6-53. The indication of borehole failure is shown by the flat displacement in the horizontal direction. Borehole displacement measurements were utilized to compute tangential strains at the principal directions. Figure 6-54 and 6-55 show the comparison of the measured and computed tangential strains at $\theta = 0^{\circ}$ and $\theta = 90^{\circ}$ from borehole strain gages and displacements, respectively. The measured strains along the borehole (z-axis) at the two principal directions are shown in Figure 6-56. The axial strain measurement at $\theta = 90^{\circ}$ indicates the tensile failure at the borehole.

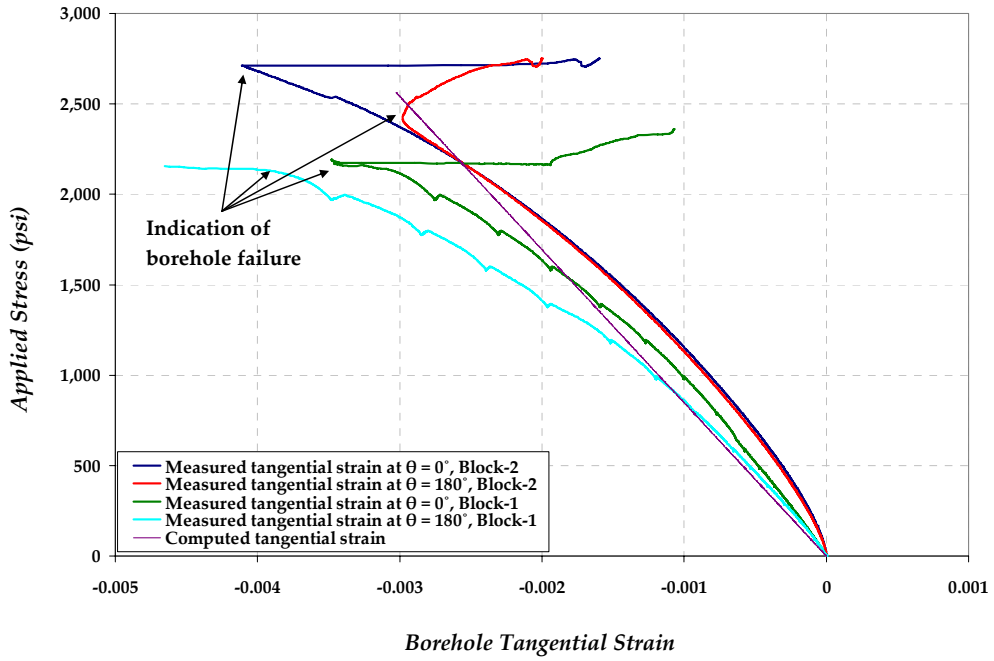

Figure 6-49: Measured tangential strain for white limestone samples from strain gages placed at θ = 0° and θ = 180° compared with computed analytical tangential strains at same orientations.

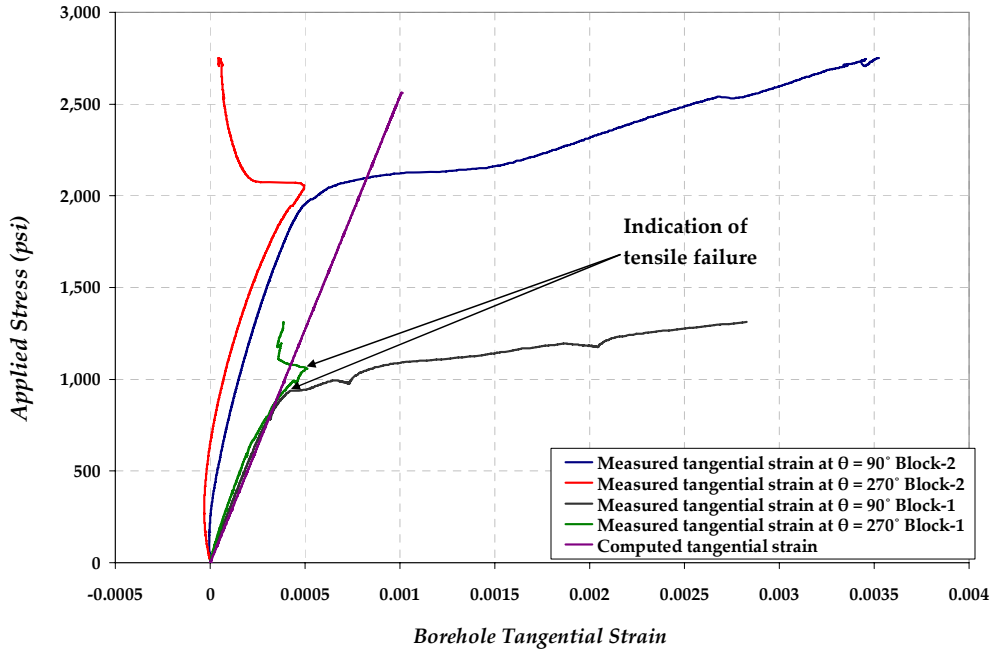

Figure 6-50: Measured tangential strain for white limestone samples from strain gages placed at θ = 90° and θ = 270° compared with computed analytical tangential strain at same orientations.

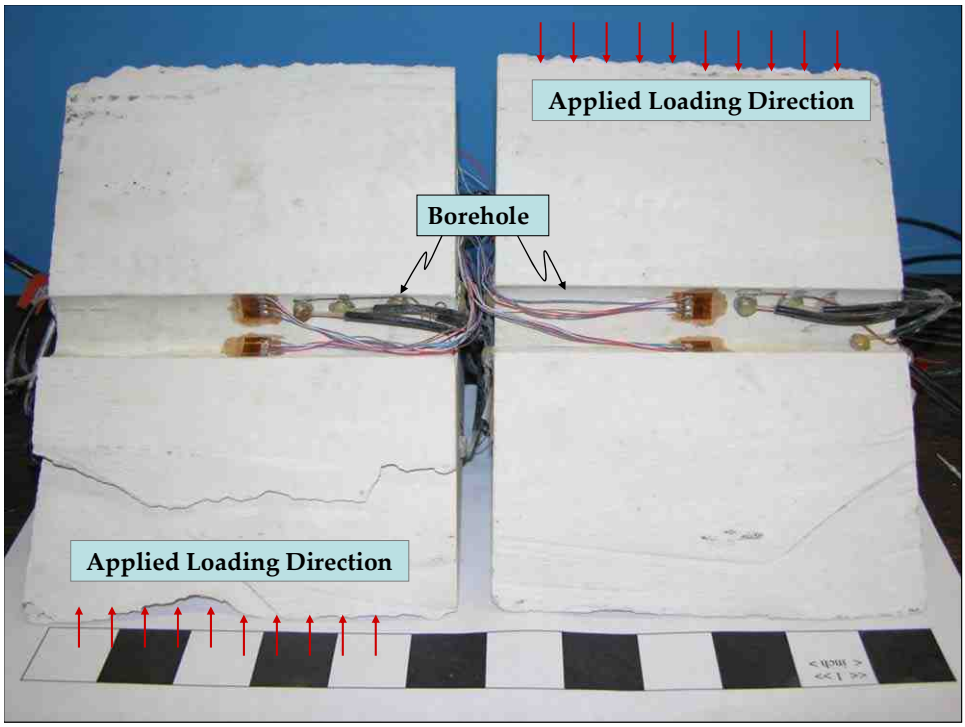

Figure 6-51: A borehole view for one of the white limestone samples cut along the diagonal in the direction of the borehole axis to investigating borehole failures.

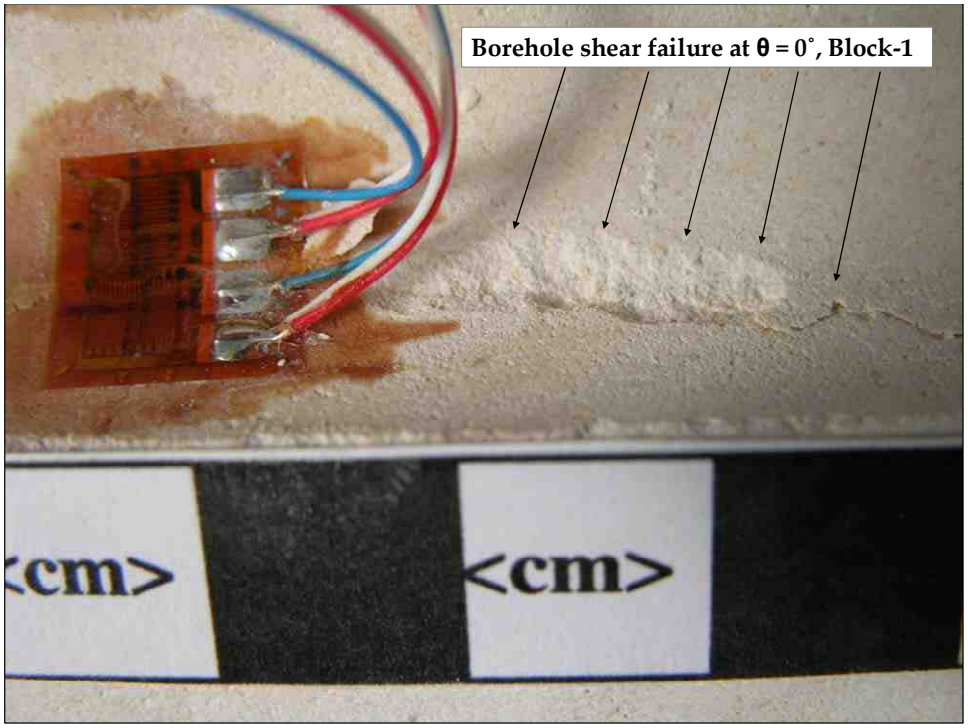

Figure 6-52: Pictorial view of the borehole shear failure and breakouts observed for white limestone block 1 after testing.

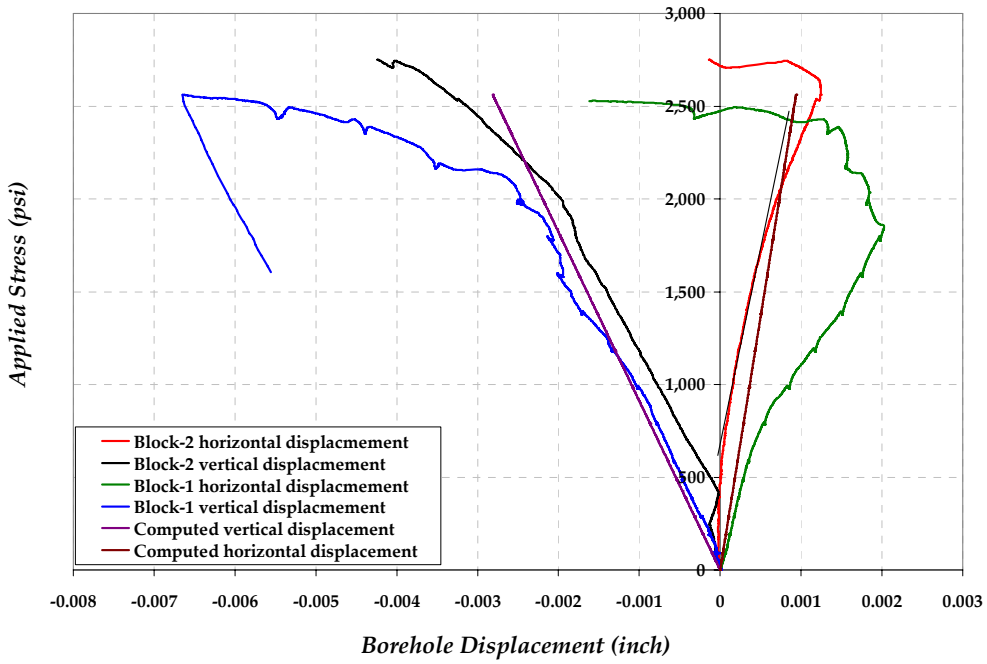

Figure 6-53: Measured and computed borehole displacements from clip gages for the white limestone block samples.

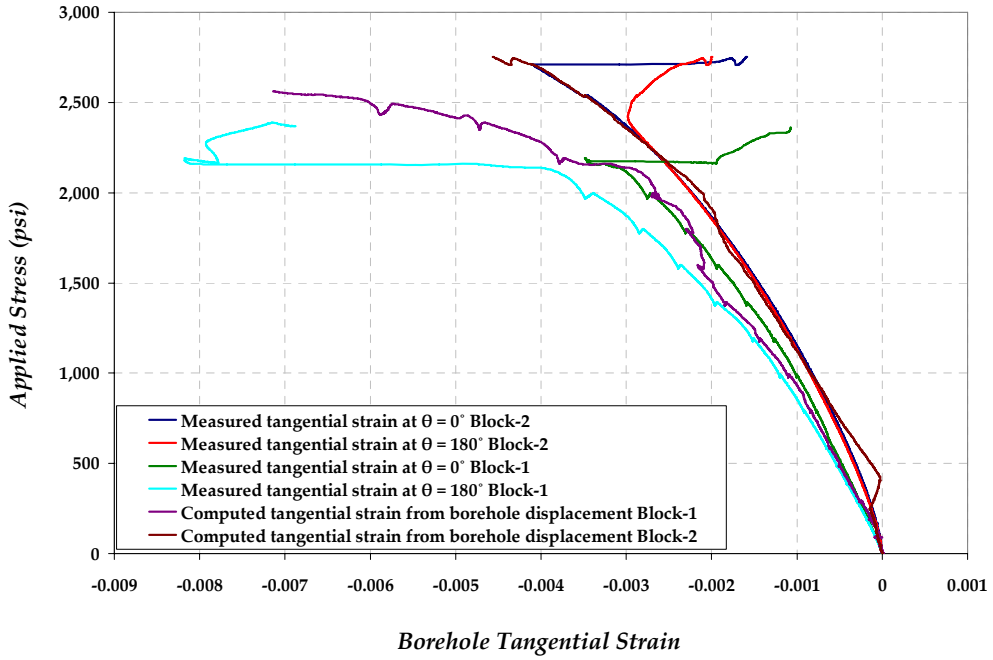

Figure 6-54: Measured and computed tangential strains for the white limestone samples from strain gages and clip displacements at the induced compressive stress directions.

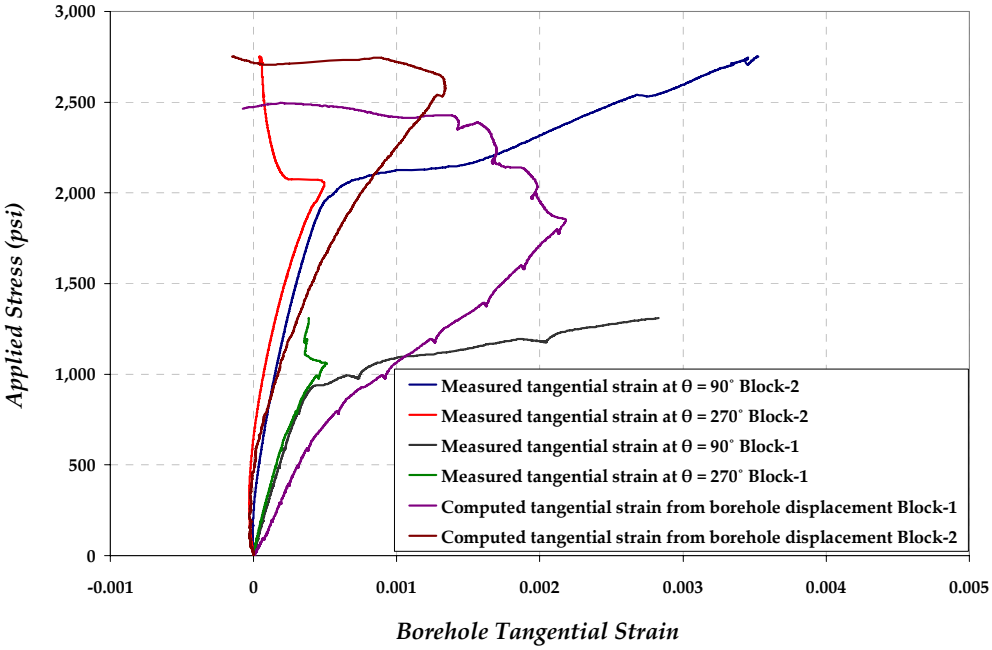

Figure 6-55: Measured and computed tangential strains for the white limestone samples from strain gages and clip displacements at the induced tensile stress directions.

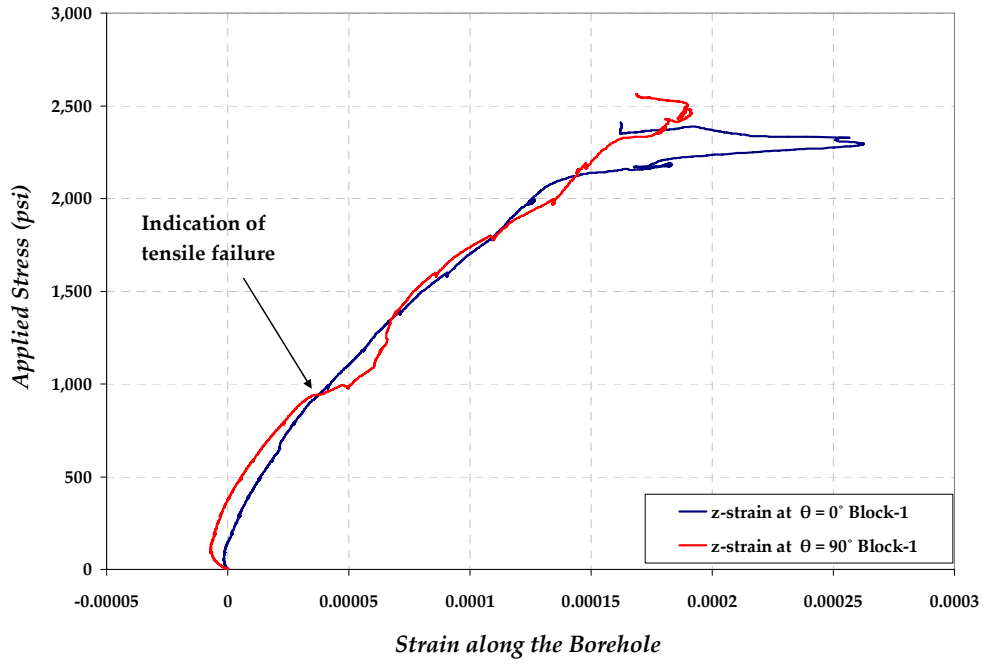

Figure 6-56: Measured strain along the generator (z-direction) at the two principal directions θ = 0° and θ = 90° as function of applied stress, white limestone block 1.

The tangential compressive stress at the borehole wall for the white limestone is computed from the average strains measured from the strain gages of block 1 at θ = 0˚ and θ = 180˚. The computed tangential compressive stress at the borehole wall, as function of applied boundary stress prior to borehole breakouts, is given in Figure 6-57. The ratio of the borehole compressive stress to the applied boundary stress taken at 50% of applied boundary stress is about 3.39 with a y-intercept of -537 psi. The relationship between borehole compressive stress, $\sigma_{\theta\theta}$, and applied boundary stress, σ_H, for the white limestone samples, over the entire experiment applied stress, is determined by regression analysis and given as (correlation coefficient is $R^2 = 0.9995$):

$$\sigma_{\theta\theta} = 2.944\times10^{-7}\sigma_H^3 + 1.389\times10^{-4}\sigma_H^2 + 2.457\sigma_H - 17.97 \qquad (6.3)$$

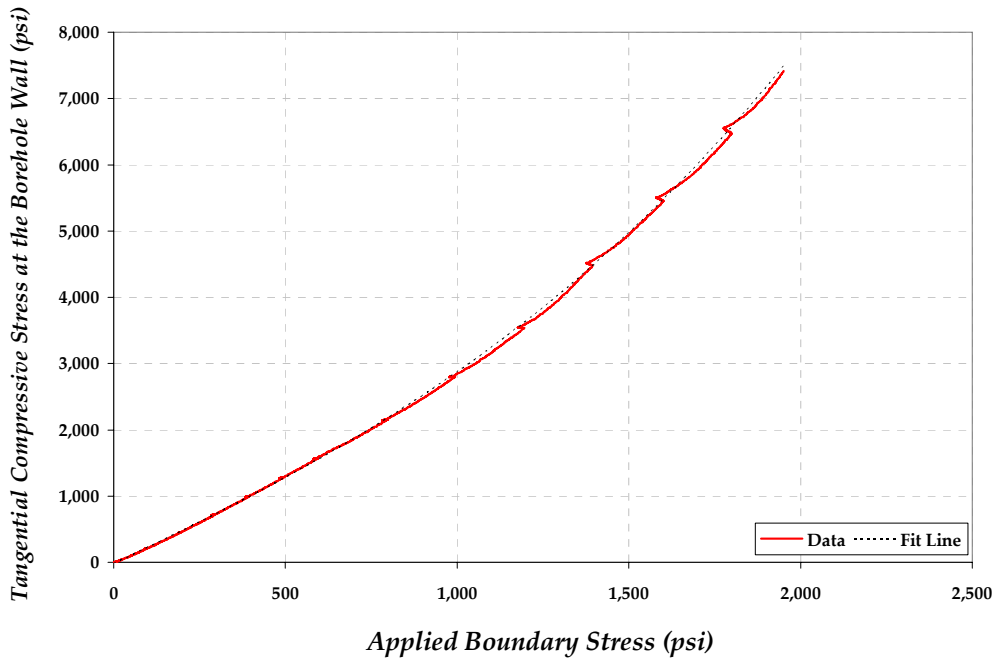

Figure 6-57: Computed average tangential compressive stress before breakouts for white limestone.

6.2.5 Pierre Shale Block Samples

Initially, two block samples were prepared for testing. As mentioned in Chapter 4, the process of gauging the borehole requires one day for each strain gage to be glued in the borehole. The first block was ruptured during installation of the third borehole strain gage. The applied pressure in the borehole required to hold the gage in place resulted in extending one of the major preexisting fractures from the borehole to the side of the sample as shown in Figure 6-58. As a result, only borehole displacements were measured during the testing of the second Pierre shale sample to minimize the time of having the shale block out of the PG-1 oil bath before testing.

The measured and computed borehole displacements are shown in Figure 6-59. Also, the computed borehole strains at the major principal directions using measured displacements are shown in Figure 6-60. Both results indicated higher displacements and strains at the borehole for Pierre shale block sample compared with other tested samples. This behavior can be linked to the low stiffness of the Pierre shale and the existence of the fractures network within the matrix and around the borehole. The Pierre shale block sample failed along one of the weak planes at a boundary applied stress of 420 psi where no observable borehole breakouts. The computed induced tangential compressive stress at the borehole as a function of applied boundary stress is shown in Figure 6-61 with regression analysis given as (correlation coefficient is $R^2 = 0.9998$):

$$\sigma_{\theta\theta} = -3.115\times10^{-6}\sigma_H^3 + 1.32\times10^{-2}\sigma_H^2 + 6.906\sigma_H - 81.47 \qquad (6.4)$$

Figure 6-58: Failure of the Pierre shale block during preparation and instrumentation (the orientation of the bedding is 60° relative to the borehole axis).

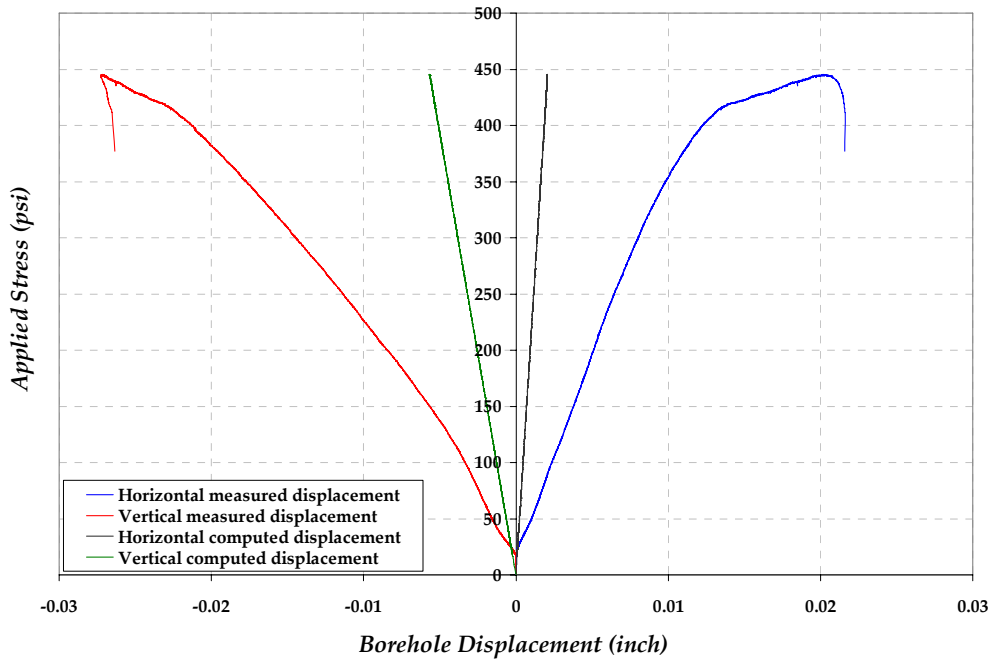

Figure 6-59: Measured and computed borehole displacements for Pierre shale block 2.

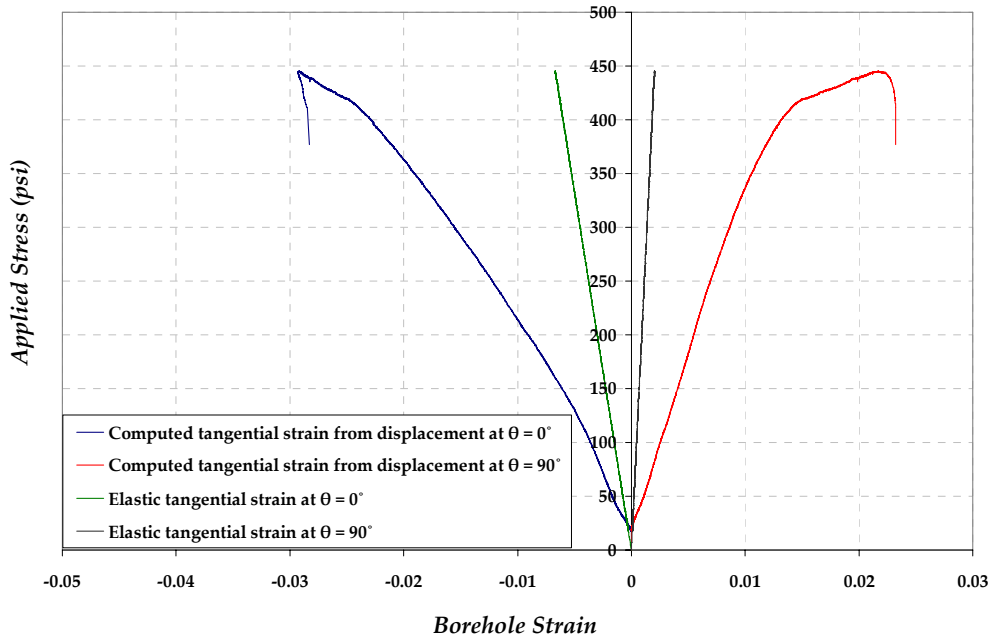

Figure 6-60: Computed borehole tangential strain from measured displacements for Pierre shale block 2.

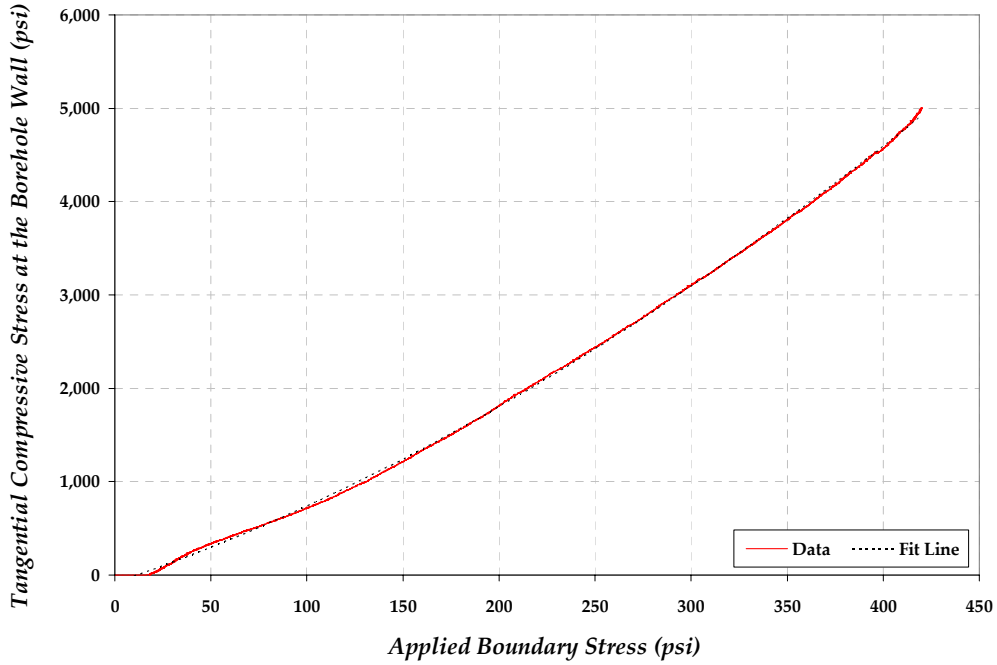

Figure 6-61: Tangential induced compressive stress computed from borehole strain for Pierre block 2.

6.3 Dynamic Block Samples Testing

As discussed in Chapter 4, compressional and polarized shear velocities (V_p, V_{s1} and V_{s2}) were measured perpendicular (radially) and parallel (axially) with reference to the borehole axis at the two preferred orientations mainly the induced compressive and tensile stress directions ($\theta = 0^\circ$ and $\theta = 90^\circ$). For the radial velocity measurements, the transmitters were placed on the side and top faces of the block samples, while the receivers were mounted inside the borehole with similar orientations. The polarizations of the two shear velocities were parallel and perpendicular to the loading direction. The configuration of the axial velocity measurements involves acquiring a velocity parallel to the axis of the borehole where the transmitters and receivers are placed at the borehole faces at $\theta = 0^\circ$ and $\theta = 90^\circ$ with respect to the loading direction. This section reviews both radial and axial measurements conducted on aluminum and rock samples. It also compares dynamic measurements with the quasi-static measurements performed in the previous section.

6.3.1 Aluminum Dynamic Measurements

Borehole compressional and shear velocities measured on aluminum showed constant velocities as a function of stress indicating the linearity of both dynamic Young's modulus and Poisson's ratio with applied stress as obtained for aluminum cylindrical sample testing. The compressional and shear waveforms acquired across the borehole as a function of applied boundary stress at $\theta = 90^\circ$

are given in Figures 6-62 and 6-63 to illustrate constant time arrivals. The measured velocities are shown in Table 6-9 and also plotted in Figure 6-64. The computed moduli for aluminum are reported in Table 6-10. The computed dynamic strains from velocities and stress are compared with measured quasi-static borehole strains at $\theta = 0^{\circ}$ and $\theta = 90^{\circ}$ as shown in Figure 6-65. The measured quasi-static and computed dynamic stress-strain data from strain gages and velocities, respectively, are identical for an elastic medium such as aluminum. Velocities along the borehole were not measured for aluminum since similar velocities are expected.

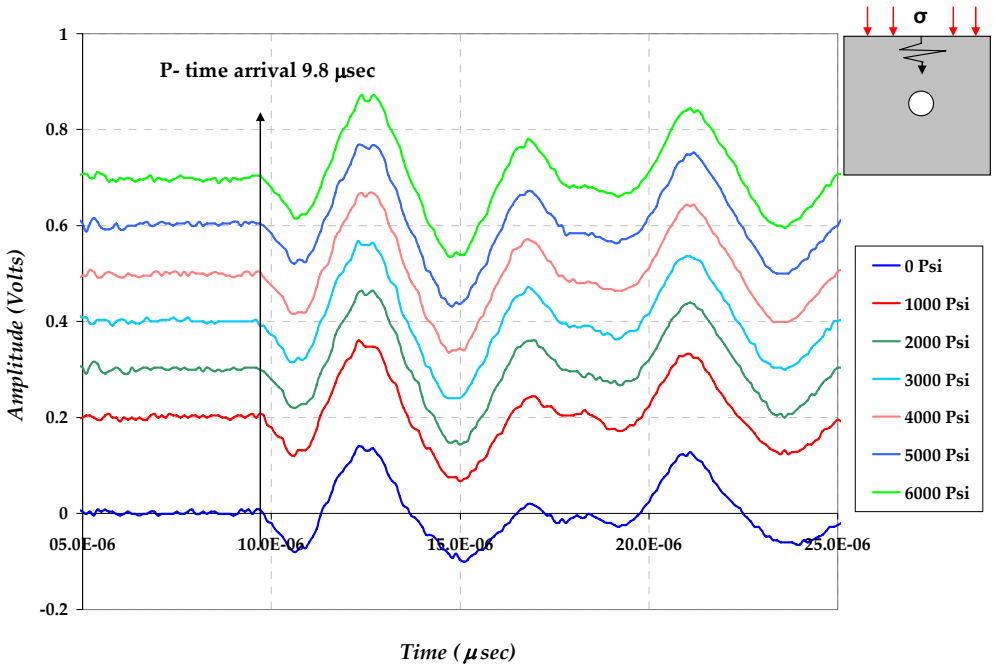

Figure 6-62: Stacked radial compressional waveforms for the aluminum block sample at $\theta = 90^{\circ}$ as a function of applied stress with constant P- arrival of 9.8 µsec.

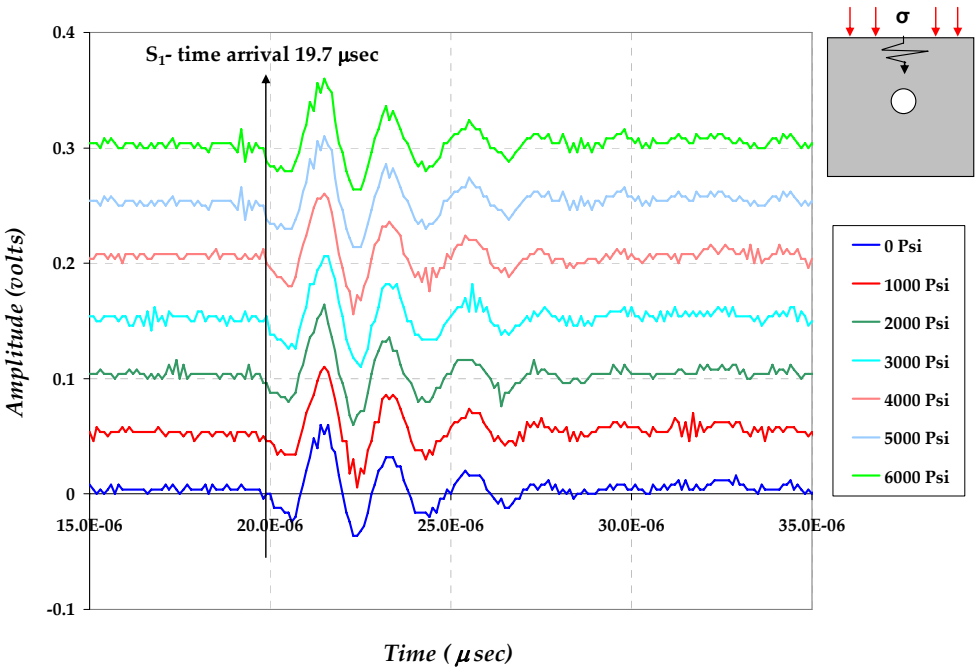

Figure 6-63: Stacked radial shear waveforms (V_{s1}) for the aluminum block sample at θ = 90° as a function of applied stress different stresses with constant S_1- arrival of 19.7 µsec.

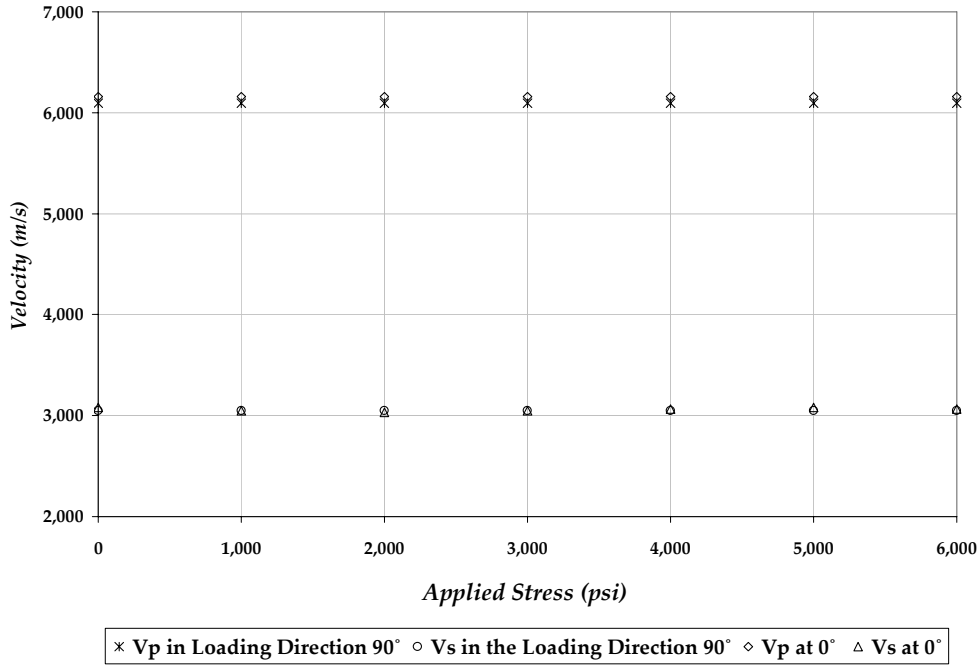

Figure 6-64: Measured compressional and average shear velocities for the aluminum at the two principal directions as a function of applied far boundary stress.

Stress (psi)	Compression side (θ = 0°)			Tension side (θ = 90°)		
	V_p (m/s)	V_s (m/s)	V_p/V_s	V_p (m/s)	V_s (m/s)	V_p/V_s
0	6,220	3,048	2.0	6,036	3,079	2.0
1,000	6,220	3,048	2.0	6,096	3,048	2.0
2,000	6,158	3,048	2.0	6,096	3,033	2.0
3,000	6,158	3,048	2.0	6,096	3,048	2.0
4,000	6,158	3,048	2.0	6,096	3,063	2.0
5,000	6,158	3,048	2.0	6,096	3,079	2.0
6,000	6,220	3,048	2.0	6,096	3,063	2.0

Table 6-9: Measured borehole radial velocities for aluminum at the two principal directions as a function of applied far boundary stress.

Stress (psi)	Compression side (θ = 0°)		Tension side (θ = 90°)	
	E (psi)	ν	E (psi)	ν
0	9.709+06	0.33	9.909E+06	0.32
1,000	9.709+06	0.33	9.709+06	0.33
2,000	9.709+06	0.33	9.709+06	0.34
3,000	9.709+06	0.33	9.709+06	0.33
4,000	9.709+06	0.33	9.709+06	0.33
5,000	9.709+06	0.33	9.709+06	0.33
6,000	9.709+06	0.33	9.709+06	0.33

Table 6-10: Computed moduli from measured velocities for aluminum at the two principal directions as a function of applied far boundary stress.

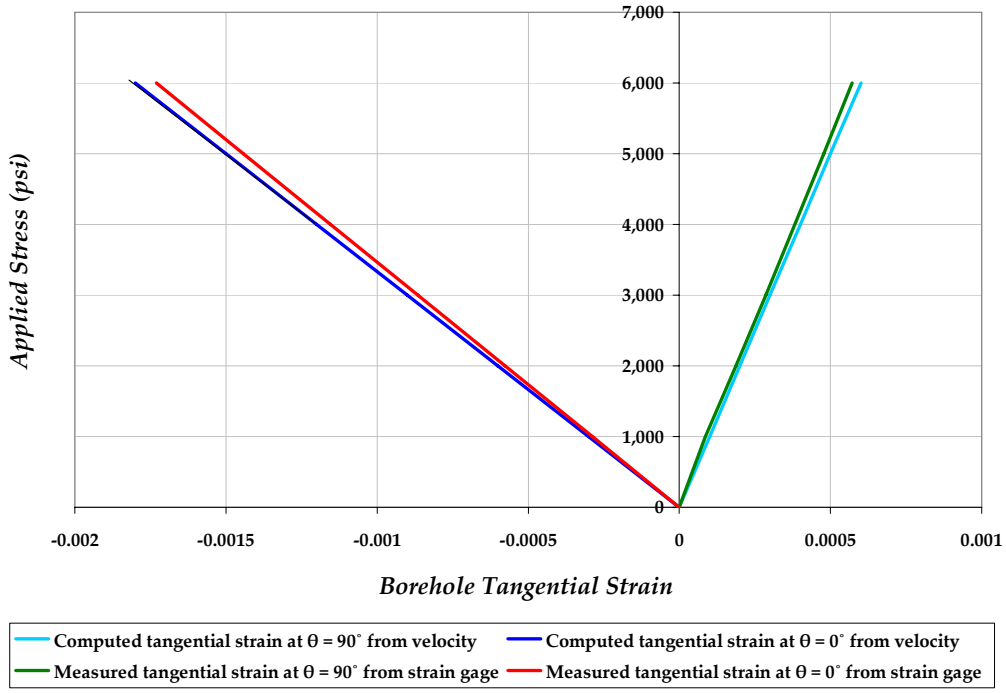

Figure 6-65: Measured and computed strains from strain gage and borehole acoustic velocities for the aluminum block sample.

6.3.2 Berea Dynamic Measurements

Measured velocities for Berea block samples were acquired at both directions, axial and radial relative to the borehole. Since Berea block samples were initially cycled at small stress to check the functionality of borehole strain gages, the repeatability of velocity measurements were also examined during initial cycling. Figure 6-66 shows the face shear wave measurements (V_{s1}) for Berea during cycling to a stress of 200 psi at $\theta = 90^{\circ}$. Radial compressional and shear velocities measured for one of the Berea samples are given in Figure 6-67. It can be noticed that the velocities are affected by the induced borehole compressive and tensile stresses at $\theta = 0^{\circ}$ and $\theta = 90^{\circ}$ although the stress profile varies in the direction of

the wave from the borehole to the outer boundaries. Compressional and shear velocities measured along the borehole axis are given in Figure 6-68 with illustration of the locations of acquired velocities around the borehole. In this case, the velocities propagate along the borehole under constant stress profile. At higher stress, the magnitude of near borehole compressional and shear face velocities are smaller compared with radial velocities (measured perpendicular to the borehole) due to the effect of breakouts and tensile failure at $\theta = 0^{\circ}$ and $\theta = 90^{\circ}$. This can be illustrated by the comparison of the compressional velocities measured parallel and perpendicular to the borehole axis as shown in Figure 6-69. The compressional velocity measured at $\theta = 0^{\circ}$ is higher across the borehole compared with the compressional velocity measured along the borehole where it is affected by borehole failure. Similarly, the compressional velocity measured at $\theta = 90^{\circ}$ is higher across the borehole compared with same velocity measured along the borehole where tensile failure is present. The influence of the stress on velocity can be also observed from the magnitude of shear velocity as a function of location around the borehole. The shear velocities measured at the maximum compressive stress concentration at the borehole (affected by $\approx 3\sigma_H$) are generally larger than shear velocity measured in the direction of high tensile stress concentration (affected by $\approx -\sigma_H$) and shear velocity measured away from the borehole (affected by $\approx \sigma_H$) as illustrated by Figure 6-70. Similar observations were obtained for other tested Berea samples. The velocity observations for Berea are similar to the results obtained by Winkler et al., (1998) presented earlier in Chapter 2 in Figures 2-3 and 2-4.

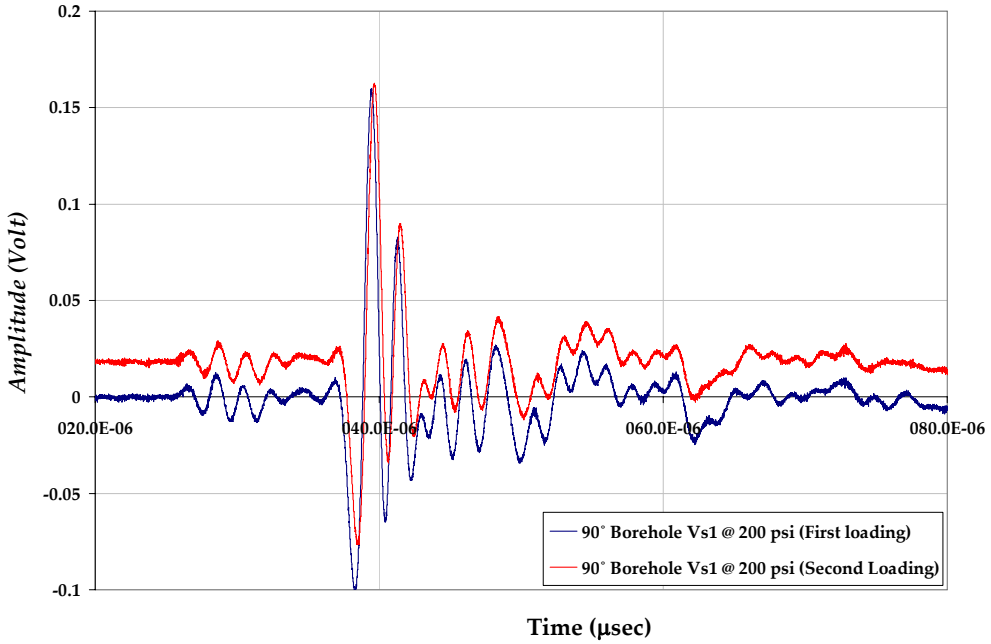

Figure 6-66: Berea shear velocity waveforms (Vs1) during load cycling.

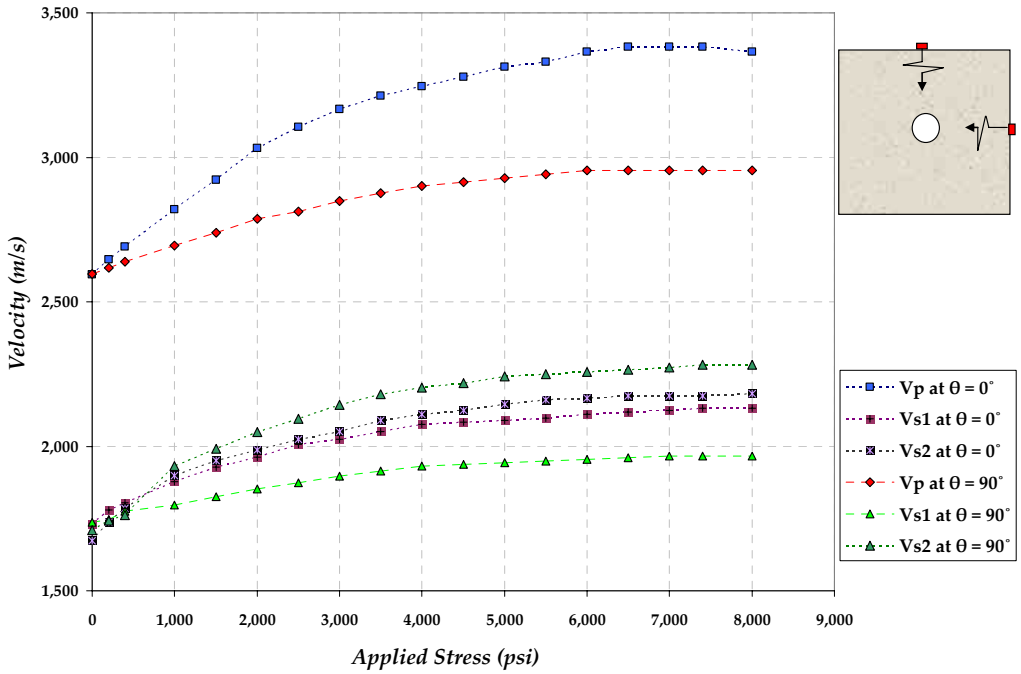

Figure 6-67: Berea borehole radial compressional and shear velocities measured perpendicular to the borehole axis where the polarization of V_{s2} is parallel to the loading direction.

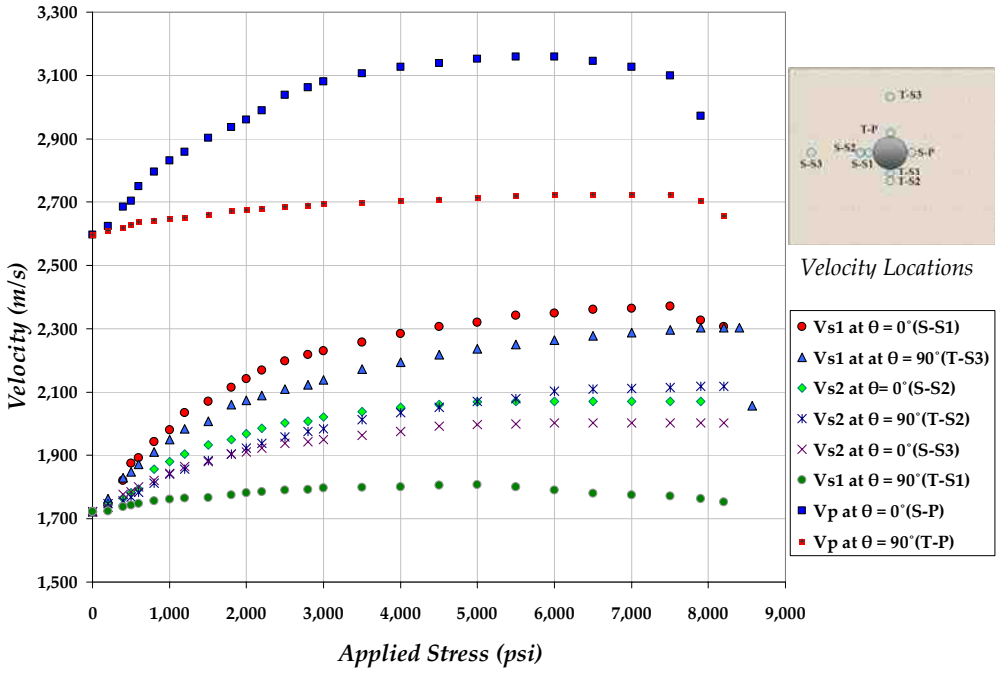

Figure 6-68: Berea measured face compressional and shear velocities (parallel to the borehole axis). The measurements included near and far shear velocity acquisitions (check Figure 4-7 for shear velocities polarization).

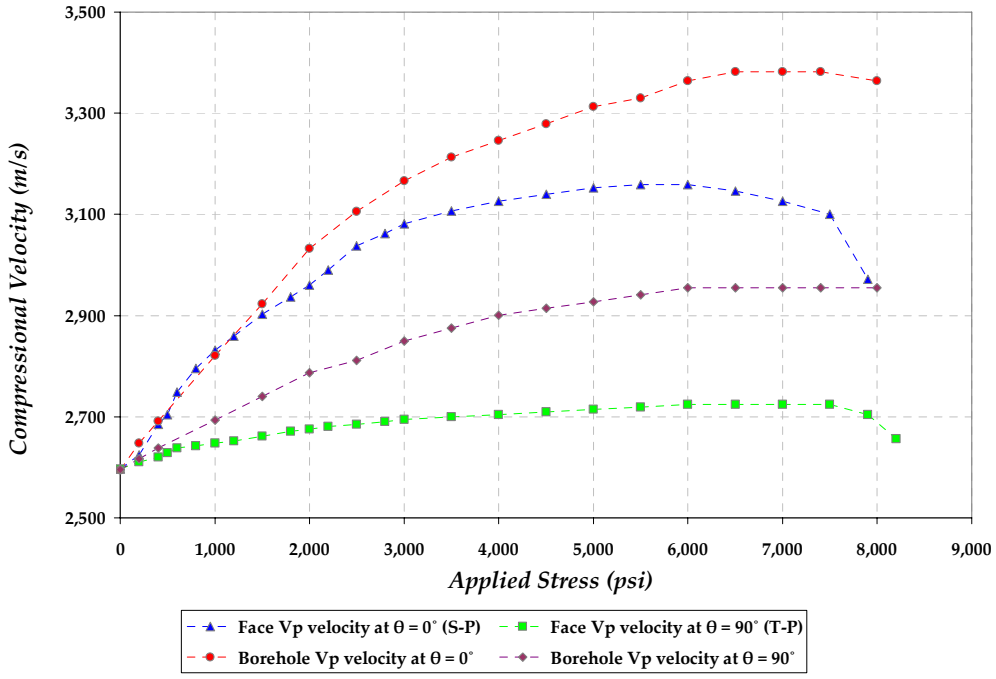

Figure 6-69: Compressional radial and face velocities comparison at the two principal orientations acquired using the two velocity configurations.

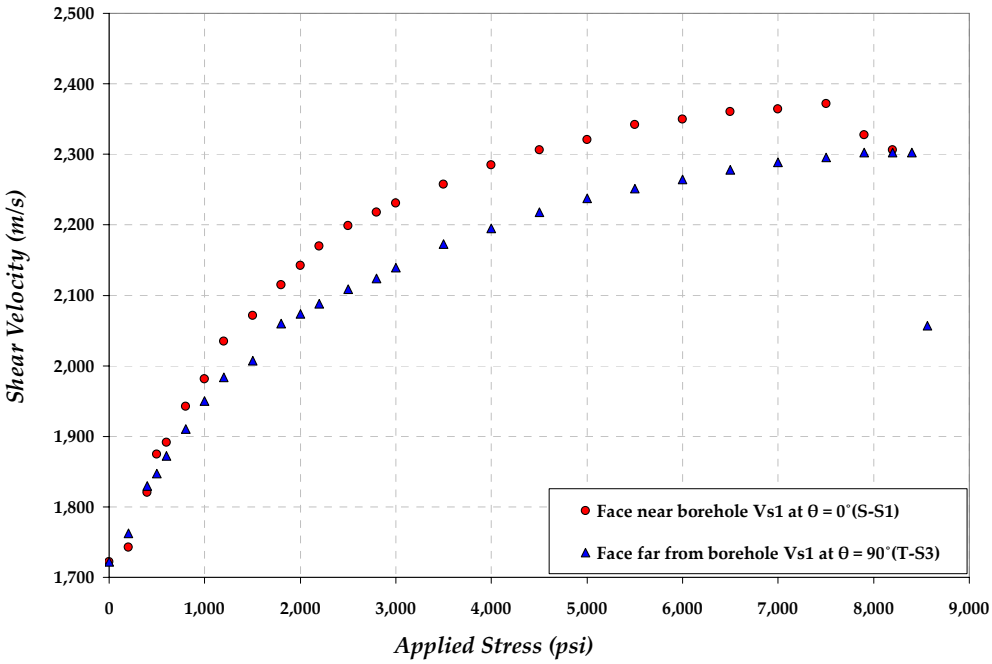

Figure 6-70: Comparison of the near borehole face shear velocity at θ = 0° (affected by $3\sigma_H$) with far shear velocity at θ = 90° (affected by σ_H). Both shear velocities polarization is parallel to the loading direction.

The measured face velocities at θ = 0° and θ = 90° right at the borehole were used to compute dynamic Young's moduli and corresponding dynamic strains using borehole stresses calculated from strain gages and theoretical stresses by Kirsch. Figures 6-71 and 6-72 show the comparison of measured quasi-static strains from strain gages and computed dynamic borehole strains from velocities based on two stress scenarios; computed borehole stress from strain gages and Kirsch (1898). The quasi-static borehole strains are comparable with borehole dynamic strains when using the magnitude of the computed induced borehole stresses from strain measurements. It can be noticed from Figure 6-71 that at a boundary applied stress of about 2,500 psi, which corresponds to borehole induced compressive stress of 10,500 psi, the quasi-static and dynamic strain measurements are

comparable. This was also observed from the Berea cylindrical test presented earlier (Tables 6-2 and 6-3) where the Young's modulus from quasi-static and dynamic measurements are comparable after a stress magnitude of 9,000 psi. When borehole dynamic strain is computed using Kirsch's solution, the quasi-static and dynamic measurements vary suggesting the importance of stress calibration around the borehole.

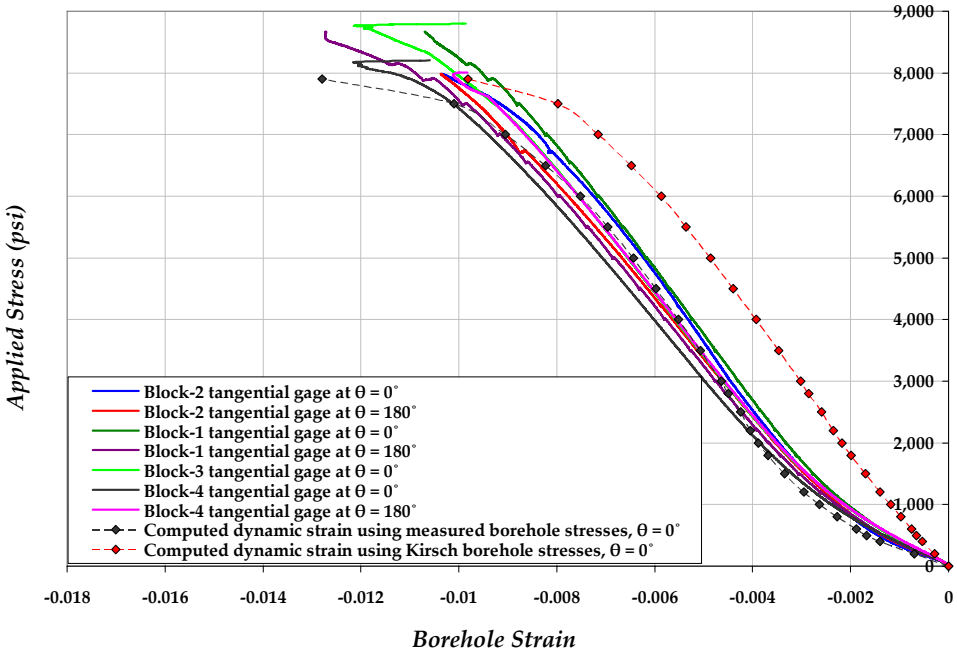

Figure 6-71: Comparison of the measured borehole strain and computed dynamic strains from borehole face velocities at θ= 0° for the Berea samples. Notice that the stresses used to compute the dynamic strain are based on stress estimated from strain measurements and from Kirsch.

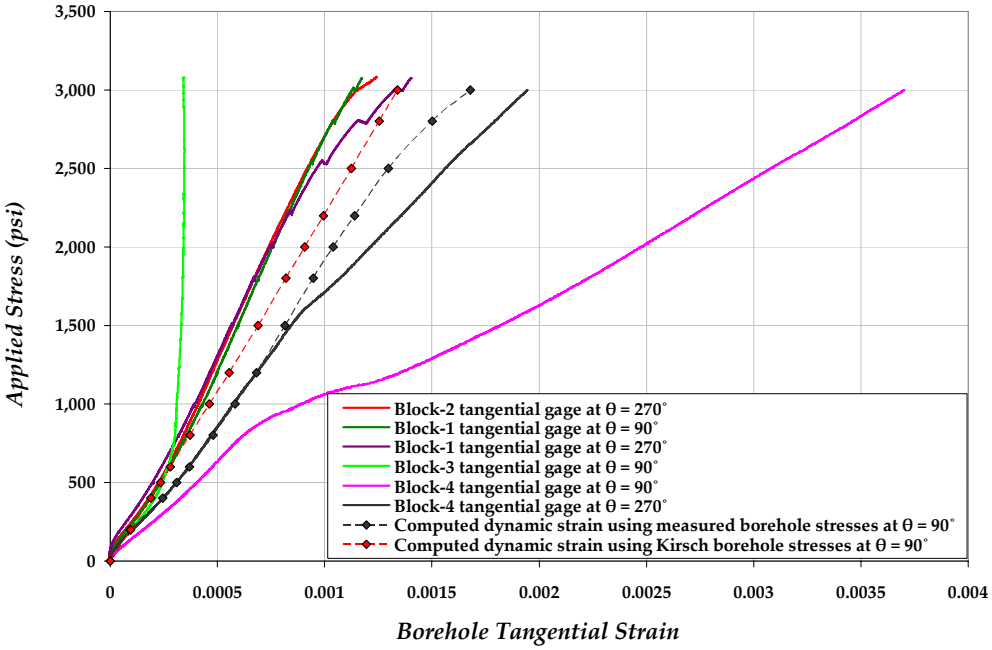

Figure 6-72: Comparison of measured borehole strain from strain gages and computed dynamic borehole strain from near borehole face velocities at θ = 90° for the Berea samples. Notice that the stresses used to compute the dynamic strains are based on stress estimated from strain measurements and from Kirsch.

6.3.3 Chalk Dynamic Measurements

Velocity measurements around the borehole of chalk block samples resulted in small variations as a function of stress around the borehole. Radial borehole velocities measured perpendicular to the borehole axis are shown in Figures 6-73 and 6-74 for the compressional and shear velocities, respectively. The velocities slightly increased at early loading before they decreased at high applied stress. Constant velocities also were observed during the measurements irrespective of applied stress. Similar observations were obtained for the face velocities acquired along the borehole as shown in Figures 6-75 and 6-76.

The decrease in velocity in these samples at early loading caused by the dilatancy occurs before shear failure while at higher loading the effect of pore collapse dominates the decrease in velocities. The velocity increase is caused by the elastic deformation and consolidation of the samples. The case of chalk samples indicated that the measured velocities are irrespective to the applied stress and most likely controlled by the characteristic of the material and its properties. The comparison of the measured quasi-static and computed dynamic borehole strains at $\theta = 0^{\circ}$ and $\theta = 90^{\circ}$ from strain gages and velocities are shown in Figures 6-77 and 6-78.

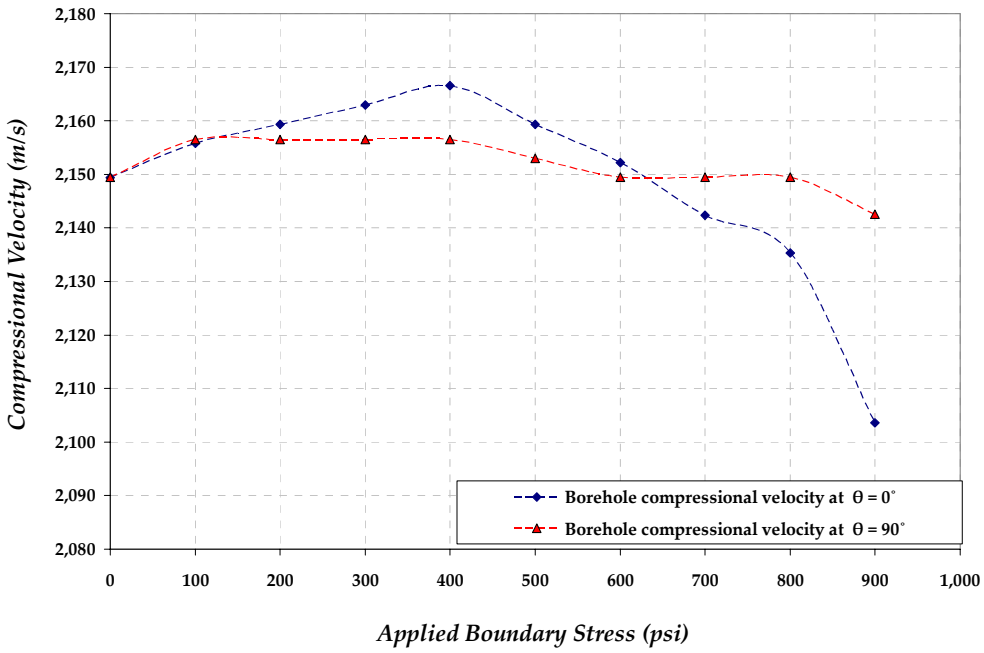

Figure 6-73: Borehole compressional velocities measured perpendicular to the borehole axis of the chalk samples.

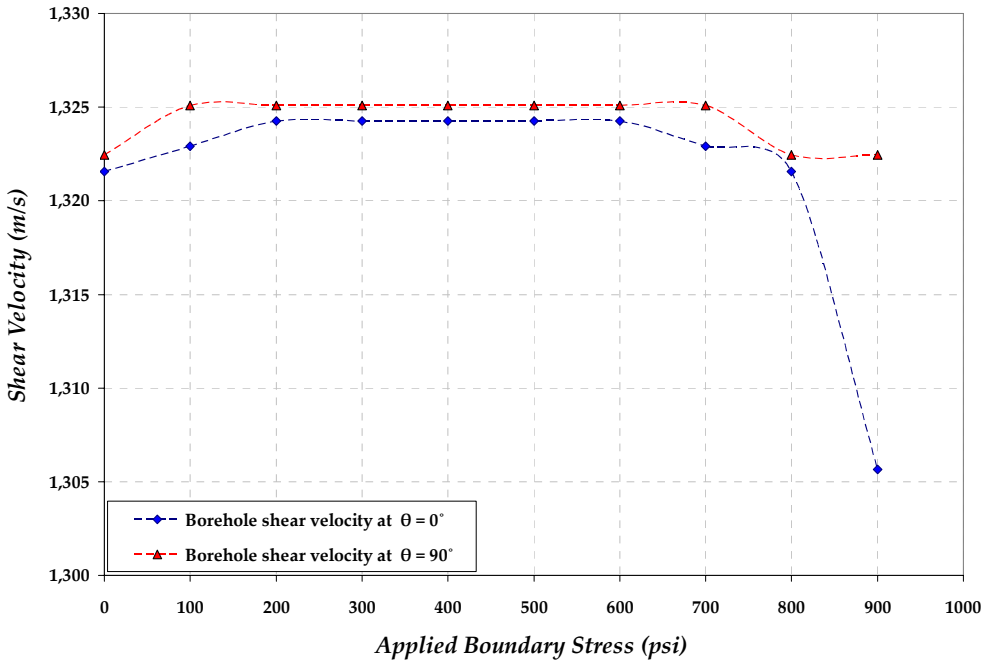

Figure 6-74: Borehole shear velocities measured perpendicular to the borehole axis for the chalk samples where the shear velocities polarization is parallel to the loading direction.

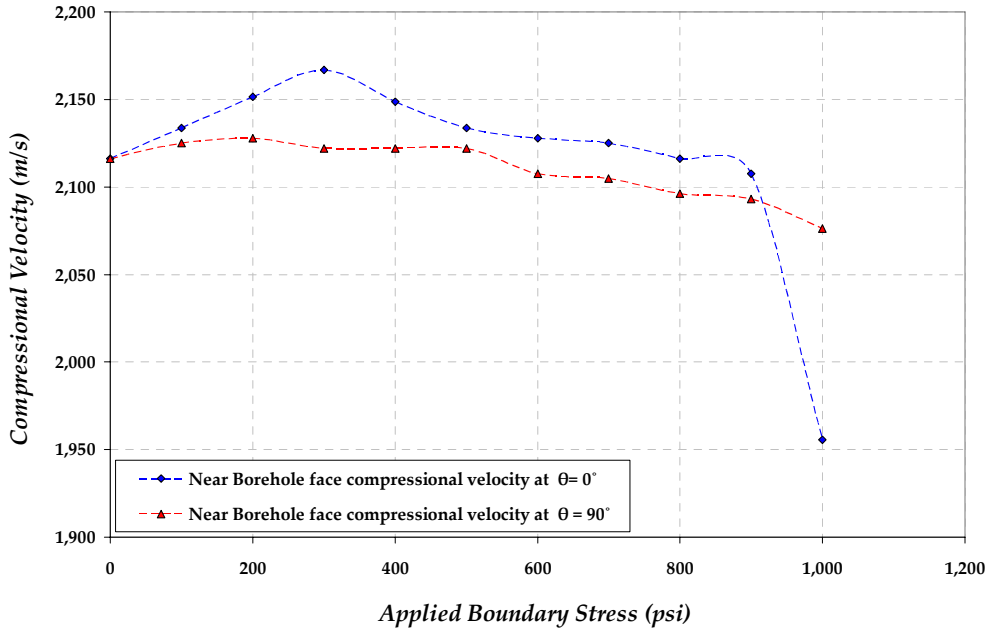

Figure 6-75: Measured near borehole face compressional velocities (parallel to the borehole axis) of the chalk samples.

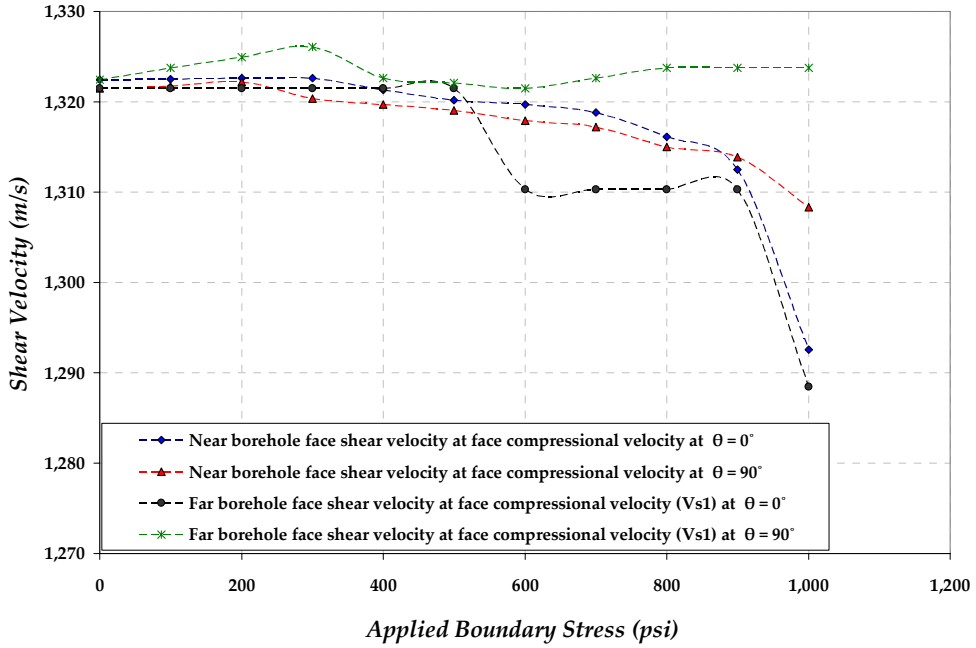

Figure 6-76: Measured face (parallel to the borehole axis) near and far borehole shear velocities for chalk. The polarization of the shear velocity is parallel to the loading direction at θ= 0°, and perpendicular to the loading direction at θ= 90°.

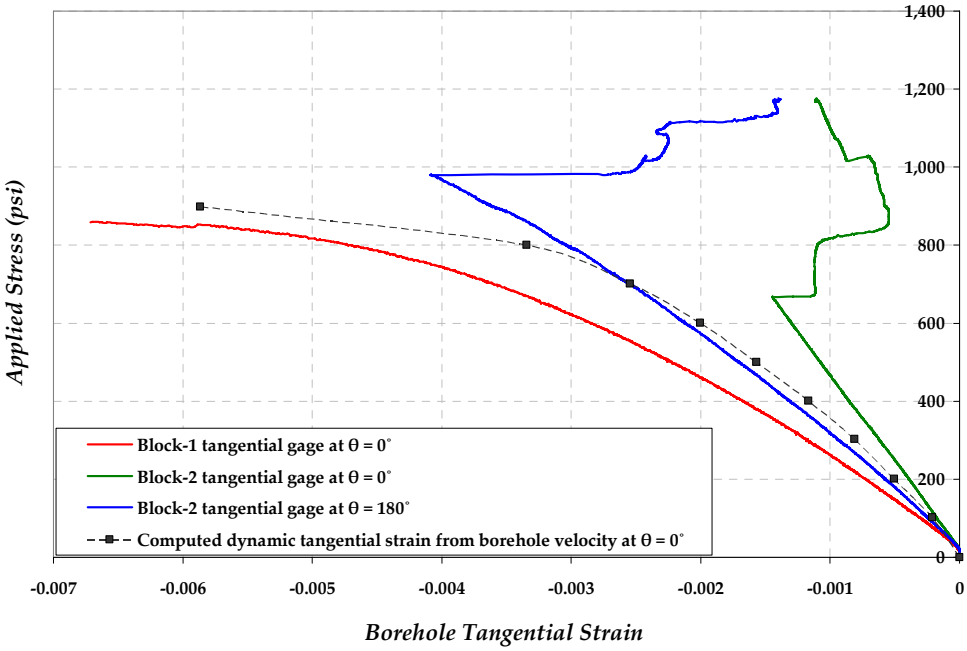

Figure 6-77: Comparison of measured borehole strain from strain gages and computed borehole dynamic strain form velocities based on computed stress from strain gages at θ= 0° for the chalk samples.

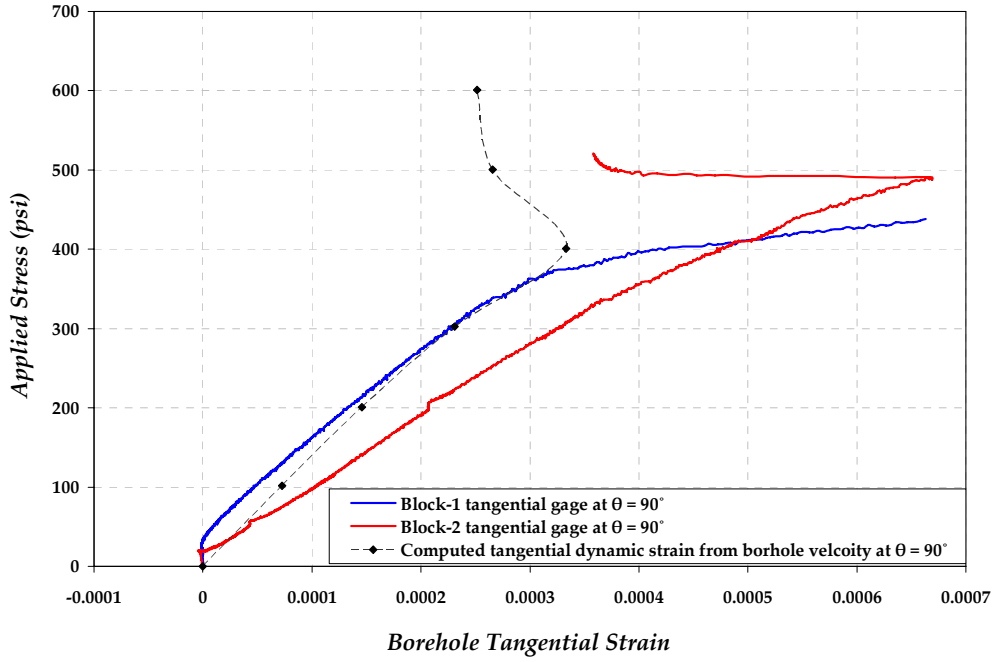

Figure 6-78: Comparison of measured borehole strain from strain gages and computed borehole dynamic strain form velocities based on computed stress from strain gages at θ= 90° for the chalk samples.

6.3.4 White Limestone Dynamic Measurements

Figures 6-79 and 6-80 show the compressional and shear velocities acquired perpendicular to the borehole axis. The compressional and shear velocities measured in the direction of the borehole including far and near borehole shear velocities are shown in Figures 6-81 and 6-82. The change in velocities as function of stress is observed to be less than the case of Berea samples, and some velocities follow the trend of chalk measurements. The comparison of the measured and computed borehole strains at θ = 0° and θ = 90° from strain gages and velocities for block 1 are shown in Figures 6-83 and 6-84. The quasi-static measured and computed dynamic strains at the maximum induced compressive and tensile stress directions (θ = 0°, θ = 90°) showed good comparison.

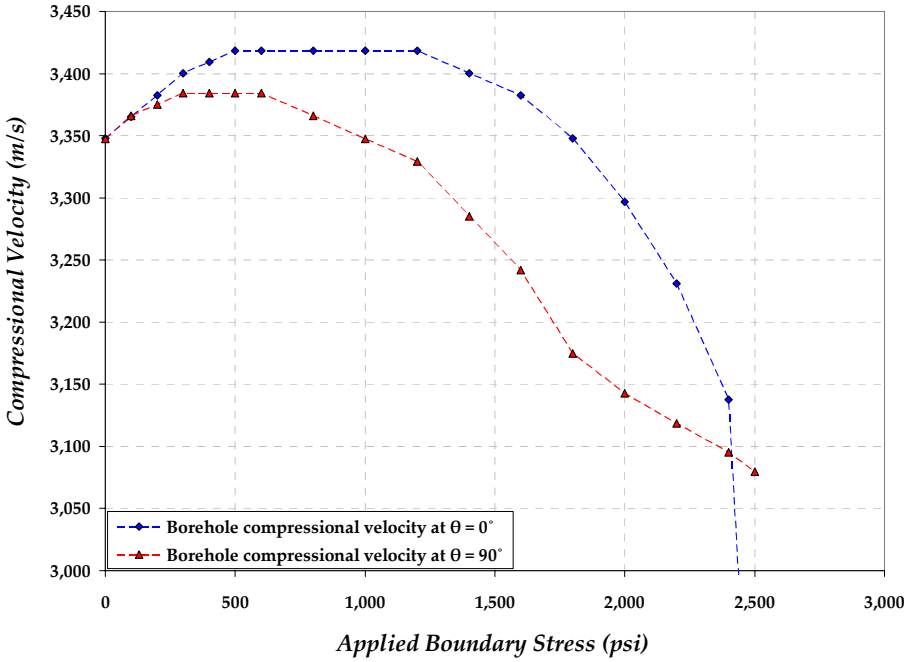

Figure 6-79: Borehole radial compressional velocities measured perpendicular to the borehole axis of the white limestone samples.

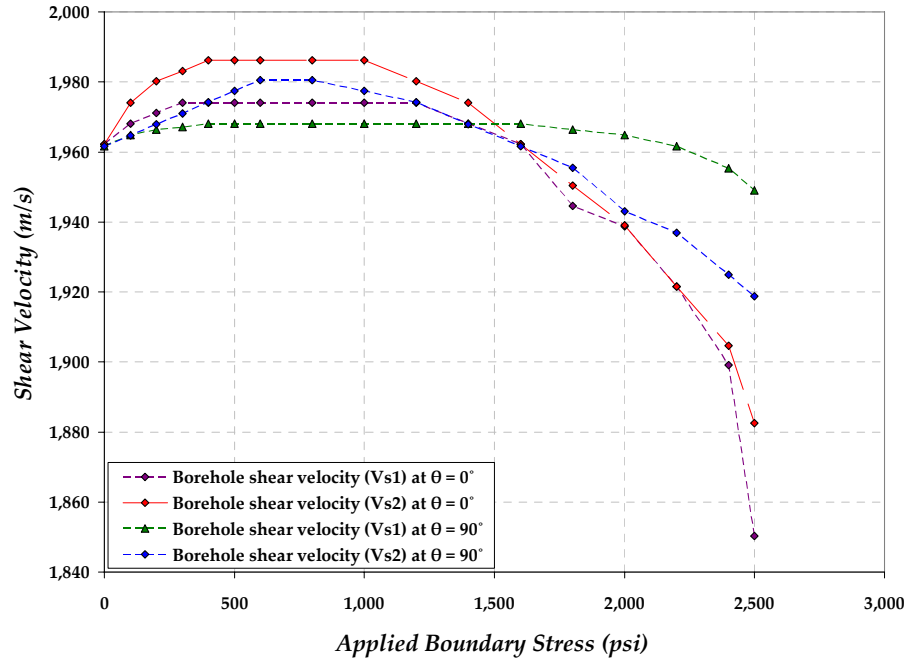

Figure 6-80: Borehole radial shear velocities measured perpendicular to the borehole axis of the white limestone samples.

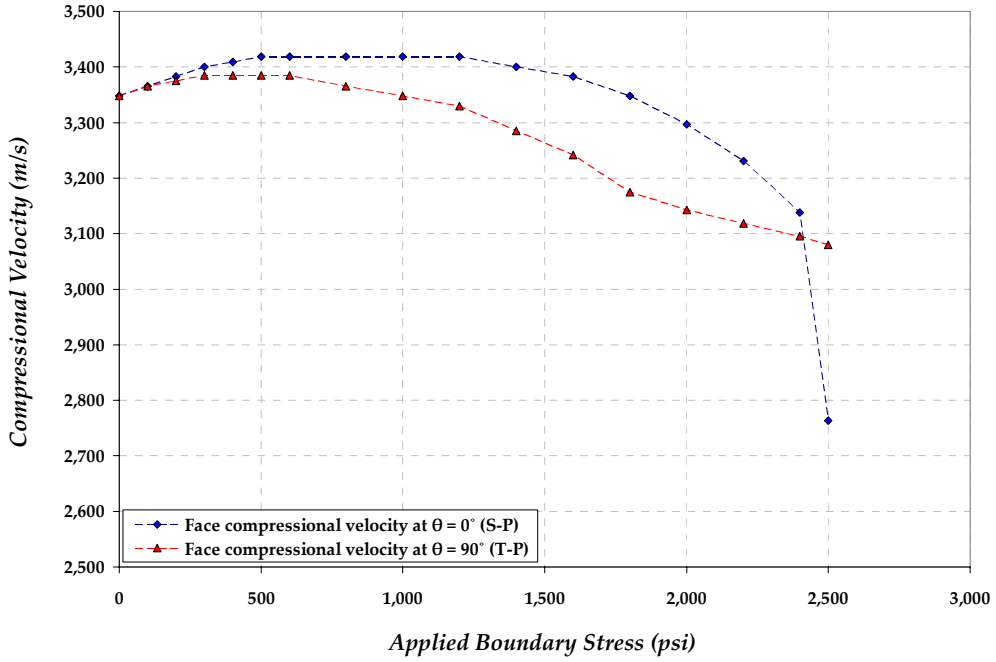

Figure 6-81: Measured near borehole face compressional velocities (parallel to the borehole axis) of the white limestone samples.

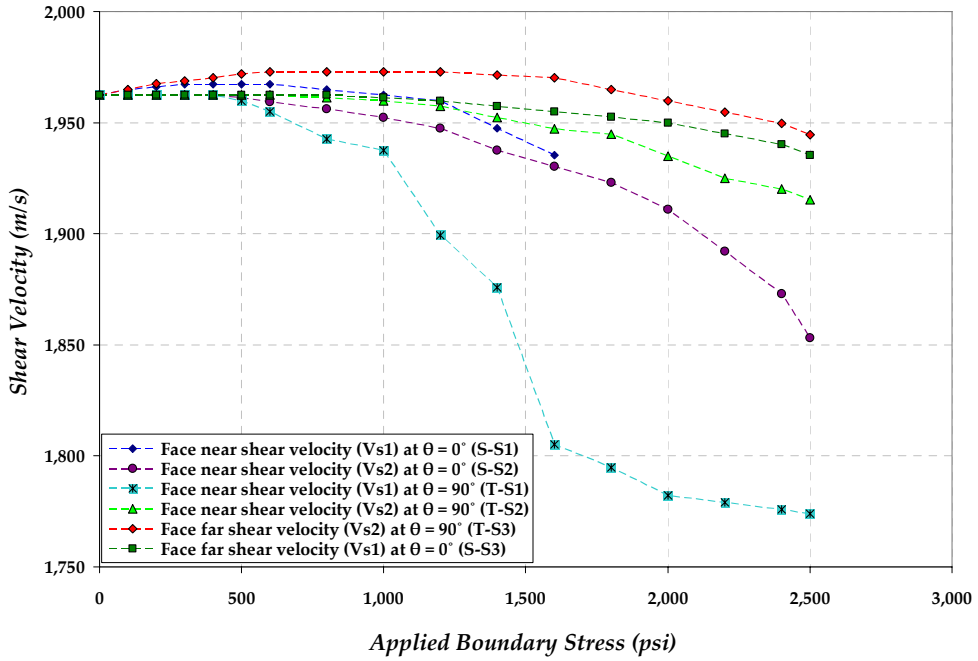

Figure 6-82: Measured face near and far borehole shear velocities (parallel to the borehole axis) of the white limestone samples.

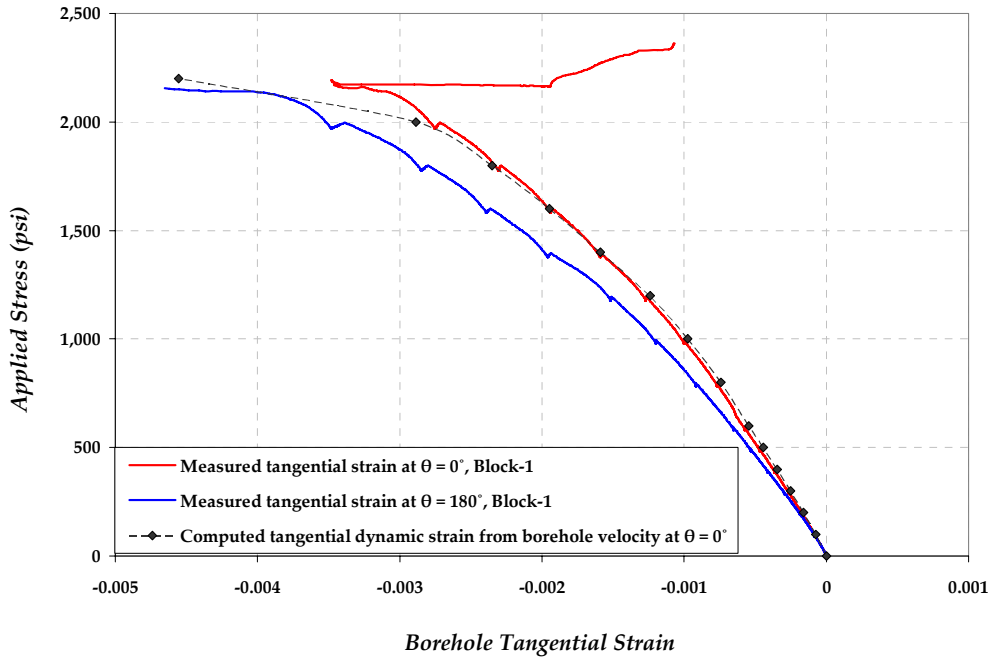

Figure 6-83: Comparison of measured borehole strain from strain gages and computed borehole dynamic strain form velocities based on computed stress from strain gages at θ= 0° for white limestone block 1.

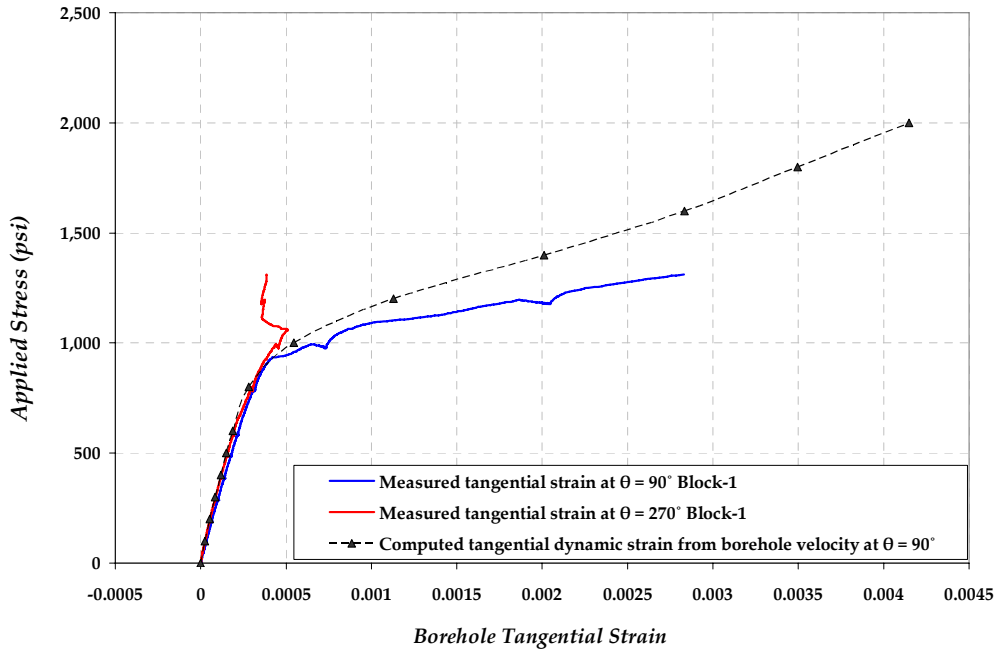

Figure 6-84: Comparison of measured borehole strain from strain gages and computed borehole dynamic strain form velocities based on computed stress from strain gages at θ= 90° for white limestone block 1.

6.3.5 Pierre Shale Dynamic Measurements

In order to minimize the time required to glue the piezoelectric crystals on the block, the crystals were clamped at a distance of 1.5 diameters from the borehole. As a result, only compressional velocity is measured at the two principal directions parallel to the borehole. Figure 6-85 displays the magnitude of the compressional velocity measurements at the two principal directions as a function of applied boundary stress.

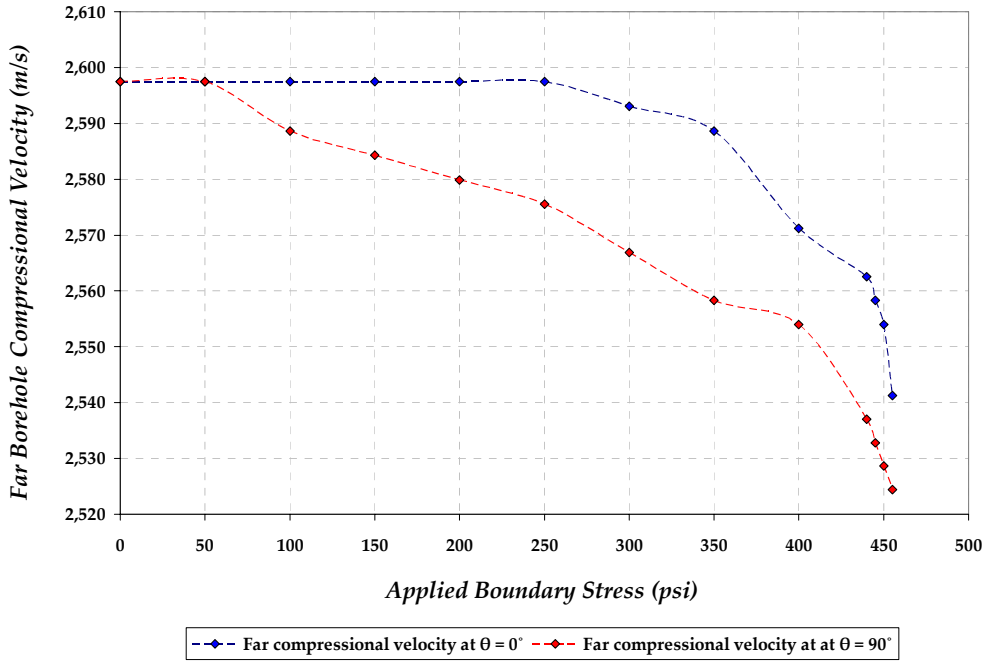

Figure 6-85: Far borehole compressional velocity at the two principal directions for Pierre shale block sample.

6.3.6 Measurements Summary

As a summary of the borehole quasi-static and dynamic measurements, Figure 6-86 shows measured borehole strain at $\theta = 0^{\circ}$ as a function of computed borehole compressive stress for Berea sandstone, chalk, and white limestone plotted to a computed stress at the borehole of 15,000 psi. It can be observed that stress magnitude measured at the wellbore wall varies considerably depending on the type of rock being tested, and at any borehole stress magnitude each material behaved differently, suggesting that there is no such a universal relationship that can estimate the stress from velocity without calibrating velocity measurements for the type of rock material. The comparison of the static and dynamic stress-strain data (Young's modulus) measured from borehole strain gages and computed from velocities indicated that velocity has to be calibrated to take into account material properties and their stress dependence when stress is estimated from velocity around the borehole.

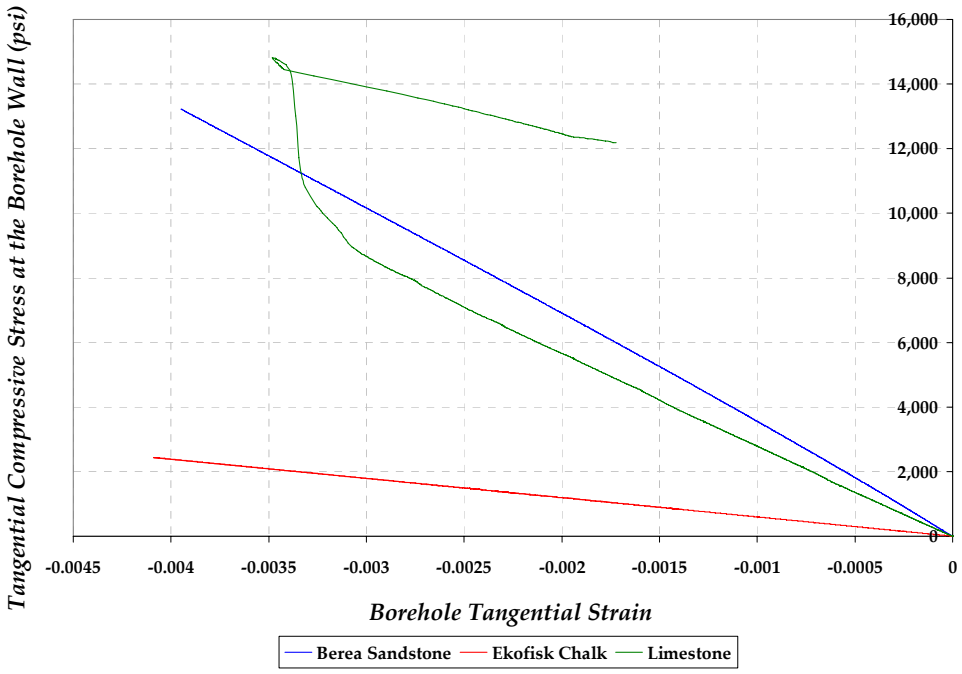

Figure 6-86: Summary of the measured borehole strain as a function of the induced compressive stress at $\theta = 0^{\circ}$ for the three tested rock types (plotted to borehole stress of 15,000 psi).

6.3.7 Low Frequency Dynamic Measurements

The frequency effect on measured velocities was examined for the tested rock samples. Commercial logging tools operate using frequencies in the band from 80 Hz to 8 kHz (Kane, 2001) while the measured velocities presented in this work were acquired using ultrasonic measurements with a 600 kHz source of frequency. The comparison of the measured compressional and shear velocity waveforms using two different transducer frequencies (600 kHz and 100 kHz) are shown in Figures 6-87 through 6-90 for Berea and white limestone samples, where a pulse generator with a square wave pulse and amplitude of 100 volts is used.

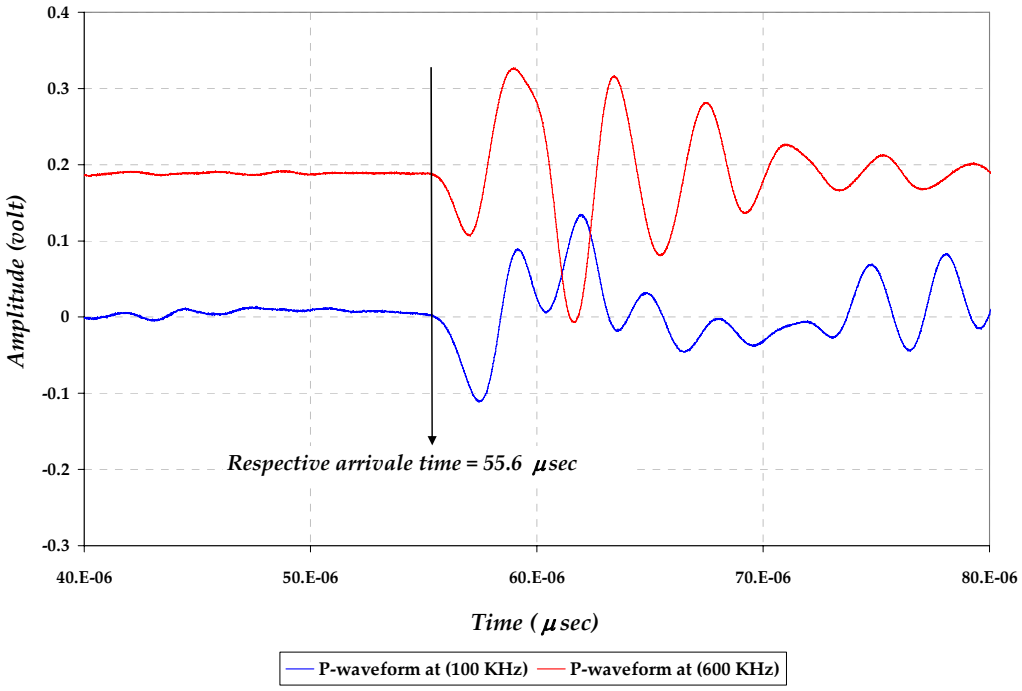

Figure 6-87: Compressional waveforms comparison for low and high frequency measurements for Berea sandstone block samples.

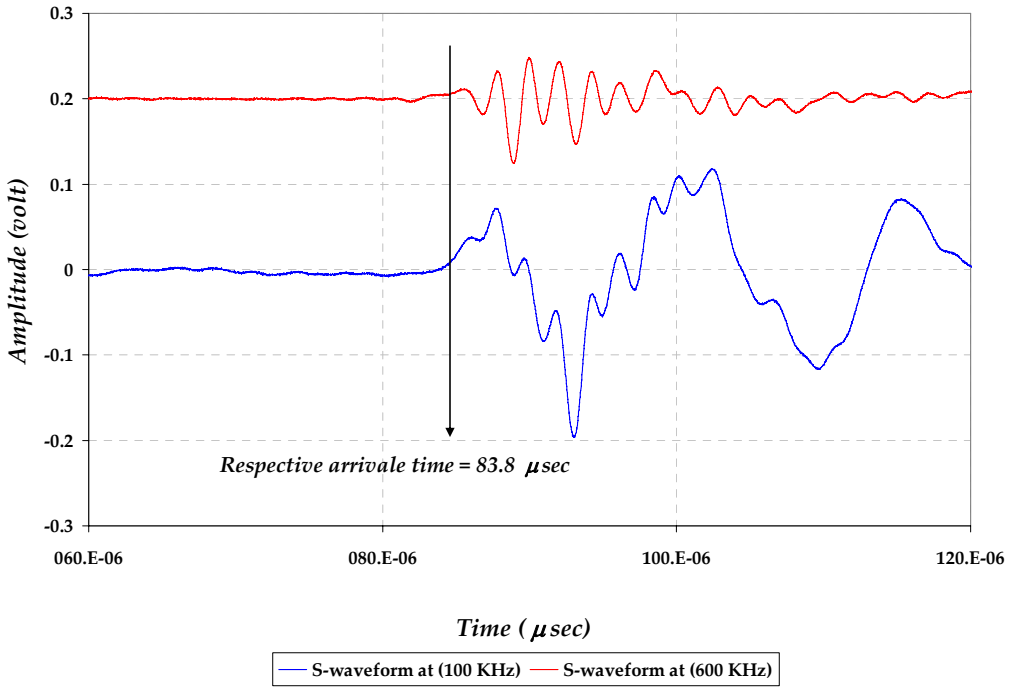

Figure 6-88: Shear waveforms comparison for high frequency measurements for Berea sandstone block samples.

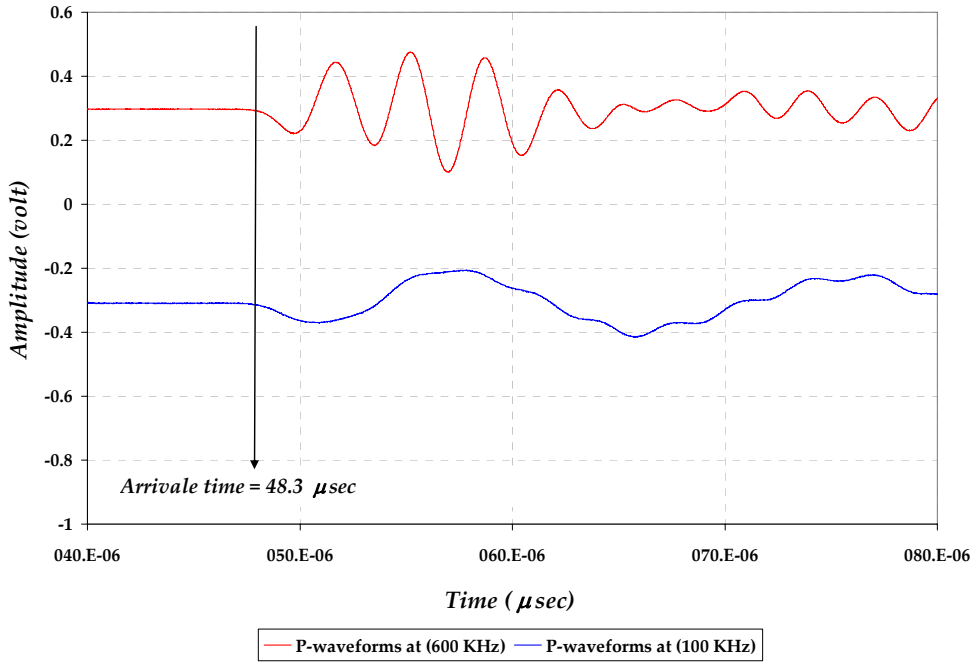

Figure 6-89: Compressional waveforms comparison for low and high frequency measurements for white limestone block samples.

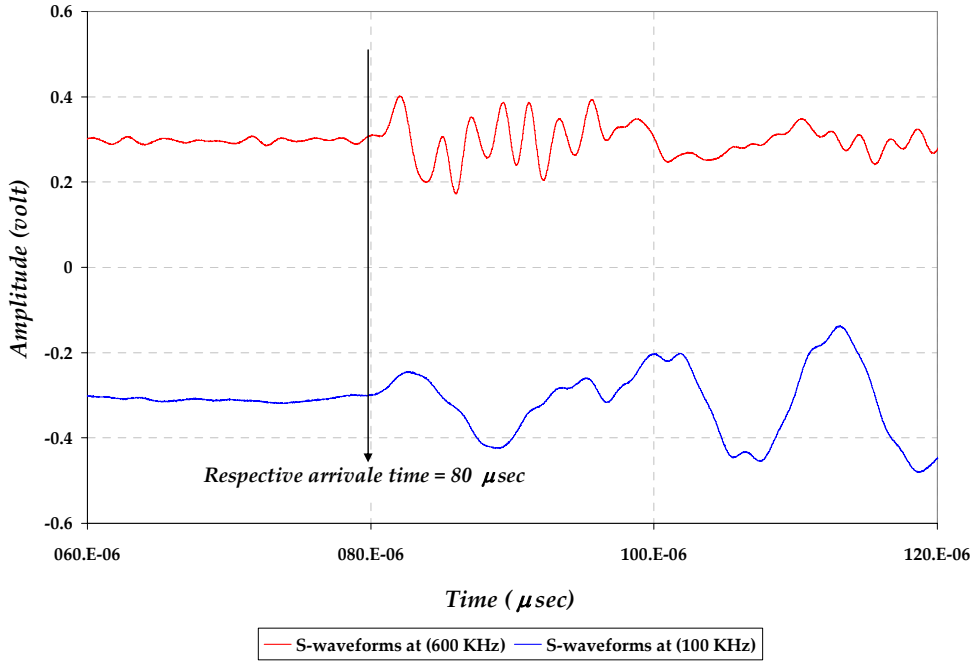

Figure 6-90: Shear waveforms comparison for low and high frequency measurements for white limestone block samples.

6.4 Stress Estimation using Non-linear Model for Berea Sandstone

The measurement of shear velocities at a distance from the borehole were used to compute the magnitude of applied stresses using the non-linear model given earlier of Sinha and Winkler (1996) in Equation (2.1). The published values of the non-linear parameters C_{111}, C_{112} and C_{123} of Berea sandstone were used to compute the constant C_{456} and the stresses from shear velocity measurements. The shear modulus C_{66} was computed from the density and shear velocity of Berea at zero applied stress. Table 6-11 displays the parameters used to obtain the stresses from measured far borehole shear velocities. The shear velocities measured at a distance from the borehole as a function of applied boundary stress is given in Table 6-12. The computed stresses using the non-linear constants and measured shear velocities are shown and compared with actual applied stresses of Berea samples in Table 6-13. They are also plotted in Figure 6-91. It can be noticed that at early loading (to about 1,000 psi) the computed boundary stress is within the range of actual applied stress during Berea block samples testing. At a higher stress differential, the offset between the computed and measured stresses is getting larger suggesting that the velocity measurements have to be calibrated if used to estimate in-situ stress field.

Bulk density, ϱ_b (Kg/m)	**C_{111} (GPa)**	**C_{112} (GPa)**	**C_{123} (GPa)**	**C_{456} (GPa)**	**C_{66} (GPa)**
2,175	-21,217	-3,044	2,361	920.4	6.54

Table 6-11: Non-linear parameters used to compute the stress from far borehole velocity measurements for Berea sandstones (Kane, 2001).

Stress (psi)	**V_{12}** (m/s)	**V_{13}** (m/s)	**Stress** (psi)	**V_{12}** (m/s)	**V_{13}** (m/s)	**Stress** psi	**V_{12}** (m/s)	**V_{13}** (m/s)
0	1,722	1,722	1,800	2,060	1,903	5,000	2,238	1,997
200	1,763	1,736	2,000	2,074	1,911	5,500	2,251	2,000
400	1,829	1,777	2,200	2,088	1,923	6,000	2,265	2,002
500	1,847	1,786	2,500	2,109	1,938	6,500	2,278	2,002
600	1,873	1,801	2,800	2,124	1,943	7,000	2,289	2,002
800	1,911	1,820	3,000	2,139	1,950	7,500	2,296	2,002
1,000	1,950	1,843	3,500	2,173	1,963	7,900	2,303	2,002
1,200	1,984	1,866	4,000	2,195	1,976	8,200	2,303	2,002
1,500	2,008	1,880	4,500	2,218	1,992	8,400	2,303	N/A

Table 6-12: Magnitude of the far borehole shear velocities measured for Berea samples over the entire applied stress range.

Applied Stress (psi)	Estimated Stress (psi)	Applied Stress (psi)	Estimated Stress (psi)	Applied Stress (psi)	Estimated Stress (psi)
0	0	1,800	1,400	4,500	2,149
200	209	2,000	1,470	5,000	2,301
400	423	2,200	1,499	5,500	2,413
500	504	2,500	1,564	6,000	2,527
600	595	2,800	1,663	6,500	2,668
800	760	3,000	1,741	7,000	2,775
1,000	921	3,500	1,960	7,900	2,847
1,200	1,027	4,000	2,064	8,200	2,920

Table 6-13: Tabulated data of the actual and computed stresses over the entire Berea experiment stress range.

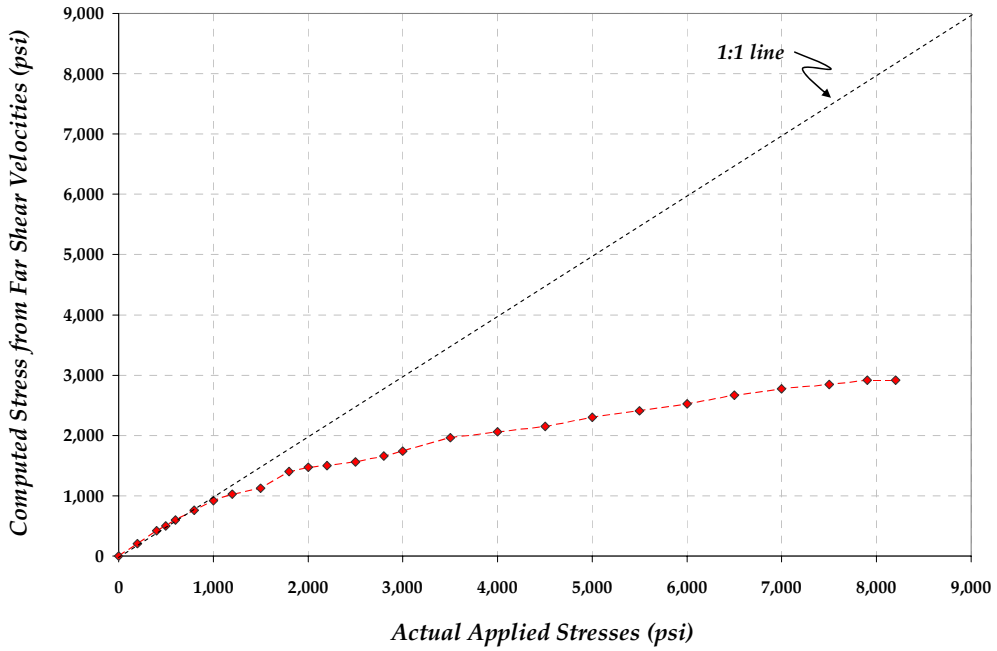

Figure 6-91: Comparison between actual and computed stresses over the entire Berea experiment stress range.

6.5 Comparison of Experimental and Numerical Data

The comparison between experimental measurements and ABAQUS simulation results are presented for Berea and chalk block samples. The comparison is presented in terms of measured and computed strains at $\theta = 0^{\circ}$ from strain gages and ABAQUS for Berea and chalk samples. The comparison is shown in Table 6-14. At higher applied stress where the relation between stress and measured borehole strain is linear, the difference between measured and computed circumferential strains is within 3%.

Berea Rock Type			Chalk Rock Type		
Applied Stress (psi)	Measured $\varepsilon_{\theta\theta}$ ($\theta = 0^{\circ}$)	ABAQUS $\varepsilon_{\theta\theta}$ ($\theta = 0^{\circ}$)	Applied Stress (psi)	Measured $\varepsilon_{\theta\theta}$ ($\theta = 0^{\circ}$)	ABAQUS $\varepsilon_{\theta\theta}$ ($\theta = 0^{\circ}$)
1,000	-20.8E-4	-12.4E-4	200	-7.23E-4	-10.6E-4
3,000	-42.9E-4	-37.1E-4	500	-22.2E-4	-26.5E-4
5,000	-61.6E-4	-61.8E-4	700	-36.1E-4	-37.1E-4

Table 6-14: Comparison of experimental measured and ABAQUS computed borehole strains at $\theta = 0^{\circ}$ for Berea and chalk.

Chapter 7

Conclusions

The major conclusions drawn from this study are given as:

1. The effect of stress-induced anisotropy appears to have significant control on measured stiffness components, elastic moduli and Biot's effective stress coefficients compared with inherent anisotropy effect.

2. The ratio of the uniaxial compressive strength measured in the isotropic and transverse planes for Lyons rock samples can be used to give an insight into initial anisotropy of these rocks.

3. Quasi-static borehole measurements performed on different types of rock showed that stress magnitude measured at the wellbore wall varies considerably depending on the type of rock being tested.

4. The computed stress at the borehole indicated that assumptions of borehole stress concentration factor of 3 based on Kirsch's equations for a uniaxial

stress field may under or over estimate the actual induced compressive stresses at the borehole wall in rocks.

5. Four empirical correlations were reported for each rock type being tested which estimate the maximum induced compressive stresses at the borehole by knowing far field stress which also reflect the variations of the induced stress at the borehole as function of rock type.

6. The stress at which borehole breakouts are observed was 7,500 psi for Berea sandstone, 800 psi for chalk and 2,100 psi for white limestone while the tensile failures occurred at 760 psi for Berea sandstone, 330 psi for chalk, and 950 psi for limestone.

7. The applied boundary stress level at which tensile failure occur at the borehole is observed to be correlated with the measured tensile strength from Brazilian tests of each tested rock material.

8. The applied boundary stress level at which borehole breakouts occur is observed to be correlated with the uniaxial strength of each tested rock material. The applied stress at which borehole breakouts are observed corresponds approximately to 2/3 of the measured rock uniaxial compressive strength.

9. The comparison of the static and dynamic stress-strain data (Young's modulus) measured from borehole strain gages and velocities indicated that velocity has to be calibrated to take into account material properties and their stress dependence when stress is estimated from velocity around the borehole.

References

1. Abousleiman, Y., and Cheng, A. H., (1993): "Anisotropic Poroelasticity with Applications", Report No. RMC-93-19, University of Oklahoma RMI Consortium.

2. Abousleiman, Y., and Chajlani, R., (1994): "The Effect of Stress Variation on Biot's Parameter", proceedings, *1st North American Rock mechanics symposium*, poster session abstract, 1-4.

3. Abousleiman, Y., Cheng, A.H-D., et al., "Poroviscoelastic Analyses of Borehole and Cylinder Problems," *Acta Mechanica*, 119, pp. 199-219, 1996.

4. Abousleiman Y., Cheng, A.H, Cui, L., et al., (1996): "Mandel's Problem revisited", *Geotechnique*, **46**, no. 2, 187-195.

5. Abousleiman, Y. and Cui, L., (1998): "Poroelastic Solutions in Transversely Isotropic Media for Wellbore and cylinder" *International Journal of Solids Structural*, **35**, 4905-4929.

6. Abousleiman, Y. and Cui, L., (2000) "The Theory of Anisotropic Poroelasticity with Applications," Chapter in Modeling and Applications in Geomechanics, J. Wiley & Sons, Ltd.

7. Abousleiman, Y. and Ekbote, S., "Solutions for the Inclined Borehole in a Porothermoelastic Transversely Isotropic Media,'' *Journal of Applied Mechanics*, ASME, **72**,102-114, 2005.

8. Kanj, M. and Abousleiman, Y., "Fully-Coupled Porothermoelastic Analysis of Anisotropic Hollow Cylinders with Applications," *International Journal of Numerical and Analytical Methods in Geomechanics,* **29**, no 2, pp. 103-126, 2005

9. Al-Tahini, A.M., Lauten, W.T., and Khan, M., (2001): "Application of the Kaiser Effect to the Measurements of In-situ Stresses in Hawiyah Field", *The Saudi Aramco Journal of Technology,* winter issue, 64-70.

10. Al-Tahini, A.M., Sondergeld, C.H & Rai, C.S., (2004), "The Effect of Cementation on Static and Dynamic Properties in Jauf and Unayzah Formations at Saudi Arabia", Society of Petroleum Engineering Annual Technical Conference and Exhibition, Houston 26-29.

11. Al-Tahini, A. M., and Abousleiman Y. N., (2005): "Acoustic and Quasi-static Laboratory Measurement and Calibration of the Pore Pressure

Prediction Coefficient in the Poroelastic Theory", Presented at Society of Petroleum Engineering Annual Technical Conference and Exhibition, Dallas.

12. Al-Tahini, A.M., Sondergeld, C.H & Rai, C.S. (2006). The Effect of Cementation on Mechanical Properties of Sandstones, *Society of Petroleum Engineering Reservoir Evaluation and Engineering*, **9**, 308-316.

13. Al-Tahini, A.M., (2003): The Effect of Cementation on the Mechanical Properties for Jauf Reservoir at Saudi Arabia, Master thesis, the University of Oklahoma.

14. Amadei, B., (1983): Rock Anisotropy and the Theory of Stress measurements, C.A. Brebbia and S.A. Orszag, eds., Berlin.

15. Amadei, B., (1996): "Importance of Anisotropy When Estimating and Measuring In-situ Stresses in Rock", *International Journal of Rock Mechanics and Mining Sciences and Geomechanics Abstracts*, **33**, 293-325.

16. Amadei, B., and Stephansson, O., (1997): Rock Stress and its Measurement, Chapman & Hall, London, United Kingdom.

17. Aoki, T, and Tan, C. P., (1993): "Effects of Deformation and Strength Anisotropy on Borehole Failures in Saturated Shales", *International Journal of Rock Mechanics and Mining Sciences and Geomechanics Abstracts*, **30**, 1031-1034.

18. Aydin, A. and Basu, A., (2005): "The use of Brazilian test as a Quantitative Measure of Rock Weathering", *Rock Mechanics and Rock Engineering*.

19. Boresi, A.P., and Chong, K.P., (1987): Elasticity in Engineering Mechanics, Elsevier.

20. Biot, M.A., (1941): "General Theory of Three-Dimensional Consolidation", *Journal of Applied Physics*, **12**, 155-164.

21. Biot, M. A., (1955): "Theory of Elasticity and Consolidation for a Porous Anisotropic Solid: *Journal of Applied Physics*, **26**, 155-164.

22. Biot, M.A., (1956): "General Solutions of the Equations of Elasticity and Consolidation for a Porous Material", *Journal of Applied Mechanics Transactions ASME*, **78**, 91-96, 1956.

23. Biot, M., (1956): ”Theory of Propagation of Elastic Wave in a Fluid-Saturated Porous Solid. I. low frequency range” *Journal of the Acoustic Society of America,* **28**.

24. Biot, M. A., and Willis, D. G., (1957): “The Elastic Coefficients of the Theory of Consolidation” *Journal of Applied Mechanics*, **24**, 594-601.

25. Brown, E.T. and Hoek, E, (1978): “Trends in Relationships between Measured In-situ Stresses and Depth”, *International Journal of Rock Mechanics and Mining Sciences and Geomechanics Abstracts*, **15**, no.4, 211-215.

26. Carroll, M., (1979): “An Effective Stress Law for Anisotropic Elastic Deformation”, *Journal of Geophysical Research*, **84**. 7510-7512.

27. Cheng, A. H., (1997): “Material Coefficient of Anisotropic Poroelasticity”, *International Journal of Rock Mechanics and Mining Sciences and Geomechanics Abstracts*, **34**, 199-205.

28. Cui, L., Cheng, H., and Kaliakin, V., (1996): ”Finite Element Analysis of Anisotropic Poroelasticity: a Generalized Mandel’s Problem and Inclined Borehole Problem”, *International Journal for Numerical Methods in Geomechanics*, **20**, 381-401.

29. Detournay, E. and Cheng, A.H.-D., (1993): Fundamentals of Poroelasticity, Chapter 5 in Comprehensive Rock Engineering: Principles, Practice and Projects, Vol. II, Analysis and Design Method, ed. C. Fairhurst, Pergamon Press, pp. 113-171.

30. Esmersoy, C., Boyd, A., Kane, M. and Denoo, S., (1995): “Fracture and Stress Evaluation Using Dipole-shear Anisotropy Logs”, SPWLA 36th Annual Logging Symposium, June 26-29.

31. Evert, H., (2000): Practical Rock Engineering (2000 ed.).

32. Fairhurst, C., (2003): “Stress Estimation in Rock: a Brief History and Review”, *International Journal of Rock Mechanics and Mining Sciences*, vol. **40**, 957-973.

33. Fjaer, E., Holt, R., Horsrud, P., Raaen, A. and Risnes, R., (1992): Petroleum Related Rock Mechanics. Elsevier, Amsterdam, Netherlands.

34. Gidley, J.L., Holditch, S.A., Nierode, D.E. and Veatch, R.W., (1989): Recent Advances in Hydraulic Fracturing, Society of Petroleum Engineers, Richardson, TX.

35. Haimson, B. and Fairhurst, C., (1969): "In-situ Stress Determination at Great Depth by Means of Hydraulic Fracturing", Symposium on Rock Mechanics, Chapter 28, 559-584.

36. Hoek, E., (2007): Practical Rock Engineering, course notes.

37. Herget, G., (1988): Stresses in rock, A. A. Balkema, Rotterdam, Netherlands.

38. Hubbert, M.K. and Willis, D.G., (1957): "Mechanics of Hydraulic Fracturing" *Petroleum Transactions AIME*, **210**, 153-168.

39. Hudson, J.A., (2003): "Strategy and Tactics for Rock Stress Estimation", Rock stress, Sugawara, Obara & Sato (eds).

40. Hudson, J. A., Cornet, F. H. and Christiansson, R., (2003): "ISRM Suggested Methods for Rock Stress Estimation; part 1, strategy for rock stress estimation". *International Journal of Rock Mechanics and Mining Sciences*, vol. **40**, 7-8, 991-998.

41. Jakob, B., Johnson, D., Plona, T., Sinha, B., Valero, H. and Winkler, K., (2006): "Borehole Acoustic Waves", *oilfield Review,* spring 2006.

42. Jaeger, J. C., and Cook, N. G., Fundamentals of Rock Mechanics, pages 236-239. Chapman and Hall, Ltd, 1969.

43. Jones, L. E., and Wang, H. F., (1981): "Ultrasonic Velocities in Cretaceous Shales from the Williston Basin", *Geophysics*, **46**, 288-297.

44. Kaw A.K., Mechanics of Composite Materials 2ND Edition.

45. Kane, M.R., (2001): Acoustic Rock Stress Estimation, Master Thesis, Pennsylvania State University.

46. King, M. S., (1969): "Static and Dynamic Elastic Moduli of Rocks under Pressure", Rock Mechanics-Theory and Practice Proc., 11th U.S., Somerton (eds), 329-351.

47. Kirsch, G., (1898): "Die Theorie der Elastiziät und die Bedürfnisse der Festigkeitslehre", Zcitschrift des Vereines Deutscher Ingenieure , **42**, 797.

48. Ljunggren, C., Chang, Y., Janson, T., and Christiansson, R., (2003): "An Overview of Rock Stress Measurement Methods", *International Journal of Rock Mechanics and Mining Sciences*, **40**, 7-8, 975-989.

49. Lo, T., Coyner, K. B., and Toksoz, M. N., (1986): "Experimental Determination of Elastic Anisotropy of Berea Sandstone, Chicopee Shale, and Chelmsford Granite", *Geophysics*, **51**, 64-171.

50. Lockner, D. A., and Beeler, N. M., (2003): "Stress-induced Anisotropic Poroelasticity Response in Sandstone", Presented at American Society of Civil Engineering 16th Engineering Mechanics Conference.

51. Lefrere, G., (2001): Determination of Mechanical Properties of Shales, special report, Rock Mechanics Institute, University of Oklahoma.

52. Lykke, M. and Foged, N., (2003): "Up-scaling and Stress Decency of Permeability for Soft Fractured Chalk", Rock stress, Sugawara, Obara & Sato (eds).

53. Mao, N.H., and Sweeney, J.J., (1986): "Estimation of In-situ Stresses from Ultrasonic Measurements" *SPE Formation Evaluation,* **1**, 5, 532-538.

54. Merrill, R.H. and Peterson, J.R., (1961): Deformation of a Borehole in Rock, U.S. Dep. of the Interior Bureau of Mines.

55. Middleton, G.V., Wilcock, P.R., (1996): Mechanics in the Earth and Environmental Sciences. Cambridge University Press, Australia, pp 496.

56. Mulders, F.M., (2003): "Stress Development and Possible Fault Reactivation in and Around Gas Reservoirs", Rock stress, Sugawara, Obara & Sato (eds).

57. Maher, J. C., (1954): "Lithofacies and Suggested Depositional Environment of Lyons Sandstone and Lykins Formation in Southeastern Colorado: *Bulletin of the American Association of Petroleum Geologists*, **38**, 2233-2239.

58. Nur, A., and Simmons, G., (1969): "Stress-induced Velocity Anisotropy in Rock: an Experimental Study", *Journal of Geophysical Research*, **74**, 6667-6674.

59. Plona, T. J., and Cook J. M., (1995): "Effects of Stress Cycles on Static and Dynamic Young's Moduli in Castegate Sandstone", Rock Mechanics, Daemen and Schultz (eds.), 155-160.

60. Plona, T.J., Winkler, K., D'angelo, R., Sinha, B., Papanastasiou, P., and Cook, J. M., (1997): "Acoustic Detection of Stress-Induced Effects around a Borehole", *International Journal of Rock Mechanics and Mining Sciences & Geomechanics Abstracts*, **34**, 3-4, 420.

61. Plona, T.P, Sinha, B.K., Kane, M.R., Winkler, K.W., and Frignet, B., (1999): "Stress-Induced Dipole Anisotropy: Theory, Experimental and Field Data", SPWLA 40th Annual Logging Symposium.

62. Plona, T.J., Winkler, K., Angelo, R.D., Sinha, B., Papanastasiou and Cook, J.M., (1997): "Acoustic Detection of Stress-induced Effects Around A borehole". *International Journal of Rock Mechanics and Mining Sciences*, vol. 34:3-4, paper No. 290.

63. Podio, A. L., Gregory, A. R., and Gray, K. E., (1968): "Dynamic Properties of Dry and Water-saturated Green River Shale under Stress", *Society of Petroleum Engineers Journal*, **8**, 389-404.

64. Rai, C.S. and Hanson, K.E., (1987): "Shear-wave Birefringence; A Laboratory Study", *Geophysics*, **52**, 424.

65. Rice, J. R., and Cleary, M. P., (1976): "Some Basic Stress-Diffusion Solutions for Fluid Saturated Elastic Porous Media with Compressible Constituents", Reviews of Geophysics and Space Physics, **14**, 227-241.

66. Rasolofosan, P. and Zinszner, B., (2002): "Complete Poroelastic Characterization of Arbitrarily Anisotropic Rocks using Wave Propagation-laboratory Experiments Versus Theoretical Predictions", Poromechanics II, Auriault et al., eds. (2002).

67. Russell, J.E. and Hoskins, E.R., (1973): "Residual Stresses in Rock", Proceedings - Symposium on Rock Mechanics, **14**, 1-24.

68. Prioil, R., and Lebrat, T., (2004):" Calibration of Velocity-Stress Relationships under Hydrostatic Stress for Their Use Under Non-Hydrostatic Stress" SEG 74th Annual Meeting, Denver, Colorado.

69. Scheidegger, A.E., (1962):"Stress in Earth's Crust as Determined from Hydraulic Fracturing Data" *Geologie und Bauuesen*, **27**, 45.

70. Sinha. B.K. and Kostek, S., (1996): "Stress-induced Azimuthal Anisotropy in Borehole Flexural Waves". *Geophysic*s, **61**, 6, 1899-1907.

71. Sinha, B.K., Plona, T.J, Winkler, K.W., and D'angelo, R.M., (1995):" Stress-induced Dipole Anisotropy in a Dry Berea Sandstone", SEG Annual Meeting Expanded Technical Program Abstracts with Biographies, **65**, 22-25.

72. Sinha, B., Bratton, T., Cryer, J., and Nieting, S., (2005):"Near-Wellbore Alteration and Formation Stress Parameters Using Borehole Sonic Data" Presented at Society of Petroleum Engineering Annual Technical

Conference and Exhibition, Dallas.

73. Sinha, B., Vissapragada, B., Renlie, L., and Skomedal, S., (2006):"Horizontal Stress Magnitude Estimation Using the Three Shear Moduli –A Norwegian Case Study" Presented at Society of Petroleum Engineering Annual Technical Conference and Exhibition, San Antonio.

74. Sondergeld, C.H. and Rai, C.S., (1992): "Laboratory Observations of Shear-wave Propagation in Anisotropic Medium", Geophysics: The Leading Edge of Exploration, 11, 38-43.

75. Scott, G., and Abousleiman Y.N., (2005): "Acoustic Measurements of the Anisotropy of Dynamic Elastic Poromechanics Moduli under Three Stress/Strain Pathways" *Journal of Engineering Mechanics,* September, 937-946.

76. Scott, G. and Abousleiman Y.N., (2002): "An experimental Methods for Measuring Anisotropic Poroelastic Biot's Effective Stress Parameters from Acoustic Wave Propagation" Poromechanics II, Auriault et al., eds. (2002).

77. Scott, T.E., Azeemuddin, M., at al., (1998): "Stress-Induced Variations in Acoustic Velocity in Chalk", *International Journal of Rock Mechanics and Mining Sciences*, **35,** 4-5, paper No. 125.

78. Stanchits, S. A., (2003): "Anisotropic Changes in P-wave Velocity and Attenuation during Deformation and Fluid Infiltration of Granite: Bulletin of the Seismological Society of America, **93**, 803-1822.

79. Schlumberger DSI Dipole Shear Sonic Imager, (2004): Tool Brochure.

80. Tang, X., and Cheng, A., (2004): Quantitative Borehole Acoustic Method, Klaus Helbig and Sven Treitel (eds).

81. Timoshenko S. & Goodier, J., (1951): Theory of Elasticity, second edition, McGraw-hill book, New York, 1951.

82. Terzaghi, K., (1943): Theoretical Soil Mechanics, Wiley, New York, 1943.

83. Thompson, M. and Wills, J., (1991): "A Reformation of the Equation of Anisotropic Poroelasticity" *Trans. of ASEM*, **58.**

84. Tien, Y.M., Kuo, M.C., and Juang, C.H., (2006): " An Experimental Investigation of the Failure Mechanism of Simulated Transversely

Isotropic Rocks", *International Journal of Rock Mechanics and Mining Sciences*,**43**:1163-1181.

85. Ugural, A. C. and Saul K. F., (2003): Advanced Strength and Applied Elasticity, fourth edition, upper Saddle River, New Jersey: Prentice Hall.

86. Vernik, L and Nur, A., (1992): "Ultrasonic Velocity and Anisotropy of Hydrocarbon Source Rock" *Journal of Geophysics.*, **57**, 5, 727-735.

87. Wang, H.F., (2000): Theory of Linear Poroelasticity with Applications to Geomechanics and Hydrogeology, Princeton University Press, Princeton, NJ.

88. Wang, Z., and Nur, A., (1990):"Dispersion Analysis of Acoustic Velocity in Rocks", Journal of the Acoustical Society of America, **87**, 6, 2384-2395.

89. Whyatt, J.K., (2001): "A Method for Modeling Variation of In-situ Stress Related to Lithology", Proceedings - Symposium on Rock Mechanics, **38**, 2, 1087-1094.

90. White, J. E., Martineau-Nicoletis, L., and Monash, C., (1983),"Measured Anisotropy in Pierre Shale", Geophysical Prospecting, **31**, 709-725.

91. Winkler, K.W., (1994): "Laboratory Observations of Azimuthal Velocity Variations Caused by Borehole Stress Concentrations", SEG Annual Meeting Expanded Technical Program Abstracts with Biographies, **64**, 133-1135.

92. Winkler, K.W., Plona, T., Hsu, C., Sinha, B.K. and Kostek, S., (1994): "Effects of Borehole Stress Concentrations on Dipole Anisotropy Measurements", SEG Annual Meeting Expanded Technical Program Abstracts with Biographies, **64**, 1136-1138.

93. Winkler, K.W., (1996):"Azimuthal Velocity Variations Caused by Borehole Stress Concentrations", *Journal of Geophysical Research, B, Solid Earth and Planets*, **101**, 4, 8615-8621.

94. Winkler, K.W, Sinha, B.K., and Plona, T.J., (1998): "Effects of Borehole Stress Concentrations on Dipole Anisotropy Measurements", *Geophysics*, 63, 1, 11-17.